UNIVERSITÀ
DI PAVIA

Doctoral Thesis

Control and estimation strategies in Battery Management Systems

Author:
Dr. Diego Locatelli

Supervisor:
Prof. Davide M. Raimondo

A thesis submitted in fulfillment of the requirements
for the degree of Doctor of Philosophy

in the

Identification and Control of Dynamic Systems Laboratory
Department of Electrical, Computer and Biomedical Engineering

“*I’m gasoline*
I’m burnin’ clean
Your light eclipsed the moon
Electrolite”

R.E.M.

UNIVERSITY OF PAVIA

Abstract

Faculty Name
Department of Electrical, Computer and Biomedical Engineering

Doctor of Philosophy

Control and estimation strategies in Battery Management Systems

by Dr. Diego LOCATELLI

Battery management systems (BMSs) play a critical role in the control and monitoring of battery operations, particularly for lithium-ion batteries. This thesis focuses on several key aspects of BMSs, aiming to improve their effectiveness and reliability. BMSs are essential to the control and optimization of battery performance, ensuring safety, efficiency, and longevity. This thesis focuses on strategies for control and estimation in battery systems. The challenges are posed by the complexity of lithium-ion battery systems, and only a few quantities such as temperature, current, and voltage are usually measurable.

The thesis addresses state estimation in battery systems, considering the challenges of limited number of sensors. Most used approaches in this field rely on mathematical models like Equivalent Circuit Models (ECMs) and Electrochemical Models (EMs). Novel set-based techniques, including intervals, zonotopes, and constrained zonotopes, are introduced for the first time in this field. These set-based approaches, assuming bounded uncertainty and noise, improve fault detection and analysis. The proposed scheme, utilizing constrained zonotopes, efficiently detects thermal faults in battery cells despite unknown but bounded uncertainties, surpassing traditional methods.

Furthermore, joint estimation of states and parameters in battery systems has been explored, highlighting the impact of uncertain parameters on equivalent circuit models (ECMs). The analysis emphasizes the importance of careful model selection and design for accurate estimation and observability. The results obtained in this study demonstrate the application for the first time in the battery sector of these set-based strategies based on constrained zonotopes using various equivalent circuit models. These have proven particularly effective when compared to other set-based strategies present in the literature. By harnessing the tunability, flexibility, and ability to capture mutual dependencies among the various quantities to be estimated, a joint estimation of states and parameters has been performed. This joint estimation has shown to be even more effective in terms of set volumes compared to pure state estimation.

The combination of accurate state parameter estimation and advanced modeling plays a crucial role in addressing control challenges in lithium batteries. This approach helps optimize charging strategies and mitigate the effects of aging.

Whitin this aspect the thesis focuses on optimizing the control of Battery Management Systems (BMSs), with a specific aim at finding the best charging strategies for lithium-ion batteries while minimizing the impact of aging. The approach involves utilizing surrogate models that combine static nonlinear models dependent on the state of charge with finite-dimensional linear-time-invariant model. The strategy is designed to enhance the charging process while making sure aging-related and safety limits are met, thus promoting the long-term health and performance of battery systems. To enable accurate closed-loop control, a Kalman Filter with a forgetting factor is employed for state estimation, improving the precision of the control system. In the context of lithium-ion batteries, known for their balanced performance, cost-effectiveness, and lifespan in energy storage, the Battery Management System plays a crucial role. The BMS aims to strike the right balance between fast charging and minimizing aging effects while ensuring safety requirements are met. The goal is to minimize side reactions, optimizing charging while meeting aging-related and safety constraints. Simulation results using a DFN battery model as a representation of the actual system demonstrate the effectiveness of the proposed strategy. The Kalman Filter with a forgetting factor is used for state estimation, providing adaptability to the control system.

To sum up, the results presented in this thesis establish a crucial foundation for the improvement of Battery Management Systems (BMSs), contributing to enhanced robustness and efficiency in the safe and optimal operation of battery systems.

Acknowledgements

Completing my doctoral journey was not an easy feat. Many challenges were encountered along the way, both in my academic life and in the external world. It took a good deal of patience, acceptance, resilience, and perseverance, not only on my part but also for the people who accompanied me. I would like to dedicate this thesis to all those who know everything I have felt and experienced over these years, intense joys and pains, and to all those who believe that the completion of this work is a source of pride for them and for me.

I want to express my gratitude to my family, my mother Maria and my father Luigi, who supported my sacrifices and always provided unwavering support. They have always been two individuals who cheered me on and respected me, providing a boost of self-esteem that never wavered.

Thanks to my brother Alex, there was a time when a younger version of me needed math tutoring and struggled to understand how to approach problems analytically. He may not have pursued a scientific path, but he could do anything and has always been a source of rescue with his advice.

Thanks to my grandmother Piera and her light-heartedness, even in the face of the toughest obstacles, she remains an inspiration.

Thanks to Martina, for bringing sweetness and love into my life and for sharing all the highs and lows. I want to tell you that a doctoral journey is a continuous endeavor filled with apparent disappointments for things that don't work out as planned, but they are necessary to create the beautiful moments of satisfaction, like climbing a mountain that rewards you with a breathtaking view at the top.

Thanks also to your family, Antonella, Jerry, and Emma, for all the affection and support. I am grateful to all the people I met on this long journey, and especially to those who supervised my work, Professor Raimondo, for his valuable guidance and for teaching me precision and attention to detail.

Above all, thanks to our collaboration and your availability, despite the serious threat posed by COVID to the entire experience, I have achieved several accomplishments and had the opportunity to travel extensively. In this regard, I thank all the people I met and got to know at various conferences and seminars for their advice and engaging discussions, as well as the enjoyable moments of relaxation. I would also like to thank all those who have collaborated on all my publications, especially Prof. Guilherme Raffo and Dr. Brenner Santana Rego, for their valuable advice and for everything I have been able to learn through their collaboration. One of the most beautiful moments of my research journey and my life was undoubtedly my time in Eindhoven. A big thank you goes to Professor Tijs Donkers and HJ Bergveld for welcoming me and supervising my work during that period. My luck was not only finding two great professionals but also two fantastic individuals with whom it was a pleasure to share thoughts and stories—two kindred spirits with whom I got along splendidly. In Eindhoven, I met many people who welcomed me into their families, and I do not want to let them go. Many thanks to all the members of the CS group. In particular, thanks to Feye for the great conversations and advice, and to all the students who worked with me on the same topics, Francis and Yannick. Thanks again to Gustavo and Victor for introducing me to the Hubble and the eccentric discussions on life's important dilemmas. Thanks to Cristi, Chris, and Stefanie for the great moments we shared, even in Japan. And last but not least, the colleagues who shared my academic journey in Pavia. I thank all the professors at Labsisdin for their valuable advice and fun lunch breaks. A heartfelt thank you to a kindred spirit like me, Andrea Pozzi,

from whom I have gained and learned a lot—a shining example of humanity and professionalism. I have never received a "no" from him, and he has always helped me on all fronts. I will never have the opportunity to repay him enough.

Thanks to Nikolas, Jorge, Irene, Berhouz, and Mori for always being in the game and for your companionship. Finally, a special thank you to those who started and finished the entire journey with me, Francesca and Giacomo, two true friends. One of them was even a roommate who claimed to be a great cook but would heat up pre-made risotto while me, in my suffering, I had no choice but to accept and eat it thirstily. At that moment, I believe both of us wished you were on a beautiful train headed far away. I'm joking, of course; it was touching to see you concerned after I tumbled into a canal and lost everything. The other, a lioness who, like the best characters in literature, has made her way and evolved, a bit like a Pokémon, and faced all of this as a mother to Bruno, which only women and their power know how to do.

Contents

List of Figures

List of Tables

List of Abbreviations

DP	**D**ual **P**olarisation
SOC	**S**tate **O**f **C**harge
SOH	**S**tate **O**f **H**ealth
ECM	**E**quivalent **C**ircuit **M**odel
OCP	**O**pen **C**ircuit **P**otential
EM	**E**lectrochemical **M**odel
EKF	**E**xtended **K**alman **F**ilter
RMSE	**R**oot **M**ean **S**quared **E**rror
P2D	**P**seudo **T**wo **D**imensional
DFN	**D**oyler **F**uller **N**ewman
SPM	**S**ingle **P**article **M**odel
SPMT	**S**ingle **P**article **M**odel with **T**hermal dynamics
SPMeT	**S**ingle **P**article **M**odel with **T**hermal and electrolyte dynamics
CZ	**C**onstrained **Z**onotopes
FIM	**F**isher **I**nformation **M**atrix
CSP	**C**onstrained **S**atisfaction **P**roblem
FBCP	**F**orward **B**ackward **C**onstraint **P**ropagation
MPT	**M**ulti **P**arametric **T**oolbox
OC	**O**ver **C**harging
OD	**O**ver **D**ischarging
ISC	**I**nternal **S**hort **C**ircuit
ESC	**E**xternal **S**hort **C**ircuit
BMS	**B**attery **M**anagement **S**ystem
CC	**C**onstant **C**urrent
CV	**C**onstant **V**oltage
CC-CV	**C**onstant **C**urrent **C**onstant **V**oltage
MSCC	**M**ulti **S**tage **C**onstant **C**urrent
SEI	**S**olid **E**lectrolyte **I**interphase
DAE	**D**ifferential **A**lgebraic **E**quation
PDAE	**P**artial **D**ifferential **A**lgebraic **E**quation
ODE	**O**rdinary **D**ifferential **E**quation
MPC	**M**odel **P**redictive **C**ontrol
FD-LTI	**F**inite **D**imensional **L**inear **T**ime **I**nvariant
LTI	**L**inear **T**ime **I**nvariant
SQP	**S**equantial **Q**uadratic **P**rogramming
QP	**Q**uadratic **P**rogramming
LP	**L**inear **P**rogramming
FDM	**F**inite **D**ifference **M**ethod
FVM	**F**inite **V**olume **M**ethod

List of Symbols

C_{batt}	nominal cell capacity	As
R_c	conduction resistance	K/Ws
R_u	onvective resistance	K/Ws
C_c	core heat capacity	Ws^2/K
C_s	surface heat capacity	Ws^2/K
$E_{a,\psi}$	activation energy linked ψ	J
t_+	transference number	
$D_e(T(x,t))$	electrolyte diffusion coefficient	m^2/s
p_j	Bruggeman coefficient	
L_j	length of the j-th section	m
$c_{s,n}^{\max}$	maximum concentration of ions in the solid phase	mol/L
$D_{s,i}(T(x,t))$	solid diffusion coefficient	m^2/s
a_i	specific active surface area	m^2
$R_{p,i}$	particle radius	m
$\Delta\theta_p$	battery stochiometry	mol
A	current collector area	m^2
L_j	length of the j-th electrode section	m
c_s	ion concentration in the solid phase	mol/L
c_e	ion concentration in the electrolyte	mol/L
$D_{s,i}(T(x,t))$	temperature-dependent solid diffusion coefficient	m^2/s
$j_i^{\mathrm{int}}(x,t)$	intercalation ionic flux	mol /(m^2 s)
$i_{0,j}(x,t)$	intercalation exchange current density	A/m^2
$c_s^*(x,t)$	Li-ion surface concentration	$\mathrm{mol}/\mathrm{m}^2$
$j_i^{\mathrm{side}}(x,t)$	side reactions contributing to ageing degradation	V
$U_i(\theta_i^*(x,t))$	open-circuit potential of each electrode	V
R_{SEI}	SEI resistance	Ohm
$V(t)$	terminal voltage	V
$c_s^{\mathrm{avg}}(x,t)$	volume-average concentration	$\mathrm{mol}/\mathrm{m}^3$
$C_{p,j}$	specific heat capacitance	J/K
λ_j	thermal conductivity	W/(m K)
$Q_{\mathrm{ohm}}(x,t)$	ohmic heat source	J
$Q_{\mathrm{rxn}}(x,t)$	reaction heat source	J
$Q_{\mathrm{rev}}(x,t)$	reversible heat term	J
h_c	the convective heat coefficient	W/(m^2 K)
T_{env}	environmental temperature	K
M_w	molar weight of the negative electrode	g/mol
v	film admittance	S
$j_n^{\mathrm{side}}(x,t)$	side-reaction flux	Nm^2/C
$i_{\mathrm{side},0}(t)$	side-reaction exchange current	A
U_{SEI}	reference potential for the SEI side reaction	V
U_{pl}	reference potential for the lithium-deposition side reaction	V
N	number of discretization volumes	

$\overline{q}_i(t)$	volume-averaged concentration side-reaction	mol/L
$c_{e,j}^{[k]}(t)$	electrolyte concentration	mol/L
$V_{\mathrm{OCP}}(t)$	overall open circuit potential	V
k_i	rate reaction constant	
$\overline{c}_{e,i}(t)$	average electrolyte concentration	mol/L
ϵ_j	material porosity	
τ_j	tortuosity	
$\epsilon_i^{\mathrm{act}}(t)$	active material volume fraction	m^3
$\eta_i(x,t)$	electrode overpotential	V
$\Phi_s(x,t)$	solid-phase potential	V
σ_i	electrode conductivity	S/m
$\Phi_e(x,t)$	electrolytic potential	V
$\kappa(c_e(x,t),T(x,t))$	electrolyte conductivity coefficient	S/m
$\eta^{\mathrm{side}_{n,\mathrm{SEI}}}(x,t)$	side-reaction overpotential	V
$\overline{\theta}_p(t)$	cathode average stoichiometry	mol
$\theta_i^{100\%}$	stoichiometry at battery fully charged	mol
$\theta_i^{0\%}$	stoichiometry at battery fully discharged	mol
$\kappa(c_{e,j}^{[k]}(t),T(t))$	electrolyte conductivity	S/m

Chapter 1

Introduction

Lithium-ion batteries have become widespread in many commercial sectors (see e.g. Figure 1.1), proving to be essential tools in numerous applications. Their adoption has been primarily driven by their ability to offer significant advantages, including high cell voltage, low self-discharge rate, exceptional cycling durability, and high energy density (Meesala et al., 2017). A comprehensive overview of the main advantages of lithium-ion batteries over other chemistries is shown in Figure 1.2

The demand for high-performance rechargeable batteries has become exceedingly evident in recent years, with various requirements and functions now considered common knowledge. However, this fervor for advanced lightweight batteries has not always been the norm. Battery research started relatively modestly and gained significant popularity over time. Perhaps it was the creation of the transistor, miniaturized to a sufficient scale, that ignited the quest for better rechargeable batteries. Alternatively, it could have been born out of sheer scientific curiosity. Regardless of the initial driving force, approximately three decades ago, Sony Co. successfully commercialized the world's first lithium-ion battery (LIB). This breakthrough revolutionized portable electronics, sparking a surge in research interest (Li et al., 2018). The automotive battery market has seen impressive growth in the last decade, particularly in the context of lithium-ion batteries. LIB production capacity has grown sixfold, from 11 GWh in 2006 to 78 GWh in 2016. Global demand for LIBs has been rising steadily, doubling approximately every five years. Projections suggest that by 2030, global LIB capacities could reach 390 GWh (Zubi et al., 2018).

Despite this growth, the market share of electric cars, specifically plug-in Electric Vehicles (PEVs), remains relatively low. In 2016, PEVs accounted for just 0.86% of global new car sales, although this figure had been gradually increasing in previous years. Governments have also played a role in promoting EV development through various incentives and grants. Forecasts for the automotive LIB market are positive, with expectations of substantial growth. However, challenges persist in achieving widespread electric vehicle adoption, including uncertainties around the maturity and cost-effectiveness of energy storage technologies required for long-range EVs. Government support and collaboration among stakeholders are crucial to address these challenges and advance electric vehicle technology.

Furthermore, governments worldwide became increasingly aware of the role of greenhouse gases in climate change, prompting initiatives in green energy technologies (such as solar and wind) and electric vehicles, with energy storage systems playing a central role. As a result, research into batteries experienced substantial growth, as evidenced by Figure 1.3. In just seven years, researchers globally contributed over 119,000 new publications on batteries from 2010 to 2017, marking a remarkable 260% increase in total literature volume, significantly outpacing the overall growth rate of published literature across all research fields.

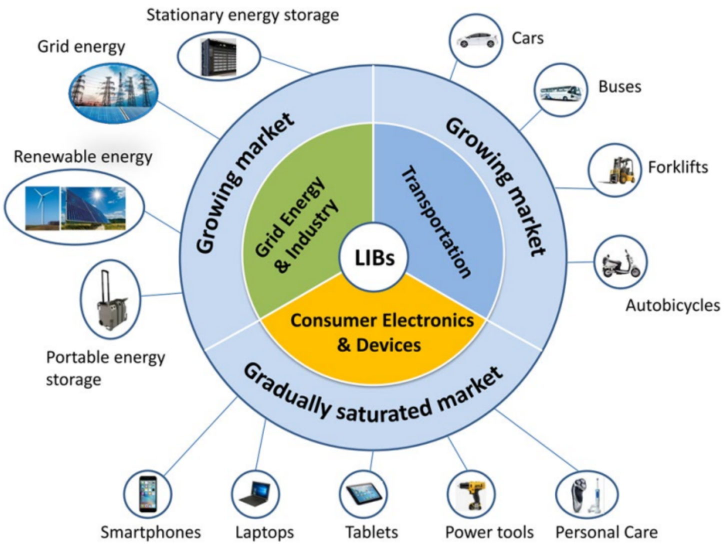

FIGURE 1.1: Lithium-ions batteries find applications in three main sectors: consumer electronics and devices, transportation, and grid energy and industry (Ding et al., 2019).

While the growth in battery research is impressive, the fundamental goals have remained constant over the years: reducing battery weight and size, enhancing cycle durability, maintaining safety, and minimizing costs have consistently been the primary objectives for battery scientists.

The world is currently facing serious environmental challenges, including global warming and greenhouse gas (GHG) emissions resulting from the extensive use of diesel and petrol in vehicle operations (Hannan et al., 2017). These emissions contribute to the release of tons of CO_2 annually (Sulaiman et al., 2015). Additionally, the volatile nature of crude oil prices poses significant challenges to the automobile industry, highlighting the need for alternative fuel-driven vehicles. In response to these pressing issues, the implementation of Electric Vehicles (EVs) has garnered substantial attention and interest among academic researchers and automotive specialists due to their potential to reduce GHG emissions (Poullikkas, 2015).

The adoption of rechargeable batteries in EV applications has witnessed a surge in popularity in recent years (Shareef, Islam, and Mohamed, 2016). This trend is driven by the intermittent nature of renewable energy sources such as solar and wind energy, which may not provide continuous and reliable power supply when needed (Daud, Mohamed, and Hannan, 2013). Various energy storage technologies, including lead-acid, NiMH, and lithium-ion batteries, have been deployed in EVs (Manzetti and Mariasiu, 2015). Among these, lithium-ion batteries have gained widespread acceptance due to their high energy density, long lifespan, and efficiency (Saw, Ye, and Tay, 2016). Recognizing the lucrative prospects of lithium-ion batteries, substantial investments have been directed towards enhancing their stability and robustness. Despite their relatively high initial cost, the market growth of lithium-ion batteries has been steadily increasing and is anticipated to continue on this trajectory.

To ensure the effective operation of such intricate devices (Bergveld et al., 2002; Notten, Veld, and Van Beek, 2005; Tarascon and Armand, 2001; Lu et al., 2013), the implementation of an appropriate Battery Management System (BMS) is imperative.

The performance of these batteries can be further elevated through the utilization

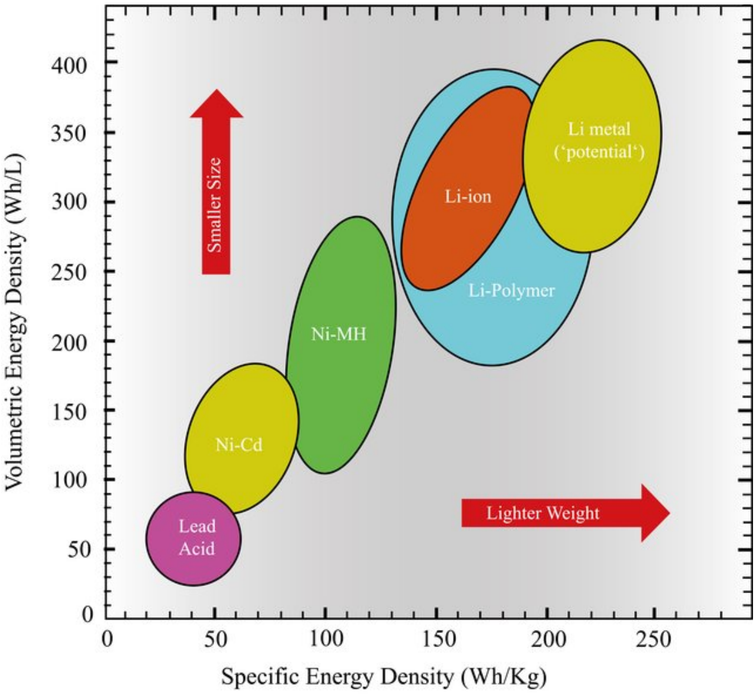

Figure 1.2: Volumetric and gravimetric energy density (for different battery technologies) (Hossein Nezhad Shirazi, 2020)

of advanced BMS solutions. These solutions rely on mathematical models of the battery (Chaturvedi et al., 2010), enabling optimization in both the battery cell design phase and routine management. Within the field of advanced BMS functionality, key areas addressed in the literature encompass state estimation, fault diagnosis, safety management, and fast charging (Fleischer et al., 2016; Lu et al., 2013).

Moreover, in-depth mathematical models play a important role in simulating battery cycles under specific initial and environmental conditions. This aids researchers in comprehending battery behavior while reducing the need for extensive and time-consuming experiments. Various open-source battery simulator software packages are available, including DUALFOIL (Albertus and Newman, 2007), Scott Moura's fastDFN, LIONSIMBA (Torchio et al., 2016), M-PET (Smith and Bazant, 2017), and PyBaMM (Sulzer et al., 2021).

In advanced BMS applications, two primary categories of models come into play: Equivalent Circuit Models (ECMs) (He, Xiong, and Fan, 2011; Nejad, Gladwin, and Stone, 2016) and Electrochemical Models (EMs) (Gomadam et al., 2002; Santhanagopalan et al., 2006; Ramadesigan et al., 2012). While ECMs offer simplicity and intuitiveness, EMs provide a detailed depiction of electrochemical processes occurring within a cell.

Among EMs, the Pseudo-Two-Dimensional (P2D) model (Doyle, Fuller, and Newman, 1993a), also known as the Doyle-Fuller-Newman (DFN) model, enjoys widespread use. However, due to its significant computational demands, the P2D model is more suited for simulations than real-time control applications. Additionally, its utility within a control framework is hampered by identifiability and observability challenges. Consequently, the research community has shown considerable interest in simplified electrochemical models. These models offer faster simulation, better identifiability, observability, and still offer a reasonable description of internal cell phenomena (Pozzi

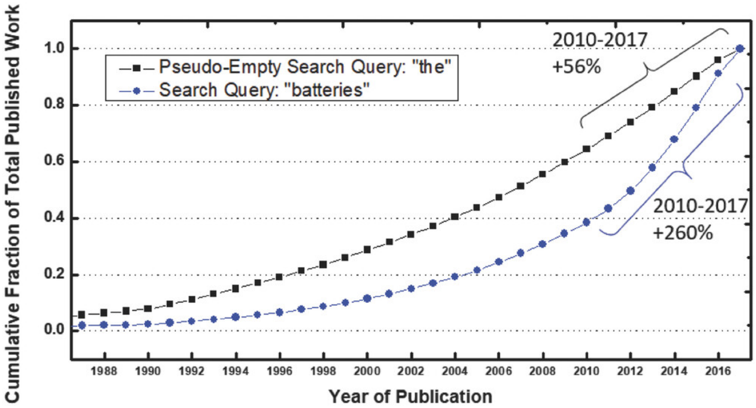

FIGURE 1.3: An analysis of literature expansion from 1987 to 2017 was conducted, comparing the growth in publications related to the search query batteries (depicted as blue circles) with that of a virtually empty search query the (represented by black squares). This analysis was carried out within the research domain designated as "topic" and utilized the Web of Science website, accessed via https://webofknowledge.com/ on October 25, 2017.

and Raimondo, 2021).

Among these simplified models, the Single-Particle Model (SPM) (Santhanagopalan et al., 2006), derived from the P2D model by representing the electrodes as single particles, has garnered significant attention.

The widespread adoption of lithium-ion batteries (lithium-ion) in various sectors has brought significant advancements in energy storage technology. However, to further harness the potential of lithium-ion, there are critical challenges that need to be addressed. This thesis aims to contribute to the ongoing efforts in tackling these challenges, which have become crucial in the context of lithium-ion and their management through Battery Management Systems (BMS).

Addressing these issues is not only essential for the continued development of lithium-ion but also has broader implications for industries relying on energy storage solutions. The safe and efficient operation of lithium-ion, managed by advanced BMS, is critical for renewable energy integration, electric transportation, and grid stability, making these challenges significant open issues in the field. This thesis contributes to provide valuable insights and solutions for the advancement of LiB technology and the role of BMS in achieving these advancements.

In the upcoming Section 1.2, we will explore several ongoing issues related to lithium-ion batteries and the contribution that this thesis aims to give. To be more specific, state estimation approaches is discussed in Section 1.2.1, which are essential for accurately assessing the current state of lithium-ion, joint state and parameter estimation in Section 1.2.2, which seeks to enhance the precision of LiB characterization, fault detection in Section 1.2.3, which is vital for identifying and mitigating potential issues in lithium-ion, and ageing-aware charging protocols in Section 1.2.4), which aim to extend the lifespan of lithium-ion by optimizing charging strategies, as the demand for quick and convenient energy replenishment grows, optimizing the charging process while ensuring the safety of lithium-ion has become a top priority

1.1 Motivation

While lithium-ion batteries have shown to be revolutionary in terms of energy density, cycle life, and reliability, several difficulties remain that prevent them from performing optimally and lasting as long as they should.

Managing the intricacies of lithium-ion demands advanced procedures and techniques for precise state estimation, fault detection, and charging protocols. Real-time monitoring and management of lithium-ion batteries are critical for maintaining effective functioning, avoiding potential risks, and extending their lifespan.

State and parameter estimates are essential components of efficient battery management systems (BMS), offering crucial information on the battery's condition, state of charge, and general functionality. Conventional estimating approaches frequently fail to accurately account for the inherent uncertainties, nonlinearities, and complexity related to LiB dynamics. As a result, this leads to lower performance and decreased reliability.

Fault detection is an essential component of battery management, with the goal of immediately identifying and addressing possible abnormalities and malfunctions. Precise and prompt identification of faults is crucial for preserving battery integrity, averting disastrous malfunctions, and guaranteeing operational safety. Traditional fault detection methods may lack the ability to effectively manage the different operating situations and uncertainties that are inherent in lithium-ion technology. This emphasises the necessity for new and creative approaches.

Moreover, as renewable energy sources like solar and wind become more integrated into the power grid, there is a growing need for charging protocols for lithium-ion batteries that are both efficient and considerate of their ageing process. Aging-aware charging procedures are designed to optimise the charging process in order to minimise deterioration, prolong battery longevity, and assure constant performance over time, while still upholding safety regulations.

Considering the difficulties and the crucial importance of lithium-ion in many applications, it is imperative to create advanced methods and strategies that are specifically designed to tackle the unique complexity and uncertainties connected with lithium-ion.

This thesis addresses the critical issues by specifically focusing on the following crucial aspects:

- **State and parameter estimation using set-based methods:** creating novel set-based methodologies to increase the reliability and sustainability of state and parameter estimates in lithium-ion batteries, effectively accounting for uncertainties and nonlinearities to enhance precision and efficiency.

- **Set-Based Fault Detection:** proposing advanced set-based fault detection techniques capable of identifying and mitigating potential anomalies and faults in lithium-ion more accurately and efficiently, enhancing safety and reliability.

- **Ageing-Aware Charging of Lithium Batteries:** developing optimal charging procedures that take into account battery ageing and degradation, optimising the charging procedure to prolong battery longevity, uphold performance, and guarantee safety.

This project intends to address the crucial areas in battery management techniques and fill the current gaps. It seeks to propose creative solutions that will improve the efficiency, safety, and lifespan of Lithium-ion batteries. This thesis makes significant contributions to the advancement of battery technology, which will facilitate its sustainable integration into many applications and promote the shift towards a cleaner and more sustainable energy future.

1.2 Thesis contributions

1.2.1 Set-based state estimation of lithium-ion batteries

Traditional methods for SOC estimation, such as look-up tables that exploit the relationship between SOC and measurable parameters like the Open Circuit Potential (OCP), have limitations in real-time operations Xiong et al., 2017. This is primarily because OCP measurements can only be obtained under stationary conditions. Coulomb counting, another commonly used method for SOC estimation Piller, Perrin, and Jossen, 2001, suffers from accuracy issues due to drift errors caused by current measurement disturbances and uncertainties in cell capacity. While SOC estimation is vital, the employment of a model-based controller necessitates the estimation of the full battery state.

In the battery field, various stochastic approaches have been applied to state estimation, including Extended Kalman filtering (Di Domenico, Stefanopoulou, and Fiengo, 2010; Bizeray et al., 2015), sliding-mode observer (Kim, 2009), Sigma-point Kalman filtering (Plett, 2006), Particle filtering (Tulsyan et al., 2016), and Moving Horizon Estimator (Hu, Cao, and Egardt, 2018). These stochastic methods assume knowledge of the probabilistic distributions of uncertainties. Conversely, set-based estimation considers unknown but bounded uncertainties, making it more reliable when physical bounds are available, as is the case with ECM parameters. In practical scenarios, knowing the exact distribution of uncertainties is rarely feasible.

Different set representations have been utilized for state estimation, including intervals (Jaulin et al., 2001), polytopes (Shamma and Tu, 1997), zonotopes (Alamo et al., 2008), and constrained zonotopes (Rego et al., 2020a). The choice of set representation depends on the desired accuracy and computational burden for describing the set of interest as they differ in precision and computational effort.

In dealing with highly nonlinear systems, it is crucial to select a methodology that can handle conservatism effectively. This conservatism can arise from factors such as the dependency effect, wrapping effect, and linearization errors. Notably, set-based estimation has been sparingly utilized in the context of batteries, with a notable example found in Zhang et al., 2020. Their study proposes a continuous-time ECM-based interval observer for SOC estimation in a parallel connected lithium-ion battery pack. However, their approach assumes continuous-time measurements, which is unrealistic as sensors have finite sampling rates. Additionally, the coupling between parameters, usually present during identification procedures, is not considered. An interval PDE observer is implemented in (Perez and Moura, 2015), for state estimation of an electrochemical model and finally an interval-based approach has been employed for SOC estimation of a single cell in (Rausch et al., 2014). In this thesis, we have developed a discrete-time interval observer for a single lithium-ion cell based on the forward-backward method as described by (Jaulin et al., 2001). Specifically, we have taken into consideration parametric uncertainties, which were obtained through an identification procedure using data collected from a well-known Single Particle Model with electrolyte dynamics (SPMe) (Pozzi et al., 2018). The primary contributions of this thesis include: (i) the identification of ECM parameter bounds based on the Fisher Information Matrix; and (ii) a discrete-time interval state estimation method based on inclusion functions and constraint propagation, capable of handling discrete-time measurements. Numerical experiments demonstrate the efficiency of the proposed methodology and its ability to provide accurate estimates for both the State of Charge (SOC) and the electric state variables of the ECM. Additionally, we incorporated a set-based state estimation approach using constrained zonotopes, which, unlike intervals, takes into account the mutual dependencies among the states. Material related to this contribution has appeared in

- (Locatelli et al., 2021) Locatelli, D., Rego, B. S., Raffo, G. V., Raimondo, D. M. (2021). Interval state estimation based on constraint propagation for a lithium-ion cell using an equivalent circuit model. IFAC-PapersOnLine, 54(3), 602-608.

- (Saccani et al., 2022) Saccani, G., Locatelli, D., Tottoli, A., Raimondo, D. M. (2022). Model-based thermal fault detection in lithium-ion batteries using a set-based approach. IFAC-PapersOnLine, 55(6), 329-334.

1.2.2 Set-based state and parameter estimation

In recent years, the field of state estimation has witnessed a surge in significance and attention across diverse research domains. This heightened interest extends to critical applications such as robot localization (Saeedi et al., 2016) and fault detection and isolation (Raimondo et al., 2016). Within this context, the estimation of parameters and the joint estimation of both states and parameters have assumed key roles.

Set-based state estimation methods have emerged as formidable tools capable of providing reliable enclosures of system trajectories. These methods do not rely on a priori knowledge of the stochastic properties of unknown variables, making them particularly valuable when dealing with uncertainties characterized by known bounds (Chisci, Garulli, and Zappa, 1996; Scott et al., 2016a). Set-based parameter estimation has gained prominence as a viable alternative to traditional stochastic methods like least squares or maximum likelihood. It offers a robust solution for scenarios where model parameters exhibit unknown stochastic properties but known bounds. Consequently, it ensures the encapsulation of model parameters within well-defined bounds.

Notably, this thesis introduces a novel approach for set-based joint state and parameter estimation within discrete-time systems described in Rego et al., 2021a. Building upon the foundational algorithms rooted in constrained zonotopes (CZs) proposed in (Scott et al., 2016a) and (Rego et al., 2021b), this strategy unifies the estimation of states and parameters within a single cohesive framework. Unlike interval-based techniques, our CZ-based approach excels at preserving and propagating existing interdependencies between states and model parameters. Furthermore, it employs generalized intersections to refine both state and parameter enclosures, a key distinction from zonotope-based methods. These advances substantially elevate the accuracy of both state and parameter estimation, as underscored by three illustrative numerical examples that encompass linear and nonlinear discrete-time systems.

Lithium - ion battery cell mathematical models encompass numerous unknown parameters, making parameter estimation a crucial step in gaining a deeper understanding of the process and refining state estimation. Various methods have been proposed in the literature to tackle this challenge.

One approach, as exemplified in (Lai et al., 2021), employs a least-squares (LS) algorithm to estimate parameters for an Equivalent Circuit Model used to describe the electrical characteristics of lithium-ion batteries. Least-squares algorithms are commonly used for parameter estimation and are known for their simplicity.

In contrast, Pozzi et al., 2018 takes a different approach by using optimal experimental design to enhance the identifiability of model parameters. Optimal experimental design allows for efficient planning of which experimental data to acquire to obtain more accurate parameter estimates.

The work in Jackey et al., 2013 proposes a layered optimization technique for parameter identification in batteries, which is based on the widely-used Matlab/Simulink platform.

It's worth noting that all of these works provide a single-point estimate as the outcome, rather than a range of possible values.

On a different note, Zhou et al., 2020 employs interval-based methods for identifying ECM model parameters, taking into account the uncertainties in model parameters to provide more robust estimates.

Some state estimation approaches aim to enhance accuracy by refining the model's parametric uncertainties, a method known as joint state and parameter estimation. In this vein, certain studies have applied extended Kalman filtering with sensitivity analysis, as seen in (Rauh and Aschemann, 2012), and sigma point Kalman filtering as illustrated in (Plett, 2006). Additionally, particle filtering has been used for online estimation, as documented in Samadi, Alavi, and Saif, 2013.

Notably, to the best of our knowledge, the application of set-based methods for joint state and parameter estimation in the battery domain has been uncharted territory. This gap in the literature prompts our exploration into this promising approach.

Within the field of set representations, Scott et al., 2016b introduces Constrained Zonotopes (CZs) as an alternative to intervals. These CZs can provide tighter estimates with a slightly higher computational cost. CZs combine the flexibility of polytopes with the scalability of zonotopes, making them an intriguing choice for estimation tasks. This contributions has previously appeared in:

- (Rego et al., 2022a) Rego, B. S., Locatelli, D., Raimondo, D. M., Raffo, G. V. (2022). Joint state and parameter estimation based on constrained zonotopes. Automatica, 142, 110425.

- (Locatelli et al., 2022a) Locatelli, D., Saccani, G., Rego, B. S., Raffo, G. V., Raimondo, D. M. (2022, November). Set-based joint state and parameter estimation of a lithium-ion cell using constrained zonotopes. In 2022 IEEE Vehicle Power and Propulsion Conference (VPPC) (pp. 1-6). IEEE.

1.2.3 Set-based fault detection

The safe operation of lithium-ion batteries is a critical aspect to consider during their use. Several different faults can occur that can result in degraded performance and hazardous consequences, such as explosions and fires. These faults can be classified into three main categories: cell faults, sensor faults, and actuator faults.

Cell faults, the most critical of the three, include overcharging (OC), overdischarging (OD), overheating, internal short circuit (ISC), external short circuit (ESC), and thermal runaway Bandhauer, Garimella, and Fuller, 2011; Hu et al., 2020. These faults can pose a significant risk to the safe operation of the battery.

Sensor faults, on the other hand, cause issues in the feedback loops of the BMS control system Xiong et al., 2019. Actuator faults, such as cooling system faults, bus faults, and connector faults Liu et al., 2014, can also impact the functioning of the battery.

The BMS plays a crucial role in maintaining the safety of lithium-ion batteries. It constantly monitors the battery pack's voltage, current, and temperature to determine the best way to operate the battery and prevent faults from occurring. When a fault does occur, the BMS can help detect it and minimize its effects. The BMS can also diagnose faults using various diagnostic methods to help ensure the safe operation of the battery.

The safe operation of lithium-ion batteries requires careful monitoring and management, with the BMS playing a critical role in preventing faults and maintaining the safety of the battery during operation.

Many fault diagnostic algorithms have been developed for lithium-ion batteries, which can be divided into two different groups based on their methodology: data-driven and model-based. Data-driven methods detect faults by analyzing data without relying on a model, while model-based methods use a mathematical representation of the battery system to identify faults.

Data-driven methods include those based on correlation coefficients, such as the interclass correlation coefficient-based method proposed in Xia et al., 2017a and Li and Wang, 2018, which can detect ISCs and off-trend voltage drops respectively. Shannon entropy theory is used in Wang et al., 2017 and Liu et al., 2018 to capture thermal abnormalities and predict faults. Probabilistic rule-based methods, such as the one proposed in Xiong et al., 2012, use unusual drops in voltage and spikes in temperature to detect OD failures. Big data statistical methods, including a neural network algorithm, are employed in Zhao et al., 2017 to find abnormal changes in cell terminal voltages.

One advantage of data-driven methods is that they can be used on both battery packs and single cells, as they do not require any prior knowledge of the battery system. However, the tuning of data-driven methods can be time-consuming and costly, and therefore is often performed offline.

Model-based methods, on the other hands, rely on the mathematical model of the cell or the battery pack to detect faults. The main advantage of this approach over data-driven methods is that it provides a better understanding of the nature of the fault and can provide insight into the underlying physical processes. However, a drawback of this approach is that the mathematical model used is by definition an approximation of the true system, which can lead to inaccuracies in the fault detection.

It is worth noting that both data-driven and model-based methods have their own strengths and weaknesses. Data-driven methods have the advantage of being able to detect faults without relying on a model, but may require large amounts of data and can be more difficult to interpret. Model-based methods, on the other hand, can provide a more in-depth understanding of the battery system, but may be limited by the accuracy of the model and the availability of data for model development and validation. To address this challenge, we incorporate parametric uncertainty into the mathematical model by treating it as a disturbance that affects the system. This helps to improve the robustness of the fault detection method and to mitigate the impact of model inaccuracies on the detection performance. It should be noted that the choice between data-driven and model-based methods depends on several factors such as the specific application, the requirements of the battery system, and the available resources.

The set-based approach presented in this thesis is grounded in the use of Constrained Zonotopes (CZs) for detecting thermal faults. CZs offer a unique advantage by seamlessly blending the efficiency and scalability characteristics of zonotopes with the adaptability of convex polytopes. Consequently, they constitute an efficient methodology capable of computing significantly tighter enclosures than, for instance, intervals, all while incurring only modest additional computational costs (Scott et al., 2016a).

Initially, our focus lay exclusively on the domain of thermal faults. However, it's important to emphasize that the methodology is inherently versatile and can be extended to address various other fault types. As a means of validating the results, we propose a comprehensive comparison between CZs and interval sets. The latter are computed using a forward-backward algorithm as outlined in Jaulin et al., 2001. It's worth noting that the pursuit of the tightest possible enclosures is of paramount importance for enabling early fault detection.

In summary, the main contributions of this work can be outlined as follows:

- The application of innovative set-based methods to the domain of battery state estimation.
- Pioneering set-based fault detection techniques specifically tailored for batteries.
- A rigorous performance evaluation, comparing fault detection efficiency between interval sets and CZs.

Moreover, we broaden our scope to encompass battery packs with interconnected thermal dynamics. This expansion is driven by the recognition that dealing with faults in such systems poses a formidable computational challenge. For an effective solution, we refer readers to Saccani, Ciaramella, and Raimondo, 2022.

Moreover, we operate under the realistic assumption of having access to only a limited number of measurements, encompassing temperature and voltage. This includes cases where faults may occur in cells without dedicated sensors. The ability to detect faults under these conditions is crucial, as it's not always feasible to equip every cell with sensors.

In summary, the key contributions of this further part encompass:

- Set-based fault detection tailored for battery packs.
- Incorporation of a coupled thermal model featuring temperature-dependent parameters.
- Comprehensive comparison of different set representations, including zonotopes and CZs, for fault detection.

An earlier version of this contribution was published in:

- (Saccani et al., 2022) Saccani, G., Locatelli, D., Tottoli, A., Raimondo, D. M. (2022). Model-based thermal fault detection in lithium-ion batteries using a set-based approach. IFAC-PapersOnLine, 55(6), 329-334.
- (Locatelli et al., 2022b) Locatelli, D., Tottoli, A., Saccani, G., Raimondo, D. M. (2022, August). Thermal fault-detection in series connected lithium-ion cells: a set-based approach using constrained zonotopes. In 2022 IEEE Conference on Control Technology and Applications (CCTA) (pp. 411-417). IEEE.

1.2.4 Ageing-aware charging of lithium-ion batteries

Rechargeable batteries are commonly charged using the Constant Current Constant Voltage (CC-CV) protocol, which has become a standard in the majority of applications due to its simplicity and ease of implementation. The charging protocol involves a CC phase that transitions to a CV phase once a specific voltage is reached, and the CV phase ends when the current falls below a predefined threshold. Tuning the values of the constant current in the CC phase and the constant voltage in the CV phase can provide a trade-off between fast charging and a long cycle life. However, the CV phase can result in long charging times, compromising battery longevity if higher currents are used.

To address this issue, alternative charging protocols have been proposed in the literature to enable faster charging without sacrificing cycle life. Multi-Stage Constant Current (MSCC) protocols have been studied in several research works, such as (Khan and Choi, 2018) and (Jiang et al., 2020), highlighting their significance in improving the longevity and performance of lithium-ion batteries. Pulse-charging protocols have also been shown to be effective in Li et al., 2001 and Bhardwaj, Hwang, and Mank, 2014, where short rest intervals or discharge pulses interrupt the charging current on a regular basis to minimize concentration polarization and the possibility of negative local anode potential. Another approach is boost-charging algorithms, presented in Lee, Jeghan, and Lee, 2021, where a high average current is followed by a CC-CV with lower currents, resulting in a reduced overall charging time.

However, these algorithms do not provide guarantees of optimality and have been developed based on the nominal chemical-physical cell characteristics. Further research is needed to develop optimal charging protocols that can balance fast charging with long cycle life and guarantee optimal performance across different battery chemistries and operating conditions.

For this reason, in recent years, there has been an increasing interest in developing model-based charging strategies for lithium-ion batteries. ECMs are macroscopic models that are capable of representing the charging loss due to internal resistance and current rate, making them suitable for real-time applications. However, ECMs are unable to capture important internal state information, such as solid and electrolyte potential, ion concentration, reaction flux, and side reactions that lead to Solid-Electrolyte-Interphase (SEI) growth.

In contrast, EMs accurately describe the chemical processes occurring inside a battery, but at the cost of increased complexity. The Pseudo-Two-Dimensional (P2D) model and the Single-Particle Model (SPM) are the most popular EMs, with the former described by Partial Differential Algebraic Equations (PDAEs) and the latter obtained from a simplification of the former. However, these models need to be extended to incorporate ageing dynamics and to predict temperature, ion concentration distribution, or overpotential for use in fast-charging strategies.

Side-reaction models have been used together with the DFN model in previous studies. For example, Khalik et al. Khalik, Bergveld, and Donkers, 2020 and Lucia et al. Lucia et al., 2017 have used side-reaction models with DFN models. ECMs have been used by Jiang et al. Jiang et al., 2014 and Zhang et al. Zhang et al., 2017 to represent cell behavior, where different cost functions are designed to achieve optimal charging efficiency or minimum charging loss while charging faster. Despite their effectiveness, the complexity and high dimensionality of these models make them unsuitable for optimal real-time control. To overcome this challenge, simplified models are often used in the context of optimal control to enable efficient computation and practical real-time implementation of control strategies. Torchia et al. Torchio et al., 2016 have explored the use of model simplifications for numerical implementation. Perez et al. Perez, Hu, and Moura, 2016 have used an SPM model for fast-charging strategies. In this thesis, we introduce an innovative online optimal-control-based approach for aging-aware charging of batteries. This method focuses on minimizing side reactions within a specified charging time while satisfying various aging-related constraints.

Our approach draws inspiration from the work of Pozzi, Torchio, and Raimondo, 2018 and implements a shrinking-horizon model-predictive control technique. To achieve this, we leverage a surrogate model introduced in Khalik, Bergveld, and Donkers, 2021, which approximates the states of the DFN (Doyle-Fuller-Newman) battery model associated with aging. This surrogate model seamlessly combines a black-box Finite-Dimensional Linear-Time-Invariant (FD-LTI) model with a state-of-charge-dependent static nonlinear model. Note that the effectiveness of the shrinking-horizon technique relies heavily on the accuracy of the battery models used for optimization.

To close the feedback control loop and enhance our approach's performance, we employ a Kalman filter with a forgetting factor, as proposed by (Beelen, Bergveld, and Donkers, 2020). The efficacy of this comprehensive strategy is rigorously demonstrated through a Pareto-front analysis.

In summary, this thesis contributes significantly to the field of battery management with the following key elements: i) The development of an innovative Model Predictive Control (MPC) strategy for aging-aware battery charging. ii) The incorporation of a shrinking-horizon approach, allowing for the adjustment of the prediction horizon as the cell charges. iii) The application of a Kalman filter with a forgetting factor as a state observer in conjunction with the surrogate model, enhancing the precision of the control strategy. Content associated with this contribution has been made available in:

- (Locatelli et al., 2023) Locatelli, D., Raimondo, D. M., Khalik, Z., Bergveld, H. J., Donkers, M. T. (2023). Closed-loop Optimal Ageing-Aware Charging of lithium-ion Batteries Using a Surrogate Model. In IFAC World Congres.

1.3 Structure of the thesis

Following this introduction, the Thesis is structured as:

- Chapter 2: this chapter provides a comprehensive overview of lithium-ion batteries, emphasizing their significance in diverse applications, such as electronics, electric vehicles, and energy storage systems. It highlights the remarkable energy and charge efficiency of Li-Ion batteries due to their low internal resistance, enabling efficient operation across varying discharge rates. The chapter underscores the role of Battery Management Systems (BMS) in optimizing Li-Ion battery performance, ensuring safety, and extending their lifespan. Different BMS implementation topologies, including centralized, distributed, and modular approaches, are discussed, along with their technical, operational, and economic advantages. The chapter also acknowledges the limitations of Li-Ion batteries, such as calendar life issues and the risk of thermal runaway, emphasizing the importance of careful design and management. It anticipates future advancements in cloud-based BMS and digital twin technologies to address these limitations and enhance battery management as Li-Ion battery demand continues to grow across industries.

- Chapter 3: This chapter explores battery modeling. It covers various battery models and techniques, including equivalent circuit models such as Thévenin models, Dual Polarisation models and electrochemical models such as the Pseudo 2 dimensional model and the Single Particle model. It also covers aging modelling and thermal modelling of lithium-ion cells.

- Chapter 4: This chapter serves as an introduction to the foundational mathematical concepts necessary for understanding zonotopes and constrained zonotopes.

It begins by highlighting the significance of set representations in modeling complex systems. Subsequently, it introduces basic set operations and associated notation. The chapter then introduces the definition of zonotopes, which are sets with central symmetry, discussing their applications and operations. Finally, it presents constrained zonotopes, which extend the representation to asymmetric convex polytopes, along with strategies for reducing the complexity of set representations.

- Chapter 5: This chapter discusses set-based state estimation and its applications. Set-based state estimation considers a range of possible system states, providing a more robust representation than point-based approaches. It explores mathematical concepts like set propagation, set intersection, convex hulls, and set-based filtering algorithms. The chapter also presents a state estimation framework using constrained zonotopes, offering precise linear representations of nonlinear functions. It provides algorithms and tools for implementing set-based state estimation for complex systems with uncertainty, such as lithium batteries.

- Chapter 6: This chapter focuses on Battery Management Systems (BMSs) for battery safety and efficiency. It discusses the importance of protecting batteries from harmful operating conditions, presents a methodology for more accurate parameter characterization, and introduces a state estimation method tailored for discrete-time measurements. The chapter also explores advanced set-based state estimation techniques using zonotopes and constrained zonotopes applied to battery cells, highlighting their potential to improve state estimation accuracy and robustness. Through numerical experiments, it validates the proposed methodology and its practical significance in lithium-ion cell estimation.

- Chapter 7: This chapter focuses on lithium-ion battery safety, including potential faults leading to performance degradation and safety hazards like explosions and fires. It introduces the role of Battery Management Systems (BMS) in monitoring and preventing faults, highlighting the use of a model-based approach for fault detection, considering both the mathematical model and uncertainties. The chapter introduces problem formulation, analysis of the faulty model, numerical results, application to a single lithium cell and a three-cell series system.

- Chapter 8: This chapter introduces a novel approach for simultaneously estimating the states and parameters of nonlinear discrete-time systems using set-based methods. Building upon algorithms from a previous chapter, it incorporates constrained zonotopes for parameter estimation within a cohesive framework, improving state and parameter estimation accuracy. The chapter covers the state-of-the-art in joint state and parameter estimation, defines the discrete-time systems considered, and outlines the proposed estimator's framework. The chapter provides numerical examples to demonstrate the approach's practicality across various system types. Finally, it concludes by summarizing key findings and implications for joint state and parameter estimation in discrete-time systems.

- Chapter 9: This chapter focuses on the practical application of a set-based joint state and parameter estimation approach in the context of Lithium-ion batteries. The objective is to enhance Battery Management Systems (BMSs) by improving precision. The chapter builds upon theoretical foundations discussed earlier and introduces Constrained Zonotopes (CZs) as a novel set representation for capturing complex relationships between battery states and parameters. The method is compared to an interval-based estimator and is applied to a lithium-ion battery's electro-thermal model. Numerical results demonstrate that CZs outperform intervals in providing tighter state and parameter estimates, particularly in the thermal states. The chapter highlights the potential of CZ-based methods for practical battery management applications.

- Chapter 10: This chapter discusses an optimal ageing-aware charging strategy for Lithium-ion batteries. It aims to balance fast charging with battery longevity, utilizing a shrinking-horizon model-predictive control (MPC) approach based on a surrogate model. The strategy minimizes side reactions during charging while adhering to ageing-related constraints. It also employs a Kalman filter with a forgetting factor for state estimation. The Pareto-optimal trade-off between charging time and battery degradation is demonstrated through simulations, highlighting the advantages of the proposed approach.

Chapter 2

Lithium-ion batteries

In this chapter, we will explore the science and safety of lithium-ion batteries. These batteries power our devices and are crucial for modern technology. We will discuss the risks, efficiency, aging, and management systems that play a key role in their operation. In an increasingly electrified world, lithium-ion batteries stand as essential enablers of technological advancement. Their influence extends beyond mere convenience; it impacts the sustainability and future of energy utilization. The chapter's subsequent sections, focusing on various facets of lithium-ion batteries, will highlight why grasping their intricacies is crucial. Section 2.1 describe the history and the evolution of lithium-ion batteries. Section 2.2 describes the main battery features and operating functions. Section 2.3 shows the different type of cells packaging. Section 2.4 assesses the safety aspects of lithium-ion batteries, addressing side reactions, thermal behaviors, and safety mechanisms, in light of real-world incidents, emphasizing the need for safety measures and research. Section 2.5 discusses the gas production and safety risks associated with overcharging lithium-ion batteries, focusing on the types of gases generated, their origins within the battery, and potential hazards. Section 2.6 emphasizes the importance of safety management systems for lithium-ion batteries, ensuring they operate within specified parameters to prevent damage and hazards. It also mentions the high energy efficiency of Li-Ion cells. Section 2.7 discusses the energy efficiency and power output characteristics of Li-Ion cells, highlighting their advantages and limitations in various applications. In section 2.8 aging phenomena are discussed. Li-Ion batteries have a longer lifespan than other types but still face limitations in terms of cycle and calendar life due to chemical processes at high voltages. Battery Management Systems can optimize capacity utilization by adjusting cutoff voltages based on internal resistance. Then Section 2.9 discusses the significance of Battery Management Systems (BMS) in overseeing and optimizing battery and energy storage module performance, ensuring safety and longevity. Finally in Section 2.10 the conclusions are drawn.

2.1 History of lithium batteries

The history of lithium batteries, like the evolution of any technological device, is deeply rooted in its historical context. Batteries, serve as devices that directly convert the energy released during a chemical reaction into electricity. While there is some debate regarding the earliest electrochemical battery, with claims dating back to the “Baghdad Battery" found during archaeological excavations near Baghdad, most credit goes to Luigi Galvani and Alessandro Volta in the late 18th century for making electrochemical cells widely known to humanity (Scrosati, 2011).

The history of lithium batteries is closely tied to the works of Luigi Galvani and Alessandro Volta. Galvani's classic experiment, in which he observed a frog's leg

FIGURE 2.1: Portrait of Alessandro Volta as an elderly man (Camnago, Volta family)

twitch when touched by different metals, suggested the possibility of animals generating electricity. In contrast, Volta demonstrated electricity production using his “voltaic pile" (Figure 2.2), consisting of alternating zinc and silver disks separated by a cloth soaked in sodium chloride solution. These two discoveries, though initially seen as opposing concepts, have their merits. Galvani’s work has a association with bioenergy, while Volta’s work is more aligned with energy storage. Volta’s writings from the late 1700s hinted at the significance of factors like the electrolyte and electrode interface, which play crucial roles in the development of modern batteries, particularly lithium batteries.

Volta’s groundbreaking work catalyzed rapid developments in electrochemical science, leading to the discovery of several significant electrochemical systems throughout the 19th century (Trasatti, 1999). In 1866, French engineer Georges-Lionel Leclanché introduced his battery, featuring a zinc rod negative electrode (anode) and a manganese oxide–carbon mixture as a positive electrode (cathode), immersed in an aqueous ammonium chloride solution. Over time, these cells have been refined, with innovations like replacing liquid electrolytes with pastes and redesigning cell container. (Scrosati, 2011). Following Leclanché’s discovery, Gaston Plantè invented the lead–acid rechargeable battery in 1859, and Waldmar Jungner discovered the rechargeable nickel–cadmium battery in 1901. These innovations, while modified for construction and materials packaging, still form the basis of many commercial batteries used today, such as those for car ignition and portable tools.

For over a century, batteries based on Leclanché, Jungner, and Planté’s concepts met the technological requirements of their time. However, significant changes occurred in the late 1960s due to various factors. Advances in implantable medical devices, requiring high-energy density and reliable energy sources, drove the need for improved batteries. Moreover the demand for high-energy and high-power sources for military purposes necessitated better battery technology. Furthermore the rapid growth of the consumer electronics market, with devices requiring portable power sources, created new demands for batteries.

Traditional batteries of the time, such as alkaline–manganese, nickel–cadmium, or lead–acid, were ill-suited to meet these evolving demands. Their main drawback

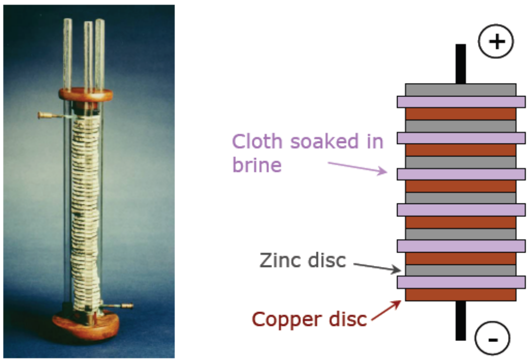

FIGURE 2.2: A diagram illustrating a copper-zinc voltaic pile. Copper and zinc discs were isolated by cardboard or felt spacers soaked in saltwater, serving as the electrolyte. Volta's original piles included an extra zinc disk at the bottom and an additional copper disk at the top, which were later determined to be unnecessary.

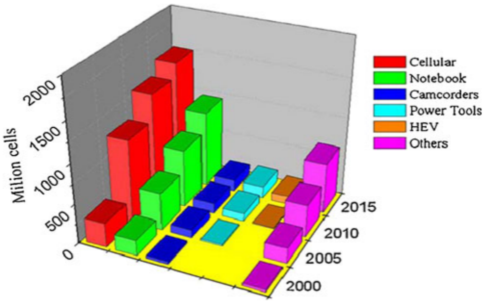

FIGURE 2.3: The changing dynamics of the electronic market for lithium-ion battery consumers over time(Scrosati, 2011)

was the lack of energy density, which stemmed from their electrode combinations offering limited specific capacity, resulting in low energy density. These batteries were heavy and bulky, failing to keep pace with technological advancements. One illustrative example is the case of cardiac pacemakers, essential devices for patients with arrhythmia. Early pacemakers relied on primary zinc–mercury batteries, which were large and heavy, occupying a significant portion of the device's size. Moreover, these batteries required frequent replacements every two years, causing stress for patients. New batteries with higher energy-to-weight and energy-to-volume ratios and longer operational lives were urgently needed.

The breakthrough came with the development of new battery concepts that utilized lithium as one of the electrode materials. Lithium, with the highest electrochemical equivalent among all metals, promised significantly higher specific capacity compared to zinc. However, the use of lithium required a shift from aqueous electrolytes to more electrochemically stable organic electrolytes, typically involving lithium salt solutions in carbonate organic solvents.

As already introduced above in this section, one significant catalyst for the evolution of lithium batteries was the demand from the military sector, which required power sources characterized by both high energy and high power capabilities. This led to the development of specialized lithium batteries using unconventional cathode materials, including soluble reagents like sulfur dioxide (SO_2) and liquid reagents such as thionyl chloride ($SOCl_2$) and sulphuryl chloride (SO_2Cl_2).

Another influential factor in the 1970s was the proliferation of consumer electronics, introducing popular devices like electronic watches, toys, and cameras. These devices demanded batteries that could deliver efficient performance within compact volumes and at an affordable cost. The response to this need was the commercialization of lithium batteries utilizing manganese dioxide cathodes, designed in coin-type cell configurations to fit seamlessly into device casings.

The focus shifted towards identifying materials for cathodes that could withstand long cycles. The breakthrough came in 1978 with the development of “insertion" or “intercalation" electrodes, typically based on compounds that could reversibly accept and release lithium ions within their open structure. Transition metal compounds like titanium sulfide proved promising, enabling the creation of the first commercial rechargeable lithium batteries in the late 1970s and early 1980s. Exxon in the USA introduced a battery with a TiS_2 cathode, while Moli Energy in Canada produced one with a MoS_2 cathode, both using liquid organic electrolytes.

However, operational issues, including fire incidents, raised concerns about the safety and longevity of these lithium batteries. These issues were primarily associated with the anode. Due to its high reactivity, lithium metal could react with the electrolyte, forming a solid electrolyte interface (SEI) on its surface. While this layer was permeable to lithium ions, allowing discharge, irregularities on the SEI surface could lead to uneven lithium deposition during charging, resulting in dendrite formation and potential cell short-circuiting. In extreme cases, these events could lead to overheating and explosions.

Consequently, the development of rechargeable lithium batteries necessitated a different approach: a novel concept involving the combination of two insertion electrodes. One electrode would accept lithium ions (anode), while the other would release them (cathode). This setup created a cyclic process where x equivalents of lithium ions moved between the two intercalation electrodes, termed concentration cells, forming a “rocking chair battery".

The concept of a rocking chair battery dates back to the late 1970s, was practically demonstrated in the early 1980s, but it took more than a decade before it reached practical application. Sony introduced a groundbreaking battery in 1991. The key to its success lay in selecting appropriate electrode materials: graphite as the anode (“lithium sink") and lithium cobalt oxide as the cathode (“lithium source"). Crucially, lithium cobalt oxide, was discovered by Goodenough in 1980 (Mizushima et al., 1981). While other cathode materials have been developed, lithium cobalt oxide remains a predominant choice for commercial lithium rocking chair batteries.

Sony’s achievement sparked global interest, and today, numerous battery manufacturers in Asia produce lithium rocking chair batteries, which have come to be known as lithium-ion batteries. Their exceptional properties, particularly in terms of energy density, surpassed conventional nickel–cadmium batteries and even younger systems like nickel–metal hydride batteries. Consequently, lithium-ion batteries have become the preferred power sources for a wide range of popular portable devices, including cellular phones, notebooks, camcorders, and MP3 players. This success is evident in the production of billions of units per year. Figure 2.3 shows the changing dynamics of the electronic market for lithium-ion battery consumers over time. In summary, the first era of lithium battery history witnessed the initial exploration of lithium’s potential, driven by diverse demands from military and consumer electronics sectors. The transition from primary to secondary batteries was marked by the development of insertion electrodes, leading to the birth of rechargeable lithium batteries. Overcoming safety concerns related to the lithium metal anode, the rocking chair battery

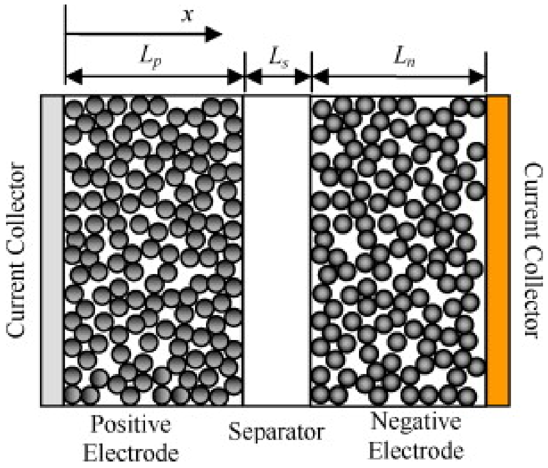

FIGURE 2.4: Schematic of a lithium ion battery

concept emerged as a groundbreaking solution, ultimately giving rise to the ubiquitous lithium-ion batteries.

The subsequent sections will go deeper into the evolution of lithium batteries, their components, and their diverse applications.

2.2 Lithium-ion battery functioning

Lithium batteries rely on a combination of chemical components that interact to produce energy. The main components of a lithium battery include (see Figure 2.4):

- *Anode*: The anode is the negative electrode of the battery and typically consists of a lithium-based material, such as graphite or lithium metal.

- *Cathode*: The cathode is the positive electrode of the battery and is typically composed of a lithium compound, often lithium cobalt oxide ($LiCoO_2$), lithium iron phosphate ($LiFePO_4$), or other lithium-based materials

- *electrolyte*: The electrolyte is a critical component that separates the anode and cathode and allows the flow of lithium ions between them. It is typically an organic solvent containing lithium salts, such as lithium hexafluorophosphate ($LiPF_6$).

- *Separator*: A separator, often made of porous materials like polyethylene or polypropylene, physically separates the anode and cathode to prevent short-circuits while allowing the passage of lithium ions.

The operation of a lithium-ion battery involves a series of chemical reactions that occur during charging and discharging. When a load is connected to the battery, such as a device or appliance, the chemical reactions at the electrodes reverse. Lithium ions move from the anode through the electrolyte and separator to the cathode. Electrons flow through the external circuit from the anode to the cathode, generating an electric current that powers the connected device. Batteries operate based on electrochemical and physical processes During charging, lithium ions move from the anode to the cathode through the electrolyte. This movement is facilitated by the electrolyte's chemical properties and the presence of the separator. As lithium ions migrate, electrons flow through the external circuit, creating an electric current. This flow of electrons powers the device connected to the battery. At the anode, lithium atoms undergo oxidation, releasing electrons into the external circuit and forming lithium ions. At the cathode, lithium ions undergo reduction, accepting electrons and forming lithium atoms. These oxidation-reduction (redox) reactions drive the flow of energy. Maintaining the chemical stability of the electrolyte and preventing unwanted side reactions is crucial to battery performance and safety. During operation, some heat is generated due to resistance in the battery components and the electrochemical reactions. Managing this heat is essential to prevent overheating and thermal runaway. Understanding these chemical and physical processes is essential for optimizing battery design, improving performance, and ensuring safety. Moreover, ongoing research in battery technology aims to enhance energy density, cycle life, and charge-discharge efficiency while minimizing environmental impacts and safety concerns.

Chemistry in the battery can be described in two steps (Figure 2.5). Reduction occurs at cathode and oxidization occurs at anode. Electrolyte in between the cathode and anode facilitates the exchange of ions. During the charging of the battery, cathode releases electrons in the external circuit and Li^+ in the electrolyte. Li^+ passes through the micro-porous separator to the anode. This reverses during the discharge cycle. The cathode reaction can be shown as follows

$$\mathrm{LiCoO_2} \rightarrow \mathrm{Li}_{1-x}\mathrm{CoO_2} + x\mathrm{Li}^+ + xe^- \tag{2.1}$$

In the anode, lithium intercalation occurs during charging. The amount of Li^+ stored in the anode determines the energy capacity of the battery. Lithium ions are released during the discharge cycle, and the anode reaction can be shown as follows:

$$6\mathrm{C} + x\mathrm{Li}^+ + e^- \rightarrow \mathrm{Li}_x C_6 \tag{2.2}$$

The overall reaction in a lithium-ion battery cell can be shown as follows

$$\mathrm{LiCoO_2} + 6\mathrm{C} \rightarrow \mathrm{Li}_{x-1}\mathrm{CoO_2} + \mathrm{Li}_x C_6 \tag{2.3}$$

Electrode compounds are chosen based on several characteristics. They should readily accept and release lithium ions, and lithium intercalation-deintercalation should not change the structure of the compound. Electronic and ionic conductivity of the electrodes play a vital role in the energy density of a lithium-ion battery. Highly conductive electrodes, such as metallic electrodes, are desirable. High porosity in electrodes is desirable since lithium ions are hosted in the anode, so a higher surface area will increase the intercalation of ions. Additionally, electrodes should be stable and safe over a long period of charging and discharging. Electrodes that are low-cost and environmentally non-hazardous are also desirable (Whittingham, 2004; Koksbang et al., 1996; Megahed and Scrosati, 1994).

2.3 Cell packaging and available forms

Lithium-ion cells come in various packaging forms, each designed to meet specific application requirements and safety standards. A comprehensive analysis of packaging technology for electrochemical accumulators is provided (Kiehne, 2003).

2.3.1 Cylindrical cells

The cylindrical packaging design, as an early form of mass-produced batteries, remains popular today due to its mechanical stability, naturally withstanding internal

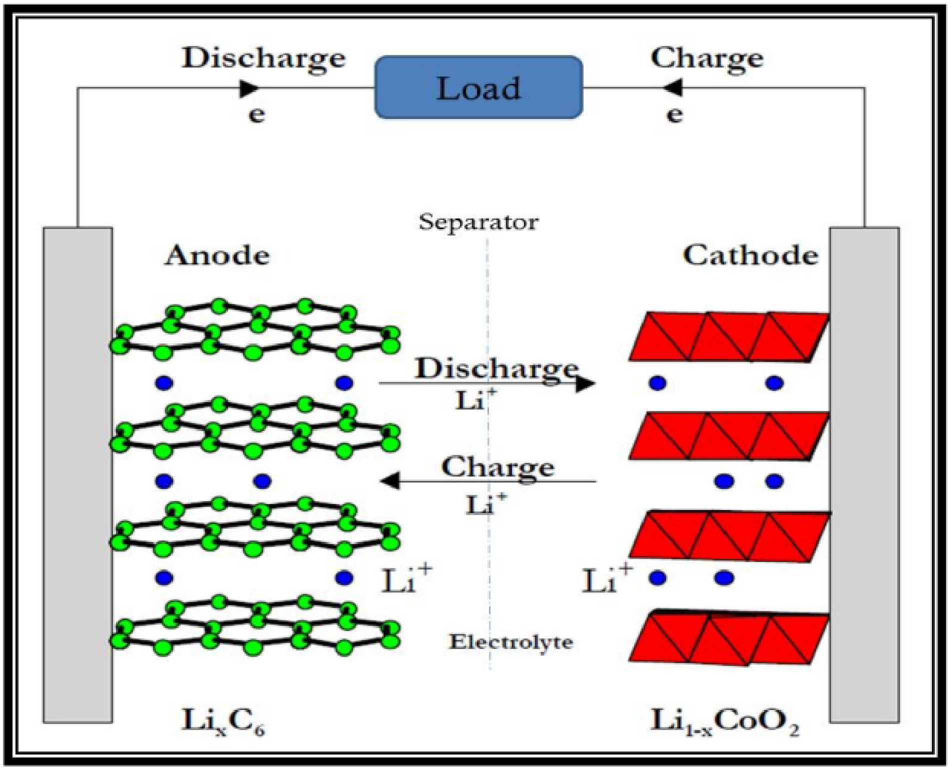

FIGURE 2.5: Schematic presentation of the operation in lithium ion battery(Khan, 2012)

pressures without deformation. Standard cylindrical cell sizes, known as AAAA, have been in use since the 1890s. As form factors became smaller, new standards were introduced, such as D, C, AA, and AAA, which are common for various consumer-type applications (Fig. 2.6). Secondary batteries of these packaging types primarily use Nickel-Cadmium (NiCd) and Nickel-Metal-Hydride (NiMH) chemistries, containing one electrochemical cell.

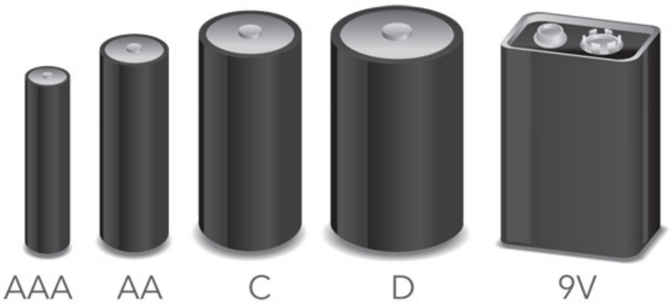

FIGURE 2.6: Common consumer-type battery packages. Left to right: AAA-cell, AA-cell, C-cell, D-cell, a Large 9V cell battery

Notably, cylindrical packaging has even been used for lead-acid batteries, particularly for small, cylindrical lead-acid cells that contain spirally-wound electrodes. These cells were the first to use a separator material known as “absorbent glass mat" (AGM), enhancing packaging density and making them suitable for rugged environments.

On the Li-ion side, the 18650 cell, introduced in the mid-1990s, became the standard cylindrical packaging format. With a diameter of 18mm and a length of 65mm, the 18650 cell contains one electrochemical cell with cathode, anode, and separator cut into stripes and rolled into a metal can. It is widely used in battery packs for laptop PCs, electric bicycles, and power tools. Although cylindrical cells have lower packaging density due to their round shape, they allow for efficient air circulation in modules or battery packs, aiding in cooling.

2.3.2 Prismatic cells

While consumer and starter batteries have been widely standardized, Li-ion battery manufacturers introduced new formats when product designs required changes. Prismatic cells, with a box-like appearance, are used in applications like mobile phones, digital cameras, video cameras, and tablet computers. Unlike cylindrical cells, there is no standard aspect ratio or size for prismatic cells, which can contain one or more electrochemical cell units.

Prismatic Li-ion cells are manufactured with cathodes, anodes, and separators in long stripes, wound up and then pressed to fit into the prismatic container. However, this design imposes more stress on the bent parts of the cell, which can challenge electrode coating and electrolyte distribution. Prismatic cells allow for flexible design and improve packaging density in a module or pack but introduce higher mechanical stress on the container and more complex thermal management.

2.3.3 Pouch cells

Pouch cells are a minimalistic packaging approach, lacking a rigid container. Instead, they are sealed by flexible foil, often referred to as “coffee bag cells". Cathodes, separators, and anodes are stacked rather than wound. This design maximizes packaging density and reduces weight, thereby increasing energy density. Pouch cells are exclusively used for Li-ion chemistries and may employ a polymer electrolyte that also acts as a separator.

Pouch cells are very flat and find applications in tablet computers (typically around 4 Ah capacity). They are also used in high-power and high-energy (EV) applications. However, high currents in charging or discharging modes can generate internal pressure, leading to serious swelling if the cell overheats or short circuits. To address this, manufacturers typically oversize the package, creating a separate “gas-bag" where excess gases can escape during the initial charging step (formation). Pouch cells require careful temperature management and support structures when integrated into a module, and there are no standard sizes for these cells.

2.3.4 Coin cells

Coin cells played an important role in enabling compact designs for portable electronic devices during the 1980s, including cordless telephones and medical devices. These cells were valued for their small size and affordability. However, a significant drawback is their susceptibility to swelling when subjected to extremely high currents. Today, coin cells are predominantly used as primary cells and find applications in medical implants, watches, hearing aids, car key fobs, and memory backup devices.

These packaging forms offer a range of options to suit various applications, from cylindrical cells providing mechanical stability to prismatic cells for flexible design and pouch cells maximizing packaging density.

2.4 Safety

The primary objective of this section is to comprehensively assess the safety characteristics of commercial primary lithium and lithium-ion battery technologies. Our focus will be on side reactions and thermal behaviors that could compromise safety during operation. Additionally, we will focus on safety mechanisms and tests designed to evaluate battery performance under normal operating conditions and abuse scenarios, all grounded in experimental evidence available in the open literature.

Hazards linked to primary lithium and lithium-ion cells have materialized not only during their intended use but also during their transportation and storage, both for new and used battery packs. Furthermore, these hazards manifest during the recycling process, which is essential to recover marketable materials and comply with regulatory requirements. Recent incidents reported in the news have highlighted the potential dangers during transport, storage, and recycling operations.

For example, a concerning trend of fires and incidents attributed to faulty lithium-ion batteries, occurring both on planes and at airports, has led to the compilation of an official list. This list, overseen and regularly updated by the Federal Aviation Administration (FAA), responsible for air safety and airport management in the USA, sheds light on the growing magnitude of the issue.

The FAA has meticulously recorded 455 total verified incidents directly linked to lithium batteries since may 2006. It is important to acknowledge that this tally likely represents only a portion of the actual incidents, as many may have gone unreported. These problematic lithium-ion batteries have been found in an array of personal electronic devices, ranging from smartphones to laptops.

The FAA emphasizes that this list should not be construed as an exhaustive record of all such incidents but rather a compilation of recent cargo and baggage-related incidents within their knowledge.

Additionally, it is worth noting that this list excludes three major aircraft accidents where lithium battery cargo shipments were suspected but not conclusively proven to be the cause of the fires. These incidents involved an Asiana Airlines 747 near South Korea on July 28, 2011; a UPS 747 in Dubai, UAE on September 3, 2010; and a UPS DC-8 in Philadelphia, PA on February 7, 2006.

To illustrate the gravity of the situation, let's consider a typical incident that transpired on August 2, 2018. During a flight bound for Salt Lake City, a passenger reported that her Apple iPhone 6, stowed in her pants' back pocket, started emitting smoke and generating heat. Alarmed by the smell of smoke and heat emanating from the phone, the passenger promptly alerted the flight crew. To manage the situation, the phone was placed within a fire-retardant bag for containment, and an emergency was declared, leading to a safe landing.

Another incident, occurring on December 24, 2022, the media reported a thermal incident occurred involving JetBlue Airlines. A subsequent Investigation determined a passenger's power bank battery began to smoke as the plane approached the arrival gate. Airline personnel conducted an emergency evacuation, several passengers reportedly required medical attention due to smoke inhalation or injury from the evacuation. And again United Airlines reported on the 21st april 2023 that a thermal event occurred during flight, a passenger possessed an e-Cigarette/ Vape Device that became warm to the touch. The operating crew secured in the e-Cigarette/ Vape Device in a Thermal Containment Bag for the duration of flight. Upon arrival the e-Cigarette/ Vape Device exhibited no signs of a thermal incident and was returned to the passenger. Figure 2.7 shows Tìthe FAA's Lithium Battery Incident charts include a running list of aviation cargo and passenger baggage events involving smoke,

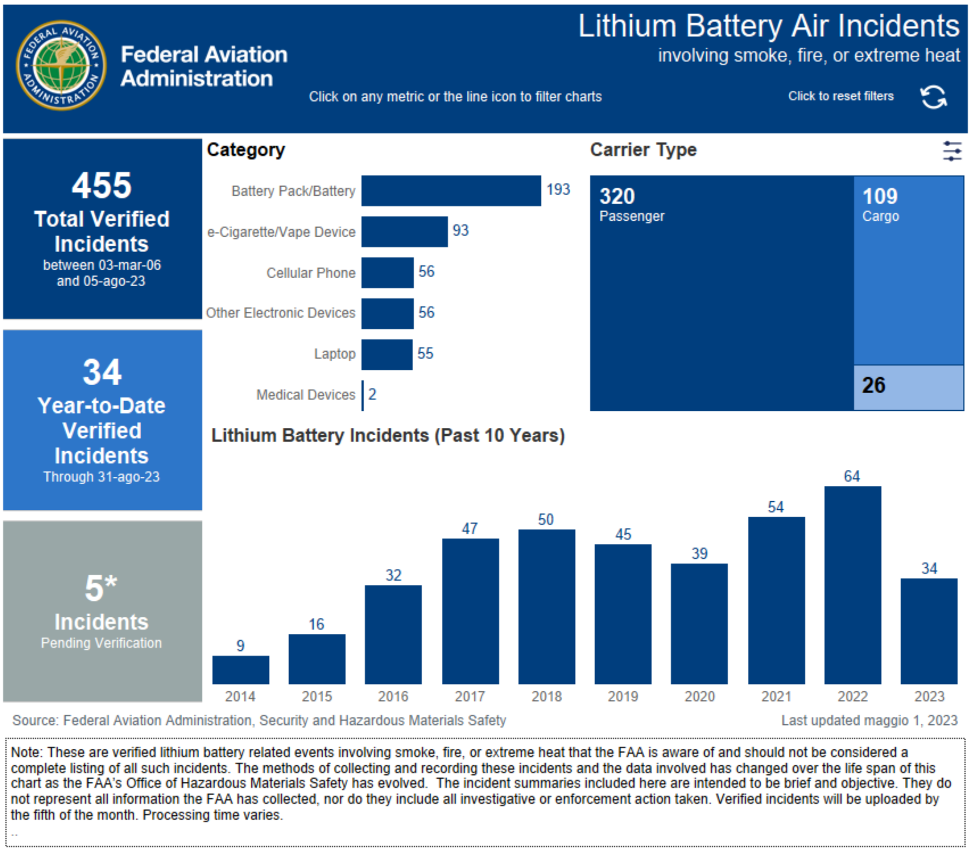

Source: Federal Aviation Administration, Security and Hazardous Materials Safety

Last updated maggio 1, 2023

Note: These are verified lithium battery related events involving smoke, fire, or extreme heat that the FAA is aware of and should not be considered a complete listing of all such incidents. The methods of collecting and recording these incidents and the data involved has changed over the life span of this chart as the FAA's Office of Hazardous Materials Safety has evolved. The incident summaries included here are intended to be brief and objective. They do not represent all information the FAA has collected, nor do they include all investigative or enforcement action taken. Verified incidents will be uploaded by the fifth of the month. Processing time varies.

FIGURE 2.7: FAA chart of incidents

fire, extreme heat or explosion involving lithium batteries or unknown battery types dating back to 2006.

These incidents underscore the serious safety concerns posed by lithium-ion batteries within personal electronic devices when used during flights and within airport premises. To mitigate the inherent risks associated with fires sparked by these batteries, more than 50 airlines worldwide, including several renowned carriers, now equip themselves with AvSax fire containment bags. Recognized with the prestigious Queen's Award for Enterprise, these bags have been employed 28 times to effectively manage emergencies linked to lithium-ion battery fires in personal electronic devices since the start of 2017.

While definitive evidence regarding the specific mechanisms initiating these events is often lacking, incidents can sometimes be traced back to improper handling, storage practices, and packaging methods that may result in mechanical damage, water ingress, and/or internal or external short-circuits in charged batteries.

For many years, lithium-ion cells have been considered a safer alternative to lithium metal-anode cells, primarily because lithium metal is not re-deposited upon charging under normal circumstances Balakrishnan, Ramesh, and Kumar, 2006. Over time, various materials for positive and negative electrodes have been proposed, with a substantial portion of conventional lithium-ion cells utilizing a carbon-based anode paired with a positive electrode containing lithium, such as $LiCoO_2$. The electrolyte typically consists of a lithium salt (e.g., $LiPF_6$) capable of dissolving in organic solvents like methyl carbonate or diethyl carbonate.

Ongoing research efforts have led to the development of novel materials for electrolyte solutions, positive and negative electrodes (Gulbinska et al., 2011). These materials aim not only to enhance electrochemical performance parameters, such as capacity, energy density, and cycle life but also to improve safety performance.

2.4.1 Side reactions

Hazards associated with lithium-ion cells can originate from various side reactions:

In lithium metal cells, molten lithium can form in the event of overcharging due to the low melting point of lithium metal (180°C). However, this occurrence is less likely in lithium-ion cells where metal lithium is replaced by lithiated carbon materials.

Reactions between organic solutions and the electrode surface can take place when the cell's temperature increases, particularly if the solid-electrolyte interface (SEI) is disrupted. The SEI is the contact surface between the electrolyte solution and the LixCoO$_2$ electrode, formed as the battery is charged for the first time. It becomes unstable when the cell temperature rises above 70–100°C and decomposes exothermically.

Thermal management and heat generation are crucial for the safe operation of lithium-ion cells. Both reversible and irreversible heat generation must be considered in the battery management system. Internal resistance contributes to irreversible heat, while reversible heat is linked to the reduction reaction at the positive electrode and the heat generated at the negative electrode. The magnitude of reversible heat effects varies across different lithium-ion chemistries, with LiCoO$_2$ cells exhibiting significantly higher reversible heat (700% of the irreversible values) and heat generation rate differences between charge and discharge (1.4 kW at 5˘40% charge). Conversely, LiFePO$_4$ cells exhibit a substantially lower reversible heat effect, approximately 50W, when operated between 2% and 95% state of charge.

2.4.2 Thermal runaway of lithium-ion batteries

The phenomenon of thermal runaway in lithium-ion batteries is well-documented (Abraham et al., 2006) and can be described as a three-stage process:

- Anodic reactions commence around 90°C, representing the rate-limiting step. As the temperature surpasses 120°C, the solid electrolyte interface (SEI) layer starts to decompose, leading to the reduction of the electrolyte at the lithiated graphite negative electrode.
- As the temperature exceeds 140°C, exothermic reactions at the positive electrode commence, resulting in the rapid evolution of oxygen.
- The third stage involves the decomposition of the positive electrode and the oxidation of the electrolyte, occurring at temperatures above 180°C. This stage is characterized by a high-rate exothermic process, with temperatures rising as much as 100°C per minute.

Thermal runaway and heat effects in lithium-ion cells are sensitive to the state of charge, with higher charged voltages lowering the onset temperature. They also depend on the cell's history and the applied load.

Studies conducted by (Zhang, Fouchard, and Rea, 1998) revealed that lithiation of the positive electrode improves thermal stability. Additionally, the composition of the electrolyte impacts thermal stability, with ethylene carbonate/dimethyl carbonate demonstrating greater stability than EC/DME. The choice of positive electrode material also influences thermal stability, with cells containing $LiCoO_2$ or $LiNiO_2$ performing less favorably than those with $LiMn_2O_4$. Abraham et al., 2006 reported thermal stability studies using accelerating rate calorimetry on $LiNi0.8Co0.15Al0.05O_2$ electrodes, observing self-heating reactions starting at 84°C and progressing until quenched at 150°C.

Alternative strategies to enhance thermal stability involve coating the positive electrode material with inert oxides to limit direct contact with the electrolyte, thus improving stability. Examples include $Li_4Ti_5O_12$ and $LiFePO_4$. Furthermore, positive electrodes different from $LiCoO_2$, such as $Li_4Ti_5O_12/LiMn_2O_4$ electrodes, have shown enhanced thermal stability. These cells exhibited no thermal runaway even at temperatures of 400°C, although cell venting occurred at 150°C due to pressurization of the organic solvents. The degree of lithiation also influences stability, with onset temperatures decreasing as x (degree of lithiation) decreases. $LixMn_2O_4$ displayed an exothermic reaction at 225°C, but the energy released was lower and less dependent on the degree of lithiation (x).

2.5 Electrolyte decomposition

In lithium-ion batteries, the buildup of heat can trigger a series of reactions that result in the production of gases within the battery cells. These gases, along with the accompanying increase in pressure, can pose significant safety risks, potentially leading to the release of gas (venting) or, in extreme cases, the rupture of the battery casing. Research has dealt the specific types of gases generated when lithium-ion batteries experience overcharging.

Studies have revealed that during overcharging, the primary gases produced are carbon dioxide (CO_2) and carbon monoxide (CO), primarily originating from the positive electrode of the battery. Additionally, a small fraction of methane (CH_4) is also detected (<10%). Importantly, this research has clarified that the generation of CO_2 is primarily linked to the oxidation of the battery's electrolyte material at the positive electrode, rather than arising from reactions within the carbonaceous negative electrode.

Furthermore, it is worth noting that potentially flammable gases, including hydrogen (H_2), have been observed in the gases produced at the negative electrode, along with minor amounts of other compounds like ethane (C_2H_6) and acetylene ($C2H_2$).

The breakdown of the electrolyte in the battery's operation can lead to the formation of various compounds, such as CO_2, ethylene (C_2H_4), fluoroethane (C_2H_5F), diethyl ether ($(C_22H_55)_2O$), highly toxic alkylfluorophosphates, and fluorophosphoric acids, especially when a 1 M $LiPF_6$ concentration is used in diethyl carbonate or in mixtures with dimethyl carbonate as the electrolyte. These decomposition products can interact with the electrode surfaces, potentially forming CO_2, oxalates, carbonates (particularly at the negative electrode), or complex fluorinated compounds known as oligoethylene oxides.

Further insights into the mechanisms of electrolyte decomposition have been gained from studies, including one by Onuki et al. in 2008, which found that electrodes made of $LiNixCoyAl1xyO_2$ (LNCAO) generate larger quantities of CO_2 compared to traditional $LiCoO_2$ electrodes. Ethylene carbonate (EC) was identified as the primary source of CO_2 in this context, while CO appeared to originate from a combination of solvent and non-solvent components. The patterns of gas generation observed in lithium-ion batteries using different electrode materials, such as $LiCoO_2$, $LiMn_2O_4$,

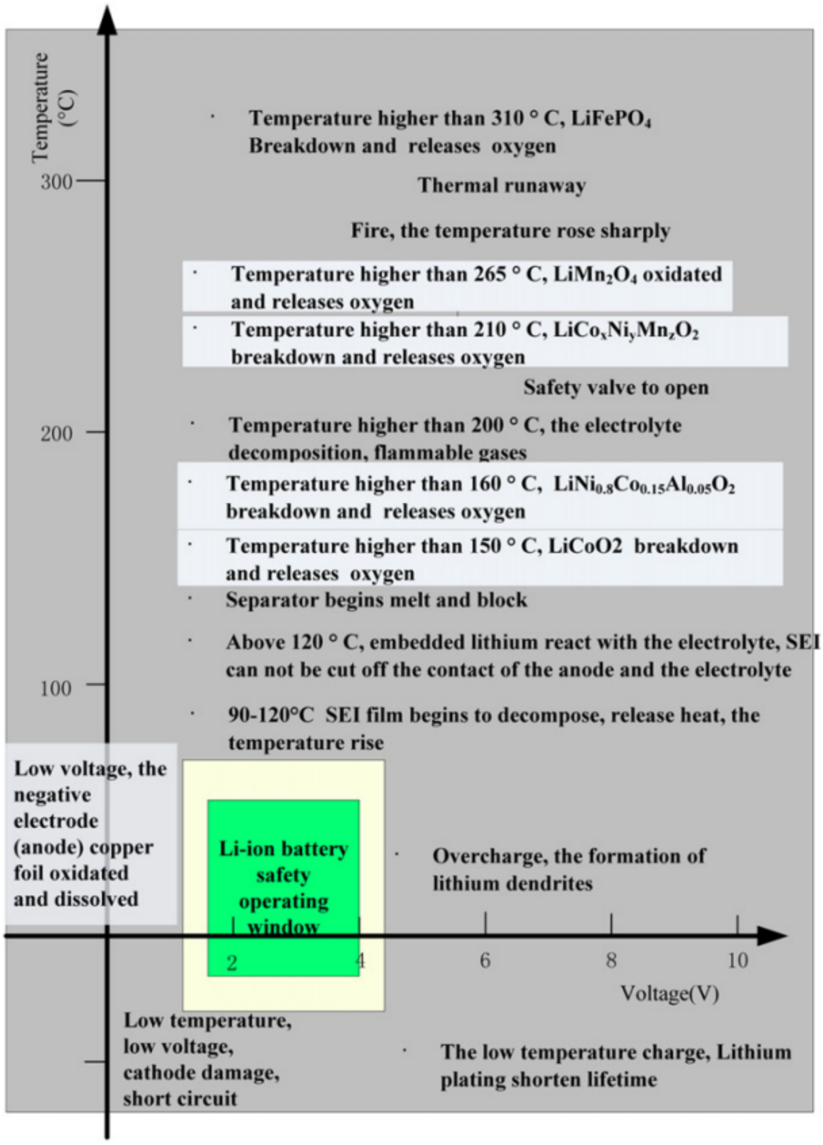

FIGURE 2.8: Safety operating window for lithium ion battery (Lu et al., 2013)

and $LiFePO_4$, were generally similar. However, $LiMn_2O_4$/C and $LiFePO_4$ systems produced higher levels of acetylene (C_2H_2) as the voltage increased.

2.6 Safe Operation of lithium-ion batteries

Commercial lithium-ion batteries currently in use must be equipped with a management system to ensure effective control and management of the lithium-ion batteries. This system is essential to ensure that each individual cell operates under optimal conditions, thereby preventing the occurrence of the faults described earlier. In other words, it is imperative that every cell operates within the established safety operating window for lithium-ion batteries, as illustrated in Figure 2.8. Lithium-ion cells are renowned for their impressive performance characteristics, but they are notably unforgiving when operated outside a narrow safe operating range (SOA). Any deviation from this prescribed range can result in a spectrum of consequences, ranging from a shortened cell lifespan to outright cell damage. In the most extreme cases, such deviations can lead to hazardous events. This includes subjecting a Li-Ion cell to various forms of abuse, such as physical damage through piercing or crushing or subjecting it to overheating due to over-voltage, over-current, or exposure to external heat sources. These actions can be exceedingly dangerous.

These incidents serve as stark reminders of the potential dangers associated with large-scale Li-Ion batteries. Therefore, exercising caution and adhering rigorously to safety precautions are paramount when working with such batteries. It is imperative to thoroughly comprehend and effectively manage the inherent risks associated with lithium-ion technology to ensure its safe utilization. Ultimately, the responsible handling and operation of lithium-ion batteries are crucial to prevent accidents and ensure the continued safe use of this technology.

The safe operating area (SOA) of Li-Ion cells is determined by factors such as current, temperature, and voltage.

- Li-Ion cells can suffer damage and even ignite if overcharged beyond a certain voltage threshold.
- Most Li-Ion cells will incur damage if discharged below a specific voltage level.
- Li-Ion cell lifespans can be significantly reduced if operated outside a certain temperature range during discharge or charged outside an even narrower temperature range.
- Exceeding a safe temperature can lead to thermal runaway and ignition, even for cells not prone to thermal runaway, due to the presence of organic electrolytes that can fuel flames.
- High discharge currents or rapid charging can decrease the lifespan of Li-Ion cells.
- Prolonged operation at high pulse currents for more than a few seconds may damage Li-Ion cells.

These limits vary depending on the cell's chemistry. For example, standard Li-Ion cells ($LiCO_2$) without additional protective mechanisms can experience thermal runaway at relatively low temperatures, whereas $LiFePO_4$ cells are inherently resistant to thermal runaway. These limits can also vary among manufacturers. (see Figure 2.10).

2.7 Efficiency

One significant advantage of Li-Ion cells, compared to other types of batteries, is their high energy and charge efficiency.

Li-Ion cells have low internal resistance, especially in power cells, which means they generate very little heat when used. For example, A123's M1 26,650 cells (used in power tools and PHEV conversions) typically have a resistance of $10\,m\Omega$. When loaded at 1C ($2.3\,A$), they only dissipate $53\,mW$ of power while delivering $7.6\,W$, resulting in an efficiency of 99.3% (98.6% when you consider both charging and discharging).

As you increase the current, a cell's energy efficiency decreases, and more energy is lost as heat due to internal resistance. Maximum power extraction from a cell occurs when the load's resistance matches the cell's resistance, with half of the power

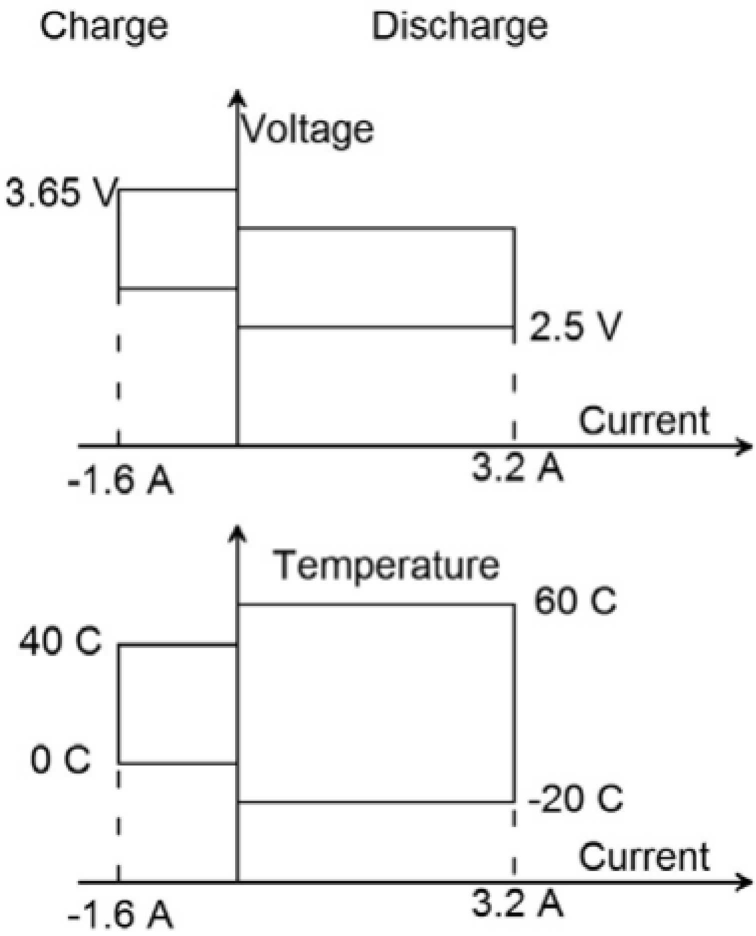

FIGURE 2.9: Safe operating area of a LiFePO 4 26,650 energy cell (Andrea, 2010)

dissipated as heat inside the cell and the other half doing external work. An A123 M1 26,650 cell can produce 150 A and 500 W under these conditions, with 250 W lost as heat inside the cells. However, this high power output can only be sustained for a very short time (less than 10 seconds) because it rapidly degrades the cell and raises its temperature to dangerous levels. This is a consideration in applications like racing vehicles, where performance matters more than cell longevity, and occasional fires may be acceptable.

From a charging perspective, Li-Ion cells are nearly 100% efficient, as long as the charge and discharge cycle happens quickly enough to prevent self-discharge from becoming a problem. This means that almost every electron that goes into the cell during charging can be discharged back out, regardless of the charging or discharging rate. However, it is important to note that this applies to charge recovery, not energy. During discharge, the cell's voltage is lower than during charging, resulting in less energy being discharged, even if the same amount of charge goes in and out of the cell.

Note that, to understand the previous statement, we cannot rely on data showing reduced charge output at higher currents in specification sheets. Infact, it is important to understand that we are referring to complete charge and discharge cycles, whereas specification sheet curves typically represent constant current conditions and stop

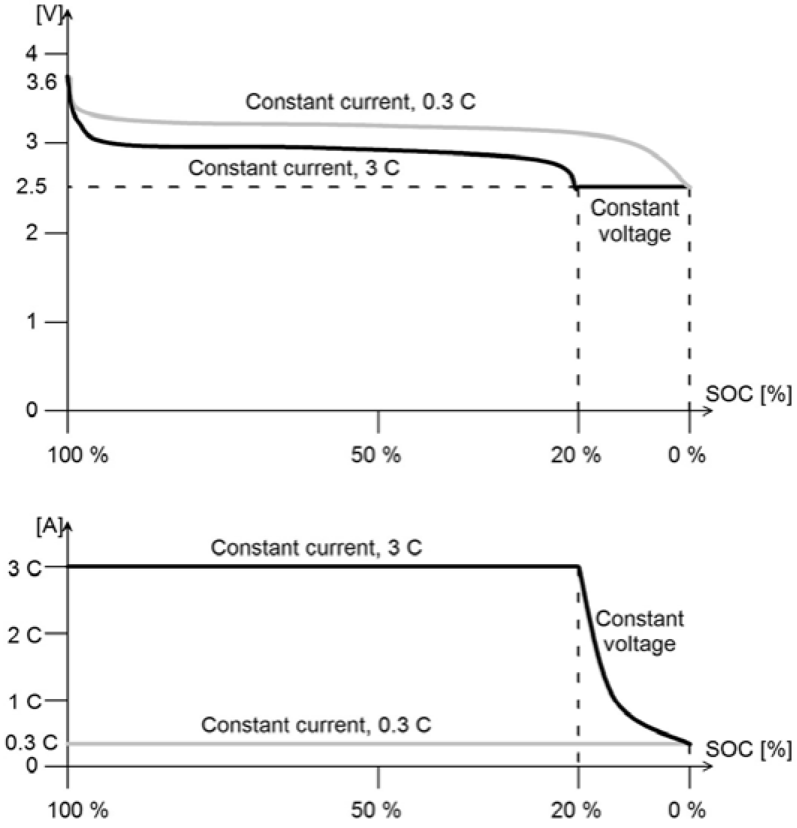

FIGURE 2.10: The capacity of Li-Ion cells to provide charge remains consistent regardless of the discharge rate. Even after a high-current discharge, it is still possible to recover the remaining charge at a lower discharge rate. (Andrea, 2010)

when the cell voltage under load drops to a specific level. At that point, the cell is not fully discharged yet. By continuing to discharge the cell at a lower current, for example, at a constant voltage equal to the cutoff voltage (see Figure 2.10), the remaining charge can still be recovered. When the current reaches zero, the total charge extracted from the cell is essentially the same, regardless of the discharge rate. However, in some applications like backup power, high currents are necessary, preventing the extraction of the cell's last bit of charge. In these cases, the ability to recover charge at lower currents is only theoretical.

Certain applications, such as electric vehicles, offer flexibility. They can switch to a “valet" mode with reduced torque, allowing the driver to “limp home." In such applications, the entire charge in the battery can be accessed.

2.8 Aging

Li-Ion cells boast a longer lifespan in comparison to other battery chemistries, but they are not immune to certain limitations, both in terms of cycle life and calendar life.

When it comes to calendar life, standard Li-Ion cells exhibit a relatively short duration. Irrespective of whether these cells undergo cycling, they tend to lose capacity

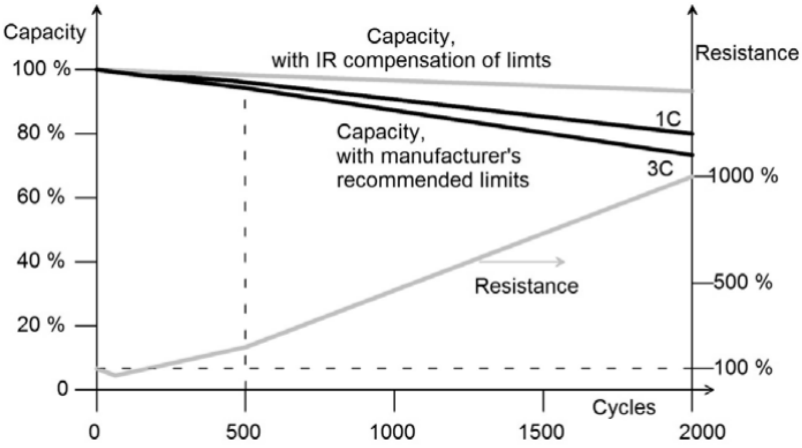

FIGURE 2.11: Cell capacity recovery, the efficiency of cell capacity, and cell resistance in relation to cycling. (Andrea, 2010)

over time, a phenomenon many users of cell phones and laptops have undoubtedly encountered. This capacity decline can be attributed to a chemical process that takes place when the cells remain fully charged at voltages exceeding 4.0V. In contrast, alternative Li-Ion chemistries, such as $LiFePO_4$ cells, operate at lower voltages specifically to mitigate this chemical effect, and as a result, they appear to have no notable calendar life limitations.

Aging is influenced by the discharge current employed.

What may not be immediately apparent is that while a portion of capacity loss can indeed be attributed to the loss of active material inside the cell, the remainder is not truly “lost" but rather remains unused. This occurs because the cell is undercharged and underdischarged due to the escalating internal resistance and the fixed cutoff voltages specified by cell manufacturers. When cell manufacturers employ fixed cutoff voltages, their testing equipment charges and discharges cells to a lesser extent with each cycle as the resistance increases. Consequently, it may seem as though the cells are losing more capacity than they genuinely are.

The capacity that becomes temporarily unavailable due to the rising internal resistance can be reclaimed by adjusting the upper cutoff voltage during charging and lowering the lower cutoff voltage during discharging, all through the application of IR (Voltage = Current * Resistance) compensation, as demonstrated in Figure 2.11. In essence, the same cell that appears to have “lost 10% of its capacity" may, in reality, still retain a substantial portion of its original capacity. To access this “hidden" capacity, charge cutoff voltages must be increased while discharge cutoff voltages are decreased to account for the additional IR voltage drop caused by heightened resistance. The implementation of a Battery Management System (BMS) equipped with the capability to measure each cell's resistance and make adjustments to cutoff voltages accordingly can serve as an effective means to optimize a battery's capacity utilization.

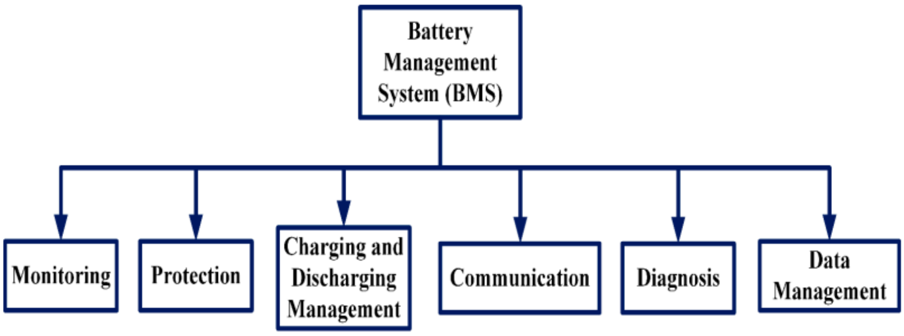

FIGURE 2.12: BMS Features (Gabbar, Othman, and Abdussami, 2021)

2.9 Battery management system

The definition of a Battery Management System (BMS) can vary depending on its application. In general, a BMS refers to a management scheme responsible for monitoring, controlling, and optimizing the performance of individual batteries or multiple battery modules within an energy storage system. In a broad sense, a BMS can be understood as any product or technology designed to oversee and manage a battery in various capacities. These functions may include, but are not limited to:

- Monitoring the battery's performance and health.
- Ensuring the battery's safety through protective measures.
- Estimating the state of the battery.
- Maximizing the battery's operational efficiency.

Figure 2.12 summarizes the main BMS features. Providing reports and information to users or external devices.In cases of abnormal conditions, a BMS can disconnect the module(s) from the system to ensure safety. Its primary role is to enhance battery performance while maintaining safety measures within the system. In power system applications, BMS is introduced to oversee, control, and efficiently deliver battery power, taking into consideration battery lifespan. In the automotive sector, BMS plays a crucial role in managing energy within various system interfaces and ensuring system safety. BMS comprises distinct functional blocks that are interconnected with batteries and other system components such as controllers, grids, and distributed resources. Employing proper architecture, functional blocks, and advanced circuitry can extend the battery system's life. Various commercial BMS solutions are available in the market. For instance, NUVATION Energy offers a flexible, reliable, UL 1973 recognized BMS suitable for mobile and stationary energy storage applications (Kang et al., 2020).

A BMS doesn't operate in isolation but is integrated with other system modules to fulfill the system's objectives. For example, in an intelligent energy automation system, it includes a battery management module (BMM), battery interface module (BIM), battery units, and battery supervisory control. This system's role is to safeguard the battery pack, extend its lifespan, manage power demand, and interface with different networks (Abbas, Cho, and Kim, 2020).

The BMS market offers three implementation topologies: centralized, distributed, and modular. In a centralized topology, a single control unit is connected to battery

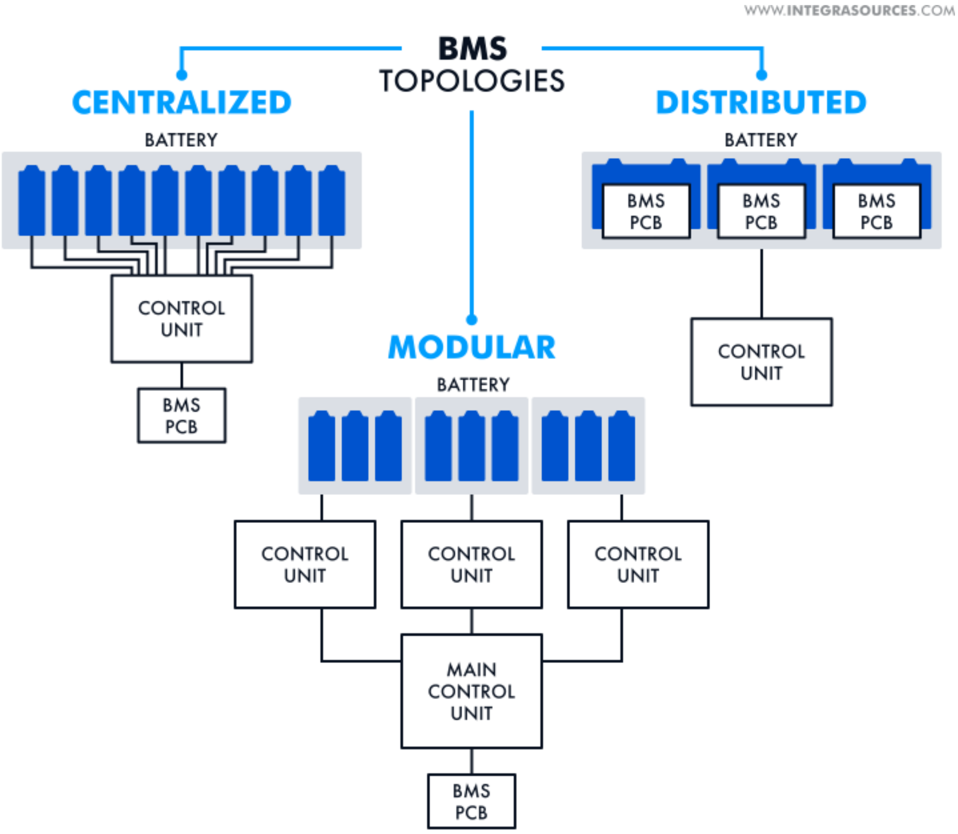

FIGURE 2.13: BMS implementation topology (https://www.integrasources.com/blog/bms-battery-management-system-battery-storage-solution/)

cells via multiple wires. In the distributed topology, each control unit is dedicated to a specific battery cell, linked by a single communication cable. In the modular topology, multiple control units handle specific battery cells, and these control units are interconnected. The centralized topology is the most cost-effective but less expandable. The distributed topology, while costlier, is easier to install and results in a cleaner assembly. The modular topology demands more hardware and programming effort, introducing a trade-off between its features and challenges. Figure 2.13 illustrates these BMS implementation topologies.

The software architecture of BMS now offers multitasking capabilities, allowing various tasks to be carried out simultaneously without interruption. Initial tasks of a BMS software architect, such as voltage/current measurement, overcurrent/voltage protection, temperature measurement, and protective relay actuation, must be executed promptly to ensure BMS safety. To achieve real-time functionalities, real-time operating systems (RTOS) are introduced in BMS software architecture.

BMS is responsible for managing battery packs, whether they are connected internally or externally. It calculates essential battery parameters, including cell voltages, pack current, pack voltage, and pack temperature. These measurements enable BMS to estimate state of charge (SOC), state of health (SOH), depth of discharge (DOD), and critical operational parameters of the cells/battery packs. These measurements also contribute to extending battery life and aligning with the demands of the power network (Uno, Ueno, and Yoshino, 2019).

BMS construction involves functional unit blocks and design techniques. The specific architecture, functional unit blocks, and electronic circuitry depend on battery requirements for various applications. Optimizing battery life relies on several features:

- An energy management system with a user interface for monitoring and controlling battery performance across different system blocks.
- Battery pack performance and safety features.
- Resilience among system units in various accident scenarios.
- Advanced technologies that integrate batteries with conventional or non-conventional energy sources.
- Internet-of-Things (IoT) for monitoring and controlling the energy management system.

BMS encompasses significant capabilities and functions, including automatic charging/discharging, protection, monitoring, stability, and resiliency. These functions are essential for battery performance and safety. BMS also contributes to increased battery life through precise operation measurements and control. Various methods, including accurate modeling, improve the accuracy of state of charge (SOC) estimation and cell balancing. This precision optimizes battery performance, ensuring that the battery operates at maximum efficiency, thus extending its lifespan. BMS also plays a critical role in protecting the battery pack, managing its lifetime, controlling power demand, and interfacing with different networks (Aiello, Crovetti, and Fiori, 2015).

BMS undergoes two types of testing: functional and non-functional testing, covering battery lifecycle, research and design, validation, verification, and manufacturing processes. Functional testing focuses on performance and operational parameters, evaluating aspects like voltage levels, current capacity, and power consumption to ensure BMS meets performance and safety standards. Non-functional testing addresses system requirements and involves dynamic charging and isolation monitoring, ensuring that BMS fulfills system requirements effectively(Fleischer et al., 2016).

Employing a BMS provides several technical, operational, and economic advantages. Technical benefits include protection against over/under voltage and cell balancing. Operationally, BMS enhances safety, reliability, and dual-purpose functionalities, reducing the likelihood of thermal runaway in high-voltage batteries and identifying faulty cells. Economically, BMS extends battery lifespan and reduces costs, with BMS costs typically accounting for only a small fraction of the total battery pack cost.

Current BMS solutions have limitations in data logging functions, hindering the development of state of charge (SOC) models for battery packs. Furthermore, they often lack SOC and state of life (SOL) estimations, which are crucial for ensuring scheduled operations and reliable battery replacements. Additionally, the individual nature of BMS units for each battery makes it challenging to create a new BMS by combining existing components. However, cloud-based BMS and digital twin technology could potentially address these limitations by enhancing data storage capabilities and computational power through cloud computing (Sarlioglu et al., 2016).

2.10 Conclusions

In conclusion, this chapter has provided a comprehensive overview of lithium-ion batteries (Li-Ion) and their crucial role in various applications, from portable electronics to electric vehicles and energy storage systems. We have explored their impressive energy and charge efficiency, emphasizing their low internal resistance and ability to operate efficiently across different discharge rates.

Furthermore, the importance of battery management systems (BMS) in optimizing Li-Ion battery performance, ensuring safety, and extending their lifespan, have been discussed. Various BMS implementation topologies, such as centralized, distributed, and modular, were examined, along with their technical, operational, and economic advantages.

While Li-Ion batteries offer significant advantages, a focus has been given to their limitations, including calendar life issues, the impact of discharge current, and the potential for thermal runaway. It is crucial to address these limitations through careful design, monitoring, and management.

Looking ahead, advancements in cloud-based BMS and digital twin technologies hold promise for addressing some of the current limitations and enhancing Li-Ion battery management. As the demand for Li-Ion batteries continues to grow across industries, understanding their characteristics and effective management becomes increasingly vital for achieving both performance and safety objectives.

Chapter 3

Battery modeling

Battery modelling has become a popular research area due to the growing demand for longer-lasting portable electronic devices and the increasing interest in battery electric vehicles by the automotive industry. While the portable electronics industry aims to maximize the operating life of a low-power electronic device, the electric vehicle industry seeks to maximize the driving range and fuel economy of hybrid and electric vehicles using large battery packs. Accurate and efficient battery modelling is crucial for both industries to enhance device and battery performance and inform the development of electronic and control systems. The control system and electronics that interface with the battery must be tailored to its behavior to optimize the overall performance and life of the device. Additionally, choosing the size and configuration of the battery pack is essential to maximize device performance while minimizing cost. The present chapter focuses on battery modelling field and the commonly used models and techniques. In the remainder of this chapter Section 3.1 introduces the main features of battery modelling. Section 3.2 describes the different equivalent circuit models. Section 3.3 defines the principal equations and simplifications of the main Electrochemical models and finally Section 3.4 concludes the chapter.

3.1 Main features

Battery modeling is an important aspect of designing and controlling battery-powered systems. Two common techniques for modeling batteries in automotive applications are Equivalent Circuit Models (ECMs) and Electrochemical Models (EMs). While ECMs abstracts away the electrochemical nature of the battery and represents it solely as electrical components, EMs are based on highly non-linear equations that describe the electrochemical physics of the battery.

The choice of the right battery model depends on the fidelity one requires for one's application. For real-time control system applications, where high fidelity models are often not required, simple circuit-based models are employed. For applications requiring higher fidelity such as vehicle performance, drive cycle simulations, and battery aging, higher fidelity circuit-based or chemistry-based models can be used to increase the accuracy of the results.

Battery models can be fused with an actual battery using techniques like an Extended Kalman Filter (EKF), a fuzzy-logic system, a least-squares regression model, set-based observers or a sliding-mode observer model for online state of charge (SOC) estimation. For control system development, battery models can be fairly simple, comprising either a simple resistor or a Thévenin resistor-capacitor network.

More accurate models are desired for fuel economy and vehicle performance simulations using drive cycles. Since these calculations are usually executed offline on workstations, one can afford to use a more computationally expensive model such as the EMs.

If one is analyzing the response of the battery to transients, a model that is based on these measurements and takes the dynamic battery response into account is desired. The Thévenin models and the electrochemical impedance spectroscopy (EIS) models are good examples of these.

An important consideration for electric vehicle applications is the battery's dependence on temperature, especially in cold climates. Many battery models do not consider temperature variations, and if this is a modeling requirement, it is necessary to use models that include the effects of temperature on the dynamic response and state-of-charge behavior of the battery.

In conclusion, the choice of the right battery model depends on the application requirements, such as the desired fidelity, computation time, and real-time simulation requirements. Battery modeling techniques are constantly evolving and improving, and it is important to stay up-to-date with the latest research to design and control efficient and reliable battery-powered systems.

3.2 Equivalent circuit models

The complicated electrochemical reactions that occur within lithium-ion batteries can be difficult to understand and quantify directly. Researchers created Equivalent Circuit Models to bridge the gap between theoretical comprehension and actual implementation. These models describe the sophisticated internal workings of batteries in a simplified manner, making it easier to study their performance, forecast behavior, and maximize their use in diverse applications. n this section, we examine the world of equivalent circuit models for lithium-ion batteries.

The field of real-time applications has fostered substantial interest in electrical equivalent circuit models, primarily attributed to their streamlined structural design and straightforward identifiability. These models intricately emulate battery dynamics through the integration of electrical components.

We will explore how these models capture the essential electrochemical phenomena within batteries while maintaining a balance between accuracy and computational efficiency. By dissecting the components of these models and understanding the significance of their parameters, we can gain valuable insights into the dynamic behavior of lithium-ion batteries under different operating conditions.

An equivalent-circuit model employs electrical components to explain complex electrochemical processes seen in batteries, such as ion diffusion and the dynamics of double-layer charging and discharging. Impedance-based models emerged as a result of the growth of battery modeling, which was first focused on frequency-domain study of the current-voltage relationship.

The next sections will examine two major ECMs utilized in the thesis's upcoming chapters.

3.2.1 Thévenin model

Thévenin models Rahimi-Eichi et al., 2013 were developed to capture the complicated interaction of electrochemical processes as research advanced. The early iterations of Thévenin models involved a substantial linear capacitor, where voltage and stored charge corresponded to battery Open-Circuit Potential (OCP) and State of Charge (SOC), respectively. Nevertheless, this configuration proved inadequate in capturing the nonlinear correlation between SOC and OCP. As a response, contemporary Thévenin models have embraced a controlled voltage source, illuminating this

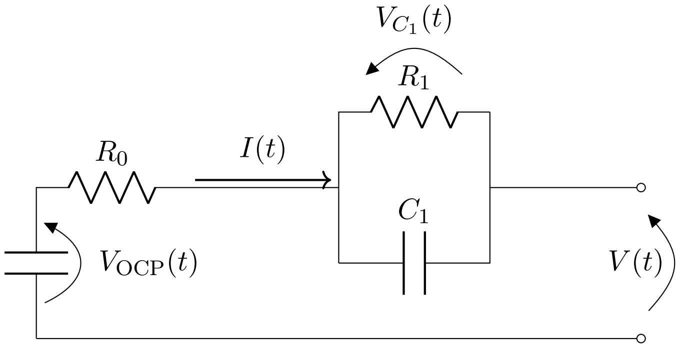

FIGURE 3.1: Thévenin equivalent circuit model of the Lithium-ion cell.

nonlinear mapping. In practical terms, these models incorporate experimentally derived lookup tables, delineating the SOC-OCP relationship through distinct curves for charging and discharging cycles. This intricate approach serves to accommodate the hysteresis effect, as outlined by Eichi and Chow, 2012. Through these advancements, the modern Thévenin models provide a more nuanced and comprehensive representation of battery behavior, enabling enhanced accuracy in diverse applications.

This model's structural composition consists of three main components, each of which contributes to its overall functionality, as it is depicted in fig. 3.1 These parts are as follows:

- Open Circuit Potential ($V_{OCP}(t)$): This component represents the battery's potential in the absence of any current flow. It serves as a pivotal reference point for understanding the cell's behavior across various operational states.
- Internal Resistors (R_0 and R_1): The model incorporates two internal resistors, R_0 and R_1, which play crucial roles in accounting for the battery's resistance to current flow. These resistors contribute to shaping the overall electrical response of the battery.
- Capacitor (C_1): The inclusion of a capacitor, C_1, facilitates the accurate depiction of transient charge and discharge dynamics within the cell. It enables the model to capture the intricate interplay of voltage fluctuations during these processes.

The electrical behavior of this Equivalent Circuit Model (ECM) is rooted in the principles of Kirchhoff's law and Ohm's law, which collectively define its operation. The underlying system equations governing the dynamics of the ECM are expressed as follows:

$$\begin{cases} \dot{z}(t) = -\dfrac{I(t)}{C_{\text{batt}}}, \\ \dot{V}_{C_1}(t) = -\dfrac{V_{C_1}(t)}{R_1(t)C_1(t)} + \dfrac{I(t)}{C_1(t)}, \end{cases} \tag{3.1}$$

In this formulation, the symbol $z(t)$ represents the cell's State of Charge (SOC), while $V_{C_1}(t)$ denotes the voltage drop across the parallel combination of the internal resistor R_1 and the capacitor C_1. The parameter C_{batt} stands for the nominal capacity of the cell, and $I(t)$ symbolizes the input current, where it is important to note that, according to our convention, a negative current indicates charging.

The open-circuit potential is then described as a nonlinear function of the SOC, i.e. $V_{\mathrm{OCP}}(t) = V_{\mathrm{OCP}}(z(t))$. The terminal voltage $V(t)$ is given as

$$V(t) = V_{\mathrm{OCP}}(z(t)) - V_{C_1}(t) - R_0(t)\, I(t), \tag{3.2}$$

where the term $R_0(t)I(t)$ accounts for the voltage drop on the internal resistance $R_0(t)$.

Drawing inspiration from Perez et al., 2017, it is possible the utilization of electrical parameters influenced by the State of Charge (SOC). The essence of this strategy involves encapsulating these parameters as nonlinear functions of the SOC, manifesting as:

$$R_1(t) = R_{1,0} + R_{1,1}z(t) + R_{1,2}z(t)^2, \tag{3.3}$$

$$C_1(t) = C_{1,0} + C_{1,1}z(t) + C_{1,2}z(t)^2. \tag{3.4}$$

This conceptual framework highlights the complex interplay of various variables, effectively encapsulating the battery's activity within a dynamic system. As the model runs in real-world circumstances, it uses these components and equations to provide insights into the complex electrochemical dynamics of lithium-ion batteries.

3.2.2 Dual polarisation model

In this section, we present the mathematical framework of the Dual Polarization (DP) model, which entails a second-order Electrochemical Circuit Model (ECM). Let consider the core of our investigation by introducing the Dual Polarization (DP) model, portrayed schematically in Figure 3.2. This model comprises three distinctive components:

- The first one is the Open Circuit Potential ($V_{\mathrm{OCP}}(z(t))$): Representing the voltage when no current is passing through the cell.
- Parallel Resistor-Capacitor (RC) Blocks: Two parallel RC blocks, each composed of a resistor (R_1 and R_2 respectively) and a capacitor (C_1 and C_2 respectively). These elements encapsulate the intricate charge and discharge dynamics.
- Internal Ohmic Resistance (R_0): This resistance characterizes the internal losses within the cell.

The current coursing through the cell, labeled as $I(t)$, is regarded as a known input parameter, with its positivity indicating discharging. The governing equations of this complex system are delineated as follows:

$$\dot{z}(t) = -\frac{I(t)}{C_{\mathrm{batt}}}, \tag{3.5}$$

$$\dot{V}_{C_1}(t) = -\frac{V_{C_1}(t)}{R_1(t)C_1(t)} + \frac{I(t)}{C_1(t)}, \tag{3.6}$$

$$\dot{V}_{C_2}(t) = -\frac{V_{C_2}(t)}{R_2(t)C_2(t)} + \frac{I(t)}{C_2(t)}, \tag{3.7}$$

$$V(t) = V_{\mathrm{OCP}}(z(t)) - V_{C_1}(t) - V_{C_2}(t) - R_0(t)\, I(t). \tag{3.8}$$

Here, the State of Charge serves as an essential metric, gauging the charge level relative to the battery capacity C_{batt}. It is important to note that for the remainder of this

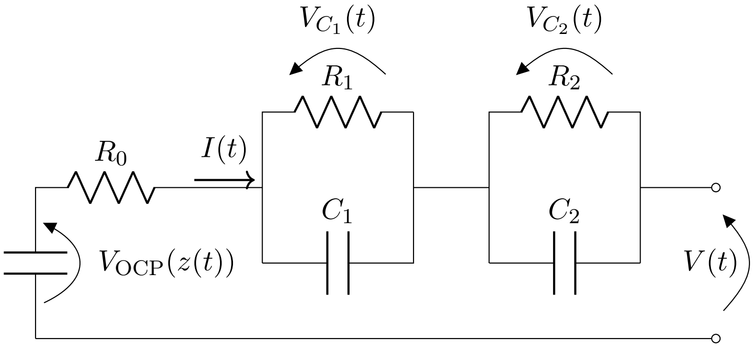

FIGURE 3.2: Dual Polaralisation equivalent circuit model of the Lithium-ion cell.

discourse, we shall denote the State of Charge as SOC(t) with the simplified notation z.

Similarly to what has been done for the Thévenin model, it is possible employ SOC dependent electrical parameters. This involves representing them as nonlinear functions of the State of Charge (SOC):

$$R_1(t) = R_{1,0} + R_{1,1}z(t) + R_{1,2}z(t)^2, \tag{3.9}$$

$$R_2(t) = R_{2,0} + R_{2,1}z(t) + R_{2,2}z(t)^2, \tag{3.10}$$

$$C_1(t) = C_{1,0} + C_{1,1}z(t) + C_{1,2}z(t)^2. \tag{3.11}$$

$$C_2(t) = C_{2,0} + C_{2,1}z(t) + C_{2,2}z(t)^2. \tag{3.12}$$

.

The intricate interplay of these constituents in the DP model establishes a holistic framework to comprehensively analyze the intricacies of lithium-ion cell behavior, shedding light on their electrochemical and thermal dynamics.

3.2.3 Open circuit potential formulation

The overall open circuit potential ($V_{\mathrm{OCP}}(z(t))$) finds its expression as a polynomial function of the State of Charge through a ninth-degree polynomial equation:

$$\begin{aligned} V_{\mathrm{OCP}}(z(t)) = a + b \cdot z + c \cdot z^2 + d \cdot z^3 + e \cdot z^4 + f \cdot z^5 + \\ + g \cdot z^6 + h \cdot z^7 + i \cdot z^8 + j \cdot z^9, \end{aligned} \tag{3.13}$$

with the coefficients shown in Table 3.1.

Coeff.	a	b	c	d	e
Value	2.611	17.04	-204.4	1369	-5423
Coeff.	f	g	h	i	j
Value	13210	-19970	18260	-9247	1990

TABLE 3.1: Coefficient values for $V_{\mathrm{OCP}}(z(t))$

This formulation, derived from a fitting procedure, is a manifestation of our endeavor to align with the principles articulated in (14) by Pozzi et al. (2018). It is pertinent to highlight that this approach becomes requisite in light of our ECM's scope, where we refrain from incorporating surface stoichiometries θ_p and θ_n (as seen in (3.1)). Importantly, it is worth noting that under steady-state conditions, the surface stoichiometries have the capacity to be defined as functions of SOC.

A comparative evaluation beckons juxtaposing the polynomial representation in (3.13) against the non-linear OCP function of the Single Particle Model with Electrolyte (SPMe). While the latter showcases a commendable accuracy, it is intriguing to observe that the polynomial function, despite its simplicity, does not compromise precision either. The Root Mean Square Error (RMSE) of this polynomial fitting stands at RMSE $= 3.896 \cdot 10^{-4}$, thus bolstering its credibility. Furthermore, the polynomial's streamlined nature grants it an edge in terms of reduced conservatism, especially when subjected to interval arithmetic as we can see better in the next chapters.

3.2.4 Thermal model and lumped dynamics

The thermal framework adopted in this study stems from Lin et al., 2014. This model's equations are formulated as follows:

The time rate of change of the core temperature $T_c(t)$ is influenced by the difference between the surface temperature $T_s(t)$ and the core temperature, convective and resistive thermal interactions, as well as the current input $I(t)$, leading to:

$$\dot{T}_c(t) = \frac{T_s(t) - T_c(t)}{R_c C_c} + \frac{I(t)(V_{C_1}(t) + V_{C_2}(t) + R_0\, I(t))}{C_c}. \tag{3.14}$$

Likewise, the temporal evolution of the surface temperature $T_s(t)$ is guided by the disparity between the fluid temperature $T_f(t)$ and the surface temperature, convective cooling, as well as resistive heat transfer, yielding:

$$\dot{T}_s(t) = \frac{T_f(t) - T_s(t)}{R_u C_c} + \frac{T_s(t) - T_c(t)}{R_c C_s}. \tag{3.15}$$

In these equations, R_c signifies the heat conduction resistance representing heat transfer between the core and surface, while R_u denotes the convective resistance simulating convective cooling between T_s and the ambient fluid temperature T_f. The terms C_c and C_s correspond to the heat capacities of the core and surface, respectively.

It is important to underline that this thermal representation, although practical, assumes uniform temperature distribution within both the core and the surface. Furthermore, we consider the surface of the cell in contact with external air, set at a constant temperature $T_f = 298.15$ K. This model provides a valuable abstraction, allowing us to examine the overall thermal dynamics of cylindrical batteries effectively.

To summarize, by adopting the principle of longitudinal homogeneity, a two-state model is harnessed to encapsulate the aggregated thermal dynamics of a cylindrical battery, as portrayed in Figure 3.3. The heat generation term (Q) can be expressed as

$$Q(t) = |I(t)|\,|V(t) - V_{\mathrm{OCP}}(z(t))|. \tag{3.16}$$

This is a result of chemical reactions within the electrode assembly during battery operation. The value of Q is computed based on the electrical model, encompassing joule heating and energy dissipation from electrode over-potentials. For a more refined heat generation representation, reversible heat such as entropic heat can be incorporated. This model intricately weaves these elements to provide a comprehensive understanding of the thermal behaviors in cylindrical batteries.

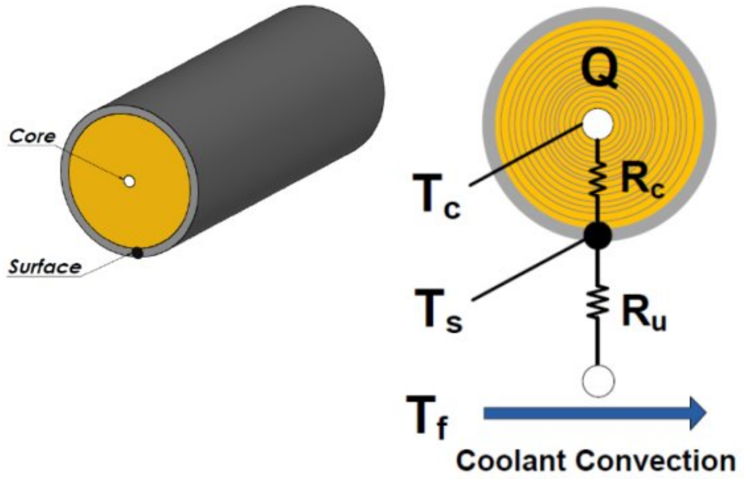

FIGURE 3.3: Lumped thermal model

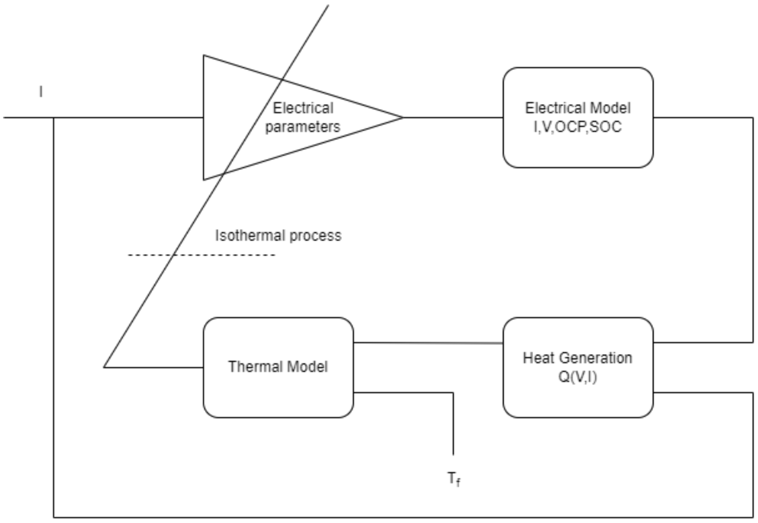

FIGURE 3.4: Interplay of the electrical and thermal models

3.2.5 Dynamic electro-thermal interaction with variable parameter dependencies

The intricate interplay between the electrical and thermal sub-models introduces a two-way coupling paradigm, as depicted in Figure 3.4. This symbiotic relationship underscores the intricate dynamics that underlie lithium-ion cell behavior. At the heart of this interaction lies the propagation of information between the electrical and thermal domains. The initial phase involves the electrical model, where the State of Charge and battery voltage are computed through the integration of input current (I) with specific electrical parameters R_s, R_i, and C_i. A crucial step emerges when the discrepancy between terminal voltage (V_T) and open-circuit voltage V_{OCP}, coupled with the applied current I, yields the heat generation Q.

On the thermal front, core temperature T_c and surface temperature (T_s) are calculated, with the heat generation Q and external temperature (T_f) as inputs. Notably, the core temperature T_c assumes an instrumental role by shaping the temperature-dependent variations of electrical parameters, thereby influencing the broader electro-thermal dynamics.

To achieve a more comprehensive portrayal of the dynamic behavior exhibited by the battery pack, it is possible to incorporate dependencies of the resistive and capacitive components of each cell on temperature, as outlined in Lin et al., 2014. Notably, the temporal dimension is omitted here for clarity.

The dependency of R_0 solely on the core temperature (T_c) follows the formulation:

$$R_0 = a_{R_0} + \exp\left(\frac{b_{R_0}}{T_c - c_{R_0}}\right). \tag{3.17}$$

For the remaining resistive elements, the relationship is expressed as:

$$R_1 = \left(a_{R_1} + b_{R_1} z + c_{R_1} z^2\right) \exp\left(\frac{d_{R_1}}{T_c - e_{R_1}}\right), \tag{3.18}$$

$$R_2 = \left(a_{R_2} + b_{R_2} z + c_{R_2} z^2\right) \exp\left(\frac{d_{R_2}}{T_c - e_{R_2}}\right). \tag{3.19}$$

The capacitance components can be described by the following expressions:

$$C_1 = a_{C_1} + d_{C_1} T_c + \left(b_{C_1} + e_{C_1} T_c\right) z + \left(c_{C_1} + f_{C_1} T_c\right) z^2, \tag{3.20}$$

$$C_2 = a_{C_2} + d_{C_2} T_c + \left(b_{C_2} + e_{C_2} T_c\right) z + \left(c_{C_2} + f_{C_2} T_c\right) z^2. \tag{3.21}$$

3.3 Electrochemical models

Electrochemical models are renowned for delivering precise insights into internal cell phenomena, although this accuracy comes at the cost of substantial computational time and memory resources. This is primarily due to the model being typically formulated using a set of partial differential algebraic equations, thereby necessitating intricate solving procedures. For tasks demanding greater precision, such as assessing vehicle performance, conducting drive cycle simulations, analyzing battery aging, and performing other computationally intensive simulations, opting for a more sophisticated chemistry-based model enhances result accuracy. Various methods of electrochemical modeling rely on complex equations that capture the complex behavior of batteries. These equations, known for their non-linear nature, are approached using a range of approximations. These approximations are chosen based on the desired level of accuracy and the specific objectives of the battery modeling process.

Electrochemical models (EMs) have emerged as indispensable tools within the domain of battery research and development. Their utility extends to battery manufacturers, enabling precise optimization of battery designs, and to chemistry researchers, who employ these models to replicate experiments in silico, thus anticipating potential experimental outcomes.

Within this context, the Pseudo Two Dimensional (P2D) model (Doyle, Fuller, and Newman, 1993b), also recognized as DFN, has assumed a prominent role and is widely cited within the literature. However, the P2D model carries a considerable computational load, a characteristic that has driven researchers to grapple with issues related to model complexity, identifiability, and observability (Moura, 2015). This computational bottleneck inherently limits its applicability in scenarios that necessitate real-time or near-real-time simulations.

A collective endeavor within the scientific community has thus been directed toward the creation of reduced-order models derived from the foundational P2D framework. These models are meticulously crafted to retain essential electrochemical insights while alleviating the computational burden and addressing identified shortcomings.

Among these, an efficient computational reduction of the DFN model is expounded upon in Khalik, Donkers, and Bergveld, 2021. Upon executing spatial and temporal discretization of the DFN model, it is demonstrated how, by substituting equations, the total count of equations describing the DFN model can be notably condensed into a concise set of algebraic equations. This operationalization of the model has been transformed into an open-access toolkit called TOOFAB. This toolkit empowers users to effortlessly toggle between explored simplifications, thereby offering the flexibility to strike a tailored equilibrium between model precision and computational efficiency.

In addition, the Sequential Particle Model (SPM) (Santhanagopalan et al., 2006) has garnered notable attention. The distinguishing hallmark of the SPM lies in its granularity, depicting electrodes as distinct particles rather than homogenous entities. The inherent advantage of the SPM rests in its reduced computational overhead compared to the P2D, rendering it particularly advantageous for real-time applications and control-oriented purposes.

Nonetheless, the SPM does exhibit certain limitations. Notably, it excludes considerations for electrolyte dynamics, thermal effects, and the intricate phenomena associated with battery aging. Recognizing the significance of these aspects in capturing the complete battery behavior, researchers have diligently extended the SPM to accommodate these dynamics. The Sequential Particle Model with Electrolyte Dynamics (SPMe) (Moura et al., 2016) introduces a crucial layer of accuracy by incorporating electrolyte behavior, enriching the model's fidelity for scenarios that involve ion transport and diffusion. Furthermore, the model's utility is further augmented by the incorporation of thermal dynamics (SPMeT) (Perez et al., 2017), accounting for the interplay between temperature variations and electrochemical performance. This comprehensive approach brings the model closer to real-world conditions and facilitates a deeper understanding of battery responses under varying thermal conditions.

In the remainder of this section, our focus shifts towards an in-depth examination of the foundational equations that define the DFN model, the simplfied model described in (Khalik, Donkers, and Bergveld, 2021) and the Sequential Particle Model with Electrolyte Dynamics and Thermal effects (SPMeT) model. The detailed analysis of these equations unveils their essential role in the progression of battery modeling methodologies.

3.3.1 The Doyler-Fuller-Newman model

In the following, we explore the foundational principles of the first-principles Pseudo Two Dimensional model (Doyle, Fuller, and Newman, 1993a), attributed to Doyle, Fuller, and Newman, and it is commonly known as the DFN model. This EM is designed to provide a comprehensive depiction of the electrochemical behaviors inherent in a lithium-ion cell. The model is structured as a set of tightly coupled nonlinear Partial Differential-Algebraic Equations (PDAEs), serving as a mathematical framework to capture the interdependent conservation laws of mass and charge governing the intricate processes within vital cell components.

Central to our analysis is the subdivision of the cell into distinct layers: the cathode (p), separator (s), and anode (n). This segmentation allows us to elucidate the intricate electrochemical reactions taking place. Submerged in an electrolytic solution, these electrode components, along with the separator, collaboratively facilitate the transport of ions, enabling the complex ionic conduction mechanism. During charging, ions disengage from the cathode, traverse the porous separator, and subsequently intercalate into the anode. This process is reversed during discharge, engendering a reversible sequence of electrochemical reactions.

To comprehensively model the cell's dynamics, we incorporate a one-dimensional thermal model. This addition facilitates the representation of temperature variations across discrete sections. This understanding is crucial for capturing the nuanced interplay between temperature fluctuations and electrochemical activity.

Moreover, our model accounts for the impact of aging, encompassing capacity decay and the growth of Solid Electrolyte Interface (SEI) resistance. This extension builds upon prior works, particularly the one proposed byTorchio et al., 2016. This augmentation introduces a temporal dimension, enabling the model to encompass the gradual shifts in cell behavior over extended durations.

We rely on the computational framework provided by the freely accessible Li-ION SIMulation BAttery Toolbox (LIONSIMBA).

In the following, the index $j = \{p, s, n\}$ is employed to denote the battery's distinct sections, encompassing the cathode, separator, and negative electrode respectively. Meanwhile, the index $i = \{p, n\}$ utilized solely in equations pertinent to the electrodes, pertains to the positive and negative electrodes.

Electrochemical model

Let denote the independent variable $x \in \mathbb{R}$, signifying the axial coordinate, the variable $r \in \mathbb{R}$ indicating the radial coordinate and the temporal variable $t \in \mathbb{R}$. It is important to underline that, within this proposed model, certain parameters exhibit a temperature dependency, captured through the Arrhenius law

$$\psi(T(x,t)) = \psi^0 e^{\frac{-E_{a,\psi}}{R}\left(\frac{1}{T(x,t)} - \frac{1}{T_{\text{ref}}}\right)}, \tag{3.22}$$

with $T(x,t)$ representing the temperature, while $E_{a,\psi}$ stands for the activation energy linked to the specific parameter $\psi(T(x,t))$. The universal gas constant is represented by $R = 8.314\,\text{J K}^{-1}\,\text{mol}^{-1}$), and T_{ref} denotes the reference temperature. It is noteworthy that ψ_0 signifies the pre-exponential factor, reflective of the parameter's value at the reference temperature. This correlation will be explicitly underscored for each parameter subject to temperature dependency.

The ion diffusion within the electrolyte within the electrodes is governed by the equation:

$$\epsilon_i \frac{\partial c_{e,i}(x,t)}{\partial t} = \frac{\partial}{\partial x}\left(D_{e,i}^{\text{eff}} \frac{\partial c_{e,i}(x,t)}{\partial x}\right) + a_i(t)(1 - t_+)j_i(x,t). \tag{3.23}$$

Meanwhile, in the separator, the equation simplifies to:

$$\epsilon_s \frac{\partial c_{e,s}(x,t)}{\partial t} = \frac{\partial}{\partial x}\left(D_{e,s}^{\text{eff}} \frac{\partial c_{e,s}(x,t)}{\partial x}\right). \tag{3.24}$$

In these equations, $c_{e,j}(x,t)$ represents the concentration of electrolytic ions, and $j_i(x,t)$ signifies the ionic flux, which is presumed to be negligible within the separator. Furthermore, t_+ represents the transference number, ϵ_j represents the material porosity, $D_{e,j}^{\text{eff}} = \epsilon_j D_e(T(x,t))$ indicates the effective electrolyte diffusion, where $D_e(T(x,t))$ stands for the temperature-dependent electrolyte diffusion coefficient. It is noteworthy that $D_e(T(x,t))$ is assumed to remain constant concerning $c_{e,j}(x,t)$.

In accordance with Bruggeman's theory, we define the tortuosity τ_j through the relation

$$\tau_j = \epsilon_j^{1-p}, \tag{3.25}$$

where p_j denotes the Bruggeman coefficient.

The specific active surface area, $a_i(t)$, is determined by the equation

$$a_i(t) = \frac{3\epsilon_i^{\text{act}}(t)}{R_{p,i}} \tag{3.26}$$

where $R_{p,i}$ denotes the particle radius and $\epsilon_i^{\text{act}}(t)$ represents the active material volume fraction, defined as

$$\epsilon_p^{\text{act}}(t) = -\frac{3600\, C_{\text{batt}}(t)}{\Delta\theta_p\, A\, F\, L_p c_{s,p}^{\max}}, \tag{3.27}$$

$$\epsilon_n^{\text{act}}(t) = \frac{3600\, C_{\text{batt}}(t)}{\Delta\theta_n\, A\, F\, L_n c_{s,n}^{\max}}. \tag{3.28}$$

In these expressions, $C_{\text{batt}}(t)$ represents the battery capacity expressed in ampere-hours Ah, $\Delta\theta_i = \theta_i^c - \theta_i^d$ where θ_i^d and θ_i^c correspond to the battery stochiometries at fully discharged and completely charged cell condition, L_j represents the length of the j-th section, F is the Faraday constant ($F = 96485\,\text{C/mol}$), A is the current collector area, and $c_{s,n}^{\max}$ denotes the maximum concentration of ions in the solid phase.

It is important to note that the equations in (3.27) ,(3.28) align with the observation that variations in the State of Charge-Open Circuit Potential (SOC-OCP) curve remain minor throughout the battery's operational lifespan (Waag, Fleischer, and Sauer, 2014).

Let $\hat{x}_p$ designate the position along the x-axis corresponding to the interface between the positive current collector and the cathode, $\hat{x}_{p,s} = \hat{x}_p + L_p$ for the interface between the cathode and the separator, $\hat{x}_{s,n} = \hat{x}_{p,s} + L_s$ for the interface between the separator and the anode, and finally $\hat{x}_n = \hat{x}_{s,n} + L_n$ for the interface between the anode and the negative current collector.

The boundary conditions governing ions' diffusion within the electrolyte are formulated as

$$\left.\frac{\partial c_e(x,t)}{\partial x}\right|_{x=\hat{x}_p,\hat{x}_n} = 0, \tag{3.29a}$$

$$-D_{e,p}^{\text{eff}} \left.\frac{\partial c_e(x,t)}{\partial x}\right|_{x=\hat{x}_{p,s}^-} = -\, D_{e,s}^{\text{eff}} \left.\frac{\partial c_e(x,t)}{\partial x}\right|_{x=\hat{x}_{p,s}^+}, \tag{3.29b}$$

$$-D_{e,s}^{\text{eff}} \left.\frac{\partial c_e(x,t)}{\partial x}\right|_{x=\hat{x}_{s,n}^-} = -\, D_{e,n}^{\text{eff}} \left.\frac{\partial c_e(x,t)}{\partial x}\right|_{x=\hat{x}_{s,n}^+}, \tag{3.29c}$$

where the superscripts in $\hat{x}_p^-, \hat{x}_n^-, \hat{x}_p^+, \hat{x}_n^+$ represent the left and right limits, respectively.

The ion diffusion in the active material of the electrodes is described by Fick's law

$$\frac{\partial c_s(x,r,t)}{\partial t} = \frac{D_{s,i}(T(x,t))}{r^2} \frac{\partial}{\partial r} \left(r^2 \frac{\partial c_s(x,r,t)}{\partial r} \right), \tag{3.30}$$

where $c_s(x,r,t)$ denotes the ion concentration in the solid phase, and $D_{s,i}(T(x,t))$ represents the temperature-dependent solid diffusion coefficient.

The boundary conditions for ion diffusion in the solid phase are given by:

$$\left.\frac{\partial c_s(x,r,t)}{\partial r}\right|_{r=0} = 0, \tag{3.31a}$$

$$-D_{s,i}(T(x,t))\left.\frac{\partial c_s(x,r,t)}{\partial r}\right|_{r=R_{p,i}} = j_i^{\text{int}}(x,t), \tag{3.31b}$$

where $j_i^{\text{int}}(x,t)$ denotes the intercalation ionic flux, modeled by the Butler-Volmer equation

$$j_i^{\text{int}}(x,t) = i_{0,i}(x,t)\sinh\left(\frac{0.5F}{RT(x,t)}\eta_i(x,t)\right), \tag{3.32}$$

where $\eta_i(x,t)$ represents the electrode overpotential and $i_{0,j}(x,t)$ stands for the intercalation exchange current density. The latter is computed as

$$i_{0,i}(x,t) = k_i(T(x,t))\sqrt{c_e(x,t)(c_{s,i}^{\max} - c_s^*(x,t))c_s^*(x,t)}, \tag{3.33}$$

Where $c_s^*(x,t)$ denotes the Li-ion surface concentration, and $k_i(T(x,t))$ represents the temperature-dependent kinetic reaction rate. Notably, the overall ionic flux is expressed as

$$j_i(x,t) = j_i^{\text{int}}(x,t) + j_i^{\text{side}}(x,t). \tag{3.34}$$

Here, $j_i^{\text{side}}(x,t)$ pertains to the side reactions contributing to ageing degradation, encompassing SEI resistance growth and capacity loss. These reactions are assumed to occur exclusively at the electrolyte-anode interface, specifically $j_p^{\text{side}}(x,t) = 0$.

The solid-phase potential $\Phi_s(x,t)$ within the two electrodes adheres to Ohm's law, formulated as

$$\frac{\partial}{\partial x}\left(\sigma_i^{\text{eff}}\frac{\partial \Phi_s(x,t)}{\partial x}\right) = a_i(t)Fj_i(x,t). \tag{3.35}$$

In this equation, $\sigma_i^{\text{eff}} = \epsilon_i^{p_i}\sigma_i$, where σ_i represents the electrode conductivity. The boundary conditions are specified as

$$\sigma_i\left.\frac{\partial \Phi_s(x,t)}{\partial x}\right|_{x=\hat{x}_p,\hat{x}_n} = \frac{I(t)}{A} \tag{3.36a}$$

$$\left.\frac{\partial \Phi_s(x,t)}{\partial x}\right|_{x=\hat{x}_{p,s},\hat{x}_{s,n}} = 0. \tag{3.36b}$$

Here, $I(t)$ symbolizes the current applied to the cell, with the convention that the charging current is negative.

The Ohm's law for the electrolytic potential $\Phi_e(x,t)$ is expressed by the following equations for the electrodes:

$$\frac{\partial}{\partial x}\left(\kappa_i^{\text{eff}}\frac{\partial \Phi_e(x,t)}{\partial x}\right) = \frac{2R}{F}(1-t_+)\frac{\partial}{\partial x}\left(\kappa_i^{\text{eff}}T(x,t)\frac{\partial \ln c_e(x,t)}{\partial x}\right) - a_i(t)Fj_i(x,t), \tag{3.37}$$

and for the separator

$$\frac{\partial}{\partial x}\left(\kappa_s^{\text{eff}}\frac{\partial \Phi_e(x,t)}{\partial x}\right) = \frac{2R}{F}(1-t_+)\frac{\partial}{\partial x}\left(\kappa_s^{\text{eff}}T(x,t)\frac{\partial \ln c_e(x,t)}{\partial x}\right). \tag{3.38}$$

Here, $\kappa_j^{\text{eff}} = \varepsilon_j^{pj}\kappa(c_e(x,t),T(x,t))$, where $\kappa(c_e(x,t),T(x,t))$ represents the temperature dependent electrolyte conductivity coefficient, assumed to be a nonlinear function of the electrolyte concentration.

The boundary conditions for the Ohm's law pertaining to the electrolytic potential are expressed as follows:

$$\left.\frac{\partial \Phi_e(x,t)}{\partial x}\right|_{x=\hat{x}_p} = 0 \tag{3.39a}$$

$$\Phi_e(x|_n,t) = 0, \tag{3.39b}$$

$$-k_p^{\text{eff}}\left.\frac{\partial \Phi_e(x,t)}{\partial x}\right|_{x=\hat{x}_{p,s}^-} = -\,k_s^{\text{eff}}\left.\frac{\partial \Phi_e(x,t)}{\partial x}\right|_{x=\hat{x}_{p,s}^+}, \tag{3.39c}$$

$$-k_s^{\text{eff}}\left.\frac{\partial \Phi_e(x,t)}{\partial x}\right|_{x=\hat{x}_{s,n}^-} = -\,k_n^{\text{eff}}\left.\frac{\partial \Phi_e(x,t)}{\partial x}\right|_{x=\hat{x}_{s,n}^+}. \tag{3.39d}$$

The electrode overpotentials $\eta_p(x,t)$ and $\eta_n(x,t)$ are defined as

$$\eta_p(x,t) = \Phi_s(x,t) - \Phi_e(x,t) - U_p(\theta_p^*(x,t)), \tag{3.40a}$$

$$\eta_n(x,t) = \Phi_s(x,t) - \Phi_e(x,t) - U_n(\theta_n^*(x,t)) - \frac{j_n(x,t)FR_{\text{SEI}}(t)}{AL_n a_n(t)}. \tag{3.40b}$$

Here, the open-circuit potential of each electrode, $U_i(\theta_i^*(x,t))$, is a nonlinear function of the surface stoichiometry $\theta_i^*(x,t) = \frac{c_s^*(x,t)}{c_{s,i}^{\max}}$, according to the cell's chemistry. Moreover, $R_{\text{SEI}}(t)$ denotes the SEI resistance. The terminal voltage of the cell, $V(t)$, is computed as:

$$V(t) = \Phi_s(\hat{x}_p,t) - \Phi_s(\hat{x}_n,t). \tag{3.41}$$

The normalized SOC is defined as:

$$\text{SOC}(t) = \frac{1}{L_n c_{s,n}^{\max}\epsilon_n^{\text{act}}(t)}\int_{\hat{x}_{s,n}}^{\hat{x}_{s,p}} c_s^{\text{avg}}(x,t)\,dx \tag{3.42}$$

Here, $c_s^{\text{avg}}(x,t) = \frac{3}{4\pi R_{p,n}^3 R_{p,n}}\int_0^{R_{p,n}} 4\pi r^2 c_s(x,r,t)\,dr$ denotes the volume-average concentration within the solid particles in the anode. Note that in (3.42), $\epsilon_n^{\text{act}}(t)$ functions as a renormalization factor for SOC as the cell ages. This implies that a cell can always achieve a unitary SOC value corresponding to a fully charged state under specific ageing conditions.

Thermal dynamics

The one-dimensional thermal dynamics is governed by the following equations For the electrodes:

$$\rho_i C_{p,i}\frac{\partial T(x,t)}{\partial t} = \frac{\partial}{\partial x}\left(\lambda_i\frac{\partial T(x,t)}{\partial x}\right) + Q_{\text{ohm}}(x,t) + Q_{\text{rxn}}(x,t) + Q_{\text{rev}}(x,t). \tag{3.43}$$

For the separator:

$$\rho_{\text{sep}} C_{p,\text{sep}} \frac{\partial T(x,t)}{\partial t} = \frac{\partial}{\partial x}\left(\lambda_{\text{sep}} \frac{\partial T(x,t)}{\partial x}\right) + Q_{\text{ohm}}(t), \tag{3.44}$$

with ρ_j representing the material density, $C_{p,j}$ is the specific heat capacitance, and λ_j stands for the thermal conductivity. The ohmic heat source, $Q_{\text{ohm}}(x,t)$, is described as follows. For the electrodes:

$$\begin{aligned} Q_{\text{ohm}}(x,t) = \sigma_i^{\text{eff}} \left(\frac{\partial \Phi_s(x,t)}{\partial x}\right)^2 + k_i^{\text{eff}} \left(\frac{\partial \Phi_e(x,t)}{\partial x}\right)^2 + \\ + \frac{2R}{F}\left(1 - t^+\right) k_i^{\text{eff}} T(x,t) \frac{\partial \ln c_e(x,t)}{\partial x} \frac{\partial \Phi_e(x,t)}{\partial x}. \end{aligned} \tag{3.45}$$

For the separator:

$$\begin{aligned} Q_{\text{ohm}}(x,t) = k_s^{\text{eff}} \left(\frac{\partial \Phi_e(x,t)}{\partial x}\right)^2 + \\ + \frac{2R}{F}\left(1 - t^+\right) k_s^{\text{eff}} T(x,t) \frac{\partial \ln c_e(x,t)}{\partial x} \frac{\partial \Phi_e(x,t)}{\partial x}. \end{aligned} \tag{3.46}$$

The reaction heat source, $Q_{\text{rxn}}(x,t)$, is given by

$$Q_{\text{rxn}}(x,t) = F a_i(t) j_i(x,t) \eta_i(x,t). \tag{3.47}$$

The reversible heat term, $Q_{\text{rev}}(x,t)$, is present only if the open-circuit potentials of the electrodes explicitly depend on the temperature. In such cases, it is given by

$$Q_{\text{rev}}(x,t) = F a_i(t) j_i(x,t) T(x,t) \left.\frac{\partial U_i(\theta_i^*(x,t), T(x,t))}{\partial T(x,t)}\right|_{T=T_{\text{ref}}}. \tag{3.48}$$

Boundary conditions for temperature are formulated in the following

$$-\lambda_p \left.\frac{\partial T(x,t)}{\partial x}\right|_{x=\hat{x}_p} = h_c(T_{\text{env}} - T(x,t)), \tag{3.49a}$$

$$-\lambda_n \left.\frac{\partial T(x,t)}{\partial x}\right|_{x=\hat{x}_n} = h_c(T(x,t) - T_{\text{env}}). \tag{3.49b}$$

At the separator-electrode interfaces boundary conditions are given by

$$-\lambda_p \left.\frac{\partial T(x,t)}{\partial x}\right|_{x=\hat{x}_{p,s^-}} = -\lambda_s \left.\frac{\partial T(x,t)}{\partial x}\right|_{x=\hat{x}_{p,s^-}}, \tag{3.50a}$$

$$-\lambda_s \left.\frac{\partial T(x,t)}{\partial x}\right|_{x=\hat{x}_{s,n^+}} = -\lambda_n \left.\frac{\partial T(x,t)}{\partial x}\right|_{x=\hat{x}_{s,n^+}}. \tag{3.50b}$$

.

Here, h_c represents the convective heat coefficient between the cell and the external environment (which could be a coolant system), and T_{env} is the environmental temperature. The DFN model is also employed with lumped thermal models, such as the one described in equations (3.14), (3.15) for the ECM models, as seen in works like (Campbell et al., 2019).

Ageing dynamics

: The ageing model concerns battery capacity and SEI resistance dynamics, given by

$$\frac{dC(t)}{dt} = 3\frac{3600C(t)}{R_{p,n}\, A\, \Delta\theta_n\, c_{s,n}^{\max} L_n} \int_{\hat{x}_n}^{\hat{x}_{s,n}} j_n^{\text{side}}(x,t)\, dx, \tag{3.51}$$

$$\frac{dR_{\text{SEI}}(t)}{dt} = -\frac{M_w}{\rho_n\, v\, L_n} \int_{\hat{x}_n}^{\hat{x}_{s,n}} j_n^{\text{side}}(x,t)\, dx. \tag{3.52}$$

Here, M_w is the molar weight of the negative electrode, v is the admittance of the film, and $j_n^{\text{side}}(x,t)$ represents the side-reaction flux obtained using the Tafel equation

$$j_n^{\text{side}}(x,t) = -\frac{i_0^{\text{side}}(t)}{F} \exp\left(\frac{0.5F}{RT(x,t)} \eta_{n,\text{SEI}}^{\text{side}}(x,t)\right). \tag{3.53}$$

The side-reaction exchange current, $i_{\text{side},0}(t)$, is given by

$$i_0^{\text{side}}(t) = \begin{cases} i_{0,\text{base}}(\frac{|I(t)|}{I_{1C}})^w & \text{if } I(t) < 0 \\ 0 & \text{otherwise} \end{cases} \tag{3.54}$$

where $i_{0,\text{base}}$ is the base side-reaction current, I_{1C} is the current corresponding to a 1C rate, and w is an empirical coefficient (typically $w = 2$).

Note that, as per the presented model, no degradation occurs during cell discharge or rest conditions ($I(t) \geq 0$).

The side-reaction overpotential $\eta^{\text{side}_{n,\text{SEI}}}(x,t)$, linked to SEI growth, is defined as follows

$$\eta_{n,\text{SEI}}^{\text{side}}(x,t) = \Phi_s(x,t) - \Phi_e(x,t) - U_{\text{SEI}} - j_n(x,t)F\frac{R_{\text{SEI}}}{A\, L_n\, a_n(t)}, \quad x \in [\hat{x}_{s,n}, \hat{x}_{\text{n}}] \tag{3.55}$$

where U_{SEI} denotes the reference potential for the SEI side reaction.

It is important to note that the ageing model described here is applicable under the assumption of no lithium plating deposition. This is expressed by the condition

$$\eta_{n,pl}^{\text{side}}(x,t) = \Phi_s(x,t) - \Phi_e(x,t) - U_{pl} - j_n(x,t)F\frac{R_{\text{SEI}}}{A\, L_n\, a_n(t)} > 0, \tag{3.56}$$

where U_{pl} represents the reference potential for the lithium-deposition side reaction. This constraint is generally met if the voltage does not exceed a specific threshold ($V(t) \leq V_{\max}$), although this formulation is conservative. For more extensive insights into ageing models, consult references like (Ramadass et al., 2004).

3.3.2 Simplified DFN model

Various adjustments can be applied to the DFN model to reduce its complexity. Utilizing electrochemistry-based battery models in BMS continues to pose challenges due to their computational burden. In this section we describre a highly efficient implementation of the DFN model, effecting a substantial reduction in computational time, as proposed in Khalik, Donkers, and Bergveld, 2021. This efficient implementation has been developed into an openly accessible toolbox, available for download called Toolbox for fast battery simulation (TOOFAB). In the following, first we define the simplifications made to the DFN and then we describe the model implementation that enhance the computational complexity.

Simplification assumptions

In the following, we define the simplifications made to the DFN. It is important to mention that the material characteristics that define the parameters within the DFN model (and SPM as we can see later in this chapter) must be established. Several studies (Doeff et al., 2000; Safari and Delacourt, 2010; Valøen and Reimers, 2005), has demonstrated that several of these material properties are not inherently constant and can undergo substantial variation contingent on the Li-ion concentration in the material. The concentration-dependent nature of electrolyte transport properties has been quantified and demonstrated across various electrolyte types. The concentration-dependent parameters furnished within these studies have been employed in diverse literature instances. For in-depth considerations and concentration-dependent parameters definitions we refer to Torchio et al., 2016. Let discuss about the DFN mdeol simplification introduced in Khalik, Donkers, and Bergveld, 2021.

- The rate equation Butler-Volmer (3.32) can be linearized around the origin with respect the overpotential (η), given that $\frac{F}{RT} >> |\eta|$.

  $$j_i = \frac{i_0}{RT}(\Phi_s - \Phi_e - U_i), \tag{3.57}$$

  which is reasonable up to an overpotential of approximately $|\eta| < 0.01$.

- A zero-order Taylor approximation can be applied to the concentration-dependent parameters, such as $k(c_e) = k(c_e^0)$, $D_e(c_e) = D_e(c_e^0)$, $D_s(s) = D_s(s^0)$, $v(c_e) = v(c_e^0)$, where c_e^0 is the evaluation point and $s = c_{s,e}/c_s^{\max}$ is the stoichiometry. Two approaches can be considered. (i) Dynamic evaluation points that vary over space and time. In this context, the evaluation point is selected post time discretization, utilizing the concentration-dependent parameters' values at the previous time sample t_{k-1}, i.e., $k(c_e^0) = k(c_e(t_{k-1})$ and similarly for the others parameters. (ii) Constant evaluation points that ensure concentration-dependent parameters remain invariant across space and time. In this scenario, $k(c_e^0) = k(\bar{c}_e$ and similarly for the remaining parameters. Here, $\bar{c}_e$ signifies the expected average concentration in the electrolyte, often set as $\bar{c}_e = c_{e\mathrm{eq}}$ where $c_{e\mathrm{eq}}$ is the equilibrium average concentration in the electrolyte, and $\bar{s}$ is the expected average stoichiometry, typically chosen as $\bar{s} = (\mathrm{s}_{100\%} + \mathrm{s}_{0\%})/2$.

- Lastly, a common simplification involves a two-parameter polynomial approximation of solid-phase diffusion. This approximation assumes a parabolic concentration profile within a particle over the radial dimension r. By incorporating this approximate concentration into (3.30), volume-averaging the ensuing expression, and considering the boundary conditions (3.36), expressions for bulk concentration ($c_{s,\mathrm{bulk}}$) and surface concentration ($c_{s,e}$) can be derived:

  $$\frac{\partial c_{s,\mathrm{bulk}}}{\partial t} = -\frac{3}{R_s} j, \tag{3.58}$$

  $$c_{s,e} = c_{s,\mathrm{bulk}} - \frac{R_s}{5D_s} j. \tag{3.59}$$

  This simplification notably streamlines the diffusion equation described by the Fick's law in (3.30), the only governing equation dependent on r, into a mere two equations describing the bulk and surface concentrations of solid-phase particles as functions of x and t.

Model implementation

The implementation of the DFN model, along with its corresponding simplifications, involves a series of sequential steps. Conventional spatial and temporal discretization methods are applied to yield a system of algebraic equations (AEs). In this section, we will concisely outline this process to formulate the set of AEs resulting from discretization. For more comprehensive insights into the discretization methodology, interested readers are directed to (Khalik, Donkers, and Bergveld, 2021), while for the finite-volume method (FVM) discretization, emplyed to determine the edge parameter values for the control volumes is achieved through the utilization of the harmonic mean between two adjacent control volumes, as detailed in (Torchio et al., 2016).

As an initial step, spatial discretization is applied to the partial differential equations (PDEs). The equation that describes solid-phase concentration diffusion (3.30) is discretized along the radial direction using the finite difference method (FDM), leading to a set of differential-algebraic equations (DAEs). Meanwhile, equations (3.72), (3.37), (3.38) are discretized utilizing the finite volume method (FVM), culminating in a resulting set of nonlinear DAEs, expressed as follows

$$\frac{d\mathbf{c_s}}{dt} = A_{c_s}\mathbf{c_s} + B_{c_s}\mathbf{j_i}, \tag{3.60a}$$

$$\frac{d\mathbf{c_e}}{dt} = A_{c_e}\mathbf{c_e} + B_{c_e}\mathbf{j_i}, \tag{3.60b}$$

$$0 = A_{\phi_s}\boldsymbol{\phi_s} + B_{\phi_s}\mathbf{j_i} + C_{\phi_s}I, \tag{3.60c}$$

$$0 = A_{\phi_e}\boldsymbol{\phi_e} + B_{\phi_e}\mathbf{j_i} + D_{\phi_e}, \ln(\mathbf{c_e}) \tag{3.60d}$$

where, in the above equations, the bold-faced symbols represent their respective vector variables, defined as

$$\mathbf{c_s}(t) = \begin{bmatrix} \mathbf{c}_{s,n}(x_l, t) \\ \vdots \\ \mathbf{c}_{s,n}(x_{n_n}, t) \\ \mathbf{c}_{s,p}(x_{n_n+n_s+1}, t), t) \\ \vdots \\ \mathbf{c}_{s,p}(x_{n_n+n_s+n_p}, t), t) \end{bmatrix},$$

$$\mathbf{c_{s,i}}(x, t) = \begin{bmatrix} c_s(x, r_{i,1}, t) \\ \vdots \\ c_s(x, r_{i,n_{r,i}}, t) \end{bmatrix},$$

$$\mathbf{c_e}(t) = \begin{bmatrix} c_e(x_l, t) \\ \vdots \\ c_e(x_{n_n+n_s+n_p}, t), t) \end{bmatrix},$$

$$\boldsymbol{\phi}_s(t) = \begin{bmatrix} \phi_s(x_l, t) \\ \vdots \\ \phi_s(x_{n_n}, t) \\ \phi_s(x_{n_n+n_s+1}, t), t) \\ \vdots \\ \phi_s(x_{n_n+n_s+n_p}, t), t) \end{bmatrix},$$

where x_i and r_i represent the grid points of the discretization. Additionally, $\boldsymbol{\phi}_e$ and

$\mathbf{j}_i$ are defined analogously to $\mathbf{c}_e$ and $\boldsymbol{\phi}_s$ respectively. Moreover, in the above expressions, n_n, n_s, and n_p denote the number of elements in the FVM discretization for the negative electrode, separator, and positive electrode, respectively. Similarly, $n_{r,i}$ correspond to the number of elements in the FDM discretization for the negative electrode and positive electrode. For the construction of matrices $\mathbf{A}_i$, $\mathbf{B}_i$, $i \in \{c_s, c_e, \phi_s, \phi_e\}$, C_{ϕ_s}, and $\mathbf{D}_{\phi_e}$ we refer to Xia et al., 2017b. The system of DAEs (3.60) is interconnected through the Butler-Volmer rate equation, expressed as

$$\begin{aligned}\mathbf{j}_i = \operatorname{diag}\left(\mathbf{i}_0(\bar{\mathbf{c}}_e, \bar{\mathbf{c}}_s)\frac{F}{RT}\right)\left(\exp\left(0.5\frac{F}{RT}(\boldsymbol{\phi}_s - \bar{\boldsymbol{\phi}}_e - \mathbf{U}(\bar{\mathbf{c}}_s))\right) - \right.\\ \left. - \exp\left(0.5\frac{F}{RT}(\boldsymbol{\phi}_s - \bar{\boldsymbol{\phi}}_e - \mathbf{U}(\bar{\mathbf{c}}_s))\right)\right),\end{aligned} \tag{3.61}$$

where the notation $\operatorname{diag}(\mathbf{z})$ represents a diagonal matrix with the vector $\mathbf{z}$ on its main diagonal. Additionally, the barred bold-faced variables $\bar{\mathbf{c}}_s$, $\bar{\mathbf{c}}_e$, and $\bar{\boldsymbol{\phi}}_e$ refer to selected versions of their non-barred counterparts. Specifically, $\bar{\mathbf{c}}_s$ represents the vector of solid-phase surface concentrations, and $\bar{\mathbf{c}}_e$ and $\bar{\boldsymbol{\phi}}_e$ denote the parts of $\mathbf{c}_e$ and $\boldsymbol{\phi}_e$ related to the electrodes. In particular, these quantities are related as follows

$$\begin{aligned}\bar{\mathbf{c}}_s &= \mathbf{A}_{c_s}\mathbf{c}_s,\\ \bar{\mathbf{c}}_e &= \mathbf{A}_{c_e}\mathbf{c}_e,\\ \bar{\boldsymbol{\phi}}_e &= \mathbf{A}_{\phi_e}\boldsymbol{\phi}_e,\end{aligned} \tag{3.62}$$

where

$$\bar{\mathbf{A}}_{c_s} = \operatorname{diag}\left(\mathbf{I}_{n_n} \otimes [\mathbf{0}_{1\times n_{r,n}-1}, 1],\, \mathbf{I}_{n_p} \otimes [0_{1\times n_{r,p}-1}, 1]\right),$$

$$\bar{\mathbf{A}}_{c_e} = \bar{\mathbf{A}}_{\phi_e} = \begin{bmatrix}\mathbf{I}_{n_n} & \mathbf{0} & \mathbf{0}\\ \mathbf{0} & \mathbf{0} & \mathbf{I}_{n_p}\end{bmatrix},$$

where $\otimes$ denotes the Kronecker product. Subsequently, the DAEs (3.60a) and (3.60b) are further discretized in time using a backward Euler scheme with a sampling time δt, resulting in the following set of algebraic equations (AEs)

$$0 = \hat{\mathbf{A}}_{c_s}\mathbf{c}_s(t_k) + \hat{\mathbf{B}}_{c_s}\mathbf{j}_i(t_k) + \mathbf{c}_s(t_{k-1}), \tag{3.63}$$

$$0 = \hat{\mathbf{A}}_{c_e}\mathbf{c}_e(t_k) + \hat{\mathbf{B}}_{c_e}\mathbf{j}_n(t_k) + \mathbf{c}_e(t_{k-1}), \tag{3.64}$$

$$0 = \mathbf{A}_{\phi_s}\boldsymbol{\phi}_s(t_k) + \mathbf{B}_{\phi_s}\mathbf{j}_i(t_k) + \mathbf{C}_{\phi_s}II(t_k), \tag{3.65}$$

$$0 = \mathbf{A}_{\phi_e}\boldsymbol{\phi}_e(t_k) + \mathbf{B}_{\phi_e}\mathbf{j}_i(t_k) + \mathbf{D}_{\phi_e}\ln(\mathbf{c}_e(t_k)), \tag{3.66}$$

where $t_k = k\delta t$ for $k \in \{1, \ldots, N\}$ and N is the number of simulation steps. Furthermore, $\hat{\mathbf{A}}_{c_s} = \delta t\mathbf{A}_{c_s} - \mathbf{I}_{n_n n_{r,n} + n_p n_{r,p}}$, $\hat{\mathbf{B}}_{c_s} = \delta t\mathbf{B}_{c_s}$, $\hat{\mathbf{A}}_{c_e} = \delta t\mathbf{A}_{c_e} - \mathbf{I}_{n_n+n_s+n_p}$ and $\hat{\mathbf{B}}_{c_e} = \delta t\mathbf{B}_{c_e}$.

Several solution methods for solving a set of nonlinear algebraic equations can used like Newton's method. However but due to a large number of state variables, this can be slow. In fact the main computational challenge lies in finding the inverse of the Jacobian matrix of the AEs. For in-depth understanding of the solution method has been used so far in this thesis we refer to Section 3.2 in (Khalik, Donkers, and Bergveld, 2021). With this approach, instead of solving equations one by one, equations are substituted to retain information, while reducing the total equations. This maintains the full Jacobian information while making the process more efficient.

3.3.3 Single particle model with thermal and electrolyte dynamics

The SPMeT, is an approximation of the Doyle-Fuller-Newman model and offers valuable insights into the charge/discharge behavior of dual insertion cells. In this context, the work presented by Pozzi et al., 2020 serves as a point of reference.

Designed for cells with two composite electrodes featuring active insertion material, electrolyte, and inert conducting material, the model distinguishes three vital components of the battery cell denoted as p, s, n.

The single-cell dynamics are des through a system of Ordinary Differential Equations (ODEs). To simplify the complex Fick's laws associated with each electrode, a polynomial approximation is employed to translate the solid ions concentration along the particle radius into an ODE, as seen in Subramanian, Diwakar, and Tapriyal, 2005. Additionally, the Finite Volume Method (FVM) is employed in spatially discretizing the Partial Differential Equations (PDEs) that describe the diffusion of electrolyte ions.

By incorporating aging dynamics into the SPMeT, we establish a connection with the DFN model (as explained in section 3.3.1), enhancing its suitability for integration into real-time optimization-based controllers. The core of our model originates from the SPMe framework developed by Moura et al., 2016. However, spatial discretization through the Finite Volume Method is applied to the Partial Differential Equation (PDE) governing ion diffusion within the electrolyte. By transforming the Fick's laws into Ordinary Differential Equations (ODEs) using a polynomial approximation, as the approach in (Subramanian, Diwakar, and Tapriyal, 2005), we simplify the modeling process and enhance computational efficiency.

Moreover, the equations outlined in (Perez et al., 2017) for the lumped thermal dynamics are here adapted. It is worth noting that this enhanced framework incorporates the influence of ageing phenomena, including capacity fade and Solid Electrolyte Interphase resistance growth, as discussed by Ramadass et al., 2004. The consideration of these ageing effects ensures a more comprehensive representation of the battery's behavior over time.

Similar to the methodology outlined in Section 3.3.1 , we maintain the distinction between two separate indexes, which categorize equations applicable across all sections $j = \{p, s, n\}$ and equations relevant exclusively within the electrodes $i = \{p, n\}$.

Electrochemical model dynamics

The electrochemical dynamics of the SPMeT is described by $3 + 3N$ electric state variables

$$\begin{bmatrix} \overline{\theta}_p(t) & \overline{q}_p(t) & \overline{q}_n(t) & c_{e,p}^{[1]}(t) & \dots & c_{e,n}^{[N]}(t) \end{bmatrix}, \tag{3.67}$$

where N is the number of discretization volumes for each section of the cell, $\overline{\theta}_p(t)$ the cathode average stoichiometry, $\overline{q}_i(t)$ the volume-averaged concentration flux for the i-th electrode and $c_{e,j}^{[k]}(t)$ the electrolyte concentration in the k-th volume of the j-th cell section. Note that indices j and i will be used to refer to the three cell sections $\{p, s, n\}$ and to the two electrodes $\{p, n\}$ respectively.

The dynamics of the cathodic average stoichiometry can be expressed as

$$\dot{\overline{\theta}}_p(t) = -\tfrac{\Delta\theta_p}{C^{\mathrm{S}}_{\mathrm{batt}}} I(t), \tag{3.68}$$

where C_{batt} is the nominal cell capacity, $\Delta\theta_i = \theta_i^{100\%} - \theta_i^{0\%}$ the difference between the values of the stoichiometry at battery fully charged and fully discharged, and I the current, input of the system[1]. In order to avoid a further differential equation, the anodic average stoichiometry is computed according to the algebraic condition (see Di Domenico, Stefanopoulou, and Fiengo, 2010)

$$\overline{\theta}_n(t) = \theta_n^{0\%} + \tfrac{\overline{\theta}_p(t) - \theta_p^{0\%}}{\Delta\theta_p} \Delta\theta_n. \tag{3.69}$$

For each electrode, the volume-averaged concentration flux dynamics is described by

$$\dot{\overline{q}}_i = -30 \tfrac{D_{s,i}(T)}{R^2_{p,i}} \overline{q}_i(t) - \tfrac{45\Delta\theta_i c^{\max}_{s,i}}{6R_{p,i}C^{\mathrm{S}}_{\mathrm{batt}}} I(t), \tag{3.70}$$

where $D_{s,i}$ is the solid diffusion coefficient, $c^{\max}_{s,i}$ the maximum solid concentration, $R_{p,i}$ the solid particle radius and θ_i the surface stoichiometry given by

$$\theta_i(t) = \overline{\theta}_i(t) + \tfrac{8R_{p,i}\overline{q}_i(t)}{35c^{\max}_{s,i}} - \tfrac{R^2_{p,i}\Delta\theta_i}{105D_{s,i}(T)C^{\mathrm{S}}_{\mathrm{batt}}} I(t). \tag{3.71}$$

The ODEs describing the diffusion of the electrolyte concentration derive from the finite volume discretization of the original PDEs proposed in Moura et al., 2016. Each section of the cell is divided into N finite volumes. The k-th volume in the j-th section is centered in the spatial coordinate $x_{j,k}$ and ranges within the interval $[x_{j,k-\frac{1}{2}}, x_{j,k+\frac{1}{2}}]$, with width $\Delta x_j = L_j/N$, where L_j is the section thickness. For each volume, the electrolyte concentration dynamics is given by

$$\epsilon_j \frac{\partial c^{[k]}_{e,j}(t)}{\partial t} = \left[\tfrac{\tilde{D}_e(x)}{\Delta x_j} \tfrac{\partial c_{e,j}(x,t)}{\partial x} \right]^{x_{j,k+\frac{1}{2}}}_{x_{j,k-\frac{1}{2}}} + K(j), \tag{3.72}$$

with ϵ_j the material porosity, A the contact area between solid and electrolyte phases, F the Faraday constant, t_+ the transference number and $\tilde{D}_e(x)$ the electrolyte diffusion coefficient. The term $K(j)$ is null for the separator section and $\mp(1-t_+)\, I(t)/FAL_n$ for cathode and anode respectively. The electrolyte diffusion coefficient computed as

$$\tilde{D}_e(x, T(t)) = \begin{cases} D_{e,p/s} & \text{for} \quad x \in \{x_{p,N-\frac{1}{2}}, x_{s,1-\frac{1}{2}}\} \\ D_{e,s/n} & \text{for} \quad x \in \{x_{s,N-\frac{1}{2}}, x_{n,1-\frac{1}{2}}\} \\ D^{\mathrm{eff}}_{e,j}(T(t)) & \text{otherwise} \end{cases} \tag{3.73}$$

where $D^{\mathrm{eff}}_{e,j}(T(t)) = D_{e,j}(T(t))\epsilon_j^{p_j}$ and p_j the Bruggeman coefficient and $D_{e,p/s}$, $D_{e,s/n}$ are electrolyte diffusion coefficient between the cell sections that are evaluated as the harmonic mean operator $f(\lambda_1, \lambda_2, \rho_1, \rho_2) = \frac{\rho_1\rho_2(\lambda_1+\lambda_2)}{\rho_1\lambda_1+\rho_2\lambda_2}$according to what is proposed

$$\begin{aligned} D_{e,p/s} &= f(D^{\mathrm{eff}}_{e,p}(T(t)), D^{\mathrm{eff}}_{e,s}(T(t)), \Delta x_p, \Delta x_s) \\ D_{e,s/n} &= f(D^{\mathrm{eff}}_{e,s}(T(t)), D^{\mathrm{eff}}_{e,n}(T(t)), \Delta x_s, \Delta x_n) \end{aligned} \tag{3.74}$$

---

[1] In this work, we adopt the convention that the battery is being charged when a negative current is applied.

The state of charge $z(t)$ can be computed according to the cathodic or anodic convention as it is shown by the following relation

$$z(t) = \frac{\overline{\theta}_p(t) - \theta_p^{0\%}}{\Delta\theta_p} = \frac{\overline{\theta}_n(t) - \theta_n^{0\%}}{\Delta\theta_n}. \tag{3.75}$$

Finally, the output terminal voltage is given by

$$V(t) \triangleq V_{\mathrm{oc}}(t) + \overline{\eta}_p(t) - \overline{\eta}_n(t) + \Delta\Phi_e(t), \tag{3.76}$$

where $V_{\mathrm{OCP}}(t)$ is the overall open circuit potential defined as

$$V_{\mathrm{OCP}}(t) \triangleq U_p(t) - U_n(t), \tag{3.77}$$

with $U_p(t)$ and $U_n(t)$ the cathodic and anodic open circuit potentials, respectively. The expression of these latter, given in equations (3.78)-(3.80), is obtained using a fitting procedure on the experimental data provided in Ecker et al., 2015

$$\begin{aligned} U_p =& 4.571 + 0.024140\theta_p - 7.8370\theta_p^2 + 8.07\theta_p^3 + \qquad (3.78)\\ &+ 20.94\theta_p^4 - 40.7\theta_p^5 + 18.45\theta_p^6, \qquad (3.79)\end{aligned}$$

$$U_n = \frac{0.00694 + 0.1261\theta_n}{\theta_n^2 + 0.6995\theta_n + 0.00405}. \tag{3.80}$$

The overpotentials $\overline{\eta}_i(t)$ are defined, for each electrode, as

$$\overline{\eta}_i(t) = \tfrac{2RT(t)}{F}\sinh^{-1}\left(\tfrac{\Delta\theta_i R_{p,i}}{6\bar{i}_{0,i}(t)C_{\mathrm{batt}}} I(t)\right), \tag{3.81}$$

in which the quantity $\bar{i}_{0,i}(t)$ is given by

$$\bar{i}_{0,i}(t) = Fk_i(T)\sqrt{\overline{c}_{e,i}(t)\theta_i(t)(1-\theta_i(t))}, \tag{3.82}$$

where k_i is the rate reaction constant, $\overline{c}_{e,i}(t)$ is the average electrolyte concentration in the i-th section.

$$\overline{c}_{e,i}(t) = \tfrac{1}{N}\textstyle\sum_{k=1}^{N} c_{e,i}(t)^{[k]}(t) \tag{3.83}$$

Returning to (3.76), $\Delta\Phi_e(t)$ is evaluated by

$$\Delta\Phi_e(t) = \Phi_e^{\mathrm{drop}}(t) + \frac{2RT(t)}{F}(1-t_+)\log\left(\frac{c_{e,p}^{[1]}(t)}{c_{e,n}^{[N]}(t)}\right), \tag{3.84}$$

whose terms are already defined except for $\Phi_e^{\mathrm{drop}}(t)$, which is approximated by

$$\Phi_e^{\mathrm{drop}}(t) \simeq -\tfrac{I(t)}{2N}(\phi_p(t)) + 2\phi_s(t) + \phi_n(t)), \tag{3.85}$$

The quantities $\phi_j(t)$, $j \in \{p, s, n\}$, depend on the electrolyte conductivity and are computed assuming a trapezoidal shape of the ionic current $i_e(x,t)$ along the spatial domain as

$$\phi_j(t) = \Delta x_j \textstyle\sum_{k=1}^{N} \tfrac{NUM(j)}{\kappa(c_{e,j}^{[k]}(t),T(t))\epsilon_j^{pj}} \tag{3.86}$$

where the numerator varies with the cell section j as

$$NUM(j) = \begin{cases} 2k-1 & \text{for } j = p \\ 1 & \text{for } j = s \\ 2N-2k+1 & \text{for } j = n \end{cases}$$

and $\kappa(c_{e,j}^{[k]}(t), T(t))$ is the temperature-dependent electrolyte conductivity for the k-th volume of the j-th section and it is a nonlinear function of the cell temperature and the quantity $\gamma_j^{[k]}(t) = 10^{-3} c_{e,j}^{[k]}(t)$ that is empirically derived as it follows

$$\begin{aligned} \kappa(c_{e,j}^{[k]}(t), T(t)) \quad &= (0.2667(\gamma_j^{[k]}(t))^3 - 1.2983(\gamma_j^{[k]}(t))^2 + \\ &+1.7919\gamma_j^{[k]}(t) + 0.1726)e^{-\frac{E_{\alpha,\kappa}}{RT(t)}} \end{aligned} \tag{3.87}$$

Thermal dynamics

The cell temperature dynamics is approximated by a lumped model in which R_{th} and C_{th} represent the thermal resistance and capacity respectively. These parameters model the thermal interaction between the cell and the coolant as the following equation shows

$$C_{th}\dot{T}(t) = Q(t) - \tfrac{\Delta T}{R_{th}} \tag{3.88}$$

with $\Delta T = T(t) - T_{\text{coolant}}$ the temperature difference between cell and coolant, that in this paper in assumed to be constant at $T_{coolant} = 300$ Kelvin and $Q(t)$ the heat generation term

$$Q(t) = |I(t)||V(t) - V_{\text{OCP}}(t)| \tag{3.89}$$

Ageing dynamics

The model for the primary degradation mechanisms has been revisited here. Specifically, the equations for capacity loss and SEI resistance growth, as proposed by (Ramadass et al., 2004), are as follows:

$$\frac{dC(t)}{dt} = 3\frac{3600C(t)}{R_{\text{p,n}}\, A\, \Delta\theta_n\, c_{s,n}^{max}} j_{\text{side,n}}(t) \tag{3.90}$$

$$\frac{dR_{\text{SEI}}(t)}{dt} = -\frac{M_w}{\rho_n v} j_n^{\text{side}}(t) \tag{3.91}$$

The mean side reaction flux, denoted as $j_n^{\text{side}}(t)$, is given by:

$$j_n^{\text{side}}(t) = -\frac{i_0^{\text{side}}(t)}{F} \exp\left(\frac{0.5F}{RT(t)} \eta_{n,\text{SEI}}^{\text{side}}(t)\right) \tag{3.92}$$

where $i_0^{\text{side}}(t)$ represents the initial side reaction current, F is the Faraday constant, R is the gas constant, and $T(t)$ denotes the cell temperature.

In this scenario, we assume that no degradation occurs during cell discharge, as stated in equation.

The mean side reaction overpotential, $\eta_{n,\text{SEI}}^{\text{side}}(t)$, can be expressed as

$$\eta_{n,\text{SEI}}^{\text{side}}(t) = \eta_n(t) + U_n(\theta_n^*(t)) - U_{\text{SEI}} \tag{3.93}$$

Here, it is assumed that no Lithium-ion deposition occurs, meaning:

$$\eta_{n,\text{pl}}^{\text{side}}(t) = \eta_n(t) + U_n(\theta_n^*(t)) - U_{\text{pl}} > 0 \tag{3.94}$$

.

3.4 Conclusions

This chapter has explored the key aspects of equivalent circuit models and electrochemical models used in battery research, highlighting their utility and the intricate mathematical frameworks that underlie them.

Equivalent Circuit Models (ECMs) serve as valuable bridges between theory and practical implementation. The Thévenin Model and Dual Polarization Model provide a simplified yet effective representation of lithium-ion batteries, incorporating State of Charge (SOC)-dependent electrical parameters and their interaction with thermal models.

Electrochemical models, exemplified by the Pseudo Two-Dimensional (P2D) model and its derivatives, offer in-depth insights into battery behavior but come with a significant computational cost. Researchers have developed reduced-order models based on the P2D framework, such as TOOFAB, Single Particle Models (SPM and SPMe), and SPMeT, to strike a balance between precision and computational efficiency.

Parameters dependent on Li-ion concentration, linearizing rate equations, and using polynomial approximations for solid-phase diffusion are among the concessions made to ensure computational feasibility. These models also require certain material characteristics that can change with Li-ion concentration.

Furthermore, the chapter has elucidated the practical implementation of these models, employing finite volume methods for spatial discretization and backward Euler schemes for temporal discretization, making them valuable tools for simulation and control purposes.

Chapter 4

Set mathematical background

Set representation plays a crucial role in the field of modelling and estimation, allowing us to capture the uncertainties and complexities inherent in real-world systems. One such representation that has gained prominence in recent years is the zonotope and its more versatile counterpart, the constrained zonotope. These mathematical constructs offer a unique perspective for describing complex regions in multi-dimensional spaces, making them invaluable tools in the fields of control theory, robotics, and signal processing, to name just a few.

This chapter introduces the definitions of zonotopes and constrained zonotopes, enabling the understanding of their possible practical applications. Before delving into the specifics of these mathematical representations, it is essential to grasp the broader context in which they operate.

Complex systems often defy easy characterization due to their nonlinearity, uncertainty, and multidimensionality. In such scenarios, traditional point estimates can fall short in providing a comprehensive understanding of the system's behavior. Sets, on the other hand, offer a way to encapsulate a range of possibilities, accounting for uncertainties and variations.

However, the challenge lies in representing these sets in a computationally efficient and accurate manner. Zonotopes and constrained zonotopes emerge as promising solutions to this challenge. They provide a structured framework for modeling sets in a way that enables efficient mathematical operations and analysis.

In this chapter basic set operations and notations are introduced and discussed. Then the zonotopes definition is introduced. They are known for their central symmetry. We will explore their properties, applications, and computational advantages, particularly in the context of linear mapping and Minkowski sum operations. However, we will also discover that zonotopes have limitations, especially when it comes to representing non-symmetric regions.

This limitation paves the way for the introduction of constrained zonotopes, a more flexible representation that can capture the intricacies of asymmetric convex polytopes. These representations open up new possibilities in modeling complex shapes and structures, where symmetry is not a given.

As the operations progress, there's often an increase in the number of generators and constraints, potentially leading to computational inefficiency. To address this, this chapter looks into strategies for reducing both the number of generators and constraints while preserving the representation's accuracy. This reduction process is a key factor in achieving computationally efficient and conservative results.

The remainder of this chapter is organized as it follows: Section 4.1 introduces basic set notations and operations, Section 4.2 defines the concepts of zonotopes and constrained zonotopes and how set operations between them are computed in their specific representations. Section 4.4 describes standard concepts of interval analysis and finally 4.5 concludes the chapter.

4.1 Basic set operations and notation

This section introduces and defines several fundamental set operations commonly utilized in the computation of enclosures necessary for set-based state estimation (Le et al., 2013, Scott et al., 2016a). Consider $Z, W \subset \mathbb{R}^n$, and $Y \subset \mathbb{R}^m$, with $\mathbf{R} \in \mathbb{R}^{m \times n}$. The following set operations are defined: linear mapping, Minkowski sum, and generalized intersection, represented by equations (4.1), (4.2), and (4.3), respectively.

$$RZ \triangleq \{Rz : z \in Z\}, \tag{4.1}$$

$$Z \oplus W \triangleq \{z + w : z \in Z, w \in W\}, \tag{4.2}$$

$$Z \cap RY \triangleq \{z \in Z : Rz \in Y\}. \tag{4.3}$$

The linear mapping RZ can be efficiently and accurately computed using techniques such as ellipsoids or parallelotopes. To denote the set of images obtained by applying the linear mapping R to each element $z \in Z$, we use the notation $\{Rz | z \in Z\}$.

The Minkowski sum $Z \oplus W$ represents the set of all possible element-wise sums of pairs of elements, where $z \in Z$ and $w \in W$. It is important to note that to compute the Minkowski sum (4.2) accurately, conservative outer-approximation techniques must be employed (Chisci, Garulli, and Zappa, 1996, Schweppe, 1968).

The generalized intersection $Z \cap RY$ defines the set of elements $z \in Z$ and whose images $Rz \subset Y$. We represent this operation using the notation $\{z \in Z | Rz \in Y\}$.

When dealing with ellipsoids or parallelotopes, the linear mapping can be efficiently and accurately computed. However, both the Minkowski sum and the intersection need to be approximated conservatively from the outside. On the other hand, when working with intervals, the Minkowski sum can be computed efficiently and precisely. However, the linear mapping and the intersection tend to be conservative due to the presence of the wrapping effect. This effect, well-known in interval analysis, arises from the inability of an interval variable to capture existing dependencies between its components (Moore, 1966).

In contrast, convex polytopes are closed under the operations (4.1)–(4.3). Linear mapping and Minkowski sum can be efficiently computed using the vertex representation (V-rep), while the intersection can be efficiently computed using the half-space representation (H-rep). However, if multiple computations of (4.1)–(4.3) are performed using convex polytopes, conversions between H-rep and V-rep are required, which can be computationally expensive and numerically unstable in high dimensions (Hagemann, 2015).

In the following, functions with set-valued arguments will consistently denote the exact image of the set under the function. For example, $f(X, W)$ represents the set of $f(x, w)$ values for all $x \in X$ and $w \in W$.

In addition, the following notations are defined. Let κ be a function of class C^2 and z denote its argument. Then, κ denotes the q-th component of κ, $\nabla\kappa$ denotes the gradient of κ, and $\mathbf{H}_{\kappa_q}$ is an upper triangular matrix describing half of the Hessian of κ_q. Specifically, $H_{ii}\kappa_q = \frac{1}{2}\frac{\partial^2 \kappa_q}{\partial z^2}$, $H_{ij}\kappa_q = \frac{\partial^2 \kappa_q}{\partial z_i \partial z_j}$ for $i < j$, and $H_{ij}\kappa_q = 0$ for $i > j$.

4.2 Zonotopes and constrained zonotopes

Zonotopes are sets that exhibit central symmetry (Kühn, 1998), enabling precise and computationally efficient calculations for both equations (4.1) and (4.2). Nevertheless, equation (4.3) does not typically form a zonotope. It presents challenges in terms of computation and necessitates outer-approximation as described in Bravo, Alamo, and Camacho, 2006 .

Definition 1 *A set $Z \subseteq \mathbb{R}^n$ is a zonotope if there exists $(\mathbf{G}_z, \mathbf{c}_z) \in \mathbb{R}^{n\times n_g} \times \mathbb{R}^n$ such that*

$$Z = \{\mathbf{c}_z + \mathbf{G}_z\boldsymbol{\xi} : \|\boldsymbol{\xi}\|_\infty \leq 1\}. \tag{4.4}$$

The generator representation (G-rep) of (4.4) is employed. Each column of $\mathbf{G}_z$ serves as a generator, while $\mathbf{c}_z$ represents the center. In this thesis, we denote $\boldsymbol{\xi}$ as the generator variables. By defining the n-dimensional unitary hypercube as $B_\infty^{n_g} = \boldsymbol{\xi} \in \mathbb{R}^{n_g} : |\boldsymbol{\xi}| \leq 1$, a zonotope Z can be alternatively seen as an affine transformation of $B_\infty^{n_g}$. This transformation is given by $Z = \mathbf{c}_z \oplus \mathbf{G}_z B_\infty^{n_g}$. It is important to note that the G-rep is applicable only to centrally symmetric convex polytopes due to the symmetry of $B_\infty^{n_g}$. Another interpretation of a zonotope Z involves expressing it as the Minkowski sum of line segments. This can be described as $Z = \oplus_{j=1}^{n_g} g_{z,j} B_\infty \oplus \mathbf{c}_z$, with $g_{z,j}$ the j-th column of $\mathbf{G}_z$.

Zonotopes offer computational advantages over other set representations. Let $Z = \mathbf{G}_z, \mathbf{c}_z \subseteq \mathbb{R}^n$, $W = \mathbf{G}_w, \mathbf{c}_w \subseteq \mathbb{R}^n$, and $R \in \mathbb{R}^{m\times n}$. The set operations (4.1) - (4.2) can be efficiently computed in the G-rep as follows:

$$\mathbf{R}Z = \{\mathbf{R}\mathbf{G}_z, \mathbf{c}_z\}, \tag{4.5}$$

$$Z \oplus W = \{[\mathbf{G}_z \mathbf{G}_w], \mathbf{c}_z + \mathbf{c}_w\}. \tag{4.6}$$

These operations only lead to a modest increase in the complexity of the G-rep, and there are efficient methods available to reduce this complexity.

Constrained Zonotopes (CZ) are a class of sets that extend the concept of zonotopes, as defined in Scott et al., 2016a. Compared to traditional zonotopes, CZs allow for the representation of asymmetric convex polytopes.

This means that CZs offer greater flexibility in representing more complex shapes and structures, compared to standard zonotopes, which are limited to centrally symmetric polyhedra. With their ability to represent asymmetric polyhedra, CZs are particularly useful in applications where symmetry is not present or undesired.

The computational benefits of zonotopes, such as efficient set operations and low computational burden, are also maintained in CZs.

Definition 2 *A set $CZ \subseteq \mathbb{R}^n$ is a constrained zonotope if there exists $(\mathbf{G}, \mathbf{c}, \mathbf{A}, \mathbf{v}) \in \mathbb{R}^{n\times n_g} \times \mathbb{R}^n \times \mathbb{R}^{n_c\times n_g} \times \mathbb{R}^{n_c}$ such that*

$$CZ = \{\mathbf{c}_z + \mathbf{G}_z\xi : ||\boldsymbol{\xi}||_\infty \leq 1, \mathbf{A}_z\boldsymbol{\xi} = \mathbf{b}_z\} \tag{4.7}$$

This representation is referred to as the constrained generator representation (CG-rep). In the CG-rep, each column of $\mathbf{G}$ represents a generator, $\mathbf{c}$ is the center, $\mathbf{A}\boldsymbol{\xi} = \mathbf{b}$ represents the constraints, and $\boldsymbol{\xi}$ denotes the generator variables. To further elaborate, a constrained zonotope CZ can be alternatively interpreted as an affine transformation of a constrained unitary hypercube $\mathbf{B}_\infty(\mathbf{A}, \mathbf{b})$, defined as $\{\boldsymbol{\xi} \in \mathbb{R}^{n_g} : ||\boldsymbol{\xi}||_\infty \leq 1, \mathbf{A}\boldsymbol{\xi} = \mathbf{b}\}$. This transformation is given by $CZ = \mathbf{c} \oplus \mathbf{G}\mathbf{B}_\infty(\mathbf{A}, \mathbf{b})$. Unlike zonotopes, constrained zonotopes have the ability to represent any convex polytope, provided that the complexity of the CG-rep is not limited. In fact, CZ is a constrained zonotope if and only if it is a convex polytope (Property 3.2). The compact notation CZ= $\{\mathbf{G}, \mathbf{c}, \mathbf{A}, \mathbf{b}\}$ is used to represent constrained zonotopes.

In addition to equations (4.1) and (4.2), the intersection operation (4.3) can also be computed exactly with constrained zonotopes. Let CZ= $\{\mathbf{G}, \mathbf{c}, \mathbf{A}, \mathbf{b}\} \subset \mathbb{R}^n$, $W = \{\mathbf{G}_w, \mathbf{c}_w, \mathbf{A}_w, \mathbf{b}_w\} \subset \mathbb{R}^n$, and $Y = \mathbf{G}_y, \mathbf{c}_y, \mathbf{A}_y, \mathbf{b}_y \subset \mathbb{R}^m$, with $R \in \mathbb{R}^{m \times n}$. The set operations (4.1)-(4.3) can be computed trivially in the CG-rep, as demonstrated by Scott et al., 2016a

$$\mathbf{R}Z = \{\mathbf{R}\mathbf{G}_z, \mathbf{R}\mathbf{c}_z, \mathbf{A}_z, \mathbf{b}_z\}, \tag{4.8}$$

$$Z \oplus W = \left\{[\mathbf{G}_z \;\; \mathbf{G}_w], \mathbf{c}_z + \mathbf{c}_w, \begin{bmatrix} \mathbf{A}_z & \mathbf{0} \\ \mathbf{0} & \mathbf{A}_w \end{bmatrix}, \begin{bmatrix} \mathbf{b}_z \\ \mathbf{b}_w \end{bmatrix}\right\}, \tag{4.9}$$

$$Z \cap_{\mathbf{R}} Y = \left\{[\mathbf{G}_z \;\; \mathbf{0}], \mathbf{c}_z, \begin{bmatrix} \mathbf{A}_z & \mathbf{0} \\ \mathbf{0} & \mathbf{A}_y \\ \mathbf{R}\mathbf{G}_z & -\mathbf{G}_y \end{bmatrix}, \begin{bmatrix} \mathbf{b}_z \\ \mathbf{b}_y \\ \mathbf{c}_y - \mathbf{R}\mathbf{c}_z \end{bmatrix}\right\}. \tag{4.10}$$

These operations can be executed efficiently, resulting in only a moderate increase in the complexity of the CG-representation. Much like zonotopes, there exist efficient techniques for simplifying constrained zonotopes. This involves enclosing a constrained zonotope with fewer generators and constraints, as explained in Section 4.3. This section also introduces other practical operations involving constrained zonotopes. Property 1 outlines simple methods for verifying whether a constrained zonotope is empty and determining if a given point belongs to it (as detailed in Scott et al., 2016a). Property 2 presents a method for calculating the corresponding CG-representation of a given convex polytope. Lastly, Property 3 provides a straightforward approach to compute the interval hull of a constrained zonotope through the solution of $2n$ linear programs (LPs).

Property 1 *(taken from Scott et al., 2016a) For any set* $Z = \{\mathbf{G}, \mathbf{c}, \mathbf{A}, \mathbf{b}\} \in \mathbb{R}^n$ *and* $\mathbf{z} \in \mathbb{R}^n$

$$Z \neq \emptyset \iff \min_{\boldsymbol{\xi}} \{||\boldsymbol{\xi}||_\infty : \mathbf{A}\boldsymbol{\xi} = \mathbf{b}\} \leq 1 \tag{4.11}$$

$$\mathbf{z} \in Z \iff \min_{\boldsymbol{\xi}} \left\{||\boldsymbol{\xi}||_\infty : \begin{bmatrix} \mathbf{G} \\ \mathbf{A} \end{bmatrix} \boldsymbol{\xi} = \begin{bmatrix} \mathbf{z} - \mathbf{c} \\ \mathbf{b} \end{bmatrix}\right\} \leq 1. \tag{4.12}$$

Property 2 *(taken from Scott et al., 2016a) Let* $P = \mathbf{z} : \mathbf{H}\mathbf{z} \leq \mathbf{k} \in \mathbb{R}^n$ *be a convex polytope in H-rep, and choose* $Z = \{\mathbf{G}, \mathbf{c}\} \in \mathbb{R}^n$ *and* $\sigma \in \mathbb{R}^n$ *such that* $P \subseteq Z$ *and* $\mathbf{H}\mathbf{z} \in [\sigma, \mathbf{k}]$, $\forall \mathbf{z} \in P$. *Then, the convex polytope* P *can be written in CG-rep as*

$$P = \left\{\left[\mathbf{G} \quad \mathbf{0}\right], \mathbf{c}, \left[\mathbf{H}\mathbf{G} \quad \mathrm{diag}(\tfrac{\boldsymbol{\sigma} - \mathbf{c}}{2})\right], \frac{\mathbf{k} + \boldsymbol{\sigma}}{2} - \mathbf{H}\mathbf{c}\right\}. \tag{4.13}$$

Property 3 *(taken from Rego, Raimondo, and Raffo, 2018) Let* $Z = \{\mathbf{G}, \mathbf{c}, \mathbf{A}, \mathbf{b}\} \subseteq \mathbb{R}^n$ *and let* $\mathbf{G}_j$ *denote the* j*-th row of* G. *The interval hull* $[L, U] \subseteq Z$ *is obtained by solving the following linear programs for each* $j = 1, 2, \ldots, n$:

$$\zeta_j^L = \min_{\boldsymbol{\xi}} \{c_j + \mathbf{G}_j \mid \|\boldsymbol{\xi}\|_\infty \leq 1, \mathbf{A}\boldsymbol{\xi} = \mathbf{b}\}, \tag{4.14}$$

$$\zeta_j^U = \max_{\boldsymbol{\xi}} \{c_j + \mathbf{G}_j \mid \|\boldsymbol{\xi}\|_\infty \leq 1, \mathbf{A}\boldsymbol{\xi} = \mathbf{b}\}. \tag{4.15}$$

It is possible to establish the equivalence between constrained zonotopes and polytopes. In the following we refer to (Scott et al., 2016a) as we define the advantages of CG-rep and explore the conversion between CG-rep and H-rep.

Theorem 1 *A set $Z \subset \mathbb{R}^n$ is a constrained zonotope if and only if it is a convex polytope.*

Proof. It is evident that every constrained zonotope is a convex polytope. To prove the reverse, let $P = \{\mathbf{z} : \mathbf{Hz} \leq k\}$ be a convex polytope. Due to compactness, we can select $Z_0 = \{\mathbf{G}, \mathbf{c}\} \subset \mathbb{R}^n$ and $\boldsymbol{\sigma} \in \mathbb{R}^n$ such that $P \subset Z_0$ and $\mathbf{Hz} \in [\boldsymbol{\sigma}, \mathbf{k}], \forall \mathbf{z} \in P$ (we consider the possibility of equality throughout). Hence, P can be expressed as $\{\mathbf{z} \in Z_0 : \mathbf{Hz} \in [\boldsymbol{\sigma}, \mathbf{k}]\}$. The interval $[\boldsymbol{\sigma}, \mathbf{k}]$ can be represented in G-rep. as

$$\text{diag}\left(\frac{\mathbf{k}-\boldsymbol{\sigma}}{2}, \frac{\mathbf{k}+\boldsymbol{\sigma}}{2}\right), \tag{4.16}$$

so Equation (4.10) yields:

$$P = \left\{[\mathbf{G}\ \mathbf{0}], \mathbf{c}, \left[\mathbf{HG}\ \text{diag}\left(\frac{\boldsymbol{\sigma}-\mathbf{k}}{2}\right)\right], \frac{\mathbf{k}+\boldsymbol{\sigma}}{2} - \mathbf{Hc}\right\}. \tag{4.17}$$

Thus, P satisfies Definition 2. ☐

With the introduction of slack variables, the construction (4.17) essentially reproduces the halfspaces defining P within the constraints of the CG-rep. However, some skepticism may arise about the advantages of the CG-rep. The crucial distinction lies in the fact that the constraints in (4.17) operate on the underlying variables $\boldsymbol{\xi}$ rather than $\mathbf{z}$ and are therefore unaffected by Minkowski sums and linear mappings. For instance, consider a singular linear mapping of P, $\mathbf{R}P$, which poses a worst-case exponential computation challenge in H-rep but is easily computed in CG-rep via (4.8). The enabling feature of CG-rep in this context is that the mapping R in (4.8) does not alter the underlying set $B_\infty(\mathbf{A}, \mathbf{b})$ but only modifies the mapping from this set into $\mathbb{R}^n$, $\boldsymbol{\xi} \mapsto \mathbf{G}\boldsymbol{\xi} + \mathbf{c}$.

The proof of Theorem (1) demonstrates that the conversion from H to CG requires only the computation of a bounding box for P, from which Z_0 and σ can be computed easily, and (4.17) can be applied. The conversion from CG to H relies on the following result.

Proposition 1 *(taken form (Scott et al., 2016a)). Consider $Z = \{\mathbf{G}, \mathbf{c}, \mathbf{A}, \mathbf{b}\}$ and any partition $[\mathbf{A}\ \mathbf{b}] = \begin{bmatrix} \mathbf{A}_1 & \mathbf{b}_1 \\ \mathbf{A}_2 & \mathbf{b}_2 \end{bmatrix}$. For every $\mathbf{z} \in \mathbb{R}^n$, $\mathbf{z} \in Z$ if and only if*

$$\mathbf{z}_0 \in Z^+ \equiv \left\{\begin{bmatrix} \mathbf{G} \\ \mathbf{A}_1 \end{bmatrix}, \begin{bmatrix} \mathbf{c} \\ -\mathbf{b}_1 \end{bmatrix}, \mathbf{A}_2, \mathbf{b}_2\right\}, \tag{4.18}$$

with the trivial partition $[\mathbf{A}\ \mathbf{b}] = [\mathbf{A}_1\ \mathbf{b}_1]$, Z^+ becomes a zonotope, which we refer to as the lifted zonotope for Z. This result allows for the application of certain algorithms developed for standard zonotopes to constrained zonotopes. Specifically, the H-rep of Z can be computed by first determining the H-rep of the lifted zonotope using a method such as the one described in Althoff et al. (Althoff and Krogh, 2011) and observing that $[\mathbf{H}_1\ \mathbf{H}_2]\begin{bmatrix} \mathbf{z} \\ \mathbf{0} \end{bmatrix} \leq \mathbf{k} \iff \mathbf{H}_1\mathbf{z} \leq k$. However, due to the complexity associated with the G to H conversion, CG to H scales as $n_g\,(n_g n + n_c - 1)$, which can become prohibitively large. Therefore, performing computations in CG-rep is most advantageous when a result in CG-rep suffices. This is often not problematic and can even be beneficial.

4.3 Complexity reduction

This section describes the methods used in this doctoral thesis to simplify the complexity of zonotopes and constrained zonotopes as proposed in (Scott et al., 2016a). In numerous operations involving constrained zonotopes, the outcome often results in an increase in the number of generators (n_g) and/or constraints (n_c) compared to the original arguments. Consequently, the complexity of the CG-representation increases with the application of these operations. For standard zonotopes, this issue is tackled by employing reduction techniques that approximate a given zonotope with one containing fewer generators. In this context, we describe reduction techniques tailored for constrained zonotopes. However reducing n_g becomes intricate due to the presence of constraints, making direct application of zonotopic methods impractical. Moreover a method is needed to reduce n_c as well.

For zonotopes, the order is defined as $o = n_g/n$, and reduction is typically performed when the result of an operation yields o greater than a prescribed value $\hat{o}$. The complexity of a constrained zonotope is described using n_c and the degrees-of-freedom order, $o_d = (n_g - n_c)/n$. It is important to note that $o_d = o$ when $n_c = 0$. Given a constrained zonotope Z and target values $\hat{n}_c$ and $\hat{o}_d$, reduction is carried out in three steps. Initially, the CG-representation of Z is rescaled as described in Section 4.3.2, which preserves the set Z but reduces the conservativeness of subsequent reductions. Subsequently, constraints are progressively eliminated until $n_c = \hat{n}_c$, as outlined in Section 4.3.2. The proposed method for this step eliminates one generator for each eliminated constraint, ensuring that o_d remains unchanged. Finally, o_d is reduced to $\hat{o}_d$ by eliminating generators, as detailed in Section 4.3.2. The end result is a reduced constrained zonotope $\tilde{Z}$ that satisfies $Z \subset \tilde{Z}$. Our goal is to minimize the gap in this inclusion as much as possible.

4.3.1 Zonotopes

Method proposed in Combastel, 2003 stands as the versatile technique for reducing the order of zonotopes. It enables the efficient computation of a zonotope containing a specified number of generators while over-approximating a more complex zonotope. However, it is essential to note that the resultant enclosure can exhibit a high level of conservatism.

Let $Z = \{\mathbf{G}, \mathbf{c}\} \in \mathbb{R}^n$ be a zonotope, with $\mathbf{G} \in \mathbb{R}^{n \times n_g}, \mathbf{c} \in \mathbb{R}^n$ and consider $\mathbf{s} \in \mathbb{N}$ such that $n \leq s < n_g$. Denote by $\hat{\mathbf{G}}$ the matrix resulting from reordering the columns of $\mathbf{G}$ in decreasing 2-norm. Then,

$$Z \subseteq \bar{Z} = \{[\mathbf{H}\ \mathbf{Q}], \mathbf{c}\}, \tag{4.19}$$

where $\bar{Z}$ has s generators, $\mathbf{H}$ is a matrix composed of the first $(s-n)$ columns of matrix $\hat{\mathbf{G}}$, and $\mathbf{Q}$ is a diagonal matrix given by

$$Q_{ii} = \sum_{j=s-n+1}^{ng} |\hat{G}_{ij}|, \quad \text{for } i = 1, 2, \ldots, n \tag{4.20}$$

In addiction another approach has been proposed by Scott et al., 2016a, which enhance efficiency and accuracy. Let consider $Z = \{\mathbf{G}, \mathbf{c}\} \subset \mathbb{R}^n$ be a zonotope, with $\mathbf{G} \in \mathbb{R}^{n \times n_g}, \mathbf{c} \in \mathbb{R}^n$. A new less conservative approach for generator reduction is given by:

- Rearrange the columns of $\mathbf{G}$ as $[\mathbf{T}\,\mathbf{V}]$, where $\mathbf{T} \in \mathbb{R}^{nn}$ is an invertible matrix.

- Select a column $\mathbf{v} \in \mathbb{R}^{n \times n_g - n - 1}$ and rewrite the zonotope as $Z = X \oplus Y \triangleq \{[\mathbf{T}\ \mathbf{v}], \mathbf{c}\} \oplus \{\mathbf{V}^*, \mathbf{0}\}$, where $\mathbf{V}^* \in \mathbb{R}^{n \times n_g - n - 1}$ is the matrix obtained by removing $\mathbf{v}$ from $\mathbf{V}$.
- Reduce X to a optimal parallelotope $\tilde{X}$ satisfying $X \subseteq \tilde{X}$.
- Define $\tilde{Z} = \tilde{X} + Y$, where $\tilde{Z}$ is a zonotope with $n_g - 1$ generators.

Note that, the first step is executed using Gauss-Jordan elimination, a process that employs a sequence of column pivots to achieve the desired ordering $[\mathbf{T}\ \mathbf{v}]$. Furthermore, the third step employs the optimal reduction method proposed in Chisci, Garulli, and Zappa, 1996. This method identifies the minimum volume parallelotope containing X as $\tilde{X} = \{\mathbf{T}(\mathbf{I} + \mathrm{diag}(|\mathbf{r}|)), \mathbf{c}\}$, where $\mathbf{r} = \mathbf{T}^{-1}\mathbf{v}$. It is essential to note that $||\mathbf{r}||_\infty \leq 1$. Finally, in the second step, the column $\mathbf{v}$ is selected by minimizing the volume error between $\tilde{X}$ and X. This error, denoted as $v(\tilde{X}) - v(X)$, is computed using the volume equation presented in Alamo, Bravo, and Camacho, 2005, resulting in

$$v(\tilde{X}) - v(X) = 2^n |\det(T)| \left(\prod_{i=1}^{n} (1 + |r_i|) - \left(1 + \sum_{i=1}^{n} |r_i| \right) \right). \tag{4.21}$$

4.3.2 Constrained zonotopes

When dealing with a constrained zonotope Z and having specific target values for both $\hat{n}_c$ and $\hat{o}_d$, the reduction process unfolds in three simple steps. Firstly, we rescale the CG-representation of Z, as explained in Section 4.3.2. This adjustment does not alter the set Z but reduces the degree of overestimation in subsequent reductions. Next, we gradually remove constraints until we achieve $n_c = \hat{n}_c$, as detailed in Section 4.3.2. The method we propose for this step removes one generator for each constraint eliminated, ensuring that o_d remains unchanged. Lastly, we further reduce o_d to match $\hat{o}_d$ by eliminating generators, as outlined in Section 4.3.2. The end result is a constrained zonotope $\tilde{Z}$, where $Z \subset \tilde{Z}$. Our objective is to make this containment as accurate and less over-approximated as possible.

Rescaling

The constraint reduction phase introduces some conservatism conservatism that can can be significantly reduced by initially transferring some information from the constraint data ($\mathbf{A}$, $\mathbf{b}$) to the generator data ($\mathbf{G}$, $\mathbf{c}$). To achieve this, the constraints are first utilized to tighten the bounds $\boldsymbol{\xi} \in [-1, 1]$. Subsequently, the CG-representation is rescaled to return to the standard form $\boldsymbol{\xi} \in [-1, 1]$.

Proposition 2 *Let* $Z = \{\mathbf{G}, \mathbf{c}, \mathbf{A}, \mathbf{b}\}$. *If* $\boldsymbol{\xi}_L$, $\boldsymbol{\xi}_U \in \mathbb{R}^n$ *satisfy* $B_\infty(\mathbf{A}, \mathbf{b}) \subset [\boldsymbol{\xi}_L, \boldsymbol{\xi}_U] \subset [-1, 1]$, *then an equivalent CG-representation is*

$$Z = \{\mathbf{G}\mathrm{diag}(\boldsymbol{\xi}_r), \mathbf{c} + \mathbf{G}\boldsymbol{\xi}_m, \mathbf{A}\mathrm{diag}(\boldsymbol{\xi}_r), \mathbf{b} - \mathbf{A}\boldsymbol{\xi}_m\}, \tag{4.22}$$

where $\boldsymbol{\xi}_m = \frac{1}{2}(\boldsymbol{\xi}_U + \boldsymbol{\xi}_L)$ *and* $\boldsymbol{\xi}_r = \frac{1}{2}(\boldsymbol{\xi}_U - \boldsymbol{\xi}_L)$.

Proof. Note that $\boldsymbol{\xi} \in [\boldsymbol{\xi}_L, \boldsymbol{\xi}_U]$ if and only if $\exists \delta \in B_\infty(\mathbf{A}, \mathbf{b})$ such that $\boldsymbol{\xi} = \boldsymbol{\xi}_m + \mathrm{diag}(\boldsymbol{\xi}_r)\delta$. Thus, the result follows from

$$\begin{aligned} z \in Z &\iff \exists \boldsymbol{\xi} \in B_\infty(\mathbf{A}, \mathbf{b}) : \mathbf{z} = \mathbf{G}\boldsymbol{\xi} + \mathbf{c}, \\ &\iff \exists \boldsymbol{\xi} \in [\boldsymbol{\xi}_L, \boldsymbol{\xi}_U] : \mathbf{z} = \mathbf{G}\boldsymbol{\xi} + \mathbf{c}, 0 = \mathbf{A}\boldsymbol{\xi} - \mathbf{b}, \\ &\iff \exists \boldsymbol{\delta} \in B_\infty : \mathbf{z} = \mathbf{G}(\boldsymbol{\xi}_m + \mathrm{diag}(\boldsymbol{\xi}_r)\boldsymbol{\delta}) + \mathbf{c}, 0 = \mathbf{A}(\boldsymbol{\xi}_m + \mathrm{diag}(\boldsymbol{\xi}_r)\boldsymbol{\delta}) - \mathbf{b}. \end{aligned}$$

The process of computing the interval $[\boldsymbol{\xi}_L, \boldsymbol{\xi}_U]$ and replacing $\{\mathbf{G}, \mathbf{c}, \mathbf{A}, \mathbf{b}\}$ by the expression (4.22) is referred to as rescaling. The optimal interval is obtained by solving the $2n_g$ linear programs

$$\xi_j^L \equiv \min\{\xi_j : \mathbf{A}\boldsymbol{\xi} = \mathbf{b},\ ||\boldsymbol{\xi}||_\infty \leq 1\}, \tag{4.23}$$

$$\xi_j^U \equiv \max\{\xi_j : \mathbf{A}\boldsymbol{\xi} = \mathbf{b},\ ||\boldsymbol{\xi}||_\infty \leq 1\}. \tag{4.24}$$

$\square$ However, this approach can be computationally expensive when rescaling is performed frequently. Instead, we refine the initial bounds $[-1, 1]$ using an iterative method based on interval arithmetic with a complexity of $O(n_c n_g^2)$.

We employ Algorithm 1 below to compute an interval $E \equiv [\xi_L, \xi_U]$ in a way that ensures $B_\infty(\mathbf{A}, \mathbf{b}) \subset E \subset [-1,\ 1]$. Additionally, Algorithm 1 yields $R \equiv [\rho_L, \rho_U] \subset \mathbb{R}^{n_g}$, which satisfies

$$R_j \supset \{\xi_j : \mathbf{A}\boldsymbol{\xi} = \mathbf{b}, |\boldsymbol{\xi}_i| \leq 1, \forall i \neq j\} \quad \forall j. \tag{4.25}$$

This R is subsequently utilized for constraint reduction, as elucidated in the following.

Let's consider the transformations of $\mathbf{A}\boldsymbol{\xi} = \mathbf{b}$:

$$\xi_j = (a_{ij})^{-1} b_i - \sum_{k \neq j} (a_{ij})^{-1} a_{ik} \xi_k, \quad \forall i, j : a_{ij} \neq 0. \tag{4.26}$$

Starting with $E = [-1,\ 1]$, each iteration of Algorithm 1 aims to refine each E_j by bounding the right-hand side of (4.26) using interval arithmetic, taking into account $\xi_k \in E_k$ for all $k \neq j$. By preconditioning the constraints (Neumaier, 1990), the bounds obtained from Algorithm 1 can be significantly enhanced. This preconditioning step does not impact Z because, for any invertible $\mathbf{P}$, $\{\mathbf{G}, \mathbf{c}, \mathbf{A}, \mathbf{b}\}$ is equivalent to $\{\mathbf{G}, \mathbf{c}, \mathbf{PA}, \mathbf{Pb}\}$. In our implementation, we first transform $[\mathbf{A}|\mathbf{b}]$ into its reduced row echelon form using Gauss-Jordan elimination with full pivoting before applying Algorithm 1. During elimination, we select the pivot element as the largest element (in terms of infinity norm) within the unreduced submatrix (excluding the final column $\mathbf{b}$). Since column pivoting alters the order of $\boldsymbol{\xi}$, it is necessary to perform column pivots on $\mathbf{G}$ as well. The overall complexity of preconditioning and Algorithm 1 is $O(n^2 c n_g + n_c n^2 g)$. Note that, to further refine E, the algorithm can be applied iteratively. If, at any point during these iterations, $E \cap R$ becomes empty, Z will also be empty. As a result, this approach has the potential to identify an empty constrained zonotope without the need to solve a linear program.

Algorithm 1 E_j refining

```
Assign $E := [-1, 1]$, $R := [-\infty, +\infty]$, $i = j = 1$.
while $i \leq n_c$ do
    while $j \leq n_g$ do
        if $a_{ij} \neq 0$ then
            $R_j := R_j \cap \left\{ a_{ij}^{-1} b_i - \sum_{k \neq j} a_{ij}^{-1} a_{ik} E_k \right\}$
            $E_j := E_j \cap R_j$
        end if
        $j := j + 1$
    end while
    $(i, j) := (i + 1, 1)$
end while
```

The CG-representation of Z is subject to rescaling as per Proposition 2. In order for (4.25) to remain valid, it is necessary to rescale R in the following manner:

$$R_j := \left[\frac{\rho_j^L - \xi_{m,j}}{\xi_{r,j}}, \frac{\rho_j^U - \xi_{m,j}}{\xi_{r,j}}\right], \forall j. \tag{4.27}$$

Constraints reduction

The proposed method for constraint reduction relies on the following proposition, which draws inspiration from similar results for approximating zonotope intersections found in (Alamo, Bravo, and Camacho, 2005), (Bravo, Alamo, and Camacho, 2006), and (Ocampo-Martinez et al., 2007).

Proposition 3 *Let* $Z = \{\mathbf{G}, \mathbf{c}, \mathbf{A}, \mathbf{b}\}$*. The set*

$$\tilde{Z} \equiv \{\mathbf{G} - \Lambda_G\mathbf{A}, \mathbf{c} + \Lambda_G\mathbf{b}, \mathbf{A} - \Lambda_A\mathbf{A}, \mathbf{b} - \Lambda_A\mathbf{b}\} \tag{4.28}$$

satisfies $Z \subset \tilde{Z}$ *for every* $\Lambda_G \in \mathbb{R}^{n\times n_c}$ *and* $\Lambda_A \in \mathbb{R}^{n_c\times n_c}$*.*

Proof. An element $\mathbf{z} \in Z \iff \exists \boldsymbol{\xi} \in B_\infty$ such that $\begin{bmatrix}\mathbf{z}\\ \mathbf{0}\end{bmatrix} = \begin{bmatrix}\mathbf{G}\\ \mathbf{A}\end{bmatrix}\boldsymbol{\xi} + \begin{bmatrix}\mathbf{c}\\ -\mathbf{b}\end{bmatrix}$. For any such $\boldsymbol{\xi}$, $\begin{bmatrix}\mathbf{z}\\ \mathbf{0}\end{bmatrix} = \begin{bmatrix}\mathbf{G}\\ \mathbf{A}\end{bmatrix}\boldsymbol{\xi} + \begin{bmatrix}\mathbf{c}\\ -\mathbf{b}\end{bmatrix} + \begin{bmatrix}\Lambda_G(\mathbf{b} - \mathbf{A}\boldsymbol{\xi})\\ \Lambda_A(\mathbf{b} - \mathbf{A}\boldsymbol{\xi})\end{bmatrix}$ which implies that $\mathbf{z} \in \tilde{Z}$. □

If Λ_A has the i-th unit vector as its i-th row, then $\tilde{Z}$ has the trivial i-th constraint $\mathbf{0}^T\boldsymbol{\xi} = 0$, which can be removed. This removal is referred to as dualization of the constraint. When $\Lambda_A = \mathbf{I}$, all constraints are dualized, and $\tilde{Z}$ becomes a zonotope. In any case, Λ_G and any unspecified rows of Λ_A can be used to modify $\tilde{Z}$ in order to compensate for the eliminated constraints. Here is a strategy for eliminating one constraint at a time. Keep in mind that eliminating a single constraint does not mean treating the others as if they do not exist because the remaining constraints are adjusted by Λ_A. After experimenting with various approaches, the most effective strategy we found is a heuristic called "partial solve dualization." The main concept is to solve one of the constraint equations, for a single $\boldsymbol{\xi}_j$

$$\xi_j = a_{1j}^{-1}b_j - a_{1j}^{-1}\sum_{k\neq j} a_{1k}\xi_k. \tag{4.29}$$

Next, we use equation (4.29) to eliminate ξ_j from the remaining constraints and the equations $\mathbf{z} = \mathbf{G}\boldsymbol{\xi} + \mathbf{c}$. Finally, we remove the first constraint. Straightforward algebra shows that we can achieve this by selecting

$$\Lambda_G \equiv \mathbf{G}\mathbf{E}_{j1}a_{1j}^{-1}, \quad \Lambda_A \equiv \mathbf{A}\mathbf{E}_{j1}a_{1j}^{-1}, \tag{4.30}$$

where $\mathbf{E}_{j1} \in \mathbb{R}^{n_g\times n_c}$ is a zero matrix except for a one in the $(j, 1)$ position, and then evaluating (4.28). This results in $\tilde{Z} = \{\tilde{\mathbf{G}}, \tilde{\mathbf{c}}, \tilde{\mathbf{A}}, \tilde{\mathbf{b}}\}$ such that both $\tilde{\mathbf{G}}$ and $\tilde{\mathbf{A}}$ have identically zero j-th columns due to the elimination of ξ_j. Additionally, the matrix $[\tilde{\mathbf{A}}|\tilde{\mathbf{b}}]$ has an identically zero first row, which arises from the substitution of (4.29) into the constraint $a_1^T\boldsymbol{\xi} = b_1$ to obtain the trivial constraint $\mathbf{0}^T\boldsymbol{\xi} = \mathbf{0}$. By removing these columns and rows, the dualization effectively eliminates one constraint and one generator.

The choice of which ξ_j to eliminate is crucial, but our decision to use the first constraint in (4.29) is arbitrary. In fact, using any constraint where $a_{ij} \neq 0$ yields the same result (as shown in (4.31)). To select j, we assess the Hausdorff error introduced by dualization, denoted as H_j, which is defined as $\max_{\tilde{\mathbf{z}}\in\tilde{Z}} \min_{\mathbf{z}\in Z} \|\tilde{\mathbf{z}}-\mathbf{z}\|_2$. Calculating this for every j would be impractical. Therefore, a significant contribution of our proposed strategy is an efficient method for approximating $H_1, \dots, H_{n_g}$ with a total complexity of only $O((n_g+n_c)^3)$.

Note that, the process of forming $\tilde{Z}$ by eliminating one constraint from the CG-representation of Z is detailed using the method outlined in Section 4.3.2. In particular, it remains to estimate the Hausdorff error $H_j \equiv \max_{\tilde{z}\in\tilde{Z}} \min_{\mathbf{z}\in Z}\|\tilde{\mathbf{z}}-\mathbf{z}\|_2$ for the purpose of selecting j. It is important to note that eliminating ξ_j effectively retains the constraint $\mathbf{a}_1^T\boldsymbol{\xi} = b_1$ implicitly, even though it is not explicitly present in the CG-representation of $\tilde{Z}$. However, it is essential to recognize that the capability to enforce the bound $|\xi_j| < 1$ has been forfeited since this variable is no longer a part of the CG-representation of $\tilde{Z}$. Based on this observation, it can be demonstrated that

$$\tilde{Z} = \{\mathbf{G}\boldsymbol{\xi} + \mathbf{c} : \mathbf{A}\boldsymbol{\xi} = \mathbf{b}, |\xi_i| \leq 1, \forall i \neq j\}. \tag{4.31}$$

Consequently, we have

$$H_j = \max_{\boldsymbol{\xi}} \min_{\delta\in B_\infty(\mathbf{A},\mathbf{b})} \|\mathbf{G}(\boldsymbol{\xi}-\delta)\|_2, \tag{4.32}$$
$$\text{subject to } \mathbf{A}\boldsymbol{\xi} = \mathbf{b}, |\xi_i| \leq 1, i \neq j.$$

In order to estimate H_j, consider $\mathbf{d}^* \equiv (\boldsymbol{\xi}^* - \delta^*)$, where $\boldsymbol{\xi}^*, \delta^*$ represents an optimal solution of (4.32). It should be noted that $\mathbf{A}\mathbf{d}^* = \mathbf{0}$ and $|d_i^*| \leq 2$ for all $i \neq j$. Additionally, keep in mind that we have the bounds $R = [\rho^L, \rho^U]$ satisfying (4.25). If $|\rho_j^U|, |\rho_j^U| < 1$, then (4.25) demonstrates that the bound $|\xi_j| \leq 1$ is redundant within the definition of $B_\infty(\mathbf{A},\mathbf{b})$. Conversely, if $|\rho_j^U|, |\rho_j^U| \geq 1$, then $\max(|\rho_j^L|, |\rho_j^U|) - 1$ provides an estimate of how far $B_\infty(\mathbf{A},\mathbf{b})$ would extend beyond $[1,1]$ in the δ_j-direction if the constraint $|\delta_j| \leq 1$ were omitted. Consequently, the action of the outer program in (4.32) can be approximated by the requirement that

$$d_j^* = r_j \equiv \max\left\{0, \max(|\rho_j^L|, |\rho_j^U|) - 1\right\} \tag{4.33}$$

To further simplify, the inequality constraints $|d_i^*| \leq 2$ are relaxed by introducing a penalty on the norm of $\mathbf{d}$ in the objective function. This yields the estimate $H_j \approx H_j^* \equiv \min\left(\|\mathbf{G}\mathbf{d}\|_2^2 + \|\mathbf{d}\|_2^2 : \mathbf{A}\mathbf{d} = \mathbf{0}, d_j = r_j\right)$. Since this problem is an equality-constrained quadratic program, its solution $\hat{d}$ and duality multipliers $\hat{\lambda}$ are explicitly determined as solutions of the linear system

$$\begin{bmatrix} \mathbf{G}^T\mathbf{G} + \mathbf{I}_{n_g\times n_g} & \mathbf{A}^T & \mathbf{e}_j \\ \mathbf{A} & \mathbf{0}_{n_c\times n_c} & \mathbf{0}_{n_c\times 1} \\ \mathbf{e}_j^T & \mathbf{0}_{1\times n_c} & \mathbf{0} \end{bmatrix} \begin{bmatrix} \hat{\mathbf{d}} \\ \hat{\boldsymbol{\lambda}} \end{bmatrix} = \begin{bmatrix} \mathbf{0}_{n_g\times 1} \\ \mathbf{0}_{n_c\times 1} \\ r_j \end{bmatrix}, \tag{4.34}$$

where $\mathbf{e}_j \in \mathbb{R}^{n_g}$ denotes the j-th standard unit vector. Solving (4.34) directly for each j comes with a computational complexity of $O(n_g(n_g+n_c+1)^3)$. However, in this implementation, we achieve this with a complexity of $O((n_g+n_c)^3)$ by performing factorization of the upper-left $(n_g+n_c)\times(n_g+n_c)$ submatrix in (4.34) only once. Denoting this submatrix as $\mathbf{Q}$, equation (4.34) can be reformulated as follows

$$\begin{bmatrix} \mathbf{I}_{(n_g+n_c)\times(n_g+n_c)} & \mathbf{Q}^{-1}\mathbf{e}_j \\ \mathbf{e}_j^T & \mathbf{0} \end{bmatrix} \begin{bmatrix} \hat{\mathbf{d}} \\ \hat{\boldsymbol{\lambda}} \end{bmatrix} = \begin{bmatrix} \mathbf{0}_{(n_g+n_c)\times 1} \\ r_j \end{bmatrix} \tag{4.35}$$

In this context, $\mathbf{e}_j \in \mathbb{R}^{n_g+n_c}$. Once $\mathbf{Q}^{-1}$ is computed, solving 4.35 for each j entails calculating $\mathbf{Q}^{-1}\mathbf{e}_j$, executing a single elementary row operation to eliminate the 1 in the bottom row, and solving the resulting upper triangular system. We implement this approach using the LU-factors of $\mathbf{Q}$, rather than explicitly computing $\mathbf{Q}^{-1}$. To select j, we initially check whether $r_j = 0$ for any j. If this condition holds, then (4.25) and (4.31) imply that $Z = \tilde{Z}$ when j is chosen. In cases where this condition is not met, we opt for the j that minimizes $\hat{H}_j$.

Generator reduction

For a standard zonotope, generator reduction can be done using the simple and inexpensive method in Combastel, 2005, or more accurately using the method proposed in (Althoff and Krogh, 2011). In brief, each method selects a subset of $k > n$ generators that are then replaced with n generators whose Minkowski sum overestimates that of the original k. In the first method, the new n generators form an interval. In the second, they describe a parallelotope.

For a constrained zonotope $Z = \{\mathbf{G}, \mathbf{c}, \mathbf{A}, \mathbf{b}\}$, the presence of the constraints prevents either of these zonotopic methods from being applied directly. Instead, it is here proposed a lift-then-reduce strategy, shown schematically as

$$\begin{aligned} Z \to Z^+ \equiv \left\{ \begin{bmatrix} \mathbf{G} \\ \mathbf{A} \end{bmatrix}, \begin{bmatrix} \mathbf{c} \\ -\mathbf{b} \end{bmatrix} \right\} \to \\ \to \tilde{Z}^+ \equiv \left\{ \begin{bmatrix} \tilde{\mathbf{G}} \\ \tilde{\mathbf{A}} \end{bmatrix}, \begin{bmatrix} \mathbf{c} \\ -\mathbf{b} \end{bmatrix} \right\} \to \tilde{Z} \end{aligned} \tag{4.36}$$

First, we form the lifted zonotope Z^+ corresponding to Z (see Proposition 1 in Scott et al., 2016a). Next, Z^+ is reduced using a zonotopic method to yield $\tilde{Z}^+$, where $\tilde{\mathbf{G}}$ and $\tilde{\mathbf{A}}$ have fewer columns than $\mathbf{G}$ and $\mathbf{A}$.

We define $\tilde{Z}$ as $\tilde{Z} = [\tilde{\mathbf{G}}, \mathbf{c}, \tilde{\mathbf{A}}, \mathbf{b}]$. Given that $\tilde{Z}^+ \supset Z^+$, applying Proposition (1) twice confirms that $\tilde{Z} \supset Z$ as intended.

Our numerical experiments demonstrated that the zonotopic method outlined in (Combastel, 2005) often resulted in significant overestimation of Z^+, which in turn led to substantial overestimation of Z. The approach presented in (Althoff and Krogh, 2011) exhibited better performance but had a scaling factor of $\binom{n+\kappa}{n}$, where $\kappa \leq n_g - n$ is a heuristic integer. With $\kappa = 8$, this became prohibitively costly for higher-dimensional experiments (e.g., $n = n_c = 10$). The complexity in this method is only $\mathcal{O}(n^2 n_g + knn_g)$.

Remark 1 *The proposed lift-then-reduce strategy has one significant limitation. Since $\tilde{Z}^+$ is a subset of $\mathbb{R}^{n+n_c}$, it is generally impossible to reduce $\tilde{Z}^+$ to fewer than $n + n_c$ generators, effectively resulting in a parallelotope in $\mathbb{R}^{n+n_c}$. Consequently, $\tilde{Z}$ must have at least $n + n_c$ generators, even though Z is confined to $\mathbb{R}^n$. This illustrates the additional complexity imposed by the constraints and underscores that further reductions can only be achieved by eliminating constraints.*

Now we provide a comprehensive account of the generator reduction method. Consider $Z = \{\mathbf{G}, \mathbf{c}\}$. The initial step in this process entails a reordering of the columns of $\mathbf{G}$ to $\mathbf{G} \to \begin{bmatrix} \mathbf{T} & \mathbf{V} \end{bmatrix}$, where $\mathbf{T} \in \mathbb{R}^{n \times n}$ is an invertible matrix. This reordering is carried out by transforming $\mathbf{G}$ into its reduced row echelon form $\begin{bmatrix} \mathbf{I}_n & \mathbf{R} \end{bmatrix}$ using Gauss-Jordan elimination with full pivoting. In instances where it is determined that $\mathbf{G}$ is rank-deficient, the reduction of Z is straightforwardly performed using the method outlined in (Combastel, 2005). However, if $\mathbf{G}$ is found to be non-rank-deficient, the sequence of column pivots conducted during the elimination process yields the desired reordering $\begin{bmatrix}\mathbf{T} & \mathbf{V}\end{bmatrix}$ accompanied by $\mathbf{R} = \mathbf{T}^{-1}\mathbf{V}$. During each iteration of elimination, the pivot element is carefully selected as the element within the unreduced submatrix that has the greatest magnitude with respect to the infinity norm of the row to which it belongs. Consequently, every element of $\mathbf{R}$ is either less than or equal to 1.

In the second step, a column $\mathbf{v}$ is selected from $\mathbf{V}$ according to the following procedure, and Z is expressed as follows, where $\mathbf{V}_-$ denotes the matrix formed by removing $\mathbf{v}$ from $\mathbf{V}$

$$Z = X + Y \equiv [\mathbf{T}\mathbf{v}], \mathbf{c} + [\mathbf{V}_-, \mathbf{0}]. \tag{4.37}$$

Subsequently, the $n+1$ to n order zonotope X is conservatively reduced to a parallelotope $\tilde{X}$ using the method described in (Chisci, Garulli, and Zappa, 1996). Finally, $\tilde{Z} = \tilde{X} + Y$ is defined, which possesses one fewer generator than Z. Let $\mathbf{r}$ be the column of $\mathbf{R}$ corresponding to $\mathbf{v}$, such that $\mathbf{r} = \mathbf{T}^{-1}\mathbf{v}$. Utilizing the fact that $\|\mathbf{r}\|_\infty \leq 1$, Theorem 3 in (Chisci, Garulli, and Zappa, 1996) derives that the minimum volume parallelotope containing X is $\tilde{X} = [\mathbf{T}(\mathbf{I} + \operatorname{diag}|\mathbf{r}|)], \mathbf{c}$. Consequently, $\tilde{Z} = [\mathbf{T}(\mathbf{I} + \operatorname{diag}|\mathbf{r}|)\mathbf{V}_-], \mathbf{c}$. The remaining task is to determine an effective heuristic for selecting the column $\mathbf{v}$. To achieve this, we explore the volumes of X and $\tilde{X}$. Utilizing the standard formula for the volume of a zonotope (Bravo, Alamo, and Camacho, 2006) and standard properties of the determinant, we have

$$\begin{aligned} v(\tilde{X}) &= 2^n |\det(\mathbf{T})\det(\mathbf{I} + \operatorname{diag}|\mathbf{r}|)|, \\ &= 2^n |\det(\mathbf{T})| \prod_{i=1}^{n} (1 + |r_i|), \end{aligned}$$

and, letting $\mathbf{t}_i$ denote the i-th column of $\mathbf{T}$,

$$\begin{aligned} v(X) =& 2^n \left(|\det[\mathbf{T}]| + \sum_{i=1}^{n} |\det[\mathbf{t}_1 \ldots \mathbf{t}_{i-1}\, \mathbf{v}\, \mathbf{t}_{i+1} \ldots \mathbf{t}_n]| \right) \\ =& 2^n \left(|\det[\mathbf{T}]| + \sum_{i=1}^{n} |\det[\mathbf{T}[\mathbf{e}_1 \ldots \mathbf{e}_{i-1}\, \mathbf{r}\, \mathbf{e}_{i+1} \ldots \mathbf{e}_n]]| \right) \\ =& 2^n |\det[\mathbf{T}]| \left(1 + \sum_{i=1}^{n} |r_i| \right). \end{aligned}$$

We select the column $\mathbf{v}$ in such a way that $\mathbf{r} = \mathbf{T}^{-1}\mathbf{v}$ minimizes the volume error $v(\tilde{X}) - v(X)$. It is important to note that this determination can be made without the need to compute $\det \mathbf{T}$.

When directly applying this method to eliminate k generators, the computational complexity is $O(kn^2 n_g)$, mainly due to the repeated factorization of $\mathbf{G}$. However, in our implementation, we perform this factorization only once, and we update both $\mathbf{T}$ and $\mathbf{R}$ directly as follows:

$$\mathbf{T} := \mathbf{T}(\mathbf{I} + \operatorname{diag}|\mathbf{r}|), \quad \mathbf{R} := (\mathbf{I} + \operatorname{diag}|\mathbf{r}|)^{-1}\mathbf{R}_-, \tag{4.38}$$

where $\mathbf{R}_-$ is formed by removing $\mathbf{r}$ from $\mathbf{R}$. After the update, $\tilde{Z}$ can be reconstructed as $\tilde{Z} = \{[\mathbf{T}\ \mathbf{TR}], \mathbf{c}\}$. Additionally, the updated $\mathbf{R}$ matrix maintains the property that every element is less than one, as the elements of $(\mathbf{I} + \operatorname{diag}|\mathbf{r}|)$ are greater than one. Therefore, all the necessary information for further reduction is readily available. The complexity for reducing k generators is $O(n^2 n_g + k n_g n)$, where $n^2 n_g$ results from the one-time factorization of $\mathbf{G}$, and $k n_g$ results from k computations of $v(\tilde{X}) - v(X)$ and k updates as per (4.38).

4.4 Interval analysis

The set-based estimation method proposed in this doctoral thesis relies on intervals. In the following, some basic operations and notations of interval analysis are introduced.

Let $\underline{x}$, $\overline{x} \in \mathbb{R}$, such that $\underline{x} \leq \overline{x}$. An interval $[x] \subset \mathbb{R}$ is a nonempty set of real numbers defined by $[x] \triangleq \{x \in \mathbb{R} : \underline{x} \leq x \leq \overline{x}\}$. Moreover, the midpoint and the radius of an interval $[x]$ are defined by $\text{mid}([x]) \triangleq (1/2)(\overline{x} + \underline{x})$ and $\text{rad}([x]) \triangleq (1/2)(\overline{x} - \underline{x})$ respectively. The set of all intervals over $\mathbb{R}$ is denoted by $\mathbb{IR}$. The set of all interval vectors in $\mathbb{R}^n$ is denoted by $\mathbb{IR}^n$. A box $[X] \in \mathbb{IR}^n$ is defined as $[X] = ([\underline{x}_1, \overline{x}_1], \ldots, [\underline{x}_n, \overline{x}_n])$. The midpoint and radius of $[X]$ are defined by $\text{mid}([X]) \triangleq (\text{mid}([\underline{x}_1, \overline{x}_1]), \ldots, \text{mid}([\underline{x}_n, \overline{x}_n])$ and $\text{rad}([X]) \triangleq (\text{rad}([\underline{x}_1, \overline{x}_1]), \ldots, \text{rad}([\underline{x}_n, \overline{x}_n])$, respectively. A real arithmetic operation $\odot$ is extended to intervals $[x_1], [x_2] \in \mathbb{IR}$ by $[x_1] \odot [x_2] \triangleq \{x_1 \odot x_2 : x_1 \in [x_1], x_2 \in [x_2]\}$. The intersection of two intervals is defined as $[x_1] \cap [x_2] \triangleq [\max\{\underline{x}_1, \underline{x}_2\}, \min\{\overline{x}_1, \overline{x}_2\}]$.

Inclusion functions play an important role within the domain of interval analysis. Let $\square(f(X))$ denote an interval enclosure of a real-valued function f over an interval $X \in \mathbb{R}^n$, where X represents an interval enclosure of the domain of interest. Note that, the notation $\square(f(X))$ is used even when X does not explicitly denote an interval; in such cases, it is assumed that an interval hull is applied to X. Consequently, we can assert that $f(X) \subseteq \square f(X)$. Inclusion functions for elementary operations, such as sin, cos, ln, exp, are defined by their respective mappings when applied to interval arguments. For instance, the natural inclusion function of a real function is constructed through the recursive computation of inclusion functions for all arithmetic and elementary operations that constitute it. Inclusion functions and basic operations are defined in detail in Moore, Kearfott, and Cloud, 2009.

4.5 Conclusions

This chapter has offered a comprehensive exploration of zonotopes and constrained zonotopes, diving into their mathematical foundations, practical applications, and strategies for complexity reduction. As we draw this journey to a close, let us reflect on the key takeaways and insights gained along the way.

Zonotopes, with their central symmetry and efficient computational properties, serve as valuable tools for modeling sets in a wide range of applications. Their ability to handle linear mapping and Minkowski sum operations with ease makes them a go-to choice for various mathematical tasks. However, their limitation in representing asymmetric regions has led us to seek more versatile alternatives.

Constrained zonotopes emerged as the solution, offering the flexibility to model asymmetric convex polytopes accurately. Their computational benefits, including efficient set operations, have made them indispensable in scenarios where symmetry cannot be assumed. We have witnessed how constrained zonotopes maintain the advantages of zonotopes while extending their capabilities to a broader spectrum of complex shapes and structures.

Yet, complexity reduction remains a crucial aspect of effectively utilizing constrained zonotopes. As we explored methods to reduce the number of generators and constraints, we learned that striking a balance between computational efficiency and conservatism is an art in itself. The ability to simplify representations while preserving accuracy is a valuable skill in the world of set-based estimation.

In conclusion, zonotopes and constrained zonotopes are not merely mathematical constructs but practical tools that empower us to model, analyze, and understand complex systems with precision. Their role in control theory, robotics, signal processing, and beyond continues to expand as researchers and practitioners uncover new ways to leverage their strengths.

Chapter 5

Set-based state estimation

In this chapter, we will look at the concept of set-based state estimation and its implications. State estimation refers to the process of inferring the current or future state of a system based on available measurements or observations. Traditional point-based state estimation approaches provide a single estimate of the system's state such as Luemberger filters or Kalman filters. However, set-based state estimation takes a more comprehensive approach by utilizing mathematical set theory to model and estimate the possible states of a system.

Set-based state estimation offers several advantages over point-based approaches. By considering a range of possible states rather than relying on a single point estimate, set-based techniques provide a more robust representation of the system's true state. This is particularly useful in situations where there is uncertainty or ambiguity in the measurements, or when the system exhibits non-linear or non-Gaussian behaviors. Set-based methods can capture the inherent uncertainty and provide a more accurate and reliable estimate of the system's state.

The application of set-based state estimation techniques has gained increasing attention in various domains, including robotics, autonomous systems, control theory, and fault detection. These techniques have shown promise in addressing complex state estimation problems and enhancing the performance and robustness of systems operating in uncertain environments.

In this chapter, we will begin by discussing the theoretical foundations of set-based state estimation. We will explore the mathematical concepts and techniques employed in this approach, such as set propagation, set intersection, convex hulls, and set-based filtering algorithms. Understanding these foundations is crucial for comprehending the subsequent discussions on set-based state estimation in the specific context of lithium battery applications.

Following the general overview of set-based state estimation, we will shift our focus to the state of the art in the application of these techniques to lithium battery systems. Lithium batteries have become the preferred energy storage solution in various industries due to their high energy density, long cycle life, and environmental sustainability. However, accurate estimation of the state of charge (SoC) and state of health (SoH) is crucial for maximizing battery performance, optimizing energy management, and ensuring safe and reliable operation.

We will explore the latest research and advancements in set-based state estimation tailored specifically to lithium battery systems. This will involve examining different modeling approaches, estimation algorithms, and validation techniques utilized in the context of lithium batteries. By understanding the current state of the art, we can identify the strengths, limitations, and potential applications of set-based state estimation in improving the performance, safety, and longevity of lithium battery systems.

5.1 Set-based state estimation problem formulation

Consider a category of nonlinear discrete-time systems governed by the following equations

$$\begin{aligned} \boldsymbol{x}_k &= \boldsymbol{f}(\boldsymbol{x}_{k-1}, \boldsymbol{u}_{k-1}, \boldsymbol{w}_{k-1}) && \text{for} \quad k \geq 1, \\ \boldsymbol{y}_k &= \boldsymbol{g}(\boldsymbol{x}_k, \boldsymbol{u}_k, \boldsymbol{v}_k) && \text{for} \quad k \geq 0, \end{aligned} \tag{5.1}$$

Here, $\boldsymbol{x}_k \in \mathbb{R}^{n_x}$ represents the system state vector, $\boldsymbol{u}_k \in \mathbb{R}^{n_u}$ denotes known inputs, $\boldsymbol{y}_k \in \mathbb{R}^{n_y}$ signifies measured outputs, while $\boldsymbol{w}_k \in \mathbb{R}^{n_w}$ and $\boldsymbol{v_k} \in \mathbb{R}^{n_v}$ stand for process and output uncertainties, respectively. We assume that the initial condition is $\boldsymbol{x}_0 \in X_0$, and the disturbances are bounded by $\boldsymbol{w}_k \in W$ and $\boldsymbol{v}_k \in V$, where X_0, W, and V are predefined compact sets.

The aim of set-based state estimation is to compute, for each $k \geq 0$, tight enclosures $\hat{X}_k$ that encompass the set of states consistent with the model dynamics, the bounded uncertainties X_0, W, V, and the gathered measurements $\boldsymbol{y}_k$. This is achieved through a prediction-update algorithm that calculates the compact sets $\bar{X}_k$ and $\hat{X}_k$ as follows:

$$\bar{X}_k \supseteq \{\mathbf{f}(\mathbf{x}, \mathbf{u}_{k-1}, \mathbf{w}_{k-1}) : \mathbf{x} \in \hat{X}_{k-1},\ \boldsymbol{w}_{k-1} \in W\}, \tag{5.2}$$

$$\hat{X}_k \supseteq \{\boldsymbol{x} \in \bar{X}_k : \mathbf{g}(\mathbf{x}, \mathbf{u}_k, \mathbf{v}_k) = \mathbf{y}_k,\ \mathbf{v}_k \in V\}, \tag{5.3}$$

In this context, (5.2) and (5.3) are known as the “prediction step" and the “update step", respectively. It is worth noting that, in general, exact evaluation of the set operations defined in (5.2)-(5.3) may not be feasible (Kieffer, Jaulin, and Walter, 1998). Therefore, we compute tight guaranteed enclosures, which, in this context, refer to tight outer approximations. Notably, Constrained Zonotopes (CZs) have demonstrated significant advantages over other set representations (Scott et al., 2016a).

5.2 State estimation framework

In this section, we introduce the well-known prediction-update algorithm for calculating enclosures at each step using constrained zonotopes. We also offer a complete presentation of the indispensable tools needed to execute the prediction-update algorithm (5.2)-(5.3) for nonlinear discrete-time systems employing Constrained Zonotopes (CZ). Primarily, Theorem 5.4 establishes a constrained zonotopic enclosure for the product of an interval matrix and a CZ.

Theorem 2 (Rego et al., 2020a) Let $X = \{\mathbf{G}, \mathbf{c}, \mathbf{A}, \mathbf{b}\} \subset \mathbb{R}^m$ be a constrained zonotope with n_g generators and n_c constraints, let $\mathbf{J} \in \mathbb{IR}^{n \times m}$ be an interval matrix, and consider the set $S = \mathbf{J}X \triangleq \{\hat{\mathbf{J}}\mathbf{x} : \hat{\mathbf{J}} \in \mathbf{J}, \mathbf{x} \in X\} \subset \mathbb{R}^n$. Let $\bar{\mathbf{G}} \in \mathbb{R}^{n \times \bar{n}_g}$ and $\bar{\mathbf{c}} \in \mathbb{R}^n$ satisfy $X \subseteq \{\bar{\mathbf{G}}, \bar{\mathbf{c}}\}$, and let $\mathbf{m}$ be an interval vector such that $\mathbf{m} \supseteq (\mathbf{J} - \text{mid}(\mathbf{J}))\bar{\mathbf{c}}$ and $\text{mid}(\mathbf{m}) = \mathbf{0}$. Finally, let $\mathbf{P} \in \mathbb{R}^{n \times n}$ be a diagonal matrix defined by $P_{ii} = \text{rad}(m_i) + \sum_{j=1}^{\bar{n}_g} \sum_{k=1}^{m} \text{rad}(J_{ik})|\bar{G}_{kj}|$ for all $i = 1, 2, \ldots, n$. Then, S is contained in the *CZ-inclusion*

$$S \subseteq \lhd(\mathbf{J}, X) \triangleq \mathbf{J}X \oplus \mathbf{P}B_\infty^n. \tag{5.4}$$

Proof. Take any $\mathbf{s} \in S$. We will demonstrate that $\mathbf{s} \in /(J, Z)$. According to the definition of S, there exists $z \in Z$ and $\hat{J} \in J$ such that $s = \hat{J}z$. By adding and subtracting $mid(J)z$, we can express s as $s = mid(J)z + (\hat{J} - mid(J))z$. As

$z \in Z \subset \overline{Z}$, there exists $\bar{\delta} \in \overline{B}_1^{n_g}$ such that $z = \bar{c} + \bar{G}\bar{\delta}$. Hence, we have $s = mid(J)z + (\hat{J} - mid(J))(\bar{c} + \bar{G}\bar{\delta})$. By the choice of m, there exists $\hat{m} \in m$ such that

$$\mathbf{s} = \mathrm{mid}(\mathbf{J})\mathbf{x} + \hat{m} + (\hat{J} - mid(J))\bar{G}\bar{\delta} \tag{5.5}$$

Let $\delta = \hat{m} + (\hat{J} - mid(J))\bar{G}\bar{\delta}$. Then, we can write δ_i as $\delta_i = \hat{m}_i + \sum_{j=1}^{n_g}\sum_{k=1}^{n_z}(\hat{J}_{ik} - mid(J)_{ik})\bar{G}_{kj}\delta_j$. By applying the triangle inequality and noting that $|\delta_j| \leq 1$, we get $|\delta_i| \leq |\hat{m}_i| + \sum_{j=1}^{n_g}\sum_{k=1}^{n_z}|\hat{J}_{ik} - mid(J)_{ik}| \cdot |\bar{M}_{kj}|$. Consequently, $|\delta_i| \leq \frac{1}{2}\mathrm{diam}(\hat{m}) + \frac{1}{2}\sum_{j=1}^{n_g}\sum_{k=1}^{n_z}\mathrm{diam}(J_{ik}) \cdot |\bar{M}_{kj}|$. Hence, $\delta \in PB_s^n(1)$. From (5.5), it follows that $s = mid(J)z + \delta \in mid(J)Z + PB_s^n(1) = /(J, Z)$.

Therefore, $S \subset /(J, Z)$. ☐

The proposed framework is summarized in Algorithm 2. Note that, within this algorithm, it is possible to apply complexity reduction techniques explained in Chapter 4 after each step to manage the increase in set complexity. We initiate with two essential lemmas that are prerequisites for all three steps. In particular Lemma 1 provides the mean value extension for propagating implicitly CZ through nonlinear mappings

Algorithm 2 State estimation framework

```
(Prediction Step) Given the constrained zonotopes $\tilde{X}_{k-1} \times W \subset \mathbb{R}^n \times \mathbb{R}^{n_w}$ and input $\mathbf{u}_{k-1} \in \mathbb{R}^{n_u}$, compute the predicted constrained zonotope $\overline{X}_k$ satisfying (5.2).
(Update Step) Given the constrained zonotopes $\overline{X}_k \times V \subset \mathbb{R}^n \times \mathbb{R}^{n_v}$, input $\mathbf{u}_k \in \mathbb{R}^{n_u}$, and measurement $\mathbf{y}_k \in \mathbb{R}^{n_y}$, compute a refined constrained zonotope $\hat{X}_k$ satisfying (5.3).
```

Lemma 1 *Let $\boldsymbol{\alpha} : \mathbb{R}^n \times \mathbb{R}^{n_w} \rightarrow \mathbb{R}^{n_\alpha}$ be of class $\mathcal{C}^1$ and let $\nabla_x\boldsymbol{\alpha}$ denote the gradient of $\boldsymbol{\alpha}$ with respect to its first argument. Let $X \subset \mathbb{R}^n$ and $W \subset \mathbb{R}^{n_w}$ be CZ, and let $\mathbf{J} \in \mathbb{IR}^{n \times n}$ be an interval matrix satisfying*

$$\nabla_x^T\boldsymbol{\alpha}(\square X, W) \triangleq \{\nabla_x^T\boldsymbol{\alpha}(\mathbf{x}, \mathbf{w}) : \mathbf{x} \in \square X,\ \mathbf{w} \in W\} \subseteq \mathbf{J}. \tag{5.6}$$

For every $\mathbf{x} \in X$, $\mathbf{w} \in W$, and $\boldsymbol{\gamma}_x \in \square X$, there exists $\hat{\mathbf{J}} \in \mathbf{J}$ such that $\boldsymbol{\alpha}(\mathbf{x}, \mathbf{w}) = \boldsymbol{\alpha}(\boldsymbol{\gamma}_x, \mathbf{w}) + \hat{\mathbf{J}}(\mathbf{x} - \boldsymbol{\gamma}_x)$.

Proof. Choose any $(\mathbf{x}, \mathbf{w}) \in X \times W$. Since $\mathbf{x} \in X \subseteq \square X$ and $\gamma_x \in \square X$, the Mean Value Theorem ensures that, for any $i = 1, 2, \ldots, n$, there exists $\boldsymbol{\delta}^{[i]} \in \square X$ such that $\alpha_i(\mathbf{x}, \mathbf{w}) = \alpha_i(\boldsymbol{\gamma}_x, \mathbf{w}) + \nabla_x^T\alpha_i(\boldsymbol{\delta}^{[i]}, \mathbf{w})(\mathbf{x} - \boldsymbol{\gamma}_x)$. However, reX such that $\alpha_i(\mathbf{x}, \mathbf{w}) = \alpha_i(\boldsymbol{\gamma}_x, \mathbf{w}) + \nabla_x^T\alpha_i(\boldsymbol{\delta}^{[i]}, \mathbf{w})$ is contained in the i-th row of $\mathbf{J}_x$ by hypothesis, and since this holds for all $i = 1, 2, \ldots, n$, there exists $\hat{\mathbf{J}}_x \in \mathbf{J}_x$ such that $\boldsymbol{\alpha}(\mathbf{x}, \mathbf{w}) = \boldsymbol{\alpha}(\boldsymbol{\gamma}_x, \mathbf{w}) + \hat{\mathbf{J}}_x(\mathbf{x} - \boldsymbol{\gamma}_x)$. ☐

Lemma 1 provides an exact linear representation of the nonlinear function $\boldsymbol{\alpha}$ between two points based on the Mean Value Theorem, which is useful for computations with constrained zonotopes.

The following lemma presents an alternative technique for achieving a precise linear representation of a nonlinear function between two points, utilizing Taylor's Theorem.

Lemma 2 *Let $\boldsymbol{\beta} : \mathbb{R}^m \rightarrow \mathbb{R}^n$ be of class $\mathcal{C}^2$, and let $\mathbf{z} \in \mathbb{R}^m$ represent its argument. Consider a constrained zonotope $Z = \{\mathbf{G}, \mathbf{c}, \mathbf{A}, \mathbf{b}\} \subset \mathbb{R}^m$ with m_g generators and*

m_c constraints. For each $q = 1, 2, \ldots, n$, let $\mathbf{Q}^{[q]} \in \mathbb{IR}^{m \times m}$ and $\tilde{\mathbf{Q}}^{[q]} \in \mathbb{IR}^{m_g \times m_g}$ be interval matrices such that $\mathbf{Q}^{[q]} \subseteq \mathbf{H}\boldsymbol{\beta}_q(\square Z)$ and $\tilde{\mathbf{Q}} \subseteq \mathbf{G}^T \mathbf{Q}^{[q]} \mathbf{G}$. Additionally, define

$$\begin{aligned}
\tilde{c}_q =& \frac{1}{2}\text{trace}\left\{\text{mid}(\tilde{\mathbf{Q}}^{[q]})\right\} \\
\tilde{\mathbf{G}}_{q,:} =& \left[\ldots \quad \overbrace{\text{mid}(\tilde{Q}_{ii}^{[q]}/2}^{\forall i} \quad \ldots \quad \overbrace{(\text{mid}(\tilde{Q}_{ij}^{[q]} + \text{mid}(\tilde{Q}_{ji}^{[q]}))}^{\forall i<j} \quad \ldots\right] \\
\tilde{\mathbf{G}}_d =& \text{diag}(d) \\
d_q =& \sum_{i,j} \left|\text{rad}(\tilde{Q}_{ij}^{[q]})\right| \\
\tilde{\mathbf{A}} =& \left[\tilde{\mathbf{A}}_{\boldsymbol{\zeta}} \quad \tilde{\mathbf{A}}_{\boldsymbol{\xi}} \quad \mathbf{0}_{\frac{m_c}{2}(1+m_c)\times n}\right] \\
\tilde{\mathbf{A}}_{\boldsymbol{\zeta}} =& \underbrace{\begin{bmatrix} & \vdots & \\ \ldots & \frac{1}{2}A_{ri}A_{si} & \ldots \\ & \vdots & \end{bmatrix}}_{\forall i} \forall r \leq s \\
\tilde{\mathbf{A}}_{\boldsymbol{\xi}} =& \underbrace{\begin{bmatrix} & \vdots & \\ \ldots & A_{ri}A_{sj} + A_{rj}A_{si} & \ldots \\ & \vdots & \end{bmatrix}}_{\forall i<j} \forall r \leq s \\
\tilde{\mathbf{b}} =& \begin{bmatrix} \vdots \\ b_r b_s - \frac{1}{2}\sum_i A_{ri}A_{si} \\ \vdots \end{bmatrix} \forall r \leq s
\end{aligned}$$

with indices $i, j = 1, 2, \ldots, m_g$ and $r, s = 1, 2, \ldots, m_c$. Finally, choose any $\boldsymbol{\gamma}_z \in \square Z$, and let $\mathbf{L} \in \mathbb{IR}^{n \times m}$ be an interval matrix such that $\mathbf{L}_q, :\subseteq (\mathbf{c} - \boldsymbol{\gamma}_z)^T \mathbf{Q}^{[q]}$ for all $q = 1, 2, \ldots, n$. For every $\mathbf{z} \in Z$, there exist $\boldsymbol{\xi} \in B_\infty(\mathbf{A}, \mathbf{b})$, $\tilde{\boldsymbol{\xi}} \in B_\infty(\tilde{\mathbf{A}}, \tilde{\mathbf{b}})$, and $\hat{\mathbf{L}} \in \mathbf{L}$ such that

$$\begin{aligned}
\boldsymbol{\beta}(\mathbf{z}) =& \boldsymbol{\beta}(\boldsymbol{\gamma}_z) + \nabla^T \boldsymbol{\beta}(\boldsymbol{\gamma}_z)(\mathbf{z} - \boldsymbol{\gamma}_z) + \tilde{\mathbf{c}} \\
&+ [\tilde{\mathbf{G}}\, \tilde{\mathbf{G}}_d]\tilde{\boldsymbol{\xi}} + \hat{\mathbf{L}}((\mathbf{c} - \boldsymbol{\gamma}_z) + 2\mathbf{G}\boldsymbol{\xi}).
\end{aligned}$$

Proof. Choose any $\mathbf{z} \in \square Z$ and $q \in \{1, \ldots, n\}$. Applying Taylor's theorem to β_q with the reference point $\boldsymbol{\gamma}_z$, there must exist $\mathbf{\Gamma}^{[q]} \in \mathbf{H}\beta_q(Z) \subseteq \mathbf{Q}^{[q]}$ such that

$$\beta_q(\mathbf{z}) = \beta_q(\boldsymbol{\gamma}_z) + \nabla^T \beta_q(\boldsymbol{\gamma}_z)(\mathbf{z} - \boldsymbol{\gamma}_z) + (\mathbf{z} - \boldsymbol{\gamma}_z)^T \mathbf{\Gamma}^{[q]} (\mathbf{z} - \boldsymbol{\gamma}_z).$$

Since $\mathbf{z} \in Z$, there exists $\boldsymbol{\xi} \in B_\infty(\mathbf{A}, \mathbf{b})$ such that $\mathbf{z} = \mathbf{c} + \mathbf{G}\boldsymbol{\xi}$. Therefore, by defining $\mathbf{p} = \mathbf{c} - \boldsymbol{\gamma}_z$ for brevity, we can rewrite the equation as

$$\beta_q(\mathbf{z}) = \beta_q(\boldsymbol{\gamma}_z) + \nabla^T \beta_q(\boldsymbol{\gamma}_z)(\mathbf{p} + \mathbf{G}\boldsymbol{\xi}) + (\mathbf{p} + \mathbf{G}\boldsymbol{\xi})^T \mathbf{\Gamma}^{[q]} (\mathbf{p} + \mathbf{G}\boldsymbol{\xi}).$$

Expanding the product $(\mathbf{p}+\mathbf{G}\boldsymbol{\xi})^T \mathbf{\Gamma}^{[q]} (\mathbf{p}+\mathbf{G}\boldsymbol{\xi})$ results in $\mathbf{p}^T \mathbf{\Gamma}^{[q]} (\mathbf{p}+2\mathbf{G}\boldsymbol{\xi}) + \boldsymbol{\xi}^T \tilde{\mathbf{\Gamma}}^{[q]} \boldsymbol{\xi}$, where $\tilde{\mathbf{\Gamma}}^{[q]} = \mathbf{G}^T \mathbf{\Gamma}^{[q]} \mathbf{G} \in \tilde{\mathbf{Q}}^{[q]}$. Since $\tilde{\mathbf{\Gamma}}^{[q]} \in \tilde{\mathbf{Q}}^{[q]}$, it follows that $\tilde{\Gamma}_{ij}^{[q]} = \text{mid}(\tilde{Q}_{ij}^{[q]}) + \text{rad}(\tilde{Q}_{ij}^{[q]})\Lambda_{ij}^{[q]}$ for some $\Lambda_{ij}^{[q]} \in B_\infty^1$. Additionally, $|\xi_i| \leq 1$ implies $\xi_i^2 \in [0\, 1]$, and hence

$\xi_i^2 = \frac{1}{2} + \frac{1}{2}\zeta_i$ for some $\zeta_i \in [-1,1]$. Considering these two facts, we have

$$\begin{aligned}\boldsymbol{\xi}^T\tilde{\Gamma}^{[q]}\boldsymbol{\xi} =& \frac{1}{2}\sum_i \mathrm{mid}(\tilde{Q}_{ii}^{[q]}) + \frac{1}{2}\sum_i \mathrm{mid}(\tilde{Q}_{ii}^{[q]})\xi_i + \sum_{i<j}(\mathrm{mid}(\tilde{Q}_{ij}^{[q]}) \\ &+\mathrm{mid}(\tilde{Q}_{ji}^{[q]}))\xi_i\xi_j + \sum_{i,j}\mathrm{rad}(\tilde{Q}_{ij}^{[q]})\xi_i\xi_j\epsilon_{ij}^{[q]},\end{aligned}$$

where the third summation results from the fact that $\xi_i\xi_j = \xi_j\xi_i$. Thus, by defining the new generator variables

$$\bar{\boldsymbol{\xi}} = \begin{bmatrix} \cdots & \underbrace{\zeta_i}_{\forall i} \cdots & \underbrace{\xi_i\xi_j}_{\forall i<j} & \cdots & \underbrace{\xi_i\xi_j\Lambda_{ij}^{[q]}}_{\forall i,j,q} & \cdots \end{bmatrix}^T,$$

with $i,j = 1,2,\ldots,mg$, $q = 1,2,\ldots,n$, we have $\boldsymbol{\xi}^T\tilde{\Gamma}^{[q]}\boldsymbol{\xi} = \tilde{c}_q + [\tilde{\mathbf{G}}\,\tilde{\mathbf{G}}_d]_{q,:}\bar{\boldsymbol{\xi}}$, where $\tilde{\mathbf{G}}_d = \mathrm{blkdiag}(\mathbf{N}^{[1]}, \mathbf{N}^{[2]}, \ldots, \mathbf{N}^{[n]})$, and

$$\mathbf{N}^{[q]} = \begin{bmatrix} \ldots & \mathrm{rad}(\tilde{Q}_{ij}^{[q]}) & \ldots \end{bmatrix} \in \mathbb{R}^{1\times m_g^2}$$

Therefore, we have established that $\beta_q(z) = \beta_q(\gamma_z) + \nabla^T\beta_q(\gamma_z)(z-\gamma_z) + \mathbf{p}^T\mathbf{\Gamma}^{[q]}(\mathbf{p} + 2\mathbf{G}\boldsymbol{\xi}) + \tilde{c}_q + [\tilde{\mathbf{G}}\,\tilde{\mathbf{G}}_d]_{q,:}\bar{\boldsymbol{\xi}}$. This holds for every $q = 1,2,\ldots,n$. Moreover, $\mathbf{L}$ satisfies $\mathbf{L}_{q,:} \subseteq \mathbf{p}^T\mathbf{Q}^{[q]}$ for all $q = 1,2,\ldots,n$ by definition, so there must exist $\hat{\mathbf{L}} \in \mathbf{L}$ such that $\hat{\mathbf{L}}_{q,:} = \mathbf{p}^T\mathbf{\Gamma}^{[q]}$ for all $q = 1,2,\ldots,n$. Therefore,

$$\beta(\mathbf{z}) = \beta(\boldsymbol{\gamma}_z) + \nabla^T\beta(\boldsymbol{\gamma}_z)(\mathbf{z} - \boldsymbol{\gamma}_z) + \hat{\mathbf{L}}(\mathbf{p} + 2\mathbf{G}\boldsymbol{\xi}) + \tilde{\mathbf{c}} + [\tilde{\mathbf{G}}\,\tilde{\mathbf{G}}_d]\bar{\boldsymbol{\xi}}.$$

Moreover, the equality constraints $\mathbf{A}\boldsymbol{\xi} = \mathbf{b}$ imply that $\mathbf{A}\boldsymbol{\xi}\boldsymbol{\xi}^T\mathbf{A}^T = \mathbf{b}\mathbf{b}^T$. In addition, let consider $\xi_i^2 = \frac{1}{2} + \frac{1}{2}\zeta_i$ with $\zeta_i \in [-1,1]$, the r-th row and s-th column of this matrix equality results in

$$\frac{1}{2}\sum_i A_{ri}A_{si}\zeta_i + \sum_{i<j}(A_{ri}A_{sj} + A_{rj}A_{si})\xi_i\xi_j = b_rb_s - \frac{1}{2}\sum_i A_{ri}A + si,$$

with $r,s = 1,2,\ldots,m_c$. The constraints are non-repeating for $r \le s$ and linear in $\bar{\xi}$, as a consequence $\bar{\mathbf{A}}\bar{\boldsymbol{\xi}} = \tilde{\mathbf{b}}$, with $\bar{\mathbf{A}} = \begin{bmatrix}\tilde{\mathbf{A}}_\zeta & \tilde{\mathbf{A}}_\xi & \mathbf{0}_{\bar{m}_c\times nm_g^2}\end{bmatrix}$, where $\bar{m}_c = \frac{m_c}{2}(1+m_c)$. For this reason, $\boldsymbol{\xi} \in\in B_\infty(\mathbf{A},\mathbf{b}) \Rightarrow \bar{\boldsymbol{\xi}} \in B_\infty(\tilde{\mathbf{A}},\tilde{\mathbf{b}})$. Combining this with the previous expression, it is possible to derive

$$\boldsymbol{\beta}(Z) \subseteq \boldsymbol{\beta}(\boldsymbol{\gamma}_z) \oplus \nabla^T\boldsymbol{\beta}(\boldsymbol{\gamma}_z)(Z - \boldsymbol{\gamma}_z) \oplus \mathbf{L}(\mathbf{p} + 2\mathbf{G}B_\infty(\mathbf{A},\mathbf{b}) \oplus \tilde{\mathbf{c}} \oplus [\tilde{\mathbf{G}}\,\tilde{\mathbf{G}}_d]B_\infty(\bar{\mathbf{A}},\tilde{\mathbf{b}}).$$

This latter enclosure can be simplified exploiting the fact that the columns of $(\tilde{\mathbf{A}}$ corresponding to the variables $[\ldots\ \xi_i\xi_j\Lambda_{ij}^{[q]}\ \ldots]$ are all zero, and therefore

$$[\tilde{\mathbf{G}}\,\tilde{\mathbf{G}}_d]B_\infty(\bar{\mathbf{A}},\tilde{\mathbf{b}}) = \tilde{\mathbf{G}}B_\infty([\tilde{\mathbf{A}}_\zeta\,\tilde{\mathbf{A}}_\xi],\tilde{\mathbf{b}}) \oplus \tilde{\mathbf{G}}B_\infty^{nm_g^2},$$

where $\tilde{\mathbf{G}}_d$ is defined as in the statement of the theorem. Hence,

$$\begin{aligned}[\tilde{\mathbf{G}}\,\tilde{\mathbf{G}}_d]B_\infty(\bar{\mathbf{A}},\tilde{\mathbf{b}}) =& \tilde{\mathbf{G}}B_\infty([\tilde{\mathbf{A}}_\zeta\,\tilde{\mathbf{A}}_\xi],\tilde{\mathbf{b}}) \oplus \tilde{\mathbf{G}}_dB_\infty^n, \\ =& [\tilde{\mathbf{G}}\,\tilde{\mathbf{G}}_d]B_\infty([\tilde{\mathbf{A}}_\zeta\,\tilde{\mathbf{A}}_\xi\,\mathbf{0}_{\bar{m}_c\times n}],\tilde{\mathbf{b}}) \\ =& [\tilde{\mathbf{G}}\,\tilde{\mathbf{G}}_d]B_\infty(\tilde{\mathbf{A}},\tilde{\mathbf{b}}).\end{aligned}$$

□

5.3 Prediction step

This section introduces different approaches for performing the prediction step (5.2) using constrained zonotopes. These methods extend the techniques proposed byScott et al., 2016b and have been proposed for the first time in Rego, Raimondo, and Raffo, 2018 and in Rego et al., 2020a to handle nonlinear discrete-time systems. These extensions provide a consistent framework for propagating zonotopes through nonlinear mappings.

The primary advantage of these new extensions is their ability to carry out the entire state estimation procedure using constrained zonotopes in CG-rep. With the methods developed in this section, such sets can be directly propagated to the next time step without requiring prior simplification into a symmetric set. This effectively addresses a major source of conservatism found in existing methods based on the aforementioned enclosures, all while maintaining the computational efficiency associated with zonotopes.

Proposition 4 Let $\mathbf{f} : \mathbb{R}^n \times \mathbb{R}^{n_u} \times \mathbb{R}^{n_w} \to \mathbb{R}^n$ be of class $\mathcal{C}^1$ and let $\nabla_x \mathbf{f}$ denote the gradient of $\mathbf{f}$ with respect to its first argument. Let $\mathbf{u} \in \mathbb{R}^{n_u}$, and let $X \subset \mathbb{R}^n$ and $W \subset \mathbb{R}^{n_w}$ be CZ. Choose any $\boldsymbol{\gamma}_x \in \square X$. If Z_w is a constrained zonotope such that $\mathbf{f}(\boldsymbol{\gamma}_x, \mathbf{u}, W) \subseteq Z_w$ and $\mathbf{J} \in \mathbb{IR}^{n \times n}$ is an interval matrix satisfying $\nabla_x^T \mathbf{f}(\square X, \mathbf{u}, W) \subseteq \mathbf{J}$, then $\mathbf{f}(X, \mathbf{u}, W) \subseteq Z_w \oplus \lhd(\mathbf{J}, X - \boldsymbol{\gamma}_x)$.

Proof. Consider any $(\mathbf{x}, \mathbf{w}) \in X \times W$. Lemma 1 ensures the existence of a real matrix $\hat{\mathbf{J}}_x \in \mathbf{J}_x$ such that $\mathbf{f}(\mathbf{x}, \mathbf{u}, \mathbf{w}) = \mathbf{f}(\boldsymbol{\gamma}_x, \mathbf{u}, \mathbf{w}) + \hat{\mathbf{J}}_x(\mathbf{x} - (\boldsymbol{\gamma}_x)$. By Theorem 2 and the choice of Z_w, we conclude that $\mathbf{f}(\mathbf{x}, \mathbf{u}, \mathbf{w}) \oplus Z_w \lhd (\mathbf{J}_x, X - \boldsymbol{\gamma}_x)$, as desired. □

Proposition 5 *Let $\mathbf{f} : \mathbb{R}^n \times \mathbb{R}^{n_u} \times \mathbb{R}^{n_w} \to \mathbb{R}^n$ be a function of class $\mathcal{C}^2$. Consider $\mathbf{u} \in \mathbb{R}^{n_u}$ and constrained zonotopes $X = \{\mathbf{G}_x, \mathbf{c}_x, \mathbf{A}_x, \mathbf{b}_x\}$ and $W = \{\mathbf{G}_w, \mathbf{c}_w, \mathbf{A}_w, \mathbf{b}_w\}$ with n_g generators and n_c constraints, and n_{gw} generators and n_{cw} constraints, respectively. Let $\mathbf{z} = (\mathbf{x}, \mathbf{w})$ and $Z = X \times W = \{\mathbf{G}, \mathbf{c}, \mathbf{A}, \mathbf{b}\} \subseteq \mathbb{R}^{n+n_w}$. Consider interval matrices $\mathbf{Q}^{[q]} \in \mathbb{R}^{(n+n_w)\times(n+n_w)}$ and $\tilde{\mathbf{Q}}^{[q]} \in \mathbb{R}^{(n_g+n_{gw})\times(n_g+n_{gw})}$ satisfying $\mathbf{Q}^{[q]} \subseteq \mathbf{H}_z \mathbf{f}_q(\square X, \mathbf{u}, \square W)$ and $\tilde{\mathbf{Q}}^{[q]} \subseteq \mathbf{G}^T \mathbf{Q}^{[q]} \mathbf{G}$. Define $\tilde{\mathbf{c}}$, $\tilde{\mathbf{G}}$, $\tilde{\mathbf{G}}_d$, $\tilde{\mathbf{A}}$, and $\tilde{\mathbf{b}}$ as specified in Lemma 2. Finally, choose any $\boldsymbol{\gamma}_z = (\boldsymbol{\gamma}_x, \boldsymbol{\gamma}_w) \in \square Z$, and let $\mathbf{L} \in \mathbb{IR}^{n \times m}$ be an interval matrix satisfying $\mathbf{L}_{q,:} \subseteq (\mathbf{c} - \boldsymbol{\gamma}_z)^T \mathbf{Q}^{[q]}$ for all $q = 1, \ldots, n$. Then, we can conclude that*

$$\mathbf{f}(\square X, \mathbf{u}, \square W) \subseteq \mathbf{f}(\mathbf{x}, \mathbf{u}, \mathbf{w}) \oplus \nabla_z^T \mathbf{f}(\mathbf{x}, \mathbf{u}, \mathbf{w})(Z - \boldsymbol{\gamma}_z) \oplus R, \tag{5.7}$$

where $R = \tilde{\mathbf{c}} \oplus [\tilde{\mathbf{G}}\ \tilde{\mathbf{G}}_d] B_\infty(\tilde{\mathbf{A}}, \tilde{\mathbf{b}}) \oplus \lhd(\mathbf{L}, (\mathbf{c} - \boldsymbol{\gamma}_z) \oplus 2\mathbf{G} B_\infty(\mathbf{A}, \mathbf{b}))$.

Proof. Consider any $\mathbf{z} = (\mathbf{x}, \mathbf{w}) \in Z$. Lemma 2 ensures the existence of $\boldsymbol{\xi} \in B_\infty(\mathbf{A}, \mathbf{b})$, $\tilde{\boldsymbol{\xi}} \in B_\infty(\tilde{\mathbf{A}}, \tilde{\mathbf{b}})$, and $\hat{\mathbf{L}} \in \mathbf{L}$ such that:

$$\begin{aligned} \mathbf{f}(\mathbf{x}, \mathbf{u}, \mathbf{w}) =& \mathbf{f}(\boldsymbol{\gamma}_x, \mathbf{u}, \boldsymbol{\gamma}_w) + \nabla_z^T \mathbf{f}(\boldsymbol{\gamma}_x, \mathbf{u}, \boldsymbol{\gamma}_w)(z - \boldsymbol{\gamma}_z) \\ & + \tilde{\mathbf{c}} + [\tilde{\mathbf{G}}\, \tilde{\mathbf{G}}_d]\tilde{\boldsymbol{\xi}} + \hat{\mathbf{L}}((\mathbf{c} - \boldsymbol{\gamma}_z) + 2\mathbf{G}\boldsymbol{\xi}). \end{aligned}$$

Hence, we can conclude that $\mathbf{f}(\mathbf{x}, \mathbf{u}, \mathbf{w}) \subseteq \mathbf{f}(\boldsymbol{\gamma}_x, \mathbf{u}, \boldsymbol{\gamma}_w) \oplus \nabla_z^T \mathbf{f}(\boldsymbol{\gamma}_x, \mathbf{u}, \boldsymbol{\gamma}_w)(Z - \boldsymbol{\gamma}_z) \oplus \lhd(\mathbf{L}, (\mathbf{c} - \boldsymbol{\gamma}_z) \oplus 2\mathbf{G} B_\infty(\mathbf{A}, \mathbf{b})) \oplus \tilde{\mathbf{c}} \oplus [\tilde{\mathbf{G}}\, \tilde{\mathbf{G}}_d] B_\infty(\tilde{\mathbf{A}}, \tilde{\mathbf{b}})$. Therefore the (5.7) follows directly from the definition of R.

□

Note that specifically, if X and W have n_g and n_{g_w} generators, and n_c and n_{c_w} constraints, respectively, then Proposition 4 yields $n_g + n_{g_w} + 2n$ generators and $n_c + n_{cw}$ constraints. Proposition 5, on the other hand, provides $0.5(n_g + n_{g_w})^2 + 2.5(n_g + n_{g_w}) + 2n$ generators and $0.5(n_c + n_{c_w})^2 + 2.5(n_c + n_{c_w})$ constraints.

5.4 Update step

In this section, similarly to what has been done in Section 5.3 for the prediction step, two methods relying on the mean value theorem and the first order Taylor's expansion respectively, are presented.

Lemmas 1 and 2 are utilized, respectively, to formulate the necessary enclosure in (5.3) as the extended intersection of two constrained zonotopes.

Proposition 6 Let $\mathbf{g} : \mathbb{R}^n \times \mathbb{R}^{n_u} \times \mathbb{R}^{n_v} \to \mathbb{R}^{n_y}$ be of class $\mathcal{C}^1$, let $\mathbf{u} \in \mathbb{R}^{n_u}$, let $X \subset \mathbb{R}^n$ and $V \subset \mathbb{R}^{n_v}$ be CZ, and choose any $\mathbf{y} \in \mathbb{R}^{n_y}$ such that $\mathbf{y} = \mathbf{g}(\mathbf{x}, \mathbf{u}, \mathbf{v})$ for some $(\mathbf{x}, \mathbf{v}) \in X \times V$. Choose any $\boldsymbol{\gamma}_x \in \square X$ and any $\tilde{\mathbf{J}} \in \mathbb{R}^{n_y \times n}$. If Z_v is a constrained zonotope such that $-\mathbf{g}(\boldsymbol{\gamma}_x, \mathbf{u}, V) \subseteq Z_v$, and $\mathbf{J} \in \mathbb{IR}^{n_y \times n}$ is an interval matrix satisfying $\nabla_x^T \mathbf{g}(\square X, \mathbf{u}, V) \subseteq \mathbf{J}$, then

$$\{\mathbf{x} \in X : \mathbf{g}(\mathbf{x}, \mathbf{u}, \mathbf{v}) = \mathbf{y},\ \mathbf{v} \in V\} \subseteq X \cap_{\mathbf{C}} Y,$$

where $\mathbf{C} = \tilde{\mathbf{J}}$, and $Y = (\mathbf{y} + \tilde{\mathbf{J}}\boldsymbol{\gamma}_x) \oplus Z_v \oplus \triangleleft(\tilde{\mathbf{J}} - \mathbf{J}, X - \boldsymbol{\gamma}_x)$.

Proof. Take any $(\mathbf{x}, \mathbf{v}) \in X \times V$ such that $\mathbf{g}(\mathbf{x}, \mathbf{u}, \mathbf{v}) = \mathbf{y}$. According to Lemma 1, there exists a real matrix $\hat{\mathbf{J}}_x \in \mathbf{J}_x$ ensuring that $\mathbf{g}(\mathbf{x}, \mathbf{u}, \mathbf{v}) = \mathbf{g}(\boldsymbol{\gamma}_x, \mathbf{u}, \boldsymbol{\gamma}_v) + \hat{\mathbf{J}}_x(x - \boldsymbol{\gamma}_x)$. Since $\hat{\mathbf{J}}_x = \tilde{\mathbf{J}}_x + (\hat{\mathbf{J}}_x - \tilde{\mathbf{J}}_x)$ holds, we can express $\mathbf{g}(\mathbf{x}, \mathbf{u}, \mathbf{v})$ as follows:

$$\mathbf{g}(\mathbf{x}, \mathbf{u}, \mathbf{v}) = \mathbf{g}(\boldsymbol{\gamma}_x, \mathbf{u}, \mathbf{v}) + \tilde{\mathbf{J}}_x(x - \boldsymbol{\gamma}_x) + (\hat{\mathbf{J}}_x - \tilde{\mathbf{J}}_x)(x - \boldsymbol{\gamma}_x).$$

Consequently, we get

$$\begin{aligned}\tilde{\mathbf{J}}_x\hat{x} =& \mathbf{g}(\mathbf{x}, \mathbf{u}, \mathbf{v}) + \tilde{\mathbf{J}}_x\boldsymbol{\gamma}_x - \mathbf{g}(\boldsymbol{\gamma}_x, \mathbf{u}, \mathbf{v}) + (\tilde{\mathbf{J}}_x - \hat{\mathbf{J}}_x)(\mathbf{x} - \boldsymbol{\gamma}_x)\\ =& \mathbf{y} + \tilde{\mathbf{J}}_x\boldsymbol{\gamma}_x - \mathbf{g}(\boldsymbol{\gamma}_x, \mathbf{u}, \mathbf{v}) + (\tilde{\mathbf{J}}_x - \hat{\mathbf{J}}_x)(\mathbf{x} - \boldsymbol{\gamma}_x)\\ \in& (\mathbf{y} + \tilde{\mathbf{J}}_x\boldsymbol{\gamma}_x)Z_v \oplus \triangleleft(\tilde{\mathbf{J}}_x - \mathbf{J}_x, X - \boldsymbol{\gamma}_x) = Y\end{aligned}$$

Hence, we conclude that $\{\mathbf{x} \in X : \mathbf{g}(\mathbf{x}, \mathbf{u}, \mathbf{v}) = \mathbf{y}, \mathbf{v} \in V\} \subseteq \{\mathbf{x} \in X : \tilde{\mathbf{J}}_x\mathbf{x} \in Y\} = X \cap_C Y$. □

Note that the constrained zonotope Z_v in Proposition 6 can be expressed as $Z_v = -\mathbf{g}(\boldsymbol{\gamma}_x, \mathbf{u}, \boldsymbol{\gamma}_v) \oplus \triangleleft(-\mathbf{J}_v, V - \boldsymbol{\gamma}_v) \subseteq -\mathbf{g}(\boldsymbol{\gamma}_x, \mathbf{u}, V)$ for some $\mathbf{v} \in \square V$ and interval matrix $\mathbf{J}_v$ that includes $\nabla_v^T - \mathbf{g}(\boldsymbol{\gamma}_x, \mathbf{u}, \square V)$. The matrix $\tilde{J}_x$ is a free parameter in Proposition 6. Opting for $\tilde{\mathbf{J}}_x = \text{mid}(\mathbf{J}_x)$ results in $\text{mid}(\tilde{\mathbf{J}}_x - \mathbf{J}_x) = \mathbf{0}$, and consequently, $\triangleleft(\tilde{\mathbf{J}}_x - \mathbf{J}_x, X - \boldsymbol{\gamma}_x) = \text{mid}(\tilde{\mathbf{J}}_x - \mathbf{J}_x)(X - \boldsymbol{\gamma}_x) \oplus \mathbf{P}B_\infty^{n_y} = \mathbf{P}B_\infty^{n_y}$, where $\mathbf{P}$ is defined as in Theorem 2. Remaind that this choice is maintained throughout this Thesis.

Proposition 7 *Let* $\mathbf{g} : \mathbb{R}^n \times \mathbb{R}^{n_u} \times \mathbb{R}^{n_v} \to \mathbb{R}^{n_y}$ *be of class* $\mathcal{C}^2$*. Take* $\mathbf{u} \in \mathbb{R}^{n_u}$*, and let* $X = \{\mathbf{G}_x, \mathbf{c}_x, \mathbf{A}_x, \mathbf{b}_x\}$ *and* $V = \{\mathbf{G}_v, \mathbf{c}_v, \mathbf{A}_v, \mathbf{b}_v\}$ *be constrained zonotopes with* n_g *generators and nc constraints, and* n_{g_v} *generators and* n_{g_c} *constraints, respectively. Select any* $\mathbf{y} \in \mathbb{R}^{ny}$ *such that* $\mathbf{y} = \mathbf{g}(\mathbf{x}, \mathbf{u}, \mathbf{v})$ *for some* $(\mathbf{x}, \mathbf{v}) \in X \times V$*. Denote* $\mathbf{z} = (\mathbf{x}, \mathbf{v})$ *and* $Z = X \times V = \{\mathbf{G}, \mathbf{c}, \mathbf{A}, \mathbf{b}\} \subseteq \mathbb{R}^{n+n_v}$*. For each* $q = 1, 2, \ldots, n_y$*, let* $\mathbf{Q}^{[q]} \in \mathbb{IR}^{\times(n+n_v)}(n + n_v)$ *and* $\tilde{\mathbf{Q}}^{[q]} \in \mathbb{IR}^{(n_g+n_{gv})\times(n_g+n_{gv})}$ *be interval matrices such that* $\mathbf{Q}^{[q]} \subseteq \mathbf{H}_z g_q(\square X, \mathbf{u}, \square V)$ *and* $\tilde{\mathbf{Q}}^{[q]} \subseteq \mathbf{G}^T\mathbf{Q}^{[q]}\mathbf{G}$*. Moreover, define* $\tilde{\mathbf{c}}, \tilde{\mathbf{G}}, \tilde{\mathbf{G}}_d, \tilde{\mathbf{A}}$, *and* $\tilde{\mathbf{b}}$ *as in Lemma 2. Finally, choose any* $\mathbf{z} = (\gamma_x, \gamma_v) \in Z$ *and let* $\mathbf{L} \in \mathbb{IR}^{ny \times (n+n_v)}$ *be an interval matrix such that* $\mathbf{L}_{q,:} \subseteq (\mathbf{c} - \gamma_z)^T \mathbf{Q}^{[q]}$ *for all* $q = 1, \ldots, n_y$. *Then,*

$$\{\mathbf{x} \in X : \mathbf{g}(\mathbf{x}, \mathbf{u}, \mathbf{v}) = \mathbf{y}, \mathbf{v} \in V\} \subseteq X \cap_C Y,$$

where $\mathbf{C} = \nabla_x^T \mathbf{g}(\gamma_x, \mathbf{u}, \gamma_v)$, $Y = (\mathbf{y} - \mathbf{g}(\gamma_x, \mathbf{u}, \gamma_v) + \nabla_z^T \mathbf{g}(\mathbf{x}, \mathbf{u}, \mathbf{v})\mathbf{z}) \oplus (-\nabla_v^T \mathbf{g}(\gamma_x, \mathbf{u}, \gamma_v)V) \oplus (-R)$, *and* $R = \tilde{\mathbf{c}} \oplus [\tilde{\mathbf{G}}\, \tilde{\mathbf{G}}_v] B_\infty(\tilde{\mathbf{A}}, \tilde{\mathbf{b}}) \oplus \triangleleft(\mathbf{L}, (\mathbf{c} - \gamma_z) \oplus 2\mathbf{G} B_\infty(\mathbf{A}, \mathbf{b}))$.

Proof. Consider $(\mathbf{x}, \mathbf{v}) = \mathbf{z} \in Z$ such that $\mathbf{g}(\mathbf{x}, \mathbf{u}, \mathbf{v}) = \mathbf{y}$. Lemma 2 guarantees the existence of $\boldsymbol{\xi} \in B_\infty(\mathbf{A}, \mathbf{b})$, $\tilde{\boldsymbol{\xi}} \in B_\infty(\tilde{\mathbf{A}}, \tilde{\mathbf{b}})$, and $\hat{\mathbf{L}} \in \mathbf{L}$ such that

$$\begin{aligned} \mathbf{g}(\mathbf{x}, \mathbf{u}, \mathbf{v}) =& \mathbf{g}(\gamma_x, \mathbf{u}, \gamma_v) + \nabla_x^T \mathbf{g}(\gamma_x, \mathbf{u}, \gamma_v)(\mathbf{x} - \gamma_x) + \nabla_v^T \mathbf{g}(\gamma_x, \mathbf{u}, \gamma_v)(\mathbf{v} - \gamma_v) \\ &+ \hat{\mathbf{L}}(\mathbf{p} + 2\mathbf{G}\boldsymbol{\xi}) + \tilde{\mathbf{c}} + [\tilde{\mathbf{G}}\, \hat{\mathbf{G}}_v] \hat{\boldsymbol{\xi}}. \end{aligned}$$

Here, $\mathbf{p} = \mathbf{c} - \gamma_z$. As $\mathbf{g}(\mathbf{x}, \mathbf{u}, \mathbf{v}) = \mathbf{y}$,

$$\begin{aligned} \nabla_x^T \mathbf{g}(\gamma_x, \mathbf{u}, \gamma_v)\mathbf{x} =& \mathbf{y} - \mathbf{g}(\gamma_x, \mathbf{u}, \gamma_v) + \nabla_z^T \mathbf{g}(\gamma_x, \mathbf{u}, \gamma_v)\gamma_z \\ & - \nabla_v^T \mathbf{g}(\gamma_x, \mathbf{u}, \gamma_v)\mathbf{v} - \hat{\mathbf{L}}(\mathbf{p} + 2\mathbf{G}\boldsymbol{\xi}) - \tilde{\mathbf{c}} - [\tilde{\mathbf{G}}\, \tilde{\mathbf{G}}_v]\tilde{\boldsymbol{\xi}} \\ & \in (\mathbf{y} - \mathbf{g}(\gamma_x, \mathbf{u}, \gamma_v) + \nabla_z^T g(\gamma_x, \mathbf{u}, \gamma_v)\gamma_z) \\ & \oplus (-\nabla_v^T \mathbf{g}(\gamma_x, \mathbf{u}, \gamma_v)V) \oplus (-R) = Y \end{aligned}$$

Hence, we conclude that $\{\mathbf{x} \in X : \mathbf{g}(\gamma_x, \mathbf{u}, \gamma_v) = \mathbf{y}, \mathbf{v} \in V\} \subseteq \{\mathbf{x} \in X : \nabla_x^T \mathbf{g}(\mathbf{x}, \mathbf{u}, \mathbf{v})\mathbf{x} \in Y\} = X \cap_C Y$. ☐

Note that if X and V have n_g and n_{g_v} generators, and n_c and n_{c_v} constraints, respectively, then the enclosure derived by Proposition 6 has $2n_g + n_{g_v} + 2n_y$ generators and $2n_c + n_{c_v} + n_y$ constraints, and the enclosure acquired through Proposition 7 entails $0.5(n_g + n_{g_v})^2 + 2.5(n_g + n_{g_v}) + 2n_y$ generators and $0.5(n_c + n_{c_v})^2 + 2.5(n_c + n_{c_v}) + n_y$ constraints.

5.5 Conclusions

In this chapter, we have explored the use of constrained zonotopes as a powerful tool for addressing the challenges posed by nonlinear systems state estimation. The investigation has described in detail two distinct methods, for both prediction and update steps, relying on the mean value theorem and the first order Taylor's expansion respectively.

The impact of these methods extends across various domains, including robotics, control systems, and autonomous vehicles. The ability to propagate sets accurately through nonlinear transformations opens up new avenues for robust and safe control in uncertain environments. Moreover, the reduction in conservatism achieved through these methods can lead to improved system performance and more efficient resource allocation.

In conclusion, the use of constrained zonotopes represents a significant advancement in the field of nonlinear system estimation. The methods presented in this chapter provide practical solutions to the challenges posed by complex, nonlinear dynamics.

Chapter 6

Set-based state estimation on batteries

Battery Management Systems (BMSs) play a crucial role in ensuring the safety, reliability, and efficiency of batteries. It is essential to protect batteries from hazardous operating conditions, as violating temperature, current, and voltage restrictions can lead to compromised performance and safety issues, as highlighted in the study by Lu et al., 2013. Advanced BMSs leverage mathematical models to enhance efficiency and monitor battery cells by estimating key parameters such as the State of Charge (SOC). In this chapter firstly, we present the identification of parameter bounds for the ECM described in Chapter 3.2 based on the Fisher Information Matrix. This approach allows for a more accurate characterization of the uncertainties associated with the model parameters. Secondly, we propose a discrete-time interval state estimation method utilizing inclusion functions and constraint propagation. This method is specifically designed to handle discrete-time measurements.

Furthermore we will include additional sections that explore set-based state estimation techniques using zonotopes and constrained zonotopes. These sections will discuss the application of these techniques to the Li-ion cell model, providing further insights and contributions in terms of improved state estimation accuracy and robustness. Furthermore, this chapter will focus on exploring set-based state estimation techniques using zonotopes and constrained zonotopes applied to battery cells. They offer valuable insights and advancements in improving the accuracy and robustness of state estimation for the Li-ion cell model.

Through numerical experiments, we will demonstrate the efficiency and effectiveness of the proposed methodology, showing that it provides accurate enclosures for both the state of charge and the electric state variables of the ECM. These results will further validate the contributions of this chapter and highlight the practical significance of the developed set-based observer approaches in the context of Li-ion cell estimation. In the remainder of this chapter, we develop a discrete-time interval observer for a single Li-ion cell, based on the forward-backward method described in Jaulin et al., 2001. The objective is to address parametric uncertainties in the system, which are obtained through an identification procedure using data collected from a well-known Electrochemical Model (ECM) with electrolyte dynamics, specifically the Single Particle Model (SPMe) (Pozzi et al., 2018).

6.1 Modeling and identification of the ECM parameters

In this section we refer to the model Thévenin model described in Chapter 3.2.1, where the electrical parameters are considered as SOC-dependent. For sake of simplicity here no thermal model has been used and we assume to operate in a thermally isolated chamber. Note that the considerations that will follow in this chapter can be extended to any model described in the literature. The mathematical representation of the ECM discussed in Section 3.2.1 can be formally expressed as follows:

$$\begin{cases} \dot{\mathbf{x}}(t) = \mathbf{f}(\mathbf{x}(t), \mathbf{u}(t), \boldsymbol{\phi}), \\ \mathbf{y}(t) = \mathbf{g}(\mathbf{x}(t), \mathbf{u}(t), \boldsymbol{\phi}), \\ \mathbf{x}(t_0) = \mathbf{x}_0, \end{cases} \tag{6.1}$$

$$\boldsymbol{\phi} \triangleq \begin{bmatrix} R_0 & R_{1,0} & R_{1,1} & R_{1,2} & C_{1,0} & C_{1,1} & C_{1,2} & C_{\text{batt}} \end{bmatrix}. \tag{6.2}$$

where $\mathbf{x}(t)$ represents the state variables, $\mathbf{u}(t)$ denotes the input variables, and $\boldsymbol{\phi}$ represents a vector of ECM parameters. Equation (6.2) provides the explicit definition of the parameter vector $\boldsymbol{\phi}$.

To apply the interval state estimation method proposed in this study, we first discretize the ECM using Euler's method. The resulting discrete-time model is given by:

$$\begin{cases} \mathbf{x}(k+1) = \mathbf{x}_k + T_s \mathbf{f}(\mathbf{x}(k), u(k), \boldsymbol{\phi}), \\ \mathbf{y}(k) = \mathbf{g}(\mathbf{x}(k), u(k), \boldsymbol{\phi}), \\ \mathbf{x}(k_0) = \mathbf{x}_0, \end{cases} \tag{6.3}$$

where T_s represents the sampling time, and $k \geq k_0$ denotes the time step.

In this work, we focus on the charging phase of the ECM, considering the different state-of-charge (SOC) relationship of parameters R_1 and C_1 as reported in Perez et al., 2017. The estimation of the ECM parameters is conducted using data collected from the "real plant," which we assume to be the SPMe. We assume an initial condition where the cell is almost completely discharged and at rest, given by $\mathbf{x_0} = [0.017 \; 0]^{\mathrm{T}}$ (ECM states). The input signal used for the parameter estimation, defined over a time horizon $\bar{k}$, is shown in Figure 6.1. It is worth noting that an input profile with sufficient excitation is crucial for improved identifiability and reduced parametric uncertainties.

Remark 2 *Although the ECM parameters still require estimation, the initial state* $\mathbf{x_0}$ *can be easily determined when the cell is at rest. In such cases, the voltage across the parallel* $R_1 - C_1$ *combination is zero, and the open-circuit voltage* V *coincides with* V_{oc}*. The initial state of* $z(0)$ *can be computed from* (3.13)[1].

The system under consideration is subject to measurement noise, which is assumed to lie within the interval $[-3mV, 3mV]$. In order to facilitate the subsequent identification procedure, we approximate the measurement noise as independent and identically distributed (i.i.d.) Gaussian noise $\mathbf{d}(k) \sim \mathcal{N}(0, \sigma_y^2)$, where $\sigma_y = 1mV$. Specifically, for the true value of the parameter vector $\boldsymbol{\phi}^*$, the measurements are given by $\hat{\mathbf{y}}(k, \boldsymbol{\phi}^*) = g(\mathbf{x}(k), \mathbf{u}(k), \boldsymbol{\phi}^*) + \mathbf{d}(k)$.

Let $\hat{\mathbf{Y}}(\boldsymbol{\phi}^*) \in \mathbb{R}^{\bar{k}+1}$ denote the vector of observed output data over the time horizon $k = k_0, \ldots, k_0 + \bar{k}$. It can be established that $\hat{\mathbf{Y}}(\boldsymbol{\phi}^*) \sim \mathcal{N}(\mathbf{Y}(\boldsymbol{\phi}^*), \mathbf{C}_y)$, where $\mathbf{Y}(\boldsymbol{\phi}^*)$ represents the output vector in the absence of measurement noise, and $\mathbf{C}_y \in \mathbb{R}^{(\bar{k}+1)\times(\bar{k}+1)}$ is the diagonal measurement covariance matrix given by $\mathbf{C}y = \sigma_y^2 \mathbf{I}_{\bar{k}+1}$.

The parameters can be estimated by solving the following maximum likelihood optimization problem using the collected training data:

---

[1] The open-circuit potential (OCP) is assumed to be known a priori.

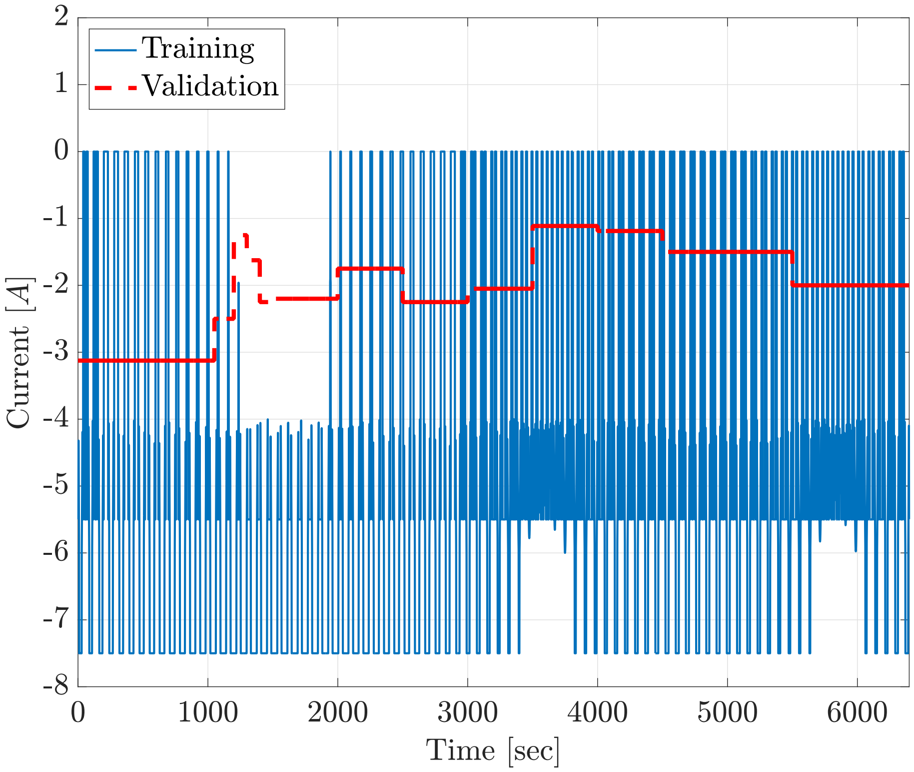

FIGURE 6.1: Training and validation current input profiles.

$$
\begin{aligned}
\hat{\phi} = \arg\min_{\phi}\ & (\hat{\mathbf{Y}}(\phi^*) - \mathbf{Y}(\boldsymbol{\phi}))^{\mathrm{T}}\, \mathbf{C}_y^{-1} (\hat{\mathbf{Y}}(\phi^*) - \mathbf{Y}(\boldsymbol{\phi})) \\
\text{s.t.}\ & \text{model dynamics (9.1)}, \\
& 0 \leq \mathbf{h}(\mathbf{x}(k), \mathbf{u}(k), \boldsymbol{\phi}), && \text{(6.4a)} \\
& \boldsymbol{\phi}^{\min} \leq \boldsymbol{\phi} \leq \boldsymbol{\phi}^{\max}, && \text{(6.4b)}
\end{aligned}
$$

The output vector $\mathbf{Y}(\boldsymbol{\phi})$ represents the results obtained by solving the system (6.3) for a given parameter $\boldsymbol{\phi}$ over the time horizon $k = k_0, \ldots, k_0 + \bar{k}$. The inequality (6.4b) ensures that the optimization problem takes into account the physical bounds on the parameters, such as $R_0 \geq 0$ and $C_{\mathrm{batt}} \geq 0$. Similarly, equation (6.4a) is necessary to constrain SOC-dependent variables like R_1 and C_1. By assuming that functions (3.9) and (3.11) exhibit the same concavity as in Perez et al., 2017, it is possible to enforce the positivity of these quantities by setting constraints on their values for $z = 1$ and $z = 0$ (concave case), or for the corresponding z value that corresponds to the minimum of the function (convex case). This latter value can be found analytically. Additional constraints can be included when prior knowledge about the parameter bounds is available.

The estimated parameter values, obtained by solving the optimization problem (6.4) using the data collected from the experiments shown in Fig. 6.1 (blue), are reported in Table 6.1.

The validation of the ECM model with the estimated parameters has been conducted by comparing it against the SPMe, utilizing the validation profile depicted in

Table 6.1: Estimated ECM parameters.

$R_0(\Omega)$	$R_{1,0}(\Omega)$	$R_{1,1}(\Omega)$	$R_{1,2}(\Omega)$
0.093	0.0221	-0.07	0.0672
$C_0(As)$	$C_{1,0}(As)$	$C_{1,1}(As)$	$C_{1,2}(As)$
235.52	7.7613×10^4	-7.0974×10^4	2.6963×10^4

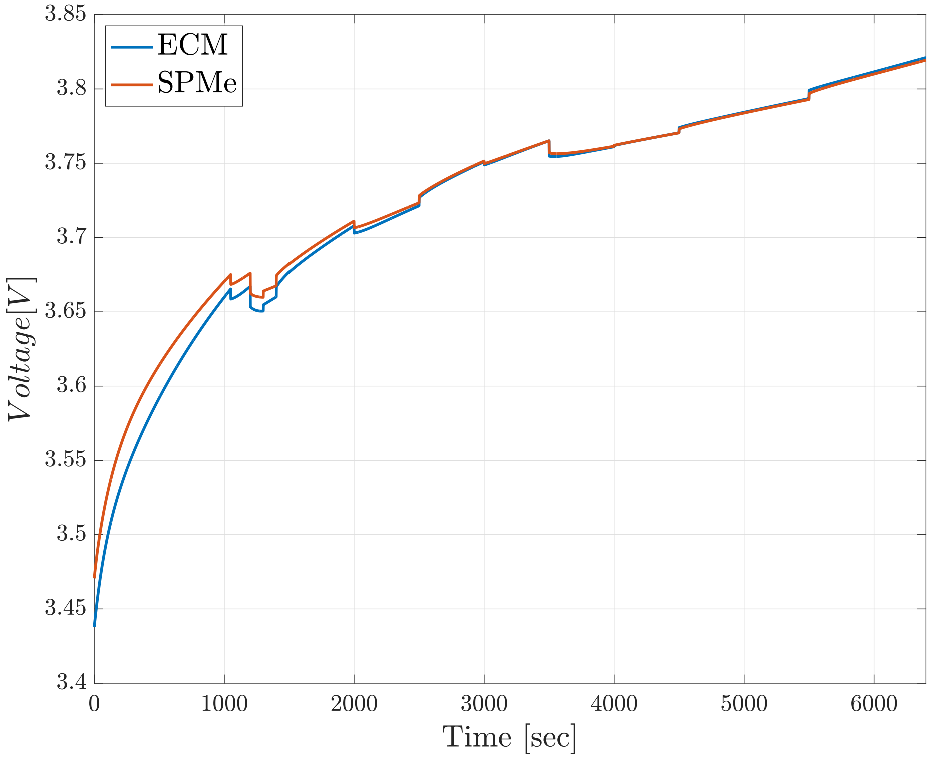

Figure 6.2: Validation profile of the terminal voltage.

Figure 6.1 (red), while maintaining the same initial condition as during the training phase. The obtained results, as shown in Figure 6.2, demonstrate a satisfactory overall agreement, although certain inconsistencies have been identified.

To assess the accuracy of the obtained parameter values for state estimation and control purposes, it is important to quantify their uncertainty. Since $\hat{\mathbf{Y}}(\boldsymbol{\phi}^*)$ is a random variable, the estimated $\hat{\boldsymbol{\phi}}$ is also a random variable with a covariance matrix $\mathbf{C}_{\hat{\boldsymbol{\phi}}} \in \mathbb{R}^{8\times 8}$. Following a similar approach as in Pozzi et al., 2018, we utilize the Fisher Information Matrix (FIM) to estimate $\mathbf{C}\hat{\boldsymbol{\phi}}$. According to the Cramer-Rao bound, the FIM provides a lower bound on the covariance matrix of the parameters:

$$\mathbf{C}_{\hat{\boldsymbol{\phi}}} \geq (\mathbf{F}(\hat{\boldsymbol{\phi}}))^{-1} = ((\mathbf{S}(\hat{\boldsymbol{\phi}}))^{\mathrm{T}}, \mathbf{C}_y^{-1}, \mathbf{S}(\hat{\boldsymbol{\phi}}))^{-1}, \tag{6.5}$$

where $\mathbf{F}(\hat{\boldsymbol{\phi}}) \in \mathbb{R}^{8\times 8}$ represents the FIM and $\mathbf{S}(\hat{\boldsymbol{\phi}})$ is the sensitivity matrix computed as $\mathbf{S}(\hat{\boldsymbol{\phi}}) \triangleq \nabla_{\hat{\boldsymbol{\phi}}} \mathbf{Y}(\hat{\boldsymbol{\phi}})$.

	1	2	3	4	5	6	7	8
1	1	-0.5815	-0.02829	0.06061	0.03614	0.6591	-0.5626	-0.0325
2	-0.5815	1	-0.7377	0.6383	0.04311	-0.4517	0.4054	0.2151
3	-0.02829	-0.7377	1	-0.9701	-0.07248	0.02897	-0.04347	-0.3015
4	0.06061	0.6383	-0.9701	1	0.06541	0.007879	0.01245	0.3736
5	0.03614	0.04311	-0.07248	0.06541	1	-0.07492	0.06956	0.02263
6	0.6591	-0.4517	0.02897	0.007879	-0.07492	1	-0.982	-0.1135
7	-0.5626	0.4054	-0.04347	0.01245	0.06956	-0.982	1	0.1706
8	-0.0325	0.2151	-0.3015	0.3736	0.02263	-0.1135	0.1706	1

FIGURE 6.3: Parametric correlation matrix.

Remark 3 *The utilization of the FIM inverse as a measure of parametric uncertainty is commonly found in the literature. However, it is important to acknowledge that this method has certain limitations and potential inaccuracies. Firstly, it provides only a lower bound estimation of* $\mathbf{C}_{\hat{\boldsymbol{\phi}}}$*. Secondly, it relies on local parameter sensitivity, assuming a linear relationship between variations in model parameters and simulation results. As a result, it may not capture non-linear effects accurately. Thirdly, it is restricted to estimating the covariance matrix and may not fully capture the non-Gaussian nature of the uncertainty distribution. Lastly, it assumes that the model structure used in the identification phase is correct, which may not always be the case. Future work will address these limitations by incorporating higher-order terms in local sensitivity analysis, employing global sensitivity analysis techniques, and considering the errors associated with approximating a high-fidelity model with a reduced one (see, for example, Weber et al., 2019).*

The estimated correlation matrix $\mathbf{R}_{\hat{\boldsymbol{\phi}}}$[2] obtained using the FIM is shown in Figure 6.3. Non-zero off-diagonal values indicate correlations among the parameters in (6.2). To account for this feature in the subsequent interval state estimation, a linear change of variables is performed by defining $\hat{\boldsymbol{\psi}} = \mathbf{T}\hat{\boldsymbol{\phi}}$, where $\mathbf{T}$ is chosen as the inverse of the eigenvector matrix of $\mathbf{C}_{\hat{\boldsymbol{\phi}}}$[3]. Consequently, the covariance matrix $\mathbf{C}_{\hat{\boldsymbol{\psi}}}$ for the new parameter set $\hat{\boldsymbol{\psi}}$ becomes diagonal.

Using an unbounded distribution to describe the parametric uncertainty is excessively conservative, as physical electric parameters cannot be negative or exceed

---

[2] Given $D = \sqrt{\mathrm{diag}(\mathbf{C}_{\hat{\boldsymbol{\phi}}})}$, the correlation matrix can be derived as $\mathbf{R}_{\hat{\boldsymbol{\phi}}} = D^{-1}\mathbf{C}_{\hat{\boldsymbol{\phi}}}D^{-1}$.

[3] Since $\mathbf{C}_{\hat{\boldsymbol{\phi}}}$ is symmetric, it possesses a complete set of orthogonal eigenvectors, making $\mathbf{T}$ invertible.

meaningful values (e.g., it is nonsensical for the Kokam SLPB 75106100 cell to have a resistance in the megohm range). Consequently, in the subsequent section, each element of the parametric uncertainty $\hat{\boldsymbol{\psi}}_i$ is restricted to the domain $[\hat{\psi}_i - 3\sqrt{C_{\hat{\boldsymbol{\psi}}}(i,i)}, \hat{\psi}_i + 3\sqrt{C_{\hat{\boldsymbol{\psi}}}(i,i)}]$, which truncates it within ± 3 times the standard deviation of the parameter. These sets are further constrained by considering the physical limits of the original parameters $\hat{\boldsymbol{\phi}}$, such as positivity for each SOC value. It is crucial to note that having a reference system with a diagonal covariance matrix is essential, as intervals alone cannot capture any coupling between variables.

The identification phase has been implemented using CasADi (Andersson et al., 2019). The optimization problem has been solved with IPOPT, a primal-dual interior point method,interfaced with CasADi.

6.2 Interval-based state estimation method

Let consider the discrete-time nonlinear model expressed in vector form as follows:

$$\begin{cases} \mathbf{x}(k) = \mathbf{f}(\mathbf{x}(k-1), \mathbf{u}(k-1), \mathbf{w}(k-1)), \\ \mathbf{y}(k) = \mathbf{g}(\mathbf{x}(k), \mathbf{u}(k), \mathbf{v}(k)), \end{cases} \tag{6.6}$$

where $k \geq 1$, $\mathbf{y}(0) = \mathbf{g}(\mathbf{x}(0), \mathbf{u}(0), \mathbf{v}(0))$, $\mathbf{f} : \mathbb{R}^n \times \mathbb{R}^{n_u} \times \mathbb{R}^{n_w} \to \mathbb{R}^n$, $\mathbf{g} : \mathbb{R}^n \times \mathbb{R}^{n_u} \times \mathbb{R}^{n_v} \to \mathbb{R}^{n_y}$. In this model, $\mathbf{w} \in [W]$ represents the unknown-but-bounded process disturbances, and $\mathbf{v} \in [V]$ represents the measurement disturbances.

Our objective is to obtain accurate interval enclosures $\hat{X}$ for the state variables $\mathbf{x}(k)$ that are consistent with the nonlinear system (6.6) and the measurement $\mathbf{y}_k$. To achieve this, we adopt the prediction-update algorithm proposed by Rego et al., 2020a. This algorithm involves computing intervals $\bar{X}$ and $\hat{X}$ satisfying the following conditions:

$$\begin{aligned} [\bar{X}](k) \supseteq \{ & \mathbf{f}(\mathbf{x}(k-1), \mathbf{u}(k-1), \mathbf{w}(k-1)) : \\ & \mathbf{x}(k-1) \in [\bar{X}](k-1),\ \mathbf{w}(k-1) \in [W]\}, \end{aligned} \tag{6.7}$$

$$\begin{aligned} [\hat{X}](k) \supseteq \{ & \mathbf{x}(k) \in \bar{X}(k) : \\ & \mathbf{g}(\mathbf{x}(\mathbf{k}), \mathbf{u}(k), \mathbf{v}(k)) = \mathbf{y}(k),\ \mathbf{v}(k) \in [V]\}, \end{aligned} \tag{6.8}$$

The expression (6.17) corresponds to the prediction step, while (6.8) represents the update step. It is assumed that an interval enclosure $\bar{X}$ for the initial state $\mathbf{x}(0)$ and the current measurement $\mathbf{y}(k)$, for $k \geq 0$, is known.

In this chapter, we propose an efficient approach for guaranteed state estimation by combining inclusion functions with the forward-backward constraint propagation (FBCP) method (Jaulin et al., 2001). The estimation process consists of two main steps: prediction and update.

In the prediction step, which is performed for each time step k, we use inclusion functions (Moore, Kearfott, and Cloud, 2009) to propagate the previous state set $\hat{X}$ through the nonlinear model $\mathbf{f}$ defined in (6.6). This propagation results in a predicted interval $\bar{X}$ that contains the possible values of the state variables $\mathbf{x}(k)$.

In the update step, we solve a Constraint Satisfaction Problem (CSP) to refine the predicted interval $\bar{X}$ and the measured interval Y. The CSP, denoted as $\mathcal{H}$, is formulated as follows:

$$\mathcal{H}: \quad \mathbf{y}(k) = \mathbf{g}(\mathbf{x}(k), \mathbf{u}(k), \mathbf{v}(k)), \quad \mathbf{x}(k) \in \bar{X}, \qquad \mathbf{y}(k) \in Y, \quad \mathbf{v}(k) \in [V],$$

where $\mathbf{g}$ is the nonlinear mapping defined in (6.6) and $\mathcal{S}$ represents the solution set of $\mathcal{H}$, given by $\mathcal{S} \triangleq \mathbf{y}(k) \in Y, \mathbf{x}(k) \in \bar{X} : \mathbf{y} = \mathbf{g}(\mathbf{x}(k), \mathbf{u}(k), \mathbf{v}(k)), \mathbf{v}(k) \in [V]$.

To solve the CSP $\mathcal{H}$, we employ a forward-backward constraint propagation algorithm. In the forward propagation phase, the state set $\bar{X}$ is propagated through the mapping $\mathbf{g}$ using inclusion functions, taking into account intermediate variables. This propagation generates an output interval Y, which is then refined by intersecting it with the measured interval $\mathbf{y}(k)$. In the backward propagation phase, the nonlinear mapping $\mathbf{g}$ is swept backwards, and the interval Y obtained during the forward propagation phase is used to further refine the state set $\bar{X}$.

The detailed FBCP algorithm for the estimation of the discrete-time nonlinear model (6.6) is described in the following.

6.2.1 State estimation of the lithium-ion cell using FBCP

The FBCP algorithm, proposed by Jaulin et al. Jaulin et al., 2001, consists of three intermediate steps: contractor decomposition, forward update, and backward update. Here, we apply these steps to the ECM example.

Considering the ECM model described by (6.3), with the output function $\mathbf{g}$ given as in Section 3.2.1, we have the process disturbance $\mathbf{w}(k)$ determined by the parametric uncertainties in the ECM. The disturbance is represented by $\mathbf{w}(k) = \mathbf{T}\hat{\boldsymbol{\phi}}$, where $\mathbf{T}$ is the transformation matrix defined in Section 6.1, and it is bounded by $\mathbf{w}(k) \in [W]$, with $[W] \triangleq \mathbf{T}[\hat{\boldsymbol{\phi}}]$. Additionally, the output disturbance $\mathbf{v}(k)$ includes both the parametric uncertainties and the additive measurement noise $\mathbf{d}(k) \in [\mathbf{d}] \subset \mathbb{R}$. Here, $[\mathbf{d}]$ is defined in Section 6.1, and $\mathbf{v}(k)$ is given by $\mathbf{v}(k) \triangleq [\mathbf{w}(k)^T, ; \mathbf{d}(k)]^T$. It's important to note that $\mathbf{v}(k)$ depends on $\mathbf{w}(k)$ due to the correlation of R_0 with the other parameters in (6.2) (refer to Fig. 6.3).

To address the dependency effect in the polynomial function (3.13), we rewrite $V_{\text{oc}}(k)$ using the centered form suggested by Hansen et al. Hansen and Walster, 2003. The centered form is given by:

$$V_{\text{oc}}(x_1) = p_0(k) + \sum_{i=1}^{9} p_i(k)(x_1 - c)^i, \tag{6.9}$$

where c is defined as the midpoint of x_1, denoted as $c \triangleq \text{mid}(x_1)$. Here, $x_1 \triangleq z$ represents the first component of $\bar{X}$. The auxiliary variables p_i are given by $p_0(k) \triangleq V_{\text{oc}}(c)$ and $p_i(k) \triangleq (1/i!)V_{\text{oc}}^{[i]}(c)$, where $V_{\text{oc}}^{[i]}(c)$ represents the i-th derivative of (3.13) with respect to $z(k)$, evaluated at c.

1) Contractor decomposition. The first step of the FBCP algorithm involves decomposing the function $\mathbf{g}$ derived from (3.2) into a "primitive" form. This form consists of simplified expressions where only one function or one elementary operation is present. To achieve this, we introduce intermediate variables $[h_i]$ defined as:

$$h_i \triangleq (x_1 - c)^i, \quad i \in 1, \ldots, 9, \tag{6.10}$$

which allow us to rewrite the polynomial function (3.13) as:

$$V_{\text{oc}} = p_0(k) + \sum_{i=1}^{9} p_i(k), h_i. \tag{6.11}$$

2) Forward update. In the second step, given the measurement $\mathbf{y}(k)$, we subtract the noise interval $[\mathbf{d}]$ to obtain $Y \triangleq \mathbf{y}(k) - [\mathbf{d}]$. We then compute the intersection:

$$Y \leftarrow Y \cap [V_{\text{oc}} + x_2 + R_0 u(k)], \tag{6.12}$$

to refine Y. It is important to note that if no measurement is available at time k, the set is initialized as $(-\infty, +\infty)$.

3) Backward update. The third step involves sweeping the decomposed function $\mathbf{g}$ backward. Each variable on the right-hand side of $\mathbf{g}$ is explicitly expressed as a function of the other variables appearing in the forward update. This is done as follows:

For V_{oc}, we perform the following intersection to refine it:

$$V_{\text{oc}} \leftarrow V_{\text{oc}} \cap [Y - x_2 - R_0 u(k)]. \tag{6.13}$$

For x_2, we refine it with the following intersection:

$$x_2 \leftarrow x_2 \cap [Y - V_{\text{oc}} - R_0 u(k)]. \tag{6.14}$$

To assess the state of charge x_1, we sweep (6.11) backward and decompose it into multiple expressions using the intermediate variables h_i for $i = 1, \ldots, 9$. The decomposition is performed as follows:

$$h_i \leftarrow h_i \cap \left[\frac{1}{p_i(k)}\left(V_{\text{oc}} - p_0(k) \quad - \sum_{j \neq i} p_j(k) h_j\right)\right]. \tag{6.15}$$

The interval h_1 is further refined to retrieve both positive and negative even roots. Since h_1 is zero-centered by definition (see (6.10)), the following logic is necessary:

$$h_1 \leftarrow h_1 \cap_{i \in 2,4,6,8} (h_i^{\frac{1}{i}}) \qquad = h_1 \cap_{i \in 2,4,6,8} ([-|\overline{h}i|^{\frac{1}{i}}, |\overline{h}i|^{\frac{1}{i}}]).$$

For odd roots, the refinement of h_1 is performed as follows:

$$h_1 \leftarrow h_1 \cap_{i \in 3,5,7,9} ([\underline{\alpha}i, \overline{\alpha}i]),$$

where $\underline{\alpha}i \triangleq \underline{h}i!,^{\frac{1}{i}}$ if $h_i > 0$, $\underline{\alpha}i \triangleq -(|\underline{h}i|^{\frac{1}{i}})$ otherwise, and $\overline{\alpha}i \triangleq -(|\overline{h}i|^{\frac{1}{i}})$ if $h_i < 0$, $\overline{\alpha}i \triangleq \overline{h}i!,^{\frac{1}{i}}$ otherwise. Here, $\underline{h}i$ and $\overline{h}i$ represent the lower and upper bounds of h_i, respectively.

Finally, the refinement of the state of charge (SOC) interval is performed by intersecting x_1 with $h_1 + c$, resulting in:

$$x_1 \leftarrow x_1 \cap h_1 + c.$$

The interval enclosure $\hat{X}$ for the update step (6.8) is then given by $\hat{X} \leftarrow x_1 \times x_2$.

Remark 4 To obtain a more precise enclosure $\hat{X}$, steps 2 and 3 can be iterated as described by Jaulin et al. (Jaulin et al., 2001). However, in the case of the ECM, it has been observed that a single iteration yields accurate enough enclosures, as demonstrated in Section 6.2.2.

Remark 5 When applying the FBCP algorithm to the ECM, it is important to note that intervals are unable to capture the constant nature of $\mathbf{w}(k)$ and the dependencies between $\mathbf{v}(k)$ and $\mathbf{w}(k)$. Consequently, the application of the FBCP algorithm results

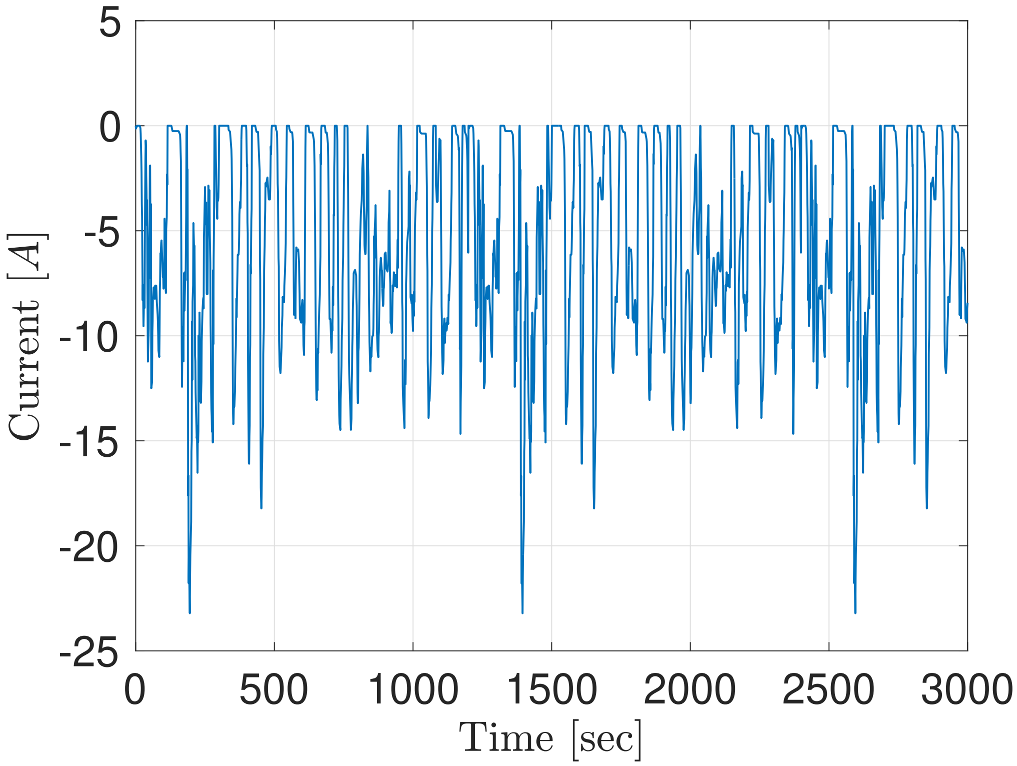

FIGURE 6.4: Current input profile $I(t)$ applied to the ECM.

in a conservative estimation. To address this limitation, future research will explore alternative set representations, such as zonotopes, which can effectively handle these dependencies and reduce conservatism.

6.2.2 Numerical results

In the following, we present the results obtained by applying the interval state estimation method to the Li-ion cell during the charging phase. The input profile used for the estimation is shown in Figure 6.4.

To start the estimation process, we consider an initial state set $\bar{X}$ centered around the initial state condition $(z(0), V_{c1}(0)) = (0.3, 0)$. The initial state uncertainty is set to 1% for the state of charge (SOC) and a much lower uncertainty of 0.0001% V for the voltage V_{c1}. This choice is based on the assumption that the battery is in a stationary condition at time $t = 0$ after a rest period (see Remark 2).

The open-loop state estimation is performed using only the prediction step (6.17) with the natural inclusion function. This involves replacing each variable with its interval enclosure and applying elementary interval operations (Moore, Kearfott, and Cloud, 2009) at each time step k.

Figure 6.5 illustrates a comparison between the state sets computed in open loop (pink) and closed loop (green). It highlights the results obtained after the refinement procedure associated with the FBCP algorithm. This refinement step improves the accuracy of the state estimation.

In Figure 6.6, a further comparison between open and closed loop estimation is presented. The areas of the state enclosures are calculated at each time step k and plotted. It is observed that, despite the improved accuracy of the closed loop

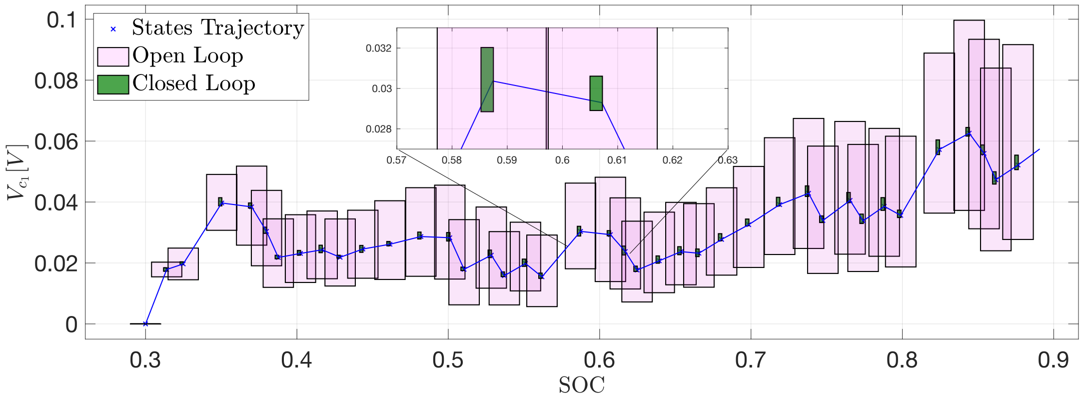

FIGURE 6.5: Enclosures obtained using interval state estimation.

estimation, the size of the state sets tends to mildly increase over time. This is primarily due to the charging process, which leads to an increase in the state of charge (SOC) over time and subsequently results in more conservative interval enclosures of the polynomial (6.11).

However, it is worth noting that the use of the FBCP approach in the closed loop estimation significantly reduces the size of the obtained intervals while still ensuring that the actual state trajectory $\mathbf{x}(k)$ (depicted in blue in Figure 6.5) lies within the state enclosure $[\hat{X}(k)]$.

The simulations were conducted using MATLAB 2020a, and all interval operations were performed using INTLAB 9 (Rump, 1999). The plots in Figure 6.5 were created using MPT (Multi-Parametric Toolbox).(Kvasnica et al., 2004).

6.3 Constrained zonotopes state estimation

In this section, we consider a class of nonlinear discrete-time systems described by the following equations:

$$\begin{aligned} \boldsymbol{x}_k &= \boldsymbol{f}(\boldsymbol{x}_{k-1}, \boldsymbol{u}_{k-1}, \boldsymbol{w}_{k-1}) \quad &\text{for} \quad k \geq 1, \\ \boldsymbol{y}_k &= \boldsymbol{g}(\boldsymbol{x}_k, \boldsymbol{u}_k, \boldsymbol{v}_k) \quad &\text{for} \quad k \geq 0, \end{aligned} \tag{6.16}$$

where $\mathbf{x}_k \in \mathbb{R}^{n_x}$ represents the system state vector, $\mathbf{u}_k \in \mathbb{R}^{n_u}$ denotes the known inputs, $\mathbf{y}_k \in \mathbb{R}^{n_y}$ indicates the measured outputs, and $\mathbf{w}_k \in \mathbb{R}^{n_w}$ and $\mathbf{v_k} \in \mathbb{R}^{n_v}$ represent process and output uncertainties, respectively. It is assumed that the initial condition $\mathbf{x}_0 \in X_0$ and the disturbances are bounded by $\mathbf{w}_k \in W$ and $\mathbf{v}_k \in V$, where X_0, W, and V are known compact sets.

The main objective of set-based state estimation is to compute, at each time step $k \geq 0$, tight enclosures $\hat{X}_k$ of the set of states consistent with the model dynamics, the bounded uncertainties X_0, W, V, and the collected measurements $\mathbf{y}_k$. This is achieved through a prediction-update algorithm that computes the compact sets $\bar{X}_k$ and $\hat{X}_k$ as follows:

$$\bar{X}_k \supseteq \{\mathbf{f}(\mathbf{x}, \mathbf{u}_{k-1}, \mathbf{w}_{k-1}) : \mathbf{x} \in \hat{X}_{k-1},\ \boldsymbol{w}_{k-1} \in W\}, \tag{6.17}$$

$$\hat{X}_k \supseteq \{\boldsymbol{x} \in \bar{X}_k : \mathbf{g}(\mathbf{x}, \mathbf{u}_k, \mathbf{v}_k) = \mathbf{y}_k,\ \mathbf{v}_k \in V\}, \tag{6.18}$$

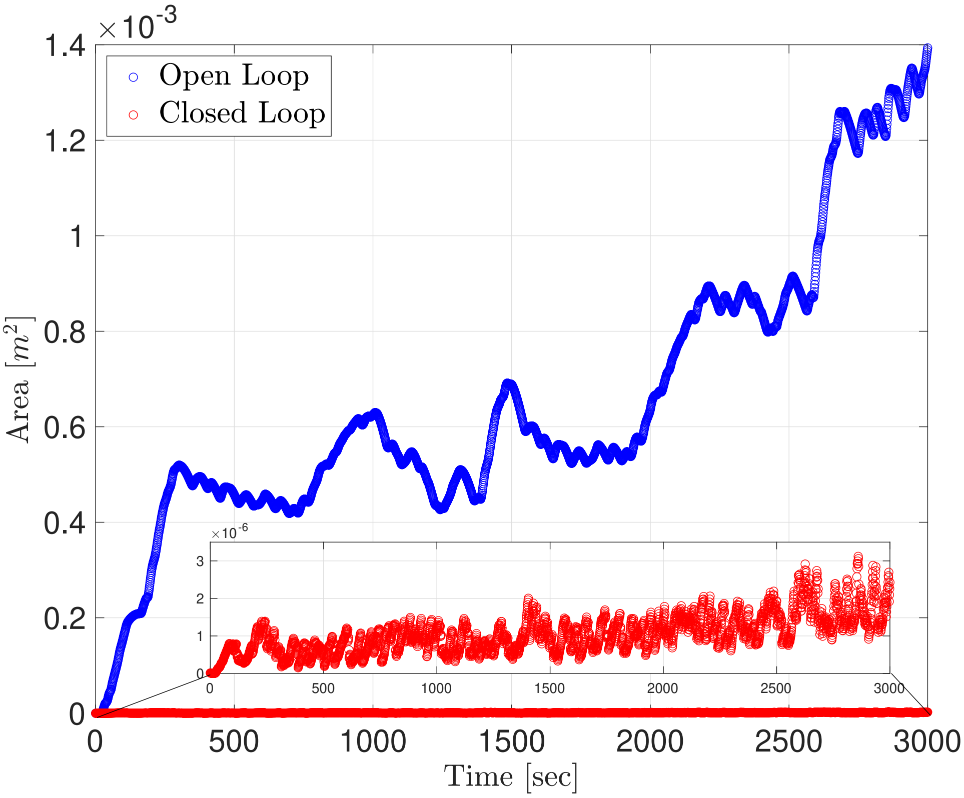

FIGURE 6.6: Area of the estimated enclosures over time.

where (6.17) and (6.18) are known as the *prediction step* and *update step*, respectively. It is important to note that, in general, the set operations defined in (6.17)-(6.18) cannot be evaluated exactly. Therefore, tight guaranteed enclosures (meaning, in this context, tight outer approximations) are computed instead.

Within this context, Constrained Zonotopes (CZs) have demonstrated significant advantages over other set representations (Scott et al., 2016a). In the following, we provide detailed information on how to perform the prediction-update algorithm for nonlinear discrete-time systems using CZs (Rego et al., 2021a). This procedure has been utilized to develop a set-based state estimation scheme for the cell model described in Section 3.2.2. The essential components necessary to execute the prediction-update algorithm (6.17)-(6.18) for discrete-time nonlinear systems employing Constrained Zonotopes (CZ), are explained in Section 5.3 and Section 5.4. Note that in the following example The mean value extension has been exploited to obtain the guaranteed state enclosures for each time step. Complexity reduction approaches (see Section 4.3) have been applied at each time step following the update step.

6.3.1 Numerical results

In this section, we present the outcomes of applying the CZ set-based estimation approach to the Dual Polarisation Li-ion cell model described in Chapter 3.2.2. Figure 6.7 illustrates the application of this approach in both open-loop and closed-loop scenarios, showcasing the prediction and prediction-update steps (6.17) and (6.18), respectively. The projections of the resulting sets onto the state-space defined by V_1,

V_2, and SOC are depicted at specific time instances, namely $k = \{2, 12, 22, 42, 95\}$ seconds.

In mirroring real-world scenarios, the quantifiable parameters comprise the terminal voltage V_t and the surface temperature T_s. To account for real-world measurement limitations, we incorporate measurement noise at levels of $\pm 1mV$ for terminal voltage and $\pm 0.1K$ for surface temperature.

In our analysis, we introduce uncertainty in the initial state conditions, which are enclosured within the zonotope:

$$\bar{X}_0 = \{\mathbf{G}_{x_0}, \mathbf{c}_{x_0}\}, \tag{6.19}$$

where $\mathbf{G}x_0 = \text{diag}([0.001; 0.001; 0.05; 1; 1])$ and $\mathbf{c}_{x_0} = [0.005; 0.005; 0.25; 298.15; 298.15]^\intercal$. Specifically, for the zonotope center, the State of Charge (SOC) has been established at 25%, while both the core and surface temperatures have been equated to the ambient temperature.

Throughout the subsequent simulations, a consistent drive cycle input current profile, serves as the basis. The utilization of this profile ensures that the simulations remain relevant and representative of real-world conditions.

In figure 6.7, the blue sets represent the open-loop estimations, achieved solely through prediction steps, while the yellow sets correspond to the closed-loop enclosures. For clarity, we have selected a subset of time instants for plotting, omitting others to prevent overlapping sets.

As anticipated, the closed-loop enclosures (yellow sets) exhibit notably reduced volume compared to their open-loop counterparts. This reduction can be attributed to the utilization of system output measurements during the update steps (6.18), which effectively constrain the feasible state values. This observation underscores the effectiveness of closed-loop estimation in enhancing accuracy and reducing uncertainty.

Furthermore, a noteworthy advantage of CZs becomes evident in this context. Unlike certain other methods, such as intervals, CZs have the capacity to capture intricate dependencies between state variables. Consequently, CZ-based estimation offers reduced conservatism and enables a more accurate representation of the true system behavior. The results depicted in Figure 6.7 provide empirical evidence of the enhanced performance achievable through closed-loop CZ-based estimation. The tighter enclosures achieved in closed-loop scenarios highlight the potential of CZs in refining state estimations through a comprehensive integration of prediction and update steps.

Note that while only a selected subset of time instances is shown in the figure, the trend of improved estimation accuracy through closed-loop CZ-based estimation is consistently observed across various time points.

6.4 Conclusions

In this chapter, we discussed about set-based state estimation for complex, nonlinear systems, with a particular focus on Li-ion battery modeling and estimation. The overarching objective was to enhance our understanding of the principles, techniques, and practical applications of set-based state estimation in real-world scenarios.

We commenced our exploration by exploring the fundamentals of set theory, introducing key concepts such as intervals and constrained zonotopes. These mathematical constructs served as the foundation for building more advanced techniques to bound system states. We elucidated the rationale behind utilizing sets for state estimation,

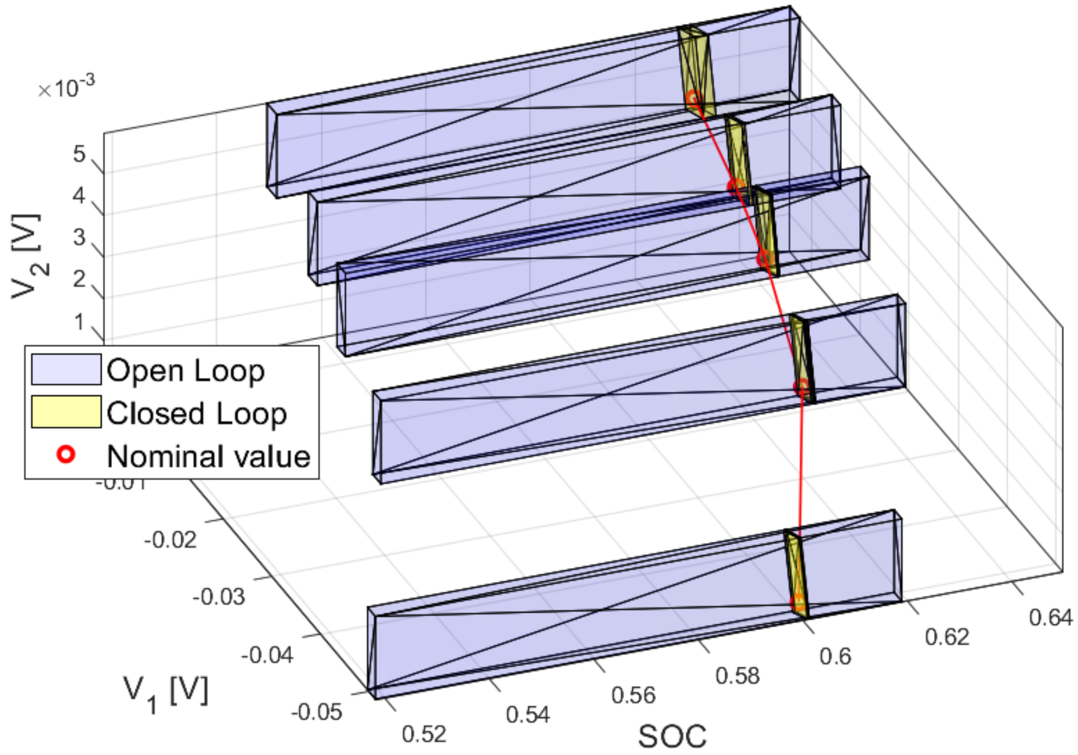

FIGURE 6.7: Comparison between open-loop and closed-loop state trajectories using CZ.

emphasizing their ability to provide rigorous bounds and robustness against uncertainties.

With our modeling framework in place, we ventured into the heart of set-based state estimation. We introduced two powerful methods, the Forward-Backward Contractor Programming (FBCP) algorithm and Constrained Zonotopes (CZs), as valuable tools for the task at hand. The FBCP algorithm enabled us to perform set-based state estimation through a series of contractor decomposition, forward update, and backward update steps. On the other hand, CZs provided an elegant means to represent and manipulate complex sets, offering enhanced accuracy and reduced conservatism in estimation.

To put theory into practice, we conducted a series of numerical experiments using the Li-ion battery model. These experiments vividly demonstrated the tangible benefits of closed-loop estimation over open-loop counterparts. By leveraging output measurements, closed-loop estimation consistently delivered tighter bounds on system states, reducing uncertainty and bolstering accuracy. CZ-based estimation, in particular, showcased its ability in capturing mutual dependencies between state variables, offering a promising course for future research in Li-ion batteries state estimation techniques.

Chapter 7

Set-based fault detection

The safe operation of Li-ion batteries is a critical aspect to consider during their use. Several different faults can occur that can result in degraded performance and hazardous consequences, such as explosions and fires. These faults can be classified into three main categories: cell faults, sensor faults, and actuator faults.

The BMS plays a crucial role in maintaining the safety of Li-ion batteries. It constantly monitors the battery pack's voltage, current, and temperature to determine the best way to operate the battery and prevent faults from occurring. When a fault does occur, the BMS can help detect it and minimize its effects. The BMS can also diagnose faults using various diagnostic methods to help ensure the safe operation of the battery.

The safe operation of Li-ion batteries requires careful monitoring and management, with the BMS playing a critical role in preventing faults and maintaining the safety of the battery during operation.

In this Chapter, a model-based method, relying on the mathematical model of the cell and the battery pack is used to detect faults. The main advantage of this approach is that it provides a complete understanding of the nature of the fault and can provide insight into the underlying physical processes. A drawback of this approach is that the mathematical model used is by definition an approximation of the true system, which can lead to inaccuracies in the fault detection. For this reason a set-based approach exploiting constrained zonotopoes has been used and model uncertainties have been taken into account. The structure of this chapter is organized as it follows: Section 7.1 formulates the problem and offers details on the fault detecion approach, Section 7.2 analyses the faulty model that has been exploited, Section 7.3 shows the numerical results applied to a single lithium cell case study, Section 7.4 applies the proposed set-based fault detection method to a three cells series system and finally Section 7.5 draws the final conclusions.

7.1 Set-based fault detection

Let consider a class of nonlinear discrete-time systems described by the equations below

$$\begin{aligned} \mathbf{x}_k &= \mathbf{f}(\mathbf{x}_{k-1}, \mathbf{u}_{k-1}, \mathbf{w}_{k-1}) \quad && \text{for} \quad k \geq 1, \\ \mathbf{y}_k &= \mathbf{g}(\mathbf{x}_k, \mathbf{u}_k, \mathbf{v}_k) \quad && \text{for} \quad k \geq 0, \end{aligned} \tag{7.1}$$

Here, $\mathbf{x}_k$ represents the system state vector, $\mathbf{u}_k$ are known inputs, $\mathbf{y}_k$ indicates measured outputs, and $\mathbf{w}_k$ and $\mathbf{v}_k$ represent process and output uncertainties. We assume bounded initial conditions and disturbances, with $\mathbf{x}_0 \in X_0$, $\mathbf{w}_k \in W$, and $\mathbf{v}_k \in V$, where X_0, W, and V are known compact sets.

The objective of set-based fault detection is first to perform state estimation. Within this context it is crucial to compute tight enclosures $\hat{X}_k$ of the set of states consistent with the model dynamics, bounded uncertainties, and collected measurements at each time step $k \geq 0$. This is achieved through a prediction-update algorithm, which computes compact sets $\bar{X}_k$ and $\hat{X}_k$ as described in equations (7.2) and (7.3) in the following. These equations correspond to the prediction step and update step, respectively.

$$\bar{X}_k \supseteq \{\mathbf{f}(\mathbf{x}, \mathbf{u}_{k-1}, \mathbf{w}_{k-1}) : \mathbf{x} \in \hat{X}_{k-1},\, \boldsymbol{w}_{k-1} \in W\}, \tag{7.2}$$

$$\hat{X}_k \supseteq \{\boldsymbol{x} \in \bar{X}_k : \mathbf{g}(\mathbf{x}, \mathbf{u}_k, \mathbf{v}_k) = \mathbf{y}_k,\, \mathbf{v}_k \in V\}, \tag{7.3}$$

The set operations in these steps cannot be evaluated exactly, which is why we compute tight guaranteed enclosures. In this context, Constrained Zonotopes (CZs) have demonstrated significant advantages over other set representations. Chapter 5 in the thesis provides details on performing the prediction-update algorithm using CZs.

Set-based fault detection involves comparing the observed measurements $\mathbf{y}_k$ to the predicted output set generated by the nominal (healthy) dynamics, i.e. performing the inclusion check at each k as it follows

$$\mathbf{y}_k \in \mathbf{g}(\bar{X}_k, \mathbf{u}_k, V). \tag{7.4}$$

As a result, a fault is detected when the measurement no longer belongs in the output set, which is expressed as $\mathbf{y}_k \notin \mathbf{g}(\bar{X}_k, \mathbf{u}_k, V)$, or, alternatively, when the update step (7.3) leaves $\hat{X}_k$ empty. The accuracy of set-based estimation is critical for early fault detection, making CZs a preferred choice due to their ability to provide tighter enclosures, at the price of a mild increase in complexity, they can lead to an earlier detection. The benefits of a set-based technique based on CZs over an interval method based on a forward-backward algorithm for the identification of thermal faults in a Li-ion cell are shown later in this chapter. More precisely a single lithium-ion cell application and three lithium-ion cells series applications have been taken as case studies.

7.2 Lithium ion battery applications

In this section we present the mathematical model used to describe the Li-ion cell faulty behaviour. We consider the coupled electro-thermal model which consists of a Dual-Polarisation ECM described in Section 3.2.2, augmented with a two-state thermal model describing the core and surface temperature dynamics as previously described in Section 3.2.4. Note that the Open Circuit Potential is defined according to Section 3.2.3. The interplay between Electrical and thermal part is shown in Figure 3.4.

Our major focus in this research is on temperature concerns within the battery cell, and our work expands on the landmark study performed by Dey et al., 2015. Within this thermal environment, we focus our attention on a trio of distinct thermal anomalies, each of which plays a critical role in shaping our knowledge of the system's behaviour.

Let us investigate the complexities of these thermal faults:

- *Fault 1*: this initial anomaly arises when the thermal resistance represented by R_u deviates significantly from its nominal value. This deviation indicates a convective cooling problem, in which the system's heat dissipation by convection is disturbed or damaged.

- *Fault 2*: the second anomaly, occurs when the thermal resistance R_c deviates significantly from its predicted nominal value. This deviation indicates the presence of an internal thermal resistance defect, which occurs when the system's internal resistance to heat flow is disrupted.
- *Fault 3*: in the last anomaly, an extra heat production factor is incorporated into the equation, which contributes to the slow rise in the core temperature T_c. Thermal runaway is an insidious process that can have serious effects, potentially leading to system failure.

To capture the implications of these thermal anomalies, we have modified the underlying thermal model. This modified model accounts for the presence of the aforementioned faults and is presented below in mathematical form for any single cell

$$\begin{aligned} C_c\dot{T}_c(t) &= \frac{T_s(t)-T_c(t)}{(R_c+\Delta R_c)} + u(t)\left(V_1(t)+V_2(t)+R_0u(t)\right)+ \\ &\quad + \Delta r, \qquad (7.5) \\ C_s\dot{T}_s(t) &= \frac{T_f(t)-T_s(t)}{(R_u+\Delta R_u)} + \frac{T_s(t)-T_c(t)}{R_c+\Delta R_c}, \qquad (7.6) \end{aligned}$$

In this model, we introduce the variables ΔR_c and ΔR_u to account for the effects of the first two faults, while the parameter Δr is included to represent the phenomenon of thermal runaway. It is crucial to note that we operate under the assumption that multiple faults cannot simultaneously occur within the system. Furthermore, we assume that these faults manifest suddenly, signifying that at a precise moment in time, the affected value instantaneously deviates from its expected norm.

It is worth highlighting that these faults can potentially interact with one another in a causal manner, creating a cascading effect that could further exacerbate system instability. Nevertheless, for the purposes of this research, we make the assumption that fault detection mechanisms operate with sufficient speed to preclude such cascading effects.

In essence, our study investigate the field of thermal faults within the Li-ion cell, with a specific focus on these three distinctive fault scenarios. Our modified thermal model serves as a tool to comprehensively explore their impact and implications.

7.3 Single cell numerical results

In this section, we apply the method we have introduced to the model described early in this section, and we present numerical results.

When manufacturing cells, it is impossible to produce two cells that are exactly identical. As a result, the batteries exhibit variations in characteristics such as capacity, charging speed, and lifespan.

Additionally, when working with mathematical models, parameter identification can lead to imprecise estimates for the parameter values. We address this issue in our model by considering parametric uncertainties, as discussed in Locatelli et al., 2021. In our research, we initially adopted base values for electrical and thermal parameters (as shown in Table 7.1), which were obtained from Lin et al., 2014. We introduced an uncertainty of ±2.5% for each parameter.

In a real-world scenario, we have two measurable quantities: terminal voltage (V_t) and surface temperature (T_s). We have considered measurement noise levels of

Parameter	**Value**	**Unit**
C_1	2100	Ah
C_2	70000	Ah
C_{bat}	2.3	Ah
R_0	0.01	Ω
R_1	0.02	Ω
R_2	0.02	Ω
R_u	3.08	KW^{-1}
R_c	1.94	KW^{-1}
C_c	62.7	JK^{-1}
C_s	4.5	JK^{-1}

TABLE 7.1: Electro-thermal model parameters

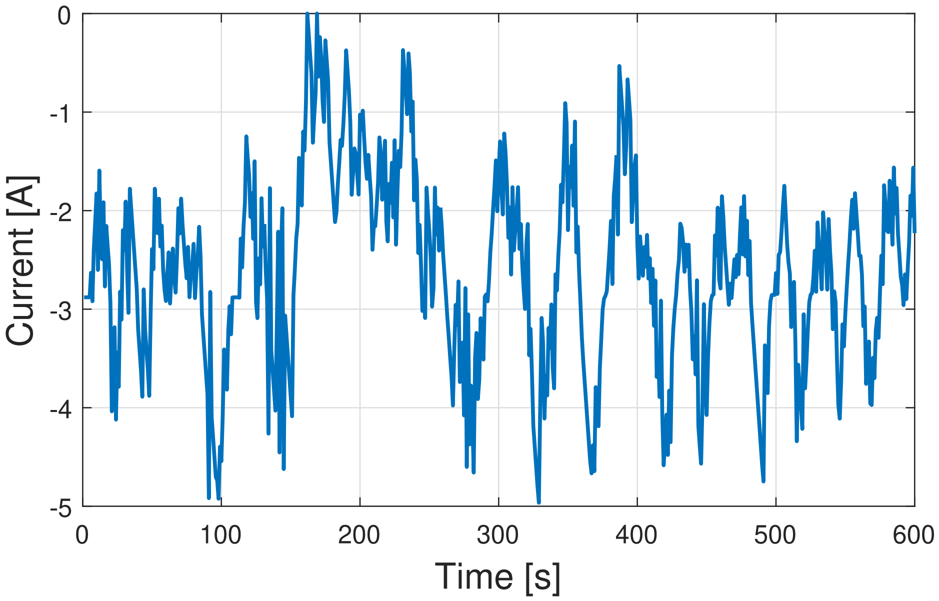

FIGURE 7.1: Input current profile $u(t)$ applied to the cell.

±1 mV and ±0.1 K for these quantities, respectively. We assume that the initial state condition is uncertain and lies in the zonotope

$$\bar{X}_0 = \{\mathbf{G}_{x_0}, \mathbf{c}_{x_0}\}, \tag{7.7}$$

with $\mathbf{G}_{x_0} = \mathrm{diag}([0.001\ 0.001\ 0.05\ 1\ 1])$ and $\mathbf{c}_{x_0} = [0.005\ 0.005\ 0.25\ 298.15\ 298.15]^\intercal$. In particular, when considering the center of the zonotope, the state of charge (SOC) has been set to 25%, and both the core and surface temperatures have been set to the ambient temperature.

All the simulations described in the following sections depend on the input current profile shown in Figure 9.1. This profile can represent a driving cycle for an electric vehicle.

The cell parameters used for simulating the healthy cell were randomly selected from within the specified parameter bounds, as mentioned earlier. Similarly, the initial condition used in all simulations was randomly chosen from within $\bar{X}_0$. Measurements were collected by simulating both the nominal and faulty cell models (as described

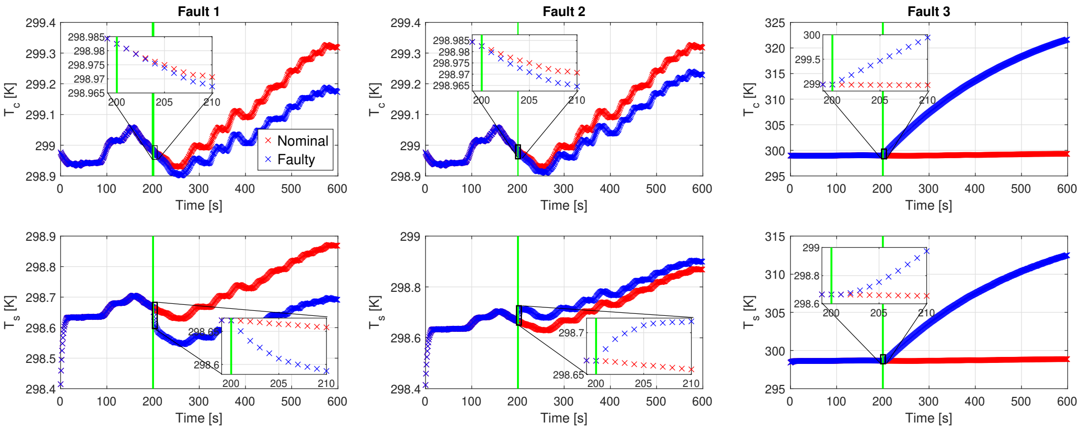

FIGURE 7.2: Comparison between nominal (in red) and faulty thermal states (in blue) for all the three types of faults presented. In green the time instant in which the fault is injected.

in Section 7.2) over a time interval of $[0, 600]$ seconds. The fault was introduced at $k = 200\ s$.

Figure 7.2 illustrates the impact of three different faults on the system: $\Delta R_u = -30\%$, $\Delta R_c = -30\%$, and $\Delta u = 0.1\ K$ (expressed as a percentage change from the base values). These are compared with the system's normal behavior.

Once a fault occurs, you can see from the state trajectory (in this case, we show only T_c and T_s) that it starts to deviate significantly from the expected path after a few seconds. It is important to note that we've changed only one parameter (the faulty one), while all other parameters remain the same for both normal and faulty scenarios.

While it might seem easy to detect faults by observing these figures, it is actually a challenging task. This is because not all states are directly measurable, and the normal model isn't completely certain. Besides measurement uncertainty, we also have uncertainties in the initial conditions and parameter values. This means that for a certain period, the deviation in the trajectory could be explained as a result of model uncertainty, making practical fault detection difficult.

In the context of set-based estimation, strategies that can provide a more precise estimation of the sets defined in the prediction-update algorithm, like CZs, can help alleviate this problem and lead to earlier fault detection.

Finally, let's assess how well our proposed method performs in detecting faults and compare it to the performance of intervals and CZs. In Figure 7.4, we visualize the output space, which includes measurements like V_t and T_s, for the case of Fault 1 (similar results were obtained for other cases). The red line represents the actual measurements from the cell, while the green and yellow areas represent interval sets and CZ sets, respectively. These sets are generated using a method called "mean value extension" (check Chapter 5) applied to the output function, utilizing predicted states $\bar{X}_k$ (see (7.4)). Interval sets, on the other hand, are computed by solving a constraint satisfaction problem and using the forward-backward algorithm. When the measurements from the system do not fall within these sets, we can detect a fault. The initial observation is that intervals tend to be overly cautious during the prediction step. This means their size, and consequently the range of possible output values, increases as the simulation propagates, which makes fault detection practically impossible.

In terms of the time required to notice the fault, a study was carried out by

Fault	Magnitude	Detection time
Fault 1	$\Delta R_u = -30\%$	$4\ s$
Fault 2	$\Delta R_c = -30\%$	$6\ s$
Fault 1	$\Delta R_u = -45\%$	$3\ s$
Fault 2	$\Delta R_c = -45\%$	$5\ s$
Fault 3	$\Delta r = 0.01\ K$	$16\ s$
Fault 3	$\Delta r = 0.1\ K$	$6\ s$

TABLE 7.2: Time needed for the developed method to detect the fault.

altering the magnitude of the fault. The time at which the fault is found is shown in Table 7.2 (the resistive fault is expressed as a percentage of the base value). We can observe that the larger the problem, the faster it is detected. Refer to Scott et al., 2016a for a comparison of the calculation times of CZs and interval sets (and other set representations).

Remark 6 In Figure 7.3 the radius[1] of the output sets defined in (7.4), obtained using intervals and CZs, are depicted for every time instant within the time window $[0, 200]s$. As it can be noticed, the intervals explode over time. Investigating the reasons behind this issue, we can see that a significant expansion of the boundaries occurs for the component T_c during the prediction phase. This expansion happens because of the uncertainty in the system's parameters. While the update phase is supposed to reduce this uncertainty, intervals are only refined for the state components that directly affect the output equation (refer to Locatelli et al., 2021). Unfortunately, this doesn't apply to T_c, and as a result, it remains unrefined, leading to the same estimation in both closed-loop and open-loop cases. A poor estimation of T_c has a considerable impact on the estimation of other sets as well. This situation makes it impossible to detect the fault using the interval method. If the set is large, the measurement will always be consistent with the prediction (i.e., it will fall within the set), making fault detection unfeasible.

7.4 Three cells in series numerical results

Before showing in detail the numerical part of this three cells in series application it is important to put the explanation in the right context, explaining the thermal model of a series of three cells and the appropriate modifications made to the model to reduce conservatism

7.4.1 Thermal model

The cell thermal model is a two state system, that includes, for each cell, core and surface temperature as proposed in Lin et al., 2014 and as it has been explained for

---

[1] This is computed as half the length of the longest edge of the interval hull, as in Scott et al., 2016a.

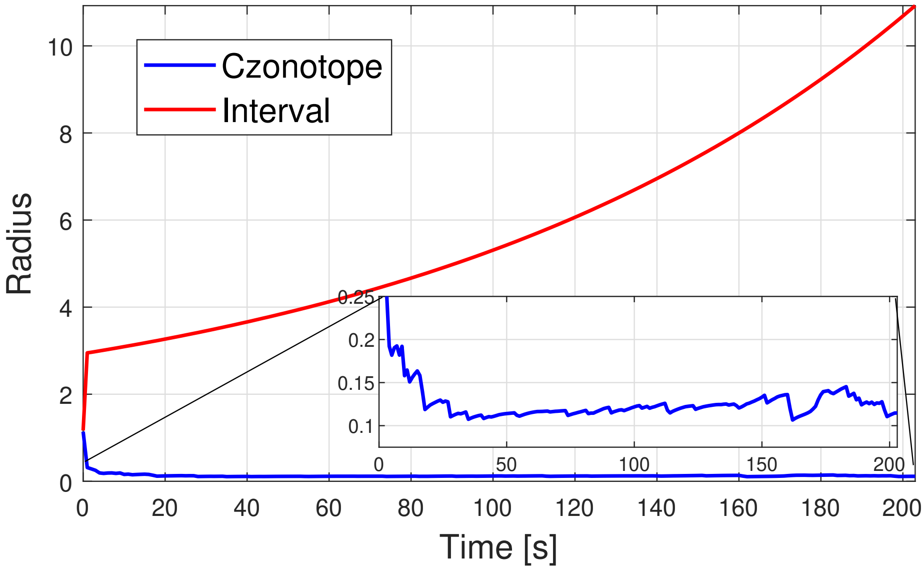

FIGURE 7.3: Comparison between radii of interval and CZ on the output (Fault 1).

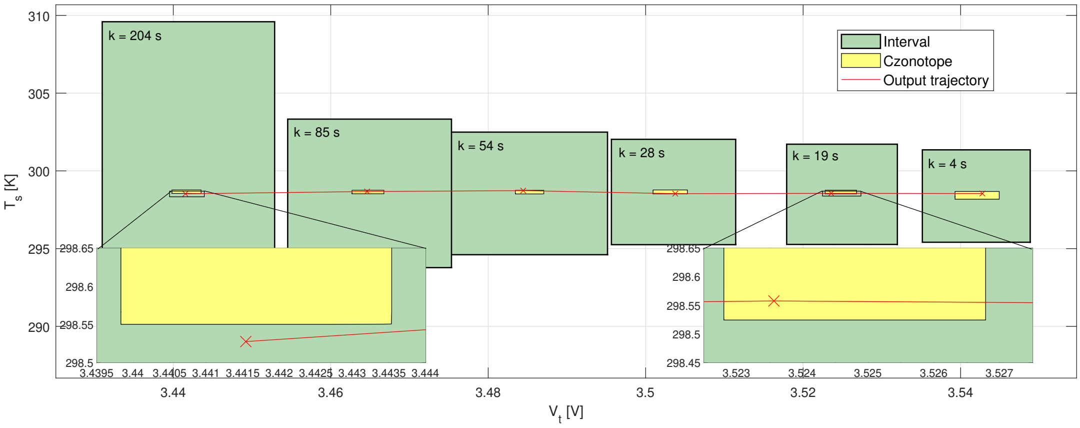

FIGURE 7.4: Comparison between interval and CZ on output trajectories (Fault 1).

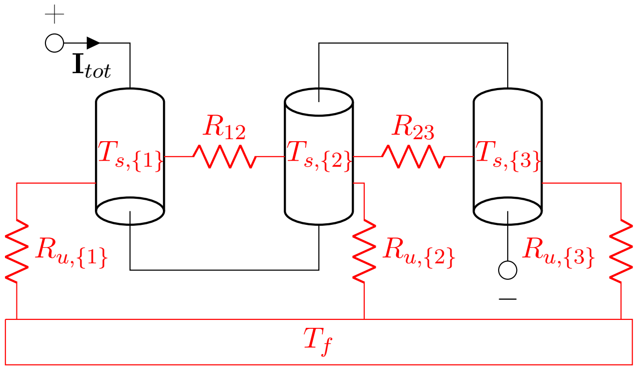

FIGURE 7.5: Series-connected cells with thermal resistances.

the single cell early in this thesis in Section 3.2.4:

$$\begin{aligned}\dot{T}_{c,\{i\}}(t) &= \frac{|I(t)||(V_{1,\{i\}}(t)+V_{2,\{i\}}(t)+R_{0,\{i\}}I(t))|}{C_{c,\{i\}}} \\ &\quad +\frac{T_{s,\{i\}}(t)-T_{c,\{i\}}(t)}{R_{c,\{i\}}C_{c,\{i\}}}, \qquad (7.8)\end{aligned}$$

$$\begin{aligned}\dot{T}_{s,\{i\}}(t) &= -\frac{T_{s,\{i\}}(t)-T_{\text{sink}}(t)}{R_{\text{sink},\{i\}}C_{s,\{i\}}}-\frac{T_{s,\{i\}}(t)-T_{c,\{i\}}(t)}{R_{c,\{i\}}C_{s,\{i\}}} \\ &\quad +\sum_{i\neq j}\frac{T_{s,\{j\}}(t)-T_{s,\{i\}}(t)}{R_{ij}C_{s,\{i\}}}. \qquad (7.9)\end{aligned}$$

Equation (7.8) considers both the generation of heat within the cell and the transfer of heat between its core and surface. In this equation, $C_{c,\{i\}}$ and $R_{c,\{i\}}$ represent the thermal capacity of the core and the thermal resistance between the core and the cell's surface, respectively.

Equation (7.9) accounts for heat exchange involving the cell's surface with three components: i) the core, ii) a liquid coolant (at temperature $T_{\text{sink}}(t)$), and iii) other adjacent cells. In this equation, $R_{\text{sink},\{i\}}$, R_{ij}, and $C_{s,\{i\}}$ correspond to the thermal resistance between the cell's surface and the coolant, the thermal resistance between adjacent cells, and the thermal capacity of the cell's surface, respectively.

The dynamics of the coolant are described by:

$$\dot{T}_{\text{sink}}(t)=\sum_{i=1}^{N}\frac{T_{s,\{i\}}(t)-T_{\text{sink}}(t)}{R_{\text{sink},\{i\}}C_{\text{sink}}}-\frac{\zeta(t)}{C_{\text{sink}}}, \qquad (7.10)$$

where C_{sink} represents the thermal capacity of the coolant, and $\zeta(t)$ signifies the thermal power released by the coolant to the external environment. Figure 7.5 illustrates the series-connected configuration discussed in this paper, along with the thermal resistances. Electrical components are shown in black, while thermal components are depicted in red. In the thermal aspect of the system, we assume a practical scenario where only one thermal sensor measurement, $T_{s,\{i\}}(t)$, from one cell is available. In order to better capture the dynamical behaviour of the battery pack, we introduce a dependency of the resistive and capacitive elements of each cell from SOC and temperature as introduced in Section 3.2.5.

7.4.2 Model adaptation for set-based fault detection

To mitigate the conservativeness resulting from the application of the mean value theorem in the set-based estimation procedure, the following approach is employed: after discretizing the model using Forward Euler's method with a sampling time t_s, the uncertain electrical and thermal parameters in the system equations

$$\begin{aligned}\dot{V}_{1,\{i\}}(t) &= -\frac{V_{1,\{i\}}(t)}{R_{1,\{i\}}C_{1,\{i\}}} + \frac{I(t)}{C_{1,\{i\}}}, && (7.11)\\ \dot{V}_{2,\{i\}}(t) &= -\frac{V_{2,\{i\}}(t)}{R_{2,\{i\}}C_{2,\{i\}}} + \frac{I(t)}{C_{2,\{i\}}}, && (7.12)\\ \dot{z}_{\{i\}}(t) &= \frac{I(t)}{3600C_{\mathrm{batt},\{i\}}}. && (7.13)\end{aligned}$$

taken from Section 3.2.2 and (7.8)-(7.10) have been replaced with their reciprocals which are denoted by $Y_{\{\cdot\}}$. Regarding the electrical parameters, to maintain the dependency of $Y_{\{\cdot\}}$ on temperature and SOC, we utilized fourth-degree polynomial expressions of the following form for each cell

$$\begin{aligned}&p_{00} + p_{10}\cdot z + p_{01}\cdot T_c + p_{20}\cdot z^2 + p_{11}\cdot z\cdot T_c + p_{02}\cdot T_c^2 +\\ &p_{30}\cdot z^3 + p_{21}\cdot z^2\cdot T_c + p_{12}\cdot z\cdot y^2 + p_{03}\cdot T_c^3 + p_{40}\cdot z^4 +\\ &p_{31}\cdot z^3\cdot T_c + p_{22}\cdot z^2\cdot T_c^2 + p_{13}\cdot z\cdot T_c^3 \qquad (7.14)\end{aligned}$$

whose nominal coefficients for the electrical parameters were determined through a fitting procedure applied to the curves $1/C_j$ and $1/R_jC_j$, where $j \in \{1,2\}$.

The resulting discretized system, assuming a series-connected configuration of $N = 3$ cells, can be summarized as shown in (7.15), where $\mathbf{x} = \begin{bmatrix}\mathbf{x}_{\{1\}} & \mathbf{x}_{\{2\}} & \mathbf{x}_{\{3\}} & x_6\end{bmatrix}$ comprises the state variables for each cell, with $\mathbf{x}_{\{i\}} = \begin{bmatrix}V_{1,\{i\}} & V_{2,\{i\}} & z_{\{i\}} & T_{c,\{i\}} & T_{s,\{i\}}\end{bmatrix}$. Here, x_6 represents the coolant temperature T_{sink}. Notably, ζ is set to zero, simulating an active cooling system where a fan engages only when T_{sink} exceeds a specific threshold. In this case, we assume that the threshold is never reached. The input u signifies the input current I. To account for fitting errors, measurement noise, and uncertainties stemming from the identification procedure for both thermal and electrical parameter values, the model incorporates additive parameter uncertainties denoted as $w_{\{\cdot\}}$. Finally, the system output, denoted as $\mathbf{y} = [y_1 \quad y_2]$, includes $V_t(t)$ and $T_{s,\{2\}}$, representing the surface temperature of the second cell, which is assumed to be the only measured variable. Please note that the outputs are considered to be affected by measurement noise v. In the following, both parameter and measurement noise will be regarded as unknown but bounded.

$$\begin{cases} x_{1,\{i\}}(k+1) = x_{1,\{i\}}(k) - t_s\left[(Y_{R_1C_1}+w_{R_1C_1})\cdot x_{1,\{i\}}(k) + (Y_{C_1}+w_{C_1})u(k)\right], \\ x_{2,\{i\}}(k+1) = x_{2,\{i\}}(k) - t_s\left[(Y_{R_2C_2}+w_{R_2C_2})\cdot x_{2,\{i\}}(k) + (Y_{C_2}+w_{C_2})u(k)\right], \\ x_{3,\{i\}}(k+1) = x_{3,\{i\}}(k) + t_s(Y_{C_{\text{batt}}}+w_{C_{\text{batt}}})u(k), \\ x_{4,\{i\}}(k+1) = x_{4,\{i\}}(k) + t_s\left[(Y_{C_c}+w_{C_c})|u(k)|(x_{1,\{i\}}(k)+ + x_{2,\{i\}}(k)\right. \\ \qquad +(R_{0,\{i\}}+w_{R_{0,\{i\}}})u(k)| + (Y_{R_c}+w_{R_c})\cdot \\ \qquad \cdot(Y_{C_c}+w_{C_c})(x_{5,\{i\}}(k)-x_{4,\{i\}}(k))], \\ x_{5,\{i\}}(k+1) = x_{5,\{i\}}(k) + t_s[(Y_{R_{\text{sink}}}+w_{R_{\text{sink}}})(Y_{C_s}+w_{C_s})(x_6(k)-x_{5,\{i\}}(k)) \\ \qquad + (Y_{R_c}+w_{R_c})(Y_{C_s}+w_{C_s})(x_{4,\{i\}}(k)-x_{5,\{i\}}(k)) \\ \qquad + \sum_{i\neq j}(Y_{R_{ij}}+w_{R_{ij}})(Y_{C_s}+w_{C_s})\cdot(x_{5,\{j\}}(k)-x_{5,\{i\}}(k))], \\ x_6(k+1) = x_6(k) \\ \qquad +t_s[\,(Y_{R_{\text{sink}}}+w_{R_{\text{sink}}})(Y_{C_{\text{sink}}}+w_{C_{\text{sink}}})\cdot\sum_{i=1}^{3}(x_{5,\{i\}}(k)-x_6(k))], \\ y_1(k) = \sum_{i=1}^{3} V_{\text{OCP},\{i\}}(x_{3,\{i\}}(k))x_{1,\{i\}}(k) + x_{2,\{i\}}(k) \\ \qquad +(R_{0,\{i\}}+w_{R_{0,\{i\}}})u(k) + v_1(k), \\ y_2(k) = x_{5,\{2\}}(k) + v_2(k), \end{cases} \tag{7.15}$$

7.4.3 Numerical results

In the following section, we evaluate the effectiveness of CZs in detecting faults, as described earlier in this chapter. The parameter values used are sourced from the literature (refer to Lin et al., 2014). Nominal values and uncertainties for both thermal and electrical parameters are presented in Tables 7.3 and 7.4.

The initial state set for each individual cell, denoted as $\bar{X}_{0,\{i\}}$, is represented as a zonotope described in G-rep by:

$$X_{0,\{i\}} = \left\{ \begin{bmatrix} 0.005 \\ 0.005 \\ 0.5 \\ 303.15 \\ 303.15 \end{bmatrix}, \ \text{diag}\begin{bmatrix} 0.0005 \\ 0.0005 \\ 0.0125 \\ 1 \\ 1 \end{bmatrix} \right\}, \tag{7.16}$$

where for T_{sink} (i.e., x_6), the initial temperature was set to $293.15K \pm 0.25K$.

As observed, we have assumed identical parameter values and initial conditions for each cell. Nevertheless, the fault detection strategy can be readily extended to the more realistic scenario where inherent differences exist.

The output measurements are affected by noise $v \in V$ with

$$V = \left\{\begin{bmatrix}0 & 0\end{bmatrix}, \ \text{diag}\begin{bmatrix}0.001 & 0.1\end{bmatrix}\right\}. \tag{7.17}$$

Please note that, in this specific example, we assumed that the temperature sensor is located on the surface of cell 2. In this case, the process disturbance $\mathbf{w}$ corresponds to the parametric uncertainty.

Parameter	**Center**	**Unit**	**Uncertainty**	**Value**
C_{batt}	2.3	Ah	$w_{C_{\text{batt}}}$	± 0.0115
Y_{R_c}	0.5155	WK^{-1}	w_{R_c}	± 0.0026
$Y_{R_{\text{sink},\{2\}}}$	0.3135	WK^{-1}	$w_{R_{\text{sink},\{2\}}}$	± 0.0016
$Y_{R_{\text{sink},\{1\},\{3\}}}$	0.0544	WK^{-1}	$w_{R_{\text{sink},\{1\},\{3\}}}$	$\pm 2.72{\cdot}10^{-4}$
$Y_{R_{ij}}$	0.1	WK^{-1}	$w_{R_{ij}}$	± 0.05
Y_{C_c}	0.0159	KJ^{-1}	w_{C_c}	$\pm 7.97{\cdot}10^{-5}$
Y_{C_s}	0.2222	KJ^{-1}	w_{C_s}	± 0.0011

Table 7.3: Model parameters

Uncertainty	**Unit**	**Value**
w_{R_0}	Ω^{-1}	$\pm 5 \cdot 10^{-5}$
$w_{R_1C_1}$	$(As\ \Omega)^{-1}$	$\pm 1.15 \cdot 10^{-4}$
$w_{R_2C_2}$	$(As\ \Omega)^{-1}$	$\pm 3.5 \cdot 10^{-6}$
w_{C_1}	$(As)^{-1}$	$\pm 2.381 \cdot 10^{-6}$
w_{C_2}	$(As)^{-1}$	$\pm 7.143 \cdot 10^{-8}$

Table 7.4: Parameter uncertainties

The thermal capacity of the coolant has been set to $C_{\text{sink}} = 4186\,JK^{-1}$. The coefficients for the polynomial expression of $V_{\text{OCP},\{i\}}(t)$ can be found in Section 3.2.3. These coefficients were obtained through interpolation of the curve provided in Lin et al., 2014.

Measurement data were gathered by simulating (7.15) with the initial state $\mathbf{x}_0$ randomly selected from X_0. Both parameter and measurement disturbances were generated following uniform random distributions.

The known input profile consists of a constant discharging current: $I(k) = -2.3$ A for all $k \geq 0$.

For each of the faults described in early in this section, two different magnitudes have been considered. Fault 1 was introduced with values $\Delta r_{\{i\}} = 0.1\ K/s$ and $\Delta r_{\{i\}} = 0.2\ K/s$, while faults 2 and 3 were introduced with $\Delta R_{\text{sink},\{i\}} = 100\%$, $\Delta R_{\text{sink},\{i\}} = 250\%$, $\Delta R_{c,\{i\}} = 70\%$, and $\Delta R_{c,\{i\}} = 250\%$.

For all these cases, it is assumed that the fault occurs 10 seconds after the start of the simulation. Three different set representations are used, and their performance is compared:

- Constrained zonotopes with a maximum number of generators and constraints set to $n_{g,\max} = 312$ and $n_{c,\max} = 40$. This method is denoted as CZ(40,17) (the order is determined as 17 based on the order definition explained in Chapter 4).
- Zonotopes obtained using the constrained zonotopic method described in Rego et al., 2021a, combined with a reduction of constraints to zero. To maintain the same complexity as CZ(40,17), the maximum number of generators is set to $n_{g,\max} = 272$. This approach is labeled as CZ(0,17).
- c) Zonotopes, denoted as Z(17), where $n_{g,\max} = 272$ is imposed to achieve the same complexity order as the other methods. These are obtained by applying the state estimation strategy from Alamo et al., 2008.

In the following examples, we assume that the fault always occurs in cell 1, while the sensor is centrally located on cell 2. Figure 7.6 displays the state trajectories of

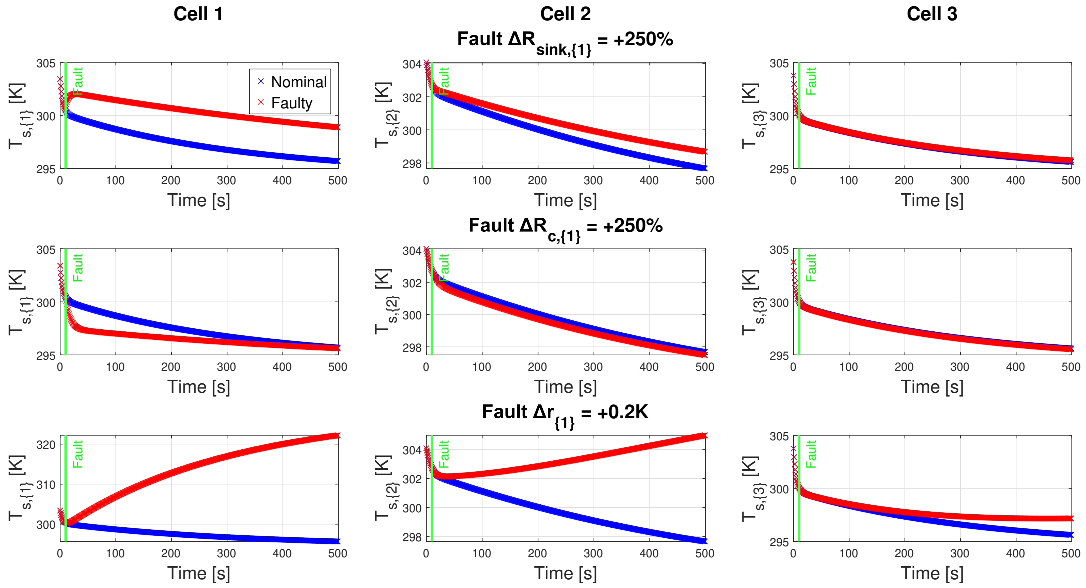

FIGURE 7.6: Comparison between nominal (blue) and faulty (red) thermal states for each cell and for all three types of faults presented. Green line represents the fault injection time (k=10).

$T_{s,\{i\}}(t)$ for all the cells in the presence of different types of faults. The fault is injected into cell 1. The blue trajectory represents the nominal behavior without any faults, while the red line depicts the state trajectory in the presence of a fault. It is important to note that even though the cells are thermally interconnected, if a fault occurs in cell 1, it may be challenging to detect it when the sensor is placed on cell 3. In this case, an effective state estimation strategy would need also an optimal positioning of the sensor.

Figure 7.7 displays the projected sets $\hat{X}_k$ at $k = 18$ for the T_c and T_s components, obtained using the three different set-based strategies. It is important to analyze this figure in conjunction with Table 7.2, which lists the time of fault detection. CZ(40,17), shown in magenta, proves to be the most effective strategy when compared to CZ(0,17) (in yellow) and Z(17) (in grey). Specifically, CZ(0,17) sometimes fails to detect the fault, and Z(17) is consistently ineffective. CZ(40,17) provides tighter enclosures, which have the advantage of identifying cases where sets of states that are initially consistent with the measurements become inconsistent with the model and disturbances sooner. Another way to compare the performance of our proposed approach with other set-based methods is by examining the radii of the enclosures. Figure 7.8 presents the radii, computed as the sum of the absolute values of all the edges of the interval hull (using the 1-norm), of the sets $\hat{X}_k$ for $k \geq 0$.

This figure illustrates the advantage of using (CZs), even with zero constraints, over zonotopes for state estimation and, consequently, fault detection. It shows that CZs provide tighter and more effective enclosures across all state components.

7.5 Conclusions

In this chapter, we have explored an approach to capture the dynamic behavior of lithium cells and battery packs and enhance fault detection capabilities. Our primary goal was to develop a robust model adaptation for set-based fault detection in battery systems. Several key findings and insights emerge from our investigation.

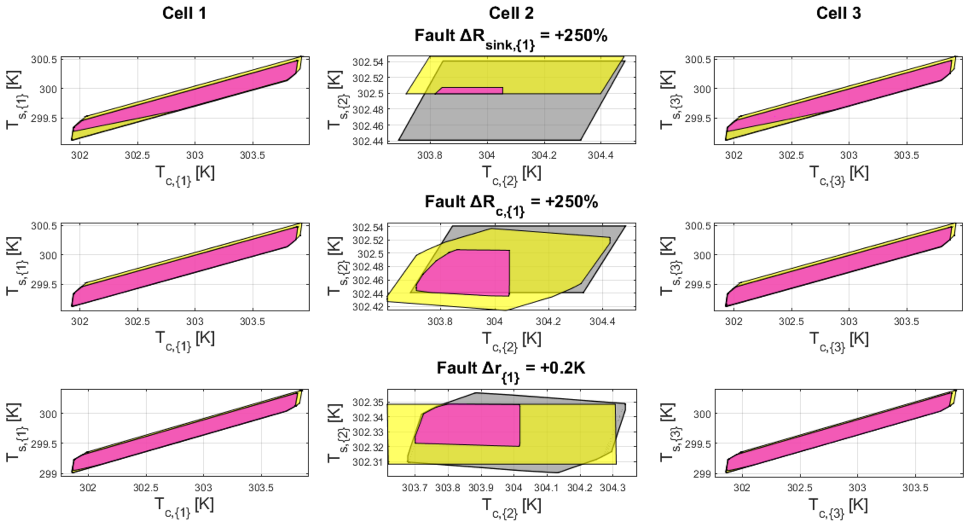

FIGURE 7.7: Comparison between CZ(40,17) (magenta), CZ(0,17) (yellow) and Z(17) (grey) on thermal states. The first two faults refers to $k = 15$, while the last one to $k = 18$. The fault is injected in cell 1 and the sensor is placed on cell 2.

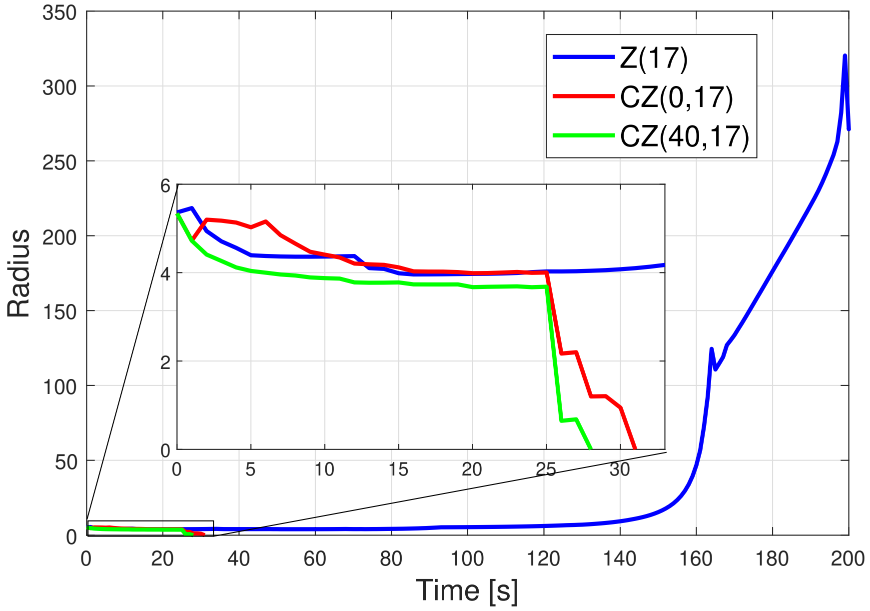

FIGURE 7.8: Comparison between radii of CZ(40,17), CZ(0,17) and Z(17) on the states for fault $\Delta r_{\{1\}} = +0.2\ K$.

A model adaptation technique has been introduced that accounts for the dynamical behavior of battery packs. This approach incorporates dependencies of resistive and capacitive elements of each cell on state of charge (SOC) and temperature, providing a more accurate representation of real-world battery behavior. We discretized the model using Forward Euler's method with a specified sampling time, enabling a practical implementation.

To ensure the model's reliability under real-world conditions, uncertainties originating from various sources has been addressed, including fitting errors, measurement noise, and identification procedure uncertainties for both thermal and electrical parameters. Our model incorporated these uncertainties as additive parameter uncertainties, allowing for more robust fault detection.

A thorough evaluation of set-based fault detection strategies has been conducted, with a focus on Constrained Zonotopes (CZs). We compared the performance of CZs with other set representations, namely CZ(0,17) and Zonotopes (Z(17)), using a series-connected configuration of battery cells.

Our results reveale that CZ outperforms the alternative approaches in fault detection, while Zonotopes consistently exhibits ineffectiveness. CZs provide tighter enclosures, allowing for the early identification of cases where sets of states initially consistent with measurements became inconsistent with the model and disturbances.

Our research provides a promising foundation for enhancing the fault detection capabilities of battery systems. Future work could focus on optimizing sensor placement for improved fault detection, extending the approach to handle diverse battery pack configurations, and considering additional sources of uncertainty for a comprehensive fault detection framework.

In conclusion, our findings underscore the significance of model adaptation and the superiority of Constrained Zonotopes (CZs) in set-based fault detection for battery packs.

Chapter 8

Joint state and parameter estimation

This chapter introduces an approach for simultaneously estimating the states and parameters of nonlinear discrete-time systems using set-based methods. The foundation of this approach builds upon the algorithms outlined in Chapter 5. By expanding upon the techniques for nonlinear state estimation through the incorporation of constrained zonotopes for parameter estimation within a cohesive framework, we preserve the inherent interdependencies between states, algebraic variables, and unknown parameters. This enhancement leads to a substantial improvement in the accuracy of both state and parameter estimation. The structure of this chapter is as follows: We begin by introducing the state of the art for what concerns the joint state and parameter estimation. Then the class of discrete-time systems under consideration is described in Section 8.1, along with the framework for our proposed estimator. Following this, we focus on the development of the method for set-based joint state and parameter estimation, leveraging the power of constrained zonotopes. This section serves as the heart of our approach, offering insight into how we unify the estimation of states and parameters. To demonstrate the effectiveness and practicality of our approach, we showcase a series of numerical examples in Section 8.2. These examples span various scenarios, including both linear and nonlinear discrete-time systems. Finally, Section 8.3 serves as the concluding segment of this chapter, summarizing the key findings and implications of our approach for the joint estimation of states and parameters within discrete-time systems.

8.1 Joint state and parameter estimation

Before going into the details of joint state and parameters estimation, Let summarize the set-based prediction-update structures proposed in Scott et al., 2016b and Rego et al., 2020b and explained in this thesis in Chapter 5. The following notions will be useful for the development of the method proposed in this Chapter. Consider a linear discrete-time system with time k, state $\mathbf{x}_k \in \mathbb{R}^n$, input $\mathbf{u}_k \in \mathbb{R}^{n_u}$, process disturbances $\mathbf{w}_k \in \mathbb{R}^{n_w}$, measured output $\mathbf{y}_k \in \mathbb{R}^{n_y}$, and measurement disturbances $\mathbf{v}_k \in \mathbb{R}^{n_v}$. In each time interval $[k-1, k]$, $k = 1, 2, \ldots$, the system evolves according to the model

$$\begin{aligned} \mathbf{x}_k &= \mathbf{A}\mathbf{x}_{k-1} + \mathbf{B}\mathbf{u}_{k-1} + \mathbf{B}_w\mathbf{w}_{k-1}, \\ \mathbf{y}_k &= \mathbf{C}\mathbf{x}_k + \mathbf{D}\mathbf{u}_k + \mathbf{D}_v\mathbf{v}_k, \end{aligned} \tag{8.1}$$

with $\mathbf{A} \in \mathbb{R}^{n\times n}$, $\mathbf{B} \in \mathbb{R}^{n\times n_u}$, $\mathbf{B}_w \in \mathbb{R}^{n\times n_w}$, $\mathbf{C} \in \mathbb{R}^{n_y\times n}$, $\mathbf{D} \in \mathbb{R}^{n_y\times n_u}$, and $\mathbf{D}_v \in \mathbb{R}^{n_y\times n_v}$. The disturbances are assumed to be bounded, i.e., $\mathbf{w}_k \in W$ and $\mathbf{v}_k \in V$, where W and V are known polytopes representable as CZ.

Given an initial condition $\mathbf{x}_0 \in \bar{X}_0$, the prediction-update algorithm consists in computing sets $\bar{X}_k$ and $\hat{X}_k$ such that

$$\begin{aligned}\bar{X}_k \supseteq \{&\mathbf{A}\mathbf{x}_{k-1} + \mathbf{B}\mathbf{u}_{k-1} + \mathbf{B}_w \mathbf{w}_{k-1} : \\ &\qquad \mathbf{x}_{k-1} \in \hat{X}_{k-1},\, \mathbf{w}_{k-1} \in W\}, \end{aligned} \tag{8.2}$$

$$\hat{X}_k \supseteq \{\mathbf{x}_k \in \bar{X}_k : \mathbf{C}\mathbf{x}_k + \mathbf{D}\mathbf{u}_k + \mathbf{D}_v \mathbf{v}_k = \mathbf{y}_k,\, \mathbf{v}_k \in V\}, \tag{8.3}$$

in which (8.2) is referred to as the prediction step, and (8.3) as the update step, with the scheme initialized in the update step ($k = 0$).

Both the prediction and update steps can be computed using CZs, according to Scott et al., 2016b

$$\bar{X}_k = \mathbf{A}\hat{X}_{k-1} \oplus \mathbf{B}_u \mathbf{u}_{k-1} \oplus \mathbf{B}_w W, \tag{8.4}$$

$$\hat{X}_k = \bar{X}_k \cap_{\mathbf{C}} ((\mathbf{y}_k - \mathbf{D}_u \mathbf{u}_k) \oplus (-\mathbf{D}_v V)). \tag{8.5}$$

On the other side, if in each time interval $[k-1, k]$, $k = 1, 2, \ldots$, the system evolves according to $\mathbf{x}_k = \mathbf{f}(\mathbf{x}_{k-1}, \mathbf{u}_{k-1}, \mathbf{w}_{k-1})$, where the nonlinear function $\mathbf{f} : \mathbb{R}^n \times \mathbb{R}^{n_u} \times \mathbb{R}^{n_w} \to \mathbb{R}^n$ is of class $\mathcal{C}^1$, then the prediction step is defined by $\bar{X}_k \supseteq \{\mathbf{f}(\mathbf{x}_{k-1}, \mathbf{u}_{k-1}, \mathbf{w}_{k-1}) : \mathbf{x}_{k-1} \in \hat{X}_{k-1},\, \mathbf{w}_{k-1} \in W\}$, while the update step (assuming linear output equation) is given by (8.3). In this case, the prediction-update steps can be conputed according to what has been described in Section 5.3 and 5.4 respectively. In the remainder of this section we will describe the joint state and parameter estimation for both linear and nonlinear cases.

8.1.1 Linear systems

Consider a linear discrete-time system with unknown-but-bounded disturbances and model parameters, given by

$$\mathbf{x}_k = \mathbf{A}\mathbf{x}_{k-1} + \mathbf{B}\mathbf{u}_{k-1} + \mathbf{B}_p \mathbf{p} + \mathbf{B}_w \mathbf{w}_{k-1}, \tag{8.6a}$$

$$\mathbf{y}_k = \mathbf{C}\mathbf{x}_k + \mathbf{D}\mathbf{u}_k + \mathbf{D}_p \mathbf{p} + \mathbf{D}_v \mathbf{v}_k. \tag{8.6b}$$

with $\mathbf{x}_k \in \mathbb{R}^n$ the system state, while $\mathbf{u}_k \in \mathbb{R}^{n_u}$ is the known input, $\mathbf{w}_k \in \mathbb{R}^{n_w}$ are the process disturbances, $\mathbf{y}_k \in \mathbb{R}^{n_y}$ is the measured output, $\mathbf{v}_k \in \mathbb{R}^{n_v}$ is the measurement disturbances, and $\mathbf{p} \in \mathbb{R}^{n_p}$ are the unknown parameters. In addition, $\mathbf{A} \in \mathbb{R}^{n \times n}$, $\mathbf{B} \in \mathbb{R}^{n \times n_u}$, $\mathbf{B}_p \in \mathbb{R}^{n \times n_p}$, $\mathbf{B}_w \in \mathbb{R}^{n \times n_w}$, $\mathbf{C} \in \mathbb{R}^{n_y \times n}$, $\mathbf{D} \in \mathbb{R}^{n_y \times n_u}$, $\mathbf{D}_d \in \mathbb{R}^{n_y \times n_p}$, and $\mathbf{D}_v \in \mathbb{R}^{n_y \times n_v}$. The initial state, model parameters, and disturbances are assumed to be unknown-but-bounded, i.e., $(\mathbf{x}_0, \mathbf{p}, \mathbf{w}_k, \mathbf{v}_k) \in X_0 \times P \times W \times V$, $\forall k \geq 0$, where X_0, P, W, and V are polytopes representable as CZs.

For any $k \geq 0$, the goal is to find the best possible approximation for the set of solutions consisting of both $\mathbf{x}_k$ and $\mathbf{p}$ as defined in (8.6). This approximation should be enclosed within a set denoted as $\hat{Z}_k$, which is a guaranteed region in $\mathbb{R}^{n+n_p}$ containing the pairs $(\mathbf{x}_k, \mathbf{p})$.

In this context, we achieve this goal by expanding upon the prediction-update method introduced in Scott et al., 2016a, adapting it to a unified framework for both state and parameter estimation. We specifically focus on enhancing the precision of our understanding of the uncertain parameters $\mathbf{p} \in P$. Our approach involves employing the subsequent iterative process

$$\begin{aligned}\bar{Z}_k \supseteq \{(\mathbf{A}\mathbf{x}_{k-1} + \mathbf{B}\mathbf{u}_{k-1} + \mathbf{B}_p\mathbf{p} + \mathbf{B}_w\mathbf{w}_{k-1}, \mathbf{p}) :& \\ (\mathbf{x}_{k-1}, \mathbf{p}) \in \hat{Z}_{k-1},\ \mathbf{w}_{k-1} \in W\},& \qquad (8.7)\end{aligned}$$

$$\begin{aligned}\hat{Z}_k \supseteq \{(\mathbf{x}_k, \mathbf{p}) \in \bar{Z}_k :& \\ \mathbf{C}\mathbf{x}_k + \mathbf{D}_u\mathbf{u}_k + \mathbf{D}_p\mathbf{p} + \mathbf{D}_v\mathbf{v}_k = \mathbf{y}_k,\ \mathbf{v}_k \in V\},& \qquad (8.8)\end{aligned}$$

with (8.7) the *joint prediction step*, (8.8) the *joint update step*, and the scheme is initialized with $\bar{Z}_0 \triangleq \bar{X}_0 \times P$ in the joint update step. If $\hat{Z}_{k-1}$ is a effective enclosure of $(\mathbf{x}_{k-1}, \mathbf{p})$ for some $k \geq 1$, then $(\mathbf{x}_k, \mathbf{p}) \in \bar{Z}_k$ given by (8.7). Through its structure, this leads to $(\mathbf{x}_k, \mathbf{p}) \in \hat{Z}_k$ from (8.8).

Exact enclosures for the joint prediction step (8.7) and joint update step (8.8)Can be acquired easily using CZs. Given the assumption that the unknown parameters $\mathbf{p}$ remain constan, i.e., $\mathbf{p}_k = \mathbf{p}_{k-1}$, Consequently, the prediction and update steps can be determined in CG-rep by specifying $\mathbf{z}_k \triangleq (\mathbf{x}_k, \mathbf{p})$, and expanding (8.4) and (8.5) to the unified structure

$$\bar{Z}_k = \begin{bmatrix} \mathbf{A} & \mathbf{B}_p \\ \mathbf{0} & \mathbf{I} \end{bmatrix} \hat{Z}_{k-1} \oplus \mathbf{B}_u\mathbf{u}_{k-1} \oplus \mathbf{B}_w W, \qquad (8.9)$$

$$\hat{Z}_k = \bar{Z}_k \cap_{[\mathbf{C}\ \mathbf{D}_p]} ((\mathbf{y}_k - \mathbf{D}_u\mathbf{u}_k) \oplus (-\mathbf{D}_v V)). \qquad (8.10)$$

Please note that the enclosure of the parameters $\mathbf{p}$ becomes more precise over time through the proposed joint update step (8.10). Furthermore, similar to linear state estimation using CZs, all the operations in (8.9)-(8.10) can be easily executed with reference to (4.8)-(4.10), resulting in a linear increase in complexity concerning the number of generators and constraints. Additionally, the connection between the system states $\mathbf{x}_k$ and the model parameters $\mathbf{p}$ remains consistent across consecutive time steps thanks to the employed framework. Moreover, the enclosures in (8.9)-(8.10) are exact when the set's complexity is not restricted. In practice, due to limited computational resources, techniques for reducing complexity, as described in Scott et al., 2016b, are applied to enclose the sets $\bar{Z}_k$ and $\hat{Z}_k$ using CZs while aiming for a specific, lower number of generators and constraints.[1]

Note that the linear method for jointly estimating the system states and parameters as outlined in (8.9)-(8.10) is applicable solely when the system exhibits linearity in both its states and parameters. It should not be employed when the parameters $\mathbf{p}$ are involved in any of the system matrices, as is the case, for example, when $\mathbf{A} \triangleq \mathbf{A}(\mathbf{p})$. In such situations, it is advisable to opt for the nonlinear approach detailed in Section 8.1.2 instead.

8.1.2 Nonlinear systems with linear output equation

Let consider a class of nonlinear discrete-time system with bounded uncertainties, evolving according to the dynamics

$$\mathbf{x}_k = \mathbf{f}(\mathbf{x}_{k-1}, \mathbf{u}_{k-1}, \mathbf{p}, \mathbf{w}_{k-1}), \qquad (8.11)$$

and featuring a linear output equation (8.6b), with the nonlinear function $\mathbf{f} : \mathbb{R}^n \times \mathbb{R}^{n_u} \times \mathbb{R}^{n_p} \times \mathbb{R}^{n_w} \to \mathbb{R}^n$ assumed to be of class $\mathcal{C}^1$. The initial state, model parameters, and disturbances are assumed to be unknown-but-bounded, i.e., $(\mathbf{x}_0, \mathbf{p}, \mathbf{w}_k, \mathbf{v}_k) \in$

---

[1] This strategy is also relevant in state estimation and maintains the connection between states and parameters, offering advantages over interval-based methods.

$X_0 \times P \times W \times V$, $\forall k \geq 0$, where X_0, P, W, and V are polytopes representable as CZs.

Just like in the linear scenario presented in (8.6), the aim here is to accurately enclosure the trajectories of (8.11) using a set $\hat{Z}_k \subset \mathbb{R}^{n+n_p}$ for all $k \geq 0$. To achieve this, we extend the approach introduced in Rego et al., 2021b to create a joint framework for state and parameter estimation. This framework enables us to refine the enclosure of parameters P over time, all while maintaining the connections between states and parameters. The suggested prediction-update scheme is given by

$$\begin{aligned}\bar{Z}_k \supseteq \{(\mathbf{f}(\mathbf{x}_{k-1}, \mathbf{u}_{k-1}, \mathbf{p}, \mathbf{w}_{k-1}), \mathbf{p}) \\ : (\mathbf{x}_{k-1}, \mathbf{p}) \in \hat{Z}_{k-1},\, \mathbf{w}_{k-1} \in W\},\end{aligned} \tag{8.12}$$

as the joint prediction step, and by (8.8) as the joint update step (which remains linear). As in the previous case, the scheme is initialized with $\bar{Z}_0 \triangleq \bar{X}_0 \times P$ in the joint update step.

Initially, we expand the prediction approach outlined in Theorem 4 to encompass both state variables and model parameters within a broader context. This outcome will serve as a prerequisite for the subsequent development of the nonlinear joint state and parameter estimation technique in this section.

The following proposition furnishes an enclosure for the state $\mathbf{x}_k$ during the prediction phase outlined in (9.7). An approach to calculate an enclosure, denoted as $\bar{Z}_k$, for the augmented variable $(\mathbf{x}_k, \mathbf{p})$ that conforms to the joint prediction step is detailed in Corollary 1. This corollary is established through the findings of Proposition 8.

Proposition 8 (State prediction) Let $\mathbf{f} : \mathbb{R}^n \times \mathbb{R}^{n_u} \times \mathbb{R}^{n_p} \times \mathbb{R}^{n_w} \to \mathbb{R}^n$ be of class $\mathcal{C}^1$, and let $\nabla_x \mathbf{f}$ denote the gradient of $\mathbf{f}$ with respect to its first argument. Let $\mathbf{u} \in \mathbb{R}^{n_u}$, and let $X \subset \mathbb{R}^n$, $P \subset \mathbb{R}^{n_p}$, and $W \subset \mathbb{R}^{n_w}$ be CZs. Let $Z = X \times P$, and choose any $\boldsymbol{\gamma}_z = (\boldsymbol{\gamma}_x, \boldsymbol{\gamma}_p) \in \square X \times \square P$. If Z_w is a CZ such that $\mathbf{f}(\boldsymbol{\gamma}_x, \mathbf{u}, \boldsymbol{\gamma}_p, W) \subseteq Z_w$ and $\mathbf{J} \in \mathbb{IR}^{n \times n}$ is an interval matrix satisfying $\nabla_z^T \mathbf{f}(\square X, \mathbf{u}, \square P, W) \subseteq \mathbf{J}$, then $\mathbf{f}(X, \mathbf{u}, P, W) \subseteq Z_w \oplus \triangleleft(\mathbf{J}, Z - \boldsymbol{\gamma}_z)$.

Proof. Choose any $(\mathbf{x}, \mathbf{p}, \mathbf{w}) \in X \times P \times W$. Let $\mathbf{r} \triangleq (\mathbf{x}, \mathbf{p})$, $\boldsymbol{\gamma}_r \triangleq (\boldsymbol{\gamma}_x, \boldsymbol{\gamma}_p)$, $R \triangleq X \times P$. Lemma 1 in Rego et al., 2021b (with $\boldsymbol{\alpha} \triangleq \mathbf{f}$, $\mathbf{x} \triangleq \mathbf{r}$, $\boldsymbol{\gamma}_x \triangleq \boldsymbol{\gamma}_r$, and $X \triangleq R$) ensures that there exists a real matrix $\hat{\mathbf{J}} \in \mathbf{J}$ such that $\mathbf{f}(\mathbf{x}, \mathbf{u}, \mathbf{p}, \mathbf{w}) = \mathbf{f}(\boldsymbol{\gamma}_x, \mathbf{u}, \boldsymbol{\gamma}_p, \mathbf{w}) + \hat{\mathbf{J}}(\mathbf{z} - \boldsymbol{\gamma}_z)$, with $\mathbf{z} = (\mathbf{x}, \mathbf{p})$. By Theorem 2 and the choice of Z_w, it follows that $\mathbf{f}(\mathbf{x}, \mathbf{u}, \mathbf{p}, \mathbf{w}) \in Z_w \oplus \triangleleft(\mathbf{J}, Z - \boldsymbol{\gamma}_z)$, as desired. $\square$

Corollary 1 (Joint prediction) Let $\mathbf{f} : \mathbb{R}^n \times \mathbb{R}^{n_u} \times \mathbb{R}^{n_p} \times \mathbb{R}^{n_w} \to \mathbb{R}^n$ be of class $\mathcal{C}^1$, and let $\nabla_x \mathbf{f}$ denote the gradient of $\mathbf{f}$ with respect to its first argument. For $k \geq 1$, let $\mathbf{u}_{k-1} \in \mathbb{R}^{n_u}$, and assume that $\mathbf{z}_{k-1} = (\mathbf{x}_{k-1}, \mathbf{p}) \in \hat{Z}_{k-1} = \{\hat{\mathbf{G}}_{k-1}, \hat{\mathbf{c}}_{k-1}, \hat{\mathbf{A}}_{k-1}, \hat{\mathbf{b}}_{k-1}\}$. Moreover, let $\mathbf{w}_{k-1} \in W = \{\mathbf{G}_w, \mathbf{c}_w, \mathbf{A}_w, \mathbf{b}_w\}$, and $\mathbf{p} \in P$. Choose any $\boldsymbol{\gamma}_z = (\boldsymbol{\gamma}_x, \boldsymbol{\gamma}_p) \in \square \hat{Z}_{k-1}$. In addition, let $\mathbf{E} = [n_p n \;\; n_p]$. Let Z_w be a CZ such that $\mathbf{f}(\boldsymbol{\gamma}_x, \mathbf{u}_{k-1}, \boldsymbol{\gamma}_p, \mathbf{w}_{k-1}) \subseteq Z_w$ for all $\mathbf{w}_{k-1} \in W$, and let $\mathbf{J}_z \in \mathbb{IR}^{n \times n}$ be an interval matrix satisfying $\nabla_z^T \mathbf{f}(\mathbf{x}_{k-1}, \mathbf{u}_{k-1}, \mathbf{p}, \mathbf{w}_{k-1}) \subseteq \mathbf{J}_z$ for all $(\mathbf{x}_{k-1}, \mathbf{p}) \in \square \hat{Z}_{k-1}$, $\mathbf{w}_{k-1} \in W$, and $\mathbf{H} \triangleq \text{mid}(\mathbf{J}_z)$. If $\{\underline{\hat{\mathbf{G}}}, \underline{\hat{\mathbf{c}}}\}$ is a zonotope with $\underline{n}_g$ generators satisfying $\hat{Z}_{k-1} - \boldsymbol{\gamma}_z \subseteq \{\underline{\hat{\mathbf{G}}}, \underline{\hat{\mathbf{c}}}\}$, $\mathbf{m} \triangleq (\mathbf{J}_z - \text{mid}(\mathbf{J}_z))\underline{\hat{\mathbf{c}}} \in \mathbb{IR}^n$, and $\hat{\mathbf{P}} \in \mathbb{R}^{n \times n}$ is a diagonal matrix with $\hat{P}_{ii} = \text{rad}(m_i) + \sum_{j=1}^{\underline{n}_g} \sum_{\ell=1}^{n+n_p} \text{rad}(J_{z,i\ell})|\underline{\hat{G}}_{\ell j}|$, then $(\mathbf{x}_k, \mathbf{p}) = \mathbf{z}_k \in \bar{Z}_k$, with

$$\bar{Z}_k = \begin{bmatrix} \mathbf{H} \\ \mathbf{E} \end{bmatrix} \hat{Z}_{k-1} \oplus \begin{bmatrix} \mathbf{H} \\ \mathbf{0} \end{bmatrix} (-\boldsymbol{\gamma}_z) \oplus \begin{bmatrix} \hat{\mathbf{P}} \\ \mathbf{0} \end{bmatrix} B_\infty^n \oplus \begin{bmatrix} \mathbf{I} \\ \mathbf{0} \end{bmatrix} Z_w. \tag{8.13}$$

Proof. Choose any $(\mathbf{x}_{k-1}, \mathbf{p}) = \mathbf{z}_{k-1} \in \hat{Z}_{k-1}$, $\mathbf{w}_{k-1} \in W$. From (8.11), Proposition 8 and Theorem 2, there must exist $\boldsymbol{\delta} \in B_\infty^n$ such that $\mathbf{x}_k = \mathbf{f}(\mathbf{x}_{k-1}, \mathbf{u}_{k-1}, \mathbf{p}, \mathbf{w}_{k-1}) = \mathbf{f}(\boldsymbol{\gamma}_x, \mathbf{u}_{k-1}, \boldsymbol{\gamma}_p, \mathbf{w}_{k-1}) + \text{mid}(\mathbf{J}_z)(\mathbf{z}_{k-1} - \boldsymbol{\gamma}_z) + \hat{\mathbf{P}}\boldsymbol{\delta}$, with $\hat{\mathbf{P}}$ defined as in the statement of the corollary. Then, by the definition of $\mathbf{z}_{k-1}$ and $\mathbf{E}$, $\mathbf{p} = \mathbf{E}\mathbf{z}_{k-1}$ holds, and we have that (considering $\mathbf{H} \triangleq \text{mid}(\mathbf{J}_z)$)

$$\begin{aligned}
(\mathbf{x}_k, \mathbf{p}) &= (\mathbf{f}(\boldsymbol{\gamma}_x, \mathbf{u}_{k-1}, \boldsymbol{\gamma}_p, \mathbf{w}_{k-1}) + \mathbf{H}(\mathbf{z}_{k-1} - \boldsymbol{\gamma}_z) \\
&\qquad\qquad\qquad\qquad + \hat{\mathbf{P}}\boldsymbol{\delta}, \mathbf{E}\mathbf{z}_{k-1}) \\
&= (\mathbf{H}\mathbf{z}_{k-1} - \mathbf{H}\boldsymbol{\gamma}_z \\
&\qquad\qquad + \hat{\mathbf{P}}\boldsymbol{\delta} + \mathbf{f}(\boldsymbol{\gamma}_x, \mathbf{u}_{k-1}, \boldsymbol{\gamma}_p, \mathbf{w}_{k-1}), \mathbf{E}\mathbf{z}_{k-1}) \\
&= \begin{bmatrix} \mathbf{H} \\ \mathbf{E} \end{bmatrix} \mathbf{z}_{k-1} + \begin{bmatrix} \mathbf{H} \\ \mathbf{0} \end{bmatrix} (-\boldsymbol{\gamma}_z) \\
&\qquad\qquad + \begin{bmatrix} \hat{\mathbf{P}} \\ \mathbf{0} \end{bmatrix} \boldsymbol{\delta} + \begin{bmatrix} \mathbf{I} \\ \mathbf{0} \end{bmatrix} \mathbf{f}(\boldsymbol{\gamma}_x, \mathbf{u}_{k-1}, \boldsymbol{\gamma}_p, \mathbf{w}_{k-1}) \\
&\in \begin{bmatrix} \mathbf{H} \\ \mathbf{E} \end{bmatrix} \hat{Z}_{k-1} \oplus \begin{bmatrix} \mathbf{H} \\ \mathbf{0} \end{bmatrix} (-\boldsymbol{\gamma}_z) \oplus \begin{bmatrix} \hat{\mathbf{P}} \\ \mathbf{0} \end{bmatrix} B_\infty^n \oplus \begin{bmatrix} \mathbf{I} \\ \mathbf{0} \end{bmatrix} Z_w,
\end{aligned}$$

which proves the corollary. □

An enclosure of the joint prediction step for the dynamics (8.11) can be obtained in CG-rep using Corollary 1. As in the linear case, and differently from interval methods, the CZ $\bar{Z}_k$ given by (8.13) preserves the existing couplings between state $\mathbf{x}_{k-1}$ and parameter $\mathbf{p}$. Moreover, due to linearity of the output equation (8.6b), an exact bound for the update step can be obtained using (8.10), which in addition refines the enclosure of the parameters $\mathbf{p}$, with $\bar{Z}_k$ given by (8.13).

Remark 7 The CZ Z_w in Corollary 1, can be obtained as $Z_w = \mathbf{f}(\boldsymbol{\gamma}_x, \mathbf{u}_{k-1}, \boldsymbol{\gamma}_p, \boldsymbol{\gamma}_w) \oplus \lhd(\mathbf{J}_w, W - \boldsymbol{\gamma}_w) \supseteq \mathbf{f}(\boldsymbol{\gamma}_x, \mathbf{u}, \boldsymbol{\gamma}_p, W)$, for a chosen $\boldsymbol{\gamma}_w \in \square W$, and interval matrix $\mathbf{J}_w \supseteq \nabla_w^T \mathbf{f}(\boldsymbol{\gamma}_x, \mathbf{u}, \boldsymbol{\gamma}_p, \square W)$.

Remark 8 Let the CZs $(\hat{Z}_{k-1}, \bar{Z}_k, W, V)$ have $(\hat{n}_g, \bar{n}_g, n_{g_w}, n_{g_v})$ generators, and $(\hat{n}_c, \bar{n}_c, n_{c_w}, n_{c_v})$ constraints, respectively. Then, the enclosure obtained by Corollary 1 has $\hat{n}_g + 2n + n_{g_w}$ generators and $\hat{n}_c + n_{c_w}$ constraints. On the other side, the enclosure $\hat{Z}_k$ obtained by (8.10) has $\bar{n}_g + n_{g_v}$ generators, and $\bar{n}_c + n_{c_v} + n_y$ constraints.

Remark 9 The computational complexities of all the operations used in this section can be found in Rego et al., 2020b.

8.2 Numerical examples

This section presents numerical results for the set-based joint state and parameter estimation method proposed in this chapter. We compare the results provided by this new framework, denoted as CZ-J for the linear case and CZMV-J for the nonlinear case, with the CZ methods proposed in previous studies Scott et al., 2016a and Rego et al., 2021b, denoted as CZ and CZMV, respectively (with prediction steps described in Proposition 8). Additionally, we compare these results with those obtained using the interval arithmetic approach presented in Jaulin et al., 2001, which relies on forward-backward propagation (FBP). We also apply the latter method within the context of our proposed joint estimation framework.

To illustrate the benefits of applying joint state and parameter estimation with CZs, we begin by examining a discrete-time system. This system exhibits linearity in

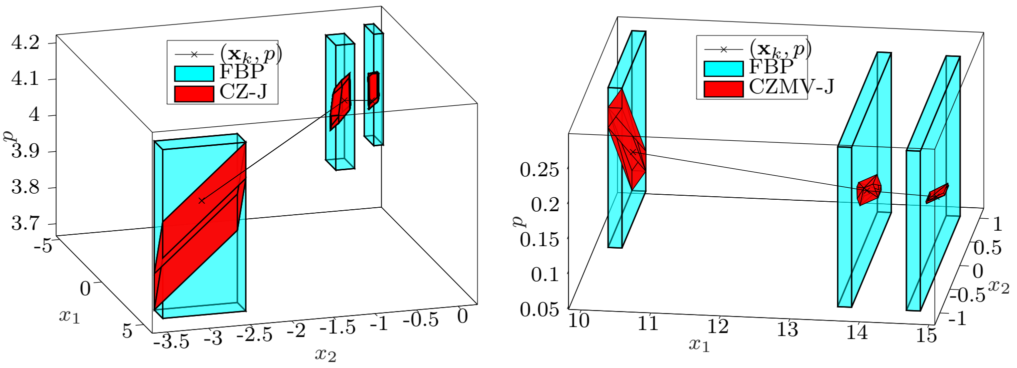

FIGURE 8.1: The variables $(\mathbf{x}_k, p)$ ($\times$), and the CZs obtained using CZ-J (red, left), using CZMV-J (red, right), and interval arithmetic (cyan), for the linear system (8.14) at $k \in \{0, 1, 4\}$ (left), and for the nonlinear system (8.16) at $k \in \{0, 1, 200\}$ (right) .

both its states and model parameters.

$$\begin{aligned} x_{1,k} &= 0.1x_{2,k-1} - p + w_{1,k-1} \\ x_{2,k} &= 0.125x_{2,k-1} + w_{2,k-1} \\ y_{1,k} &= -0.1667x_{1,k} - 0.2x_{2,k} + p + v_k \end{aligned} \tag{8.14}$$

with process and measurement disturbances satisfying $\|\mathbf{w}_k\|_\infty \leq 0.05$ and $\|\mathbf{v}_k\|_\infty \leq 0.05$ respectively, while $p \in P \subset \mathbb{R}$ is the unknown but bounded model parameter. The initial state set $\bar{X}_0$ and the parameter bounds are zonotopes given in G-rep by

$$\bar{X}_0 = \left\{ \begin{bmatrix} 0.5 & 0 \\ 0 & 0.5 \end{bmatrix}, \begin{bmatrix} 5 \\ -3 \end{bmatrix} \right\}, P = \{0.5, 4\}\,. \tag{8.15}$$

Measurement data have been collected by simulating (8.14) with an initial state of $x_0 = (5.2, -3)$ within $\bar{X}_0$ and a parameter value of $p = 4 \in P$. Process and measurement disturbances were generated following a uniform random distribution. The estimated enclosure $\hat{Z}_k$ was limited to a maximum of 6 generators and 2 constraints.

Figure 8.1 (left) presents a comparison between the enclosures $\hat{Z}_k$ obtained using CZ-J and FBP at time steps $k \in 0, 1, 4$. In this study, we applied only one iteration of the FBP algorithm, as multiple iterations did not significantly improve the resulting interval enclosures. The ability to capture the interdependencies between states and parameters enables CZs to yield tighter enclosures than intervals, as demonstrated in Figure 8.2. This figure illustrates the surface areas of $\hat{X}_k$ (top) and the radii of the estimated parameter enclosures $\hat{P}_k$ (bottom). The proposed joint framework, CZ-J, can, therefore, provide more accurate state estimates, while CZ offers only a marginal improvement compared to FBP. While intervals converge to a constant radius for $\hat{P}_k$ after a few iterations, CZ-J continuously refines the set throughout the simulation horizon.

To illustrate the effectiveness of CZ-J in higher-dimensional scenarios, we consider ten discrete-time linear systems described by (8.6), where $n = n_w = 10$, $n_p = n_v = n_y = 6$. The matrices $\mathbf{A}$ and $\mathbf{C}$ are generated from a uniform random distribution with $|a(i,j)| \leq 1/7$ and $|c(i,j)| \leq 1/4$ for all (i,j). The matrices $\mathbf{B_p}$ and $\mathbf{D_p}$ consist of values randomly selected from a uniform distribution within the range $[-1, 1]$. Additionally, we set $\mathbf{B_w} = n_w$, $\mathbf{D_v} = n_v$, $\mathbf{B} = nn_u$, and $\mathbf{D} = n_y n_u$.

Process and measurement disturbances are constrained to satisfy $|\mathbf{w}k|\infty \leq 0.05$

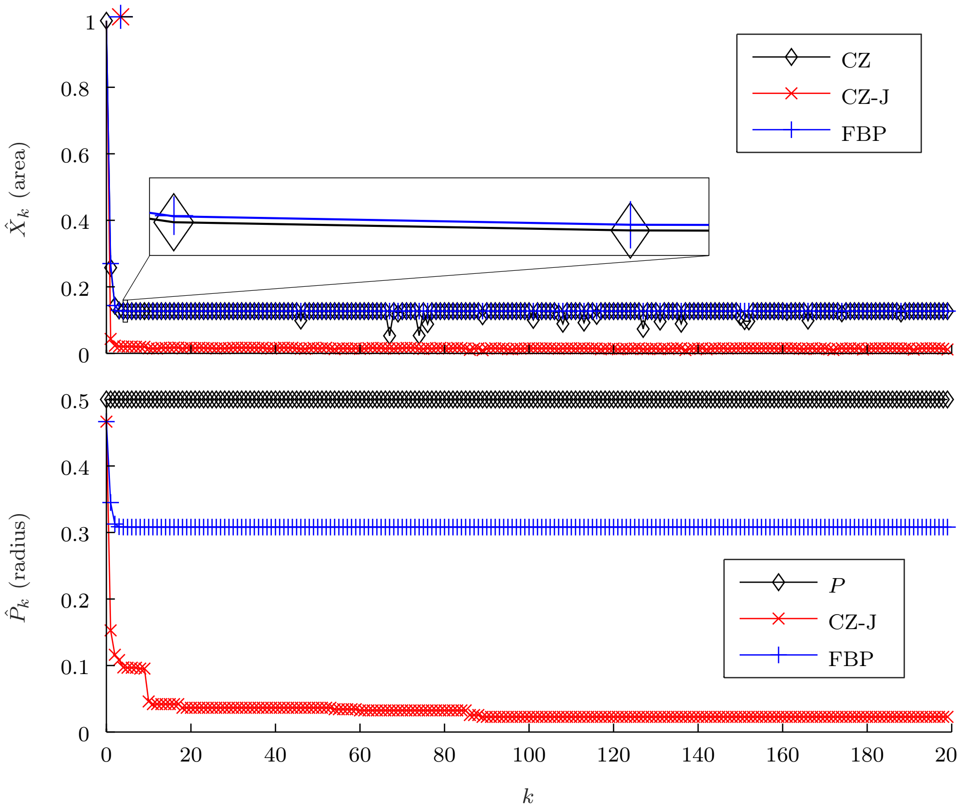

FIGURE 8.2: For the linear system (8.14) and $k \in [0, 200]$, top: the areas of the projections onto the state space of the enclosures provided by CZ ($\diamond$) and CZ-J ($\times$), and FBP ($+$); bottom: the radii of the parameter set P ($\diamond$) and the projections $\hat{P}_k$ provided by CZ-J ($\times$) and FBP ($+$).

and $|\mathbf{v}k|\infty \leq 0.05$, respectively. The sets $\bar{X}_0$ and P are defined as boxes with centers having integer values randomly chosen from $[-6, 6]$ based on a uniform discrete distribution, and their radii are set to 0.5.

To generate measurement data, we simulated each system while introducing process and measurement disturbances based on a uniform random distribution. Additionally, we initialized the systems with random initial states within the specified bounds. We set the maximum number of generators and constraints of $\hat{Z}_k$ to be 70 and 20, respectively.

Figure 8.3 presents the average radii of the projections $\hat{X}_k$ (top) and $\hat{P}_k$ (bottom) for the enclosures provided by CZ, CZ-J, and FBP. On average, FBP exhibits the worst performance in state estimation. CZ-J yields smaller sets compared to CZ because the latter does not refine the parameter set over time.

Moreover, in this example, FBP failed to guarantee any refinement of the parameter enclosure. This can be attributed to its inability to account for the dependencies between states and parameters, primarily due to the wrapping effect.

Note that also in this case only one iteration of the FBP is applied and multiple iterations did not result in any further refinement of the set.

Finally, we provide a nonlinear numerical example to showcase the efficacy of the approach introduced in Section 8.1.2. Consider the nonlinear discrete-time system

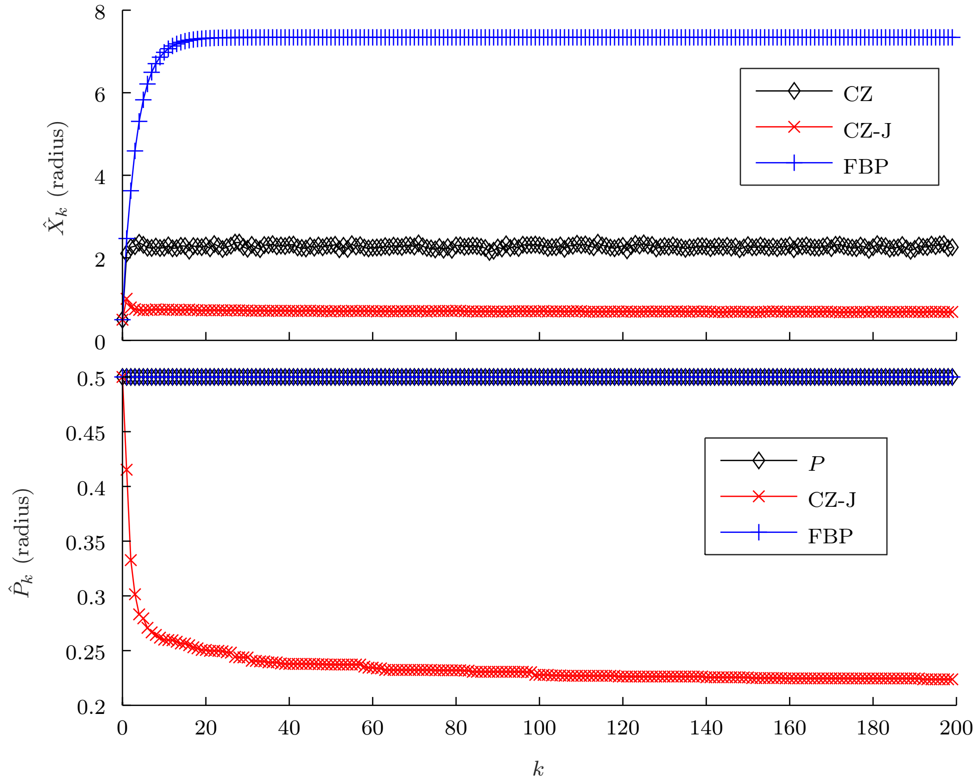

FIGURE 8.3: For the 10-dimensional linear examples and $k \in [0, 200]$, top: the average of the radii of the projections onto the state space of the enclosures provided by CZ ($\diamond$) and CZ-J ($\times$), and FBP ($+$); bottom: the radii of the parameter set P ($\diamond$) and the projections $\hat{P}_k$ provided by CZ-J ($\times$) and FBP ($+$).

described by

$$\begin{aligned} x_{1,k} &= 3x_{1,k-1} - p x_{1,k-1}^2 - \frac{4x_{1,k-1}x_{2,k-1}}{4 + x_{1,k-1}} + w_{1,k-1} \\ x_{2,k} &= -2x_{2,k-1} + \frac{3x_{1,k-1}x_{2,k-1}}{4 + x_{1,k-1}} + w_{2,k-1} \\ y_{1,k} &= x_{1,k} + v_{1,k}, \\ y_{2,k} &= -x_{1,k} + x_{2,k} + (7p - 1) + v_{2,k}, \end{aligned} \tag{8.16}$$

where $\|\mathbf{w}_k\|_\infty \leq 0.2$, $\|\mathbf{v}_k\|_\infty \leq 0.1$, and $p \in P \subset \mathbb{R}$ is an unknown model parameter. The initial state enclosure $\bar{X}_0$ and the known parameter bounds P are boxes given by

$$\bar{X}_0 = \left\{ \begin{bmatrix} 1.2 & 0 \\ 0 & 0.6 \end{bmatrix}, \begin{bmatrix} 10 \\ 0.5 \end{bmatrix} \right\}, P = \{5, 1/7\}. \tag{8.17}$$

Measurement data were acquired by simulating (8.16) with an initial state of $\mathbf{x}_0 = (10.2, 0.65) \in \bar{X}_0$ and a parameter value of $p = 1/7 \in P$. Process and measurement disturbances were generated from uniform random distributions within the specified bounds. The enclosures $\hat{Z}_k$ were constructed with a maximum of 8 generators and 3 constraints.

Fig. 8.1 (right) shows the enclosures $\hat{Z}_k$ obtained using FBP and CZMV-J, as well as the evolution of $\mathbf{x}_k$, for $k \in \{0, 1, 200\}$. As in the linear case, the state enclosures provided by CZMV-J are significantly smaller than the ones obtained with FBP, due to capability to capture the dependencies between states and parameters. Fig. 8.4,

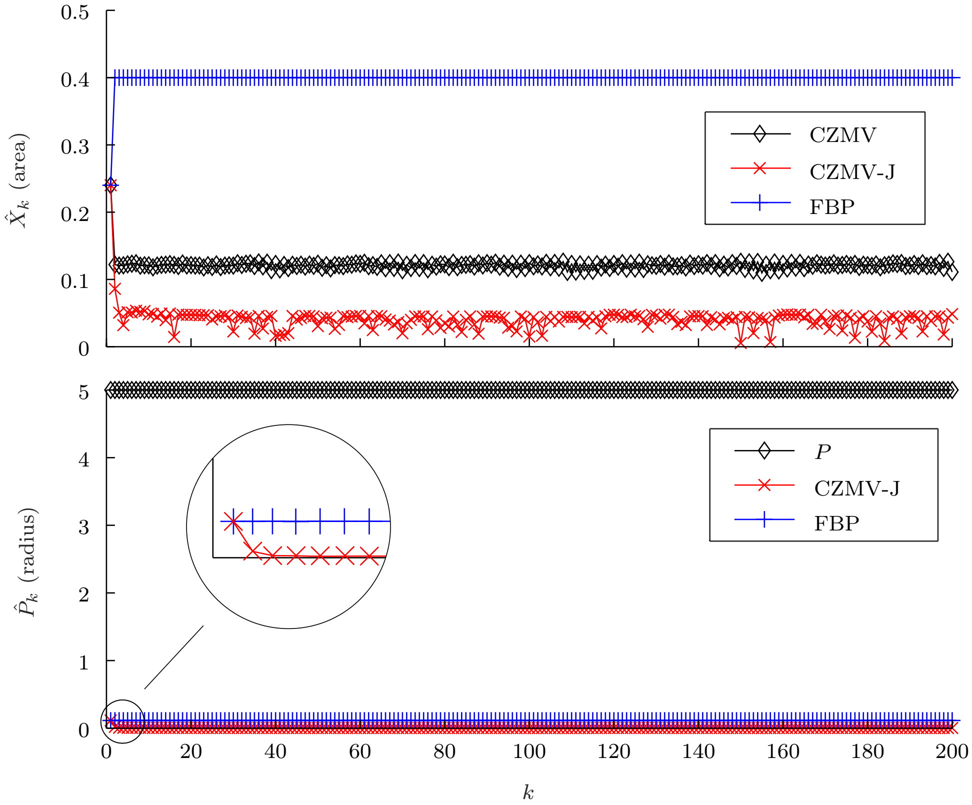

FIGURE 8.4: For the nonlinear system (8.16) and $k \in [0, 200]$, top: the areas of the projections onto the state space of the enclosures provided by CZMV ($\diamond$), CZMV-J ($\times$) and FBP ($+$); bottom: the radii of the parameter set P ($\diamond$) and the projections $\hat{P}_k$ provided by CZMV-J ($\times$) and FBP ($+$).

which shows the areas of $\hat{X}_k$ (top) and the radii of $\hat{P}_k$ (bottom), corroborates the advantages of using the proposed joint framework CZMV-J.

8.3 Conclusions

In this chapter, we have introduced an innovative approach to simultaneously estimate the states and parameters of nonlinear discrete-time systems using set-based methods. Our foundation builds upon the algorithms outlined in Chapter 5, expanding upon the techniques for nonlinear state estimation by incorporating constrained zonotopes (CZs) for parameter estimation within a cohesive framework. This integration preserves the inherent interdependencies between states, algebraic variables, and unknown parameters, resulting in a significant enhancement in the accuracy of both state and parameter estimation.

The structure of this chapter has taken us through a comprehensive exploration of this approach. We began by discussing the current state of the art in joint state and parameter estimation, highlighting the increasing importance of state estimation across various research domains. We emphasized the role of parameter estimation, especially in scenarios where model parameters exhibit unknown stochastic properties but known bounds. Set-based methods have emerged as powerful tools in this context, providing reliable enclosures of system trajectories and robust solutions for parameter estimation.

Our novel approach introduced here, based on CZs, unifies the estimation of states and parameters within discrete-time systems. Unlike interval-based techniques, our CZ-based approach excels at preserving and propagating interdependencies between states and model parameters. This feature is particularly valuable in practical applications where such interdependencies are prevalent. Our method employs generalized intersections to refine both state and parameter enclosures, resulting in substantially improved accuracy in state and parameter estimation.

To demonstrate the practicality and effectiveness of our approach, we presented a series of numerical examples spanning various scenarios, including both linear and nonlinear discrete-time systems. These examples illustrated the capabilities of our method and its superior performance compared to existing techniques.

In conclusion, our work represents a significant advancement in the field of joint state and parameter estimation. By leveraging the power of constrained zonotopes and preserving interdependencies, we have provided a robust and accurate solution for estimating both states and parameters within discrete-time systems. This has important implications for a wide range of applications, from robotics to fault detection and beyond. We believe that our approach opens up new avenues for research and application in the field of state estimation.

Chapter 9

Set-based joint state and parameter estimation of a Li-ion cell

In this chapter, we shift our focus from a theoretical exploration, as extensively discussed in the preceding chapter, to a more applied perspective within lithium-ion batteries context. Our objective remains centered on the pursuit of precision in Battery Management Systems (BMSs), with an emphasis on practical applications. Our goal is to raise awareness of cutting-edge methods that can significantly enhance Battery Management Systems (BMSs). The idea of combined state-parameter estimation, a potent strategy ready to make important contributions to the area, is at the core of our discussion. The foundation for our investigation is already laid, as we have gone deeply into the theoretical underpinnings of the methodology in the preceding chapter. Now, we turn our attention to its practical implications in the context of lithium-ion batteries. Our exploration builds upon the common scenario of dealing with uncertainties in real-world battery systems, which are often bounded but not precisely known. Within this context, we introduce Constrained Zonotopes (CZs) as an innovative set representation. CZs offer a unique advantage by effectively capturing the intricate connections between battery states and parameters. This interdependence typically arises from the measurements obtained during battery operation, making it a critical consideration for comprehensive estimation.

One notable strength of CZ-based methods is their ability to outperform traditional set-based estimation techniques, particularly those based on intervals. This chapter provides a detailed examination of how integrating CZs can lead to superior outcomes in parameter and state estimation. This enhancement, in turn, significantly bolsters the overall performance and safety of battery systems.

Based on CZs, this chapter proposes a set-based joint state and parameter estimation approach for discrete-time nonlinear systems that is applied to an electro-thermal model of a Li-ion battery. The method is an extension to the scenario of nonlinear outputs of the work provided in (Rego et al., 2022b). The obtained results are compared to those obtained using the interval-based estimator provided in Locatelli et al., 2021, which has been extended to include parameter estimation in a unified framework. The effectiveness of CZs over time is supported by numerical results from the Li-ion cell model.

This chapter proceeds as follows: Section 9.1 offers a concise review of the essential simulation setup and the model it has been used. Section 9.2 articulates the problem formulation and elucidates the joint state and parameter estimation process, emphasizing its practical relevance.

In Section 9.3, we present and analyze the numerical results obtained from applying the methodology to real-world scenarios, particularly in the context of lithium-ion batteries. These results serve as a tangible demonstration of the potential impact and benefits of our approach.

Finally, Section 9.4 brings this chapter to a close, summarizing the key findings, insights, and their implications for battery management systems in practical applications.

9.1 Simulation settings

In this chapter, a coupled electro-thermal model is used to describe the lithium-ion cell behavior. The electrical part of the system is described by the Thévenin model described in Chapter 3.2.1. This is made up of three components: (i) the open circuit potential $V_{\mathrm{OC}}(t)$, (ii) two internal resistors R_0 and R_1, and (iii) the capacitor C_1. Note that in this case study the electrical parameters has been considered as constant and no assumptions have been made regarding their dependencies on temperature and/or State of Charge. For the thermal part of the model we refer to the one proposed in Lin et al., 2014 and it is described in Chapter 3.2.4, which consists of two state equations describing the temperature in the core and on the surface. In this work we assume that the surface of the cell is in contact with the external air at a constant temperature. The measurable quantities of the system are the surface temperature $T_s(t)$ and the terminal voltage $V_t(t)$. This latter depends form the overall open circuit potential $V_{\mathrm{OCP}}(t)$ that is expressed as a State of Charge dependent function, according to what has been discussed in Chapter 3.2.3.

The electro-thermal model (3.1) is first discretized using the Forward Euler's method before employing the set-based estimate approach presented in this research. The discretized version of model (3.1) can be compactly stated as

$$\begin{cases} \mathbf{x}_k = \mathbf{x}_{k-1} + t_s\mathbf{f}(\mathbf{x}_{k-1}, \mathbf{u}_{k-1}, \mathbf{p}), & k \geq 1 \\ \mathbf{y}_k = \mathbf{g}(\mathbf{x}_k, \mathbf{u}_k, \mathbf{p}, \mathbf{v_k}), & k \geq 0 \end{cases} \tag{9.1}$$

where $\mathbf{f}(\mathbf{x}, \mathbf{u}, \mathbf{p}) : \mathbb{R}^n \times \mathbb{R}^{n_u} \times \mathbb{R}^{n_p} \rightarrow \mathbb{R}^n$ and $\mathbf{g}(\mathbf{x}, \mathbf{u}, \mathbf{p}, \mathbf{v}) : \mathbb{R}^n \times \mathbb{R}^{n_u} \times \mathbb{R}^{n_p} \times \mathbb{R}^{n_v} \rightarrow \mathbb{R}^{n_y}$ denote the continuous state and output dynamics, respectively, whereas t_s is the sampling time and $\mathbf{x}_0$ is the initial condition. The goal of this work is to estimate the set of states that are consistent with the model dynamics and the collected measurements while assuming unknown but bounded errors in terms of initial conditions, measurement noise, and parameters. Unlike traditional set-based state estimation, we plan to use the measurement data to refine the uncertain parameter set. To do this, we employ CZs (explained in Chapter 8), which allow for the combined refinement of states and parameters, resulting in more effective results as compared to interval-based approaches.

9.2 Problem formulation

Consider a nonlinear discrete-time dynamical system described as:

$$\mathbf{x}_k = \mathbf{f}(\mathbf{x}_{k-1}, \mathbf{u}_{k-1}, \mathbf{p}, \mathbf{w}_{k-1}) \qquad k \geq 1, \tag{9.2a}$$

$$\mathbf{y}_k = \mathbf{g}(\mathbf{x}_k, \mathbf{u}_k, \mathbf{p}, \mathbf{v}_k) \qquad k \geq 0, \tag{9.2b}$$

Here, $\mathbf{x}_k \in \mathbb{R}^n$ represents the system state, $\mathbf{u}_k \in \mathbb{R}^{n_u}$ is the known input signal, $\mathbf{w}_k \in \mathbb{R}^{n_w}$ denotes process uncertainties, $\mathbf{p} \in \mathbb{R}^{n_p}$ signifies uncertain parameters, $\mathbf{y}_k \in \mathbb{R}^{n_y}$ stands for the measured output, and $\mathbf{v}_k \in \mathbb{R}^{n_v}$ represents measurement uncertainties. We assume that the nonlinear functions $\mathbf{f}$ and $\mathbf{g}$ are of class $\mathcal{C}^1$. Additionally, the initial state, model parameters, and disturbances are bounded, with $\mathbf{x}_0 \in X_0$, $\mathbf{p} \in P$, $\mathbf{w}_k \in W$, and $\mathbf{v}_k \in V$, where X_0, P, W, and V are known compact sets.

The goal of joint state-parameter set-based estimation is to determine, at each time step $k \geq 0$, the set of all states and parameters $(\mathbf{x}_k, \mathbf{p})$ consistent with initial uncertainties, the known input, model uncertain dynamics, and obtained measurements. A modified prediction-update algorithm is employed, which incorporates the relationship between the output $\mathbf{y}_k$ and the state $\mathbf{x}_{k-1}$:

$$\mathbf{y}_k = \tilde{\mathbf{g}}(\mathbf{x}_{k-1}, \mathbf{u}_{k-1}, \mathbf{u}_k, \mathbf{p}, \mathbf{w}_{k-1}, \mathbf{v}_k), \quad k \geq 1. \tag{9.3}$$

The prediction-update algorithm is outlined as follows: At $k = 0$, measurement $\mathbf{y}_0$ refines the initial set $X_0 \times P$ as follows:

$$\bar{Z}_0 = X_0 \times P \tag{9.4}$$

$$\hat{Z}_0 \supseteq \{(\mathbf{x}_0, \mathbf{p}) \in \bar{Z}_0 : \mathbf{g}(\mathbf{x}_0, \mathbf{u}_0, \mathbf{p}, \mathbf{v}_0) = \mathbf{y}_0,\ \mathbf{v}_0 \in V\} \tag{9.5}$$

Starting from $k = 1$, the following steps are applied:

$$\begin{aligned}\tilde{Z}_{k-1} \supseteq \{(\mathbf{x}_{k-1}, \mathbf{p}) \in \hat{Z}_{k-1} : \tilde{\mathbf{g}}(\mathbf{x}_{k-1}, \mathbf{u}_{k-1}, \mathbf{u}_k, \mathbf{p}, \mathbf{w}_{k-1}, \mathbf{v}_k)\\ = \mathbf{y}_k, \mathbf{v}_k \in V, \mathbf{w}_{k-1} \in W\},\end{aligned} \tag{9.6}$$

$$\begin{aligned}\bar{Z}_k \supseteq \{(\mathbf{f}(\mathbf{x}_{k-1}, \mathbf{u}_{k-1}, \mathbf{p}, \mathbf{w}_{k-1}), \mathbf{p}) : (\mathbf{x}_{k-1}, \mathbf{p}) \in \tilde{Z}_{k-1},\\ \mathbf{w}_{k-1} \in W\},\end{aligned} \tag{9.7}$$

$$\hat{Z}_k \supseteq \{(\mathbf{x}_k, \mathbf{p}) \in \bar{Z}_k : \mathbf{g}(\mathbf{x}_k, \mathbf{u}_k, \mathbf{p}, \mathbf{v}_k) = \mathbf{y}_k,\ \mathbf{v}_k \in V\} \tag{9.8}$$

The extra update steps in Equation (9.6) are used to further improve the state-parameter set at time $k-1$ using the measurement at time k. The acquired set is then carried forward via the (9.7) prediction step. The set is then refined using the normal update step in (9.8) with the available measurement. It should be noted that in practice, exact computing of the processes mentioned above is usually impracticable and tight outer approximations are sought instead. Chapter 8, in particular, explains how to compute such approximations for the situation of $\mathbf{f}$ and $\mathbf{g}$ being $\mathcal{C}^1$ and sets being defined by CZ.

Remark 10 *The introduction of the extra update step* (9.6) *enables for some of the conservativeness introduced by the outer approximations to be mitigated. Accounting for the relationship between the measurement at time k and the prediction-update set at time instants earlier to $k-1$ could result in an even greater improvement. This, however, would result in an increase in computational complexity. A complexity analysis of CZ-based estimation can be found in Rego et al., 2020c.*

9.3 Numerical results

In this section, we apply the joint state-parameter estimation method introduced in Chapter 8 to the Li-ion cell model discussed in Section 9.1. We compare the results obtained using the CZ-based framework with an interval-based method proposed in Locatelli et al., 2021. This interval-based method has been modified to address the joint state-parameter estimation problem, as described in Section 9.2.

To mitigate the conservatism deriving from computing Jacobians in the set-based estimation approach, we replace uncertain parameters in the denominator of model (3.1) with their reciprocals to obtain an equivalent mathematical model. After discretizing the system using (9.1), we arrive at:

$$\begin{cases} x_{1,k} = x_{1,k-1} + t_s \dfrac{u_{k-1}}{C_{\text{batt}}}, \\ x_{2,k} = x_{2,k-1} + t_s(-x_{2,k-1} p_{R_1C_1} + u_{k-1} p_{C_1}), \\ x_{3,k} = x_{3,k-1} + t_s((x_{4,k-1} - x_{3,k-1}) p_{R_cC_c} \\ \qquad + |u_{k-1}| |x_{2,k-1} + R_0 u_{k-1}| \, p_{C_c}), \\ x_{4,k} = x_{4,k-1} + t_s((T_f - x_{4,k-1}) p_{R_uC_c} \\ \qquad + (x_{4,k-1} - x_{3,k-1}) p_{R_cC_s}), \\ y_{1,k} = V_{\text{oc}}(x_{1,k}) + R_0 u_k + x_{2,k} + v_{1,k}, \\ y_{2,k} = x_{4,k} + v_{2,k}, \end{cases} \tag{9.9}$$

where $\mathbf{x} = \begin{bmatrix} x_1 & x_2 & x_3 & x_4 \end{bmatrix}^T$ denotes the state vector $\begin{bmatrix} z & V_{C_1} & T_c & T_s \end{bmatrix}^T$, and u is the input current I.

To perform the additional update step (9.6), we express the output quantities according to (9.3) as:

$$\begin{cases} y_{1,k} = V_{\text{oc}}\left(x_{1,k-1} + t_s \dfrac{u_{k-1}}{C_{\text{batt}}} \right) + R_0 u_k + x_{2,k-1} \\ \qquad + t_s(-x_{2,k-1} p_{R_1C_1} + u_{k-1} p_{C_1}) + v_{1,k}, \\ y_{2,k} = x_{4,k-1} + t_s((T_f - x_{4,k-1}) p_{R_uC_c} \\ \qquad + (x_{4,k-1} - x_{3,k-1}) p_{R_cC_s}) + v_{2,k}. \end{cases} \tag{9.10}$$

We assume that the measurable outputs are affected by unknown-but-bounded measurement noise $\mathbf{v}_k \in V$, where V is defined as:

$$V = \left\{ \operatorname{diag}(0.001, 0.1), \begin{bmatrix} 0 & 0 \end{bmatrix}^{\mathrm{T}} \right\}. \tag{9.11}$$

The parametric uncertainty vector

$$\mathbf{p} = \begin{bmatrix} R_0 & p_{R_1C_1} & p_{C_1} & p_{R_cC_c} & p_{C_c} & p_{R_uC_c} & p_{R_cC_s} \end{bmatrix}^{\mathrm{T}} \in P$$

, where the initial parametric set P is defined as $P = \{\mathbf{G}_p, \mathbf{c}_p\}$, and with

$$\begin{aligned} \mathbf{c}_p =& [0.0100 \;\; 0.0238 \;\; 0.0004762 \;\; 0.0082 \;\; 0.0160 \\ & 0.0722 \;\; 0.1145]^T, \\ \mathbf{G}_p =& \operatorname{diag}(5{\cdot}10^{-4}, 0.0012, 2.3810{\cdot}10^{-5}, 04.111{\cdot}10^{-4}, \\ & 7.9745{\cdot}10^{-4}, 0.00361, 0.00573). \end{aligned}$$

Please note that, we solely consider the presence of parameter uncertainties in the system dynamics, without accounting for any other process uncertainties. We have assumed a known battery capacity, denoted as $C_{\text{batt}} = 2.3\text{Ah}$. The initial state set X_0 is represented as a zonotope, characterized by

$$\left\{ \operatorname{diag}(0.01, 0.001, 0.5, 0.5), \begin{bmatrix} 0.25 & 0 & 293.15 & 293.15 \end{bmatrix}^{\mathrm{T}} \right\}$$

.

The measurement data have been acquired by simulating the system in (9.9) with an initial state vector $\mathbf{x}_0 = [0.25, 0, 293.15, 293.15]^T$ within X_0 and a parameter vector $\mathbf{p} = [0.0100, 0.0238, 0.0004762, 0.0082, 0.0160, 0.0722, 0.1145]^T$ belonging to the set P. Measurement disturbances have been generated based on a uniform random distribution. It is worth noting that our focus in this paper is exclusively on the battery's charging phase. The input current profile, as illustrated in Figure 9.1, represents the known input profile applied to the cell. Figure 9.2 presents a comparison between the enclosures of the two electrical state components, State of Charge (SOC) and V_{C1}, obtained using two different methods: Contract-Zonotopes (CZs) represented in green, and intervals represented in pink. These enclosures are computed every 100 seconds, starting from $k = 0$. Notably, our approach employs a single iteration at each time step, in contrast to multiple iterations in prior work, as additional iterations did not yield improved interval enclosures.

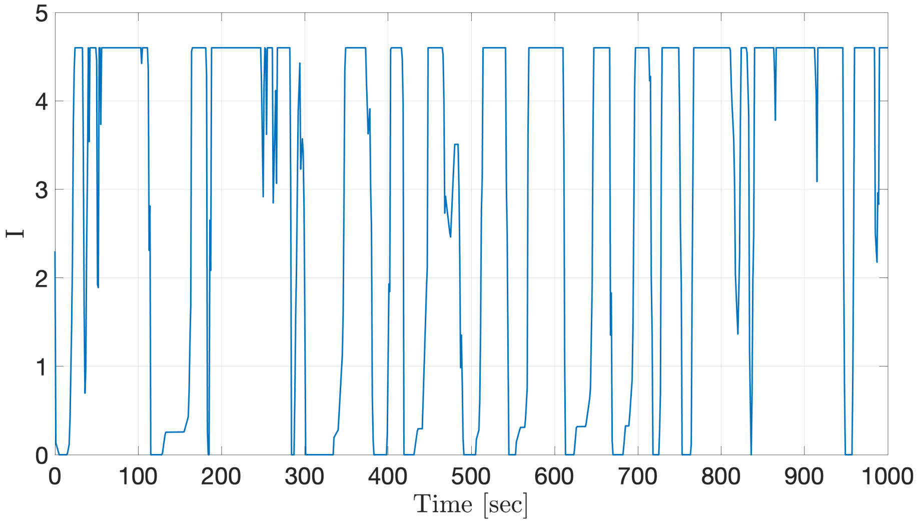

FIGURE 9.1: Input current profile I_k applied to the cell.

Figure 9.3 depicts a similar comparison, this time focusing on the thermal states (T_c and T_s). The enclosures are obtained using CZs (green) and intervals (pink) at discrete time points $k \in 0, 100, 200, 400, 900, 1000$. Notably, CZs exhibit a more significant advantage in thermal states compared to electrical states, owing to their capability to capture the interdependence between states and parameters. To further

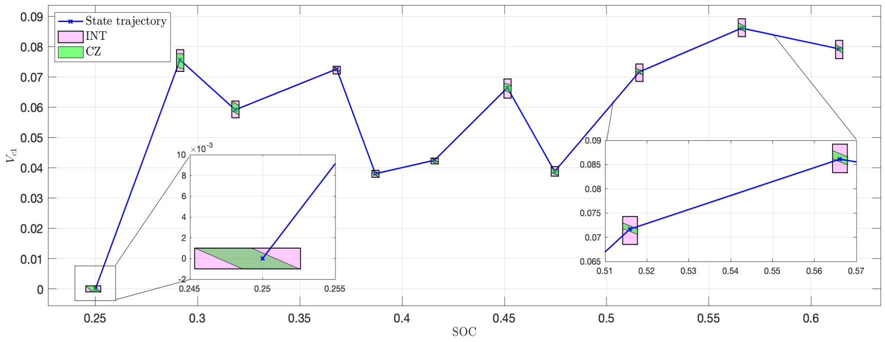

FIGURE 9.2: Enclosures of the SOC and V_{C_1} components obtained using interval (pink) and CZ (green) joint state estimation.

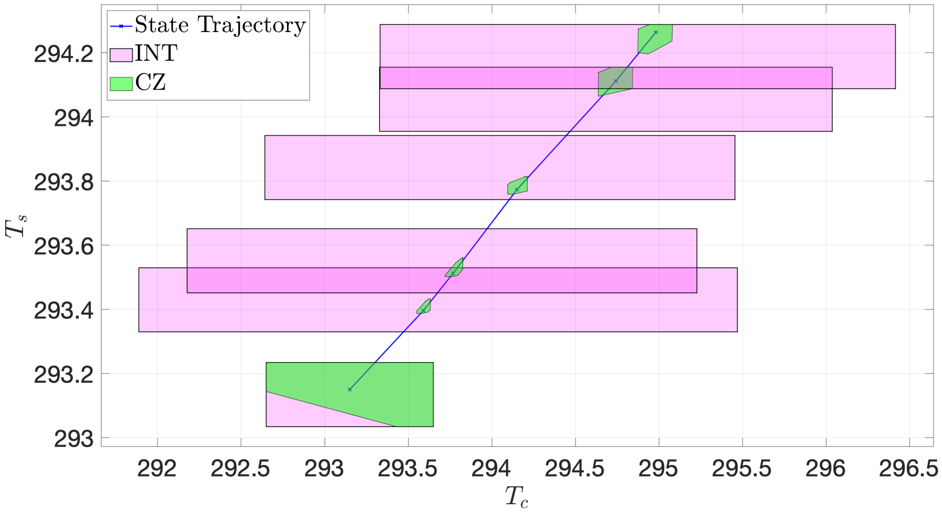

FIGURE 9.3: Enclosures of the T_c and T_s components obtained using interval (pink) and CZ (green) joint state estimation.

emphasize the effectiveness of CZs relative to intervals, we display the radii (computed as the sum of the absolute values of all edges of the interval hull, using the 1-norm) of the respective enclosures in Figure 9.4. The top portion of the figure represents the radii concerning the state variables, while the bottom section illustrates the trend of radii concerning the parametric components. It is evident that CZs outperform intervals in both state and parameter estimation. Specifically, intervals provide inferior estimates for both states and parameters, with radii remaining nearly constant along the parametric components. Conversely, CZs yield a gradual reduction of parametric uncertainty, which proves advantageous for overall state estimation.

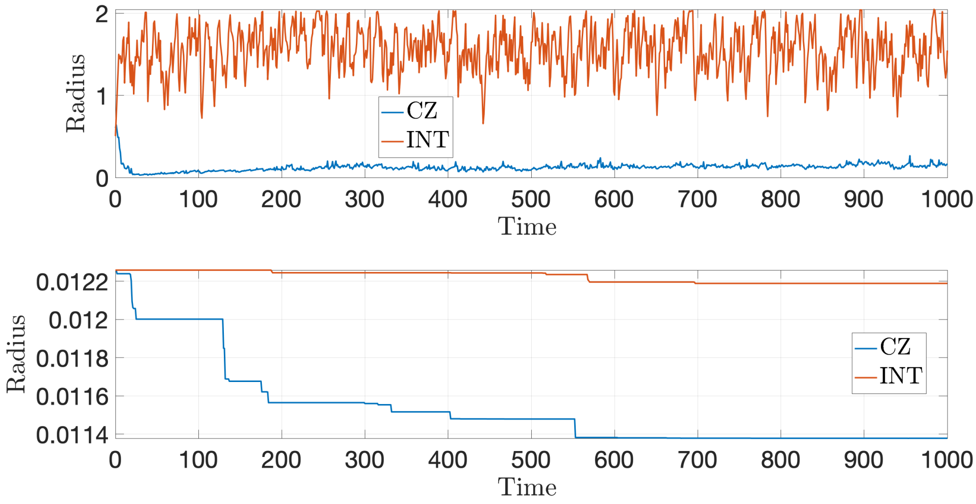

FIGURE 9.4: Radii of the state components' enclosures (upper) and the parameter components' enclosures (lower), obtained through intervals (in red) and CZs (in blue)

9.4 Conclusions

This chapter has explored into the application of a set-based joint state-parameter estimation approach in the context of a Li-ion cell model, which serves as a representative nonlinear discrete-time system. In the field of battery management, estimating the states and parameters of a battery cell poses a significant challenge due to the limited availability of measurements. To tackle this challenge, we have employed Constrained Zonotopes (CZs), showcasing their effectiveness in providing tight bounds for both states and parameters.

The effectiveness of CZs has been thoroughly demonstrated, especially when compared to the interval method. It is evident that CZs outperform intervals in terms of accuracy and precision. The key factor contributing to the superior performance of CZs is their inherent capability to capture the mutual dependencies between states and parameters within the system. This attribute leads to a substantial enhancement in the overall state estimation quality.

In summary, this chapter has advanced our understanding of state-parameter estimation for Li-ion cells and similar nonlinear discrete-time systems. By leveraging CZs, we have achieved more robust and accurate estimations of both states and parameters, ultimately contributing to the improved management and utilization of battery cells. These findings underscore the potential for CZ-based approaches to be applied in practical scenarios, where precise battery state estimation is of prime importance.

Chapter 10

Optimal ageing-aware charging of Li-ion batteries

Fast charging is a crucial area of study for battery-powered devices, particularly electrified vehicles, due to the significant benefits it provides in terms of improving usability and customer acceptance. However, depending on the charging technique used, it may negatively impact battery longevity by causing side-reactions due to high temperatures and overpotentials (Tomaszewska et al., 2019). Achieving a balance between fast charging and preserving battery life is therefore essential, and a trade-off must be made between charging time and battery ageing (Khalik, Bergveld, and Donkers, 2020). This chapter presents an online optimal-control-based method for ageing-aware charging of Lithium-ion batteries, where the side-reaction is minimized for a given charging time subject to several ageing-related constraints. To achieve this, a shrinking-horizon model-predictive control (MPC) technique is implemented, similar to what has been done in prior work (Pozzi, Torchio, and Raimondo, 2018). The approach uses a surrogate model, presented in Khalik, Bergveld, and Donkers, 2021, to approximate the states of the DFN model that are correlated with ageing. The surrogate model combines a black-box finite-dimensional linear-time-invariant (FD-LTI) model and a static nonlinear model that is state-of-charge dependent. It is important to note that the shrinking-horizon technique relies on accurate battery models for optimization.

To close the feedback control loop, a Kalman filter with forgetting factor is used as a state observer, as described in (Beelen, Bergveld, and Donkers, 2020). The effectiveness of this strategy is demonstrated with a Pareto-front analysis.

In summary, the content of the chapter will include an MPC ageing-aware charging strategy, a shrinking-horizon approach that allows for reducing the prediction horizon as the cell charges, and the application of a Kalman filter with forgetting factor as a state observer to the surrogate model.

The remaining is organized as follows: Section 10.1 presents the modelling approach, including the surrogate model and the ageing constraints. Section 10.2 discusses the optimal control problem formulation, the state observer, and the algorithm. The results are presented in Section 10.3, and the conclusions are drawn in Section 10.4.

10.1 Surrogate modeling approach

In this section, we provide an introduction to the surrogate modeling approach proposed by (Khalik, Bergveld, and Donkers, 2021). The latter is used to approximate aging-related DFN model states. In particular, the surrogate model in this work combines a static nonlinear state-of-charge-dependent model with a black-box finite-dimensional linear-time-invariant (FD-LTI) model.

In Figure 10.1, you can see a schematic diagram illustrating the surrogate modeling method, which can be visualized as an input/output model. The input is the applied current, while the model's overall outputs include the predicted voltage and virtual outputs, representing the essential components of the DFN model states. These virtual outputs specifically capture the crucial DFN states that cannot be physically measured within a real battery cell.

The vector $\mathbf{y}$ representing virtual outputs and the cell's terminal voltage can be considered as the combination of the outputs from an FD-LTI model $\bar{\mathbf{y}}$ and a state-of-charge (SOC)-dependent static model $\mathbf{h}(s)$, where s denotes the SOC for brevity. This relationship can be represented in discrete-time as follows

$$\mathbf{y}_k = \bar{\mathbf{y}}_k + \mathbf{h}(s_k), \tag{10.1}$$

with k the discrete time instant. The SOC is computed by the Coulomb counting equation as

$$s_{k+1} = s_k + \frac{\delta_t I_k}{C_b}, \tag{10.2}$$

with δ_t the sampling time, I_k the input current at time $k\delta_t$ and C_b the reversible cell battery capacity. The FD-LTI model is characterized as an AutoRegressive Exogenous (ARX) model with a single input denoted as I_k and n_y outputs. The one-step-ahead prediction, which generates an estimate $\hat{\mathbf{y}}_k$, can be formulated as follows

$$\hat{\mathbf{y}}_k = \mathbf{B}_{\text{ARX}}(q, \boldsymbol{\theta}) I_k - \mathbf{A}_{\text{ARX}}(q, \boldsymbol{\theta}) \bar{\mathbf{y}}_k, \tag{10.3}$$

with q representing the forward shift operator, defined as $I_{k-1} = (q^{-1})I_k$, and $\boldsymbol{\theta}$ denoting the parameters of the ARX model, Equation (10.3) includes $\mathbf{A}_{\text{ARX}}$, an $n_y \times n_y$ matrix of polynomials in q^{-1}. These polynomials exhibit a delay of at least one sample, commencing with zero. Additionally, $\mathbf{B}_{\text{ARX}}$ is a $n_y \times 1$ matrix of polynomials in q^{-1}, characterized by monic polynomials where the leading coefficients are set to 1.

The matrices $\mathbf{N}_A \in \mathbb{R}^{n_y \times n_y}$ and $\mathbf{N}_B \in \mathbb{R}^{n_y \times 1}$ define the orders of the polynomials in $\mathbf{A}_{\text{ARX}}$ and $\mathbf{B}_{\text{ARX}}$, respectively.

Given a specific configuration for these matrices, coupled with data collected from the DFN model simulation, the parameters of the ARX model can be derived by minimizing a least-squares criterion that takes the following form:

$$\sum_{k \in \mathcal{K}} ||\bar{\mathbf{y}} - \hat{\mathbf{y}}(\boldsymbol{\theta})||, \tag{10.4}$$

For $k \in \mathcal{K} = \{0, 1, ..., K-1\}$, with $K = t_f/\delta_t$ representing the time horizon, the estimation of $\hat{y}_k$ from measurements y_k is possible using (10.1), assuming that $\mathbf{h}(s_k)$ is known. Importantly, system (10.1)-(10.3) can also be reformulated in a state-space representation as follows

$$\begin{cases} \mathbf{x}_{k+1} = \mathbf{A}\mathbf{x}_k + \mathbf{B} I_k \\ \quad \mathbf{y}_k = \mathbf{C}\mathbf{x}_k + \mathbf{D} I_k + \mathbf{h}(s_k), \end{cases} \tag{10.5}$$

given $\mathbf{x} = \begin{bmatrix} s & \bar{\mathbf{x}} \end{bmatrix}$, $\mathbf{A} = \text{diag}(1, \bar{\mathbf{A}})$, $\mathbf{B} = \begin{bmatrix} \delta_t / C_b & \bar{\mathbf{B}} \end{bmatrix}$, $\mathbf{C} = \begin{bmatrix} \mathbf{0} & \bar{\mathbf{C}} \end{bmatrix}$ and $\mathbf{D} = \bar{\mathbf{D}}$, with $\bar{\mathbf{x}}$, $\bar{\mathbf{A}}$, $\bar{\mathbf{B}}$, $\bar{\mathbf{C}}$ and $\bar{\mathbf{D}}$ that are derived from a state-space representation of (10.3).

In this chapter, the surrogate model is constructed using a combination of DFN-related quantities chosen as virtual outputs. Specifically, in pursuit of an optimal charging strategy that considers aging effects, the surrogate model emphasizes particular DFN states associated with aging, namely $\bar{\eta}_2(t) = \eta_2(t, \delta_n)$, $\bar{s}_n(t) = s_n(t, \delta_n)$,

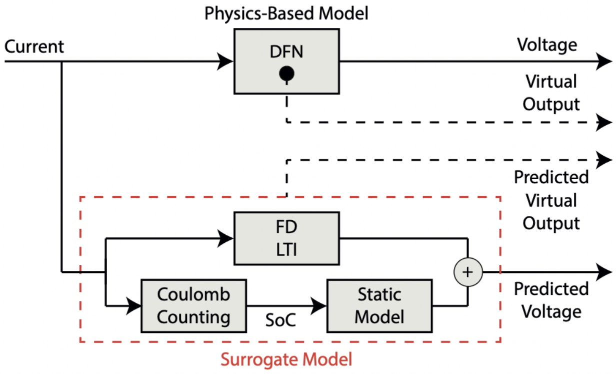

FIGURE 10.1: The schematic illustration of the surrogate modeling approach depicts the approximation of (virtual) outputs from the Doyle-Fuller Newman (DFN) model. These outputs are estimated using a surrogate model, the output of which is a combination of a finite-dimensional (FD) linear-time-invariant (LTI) model and a static model, as detailed in (Khalik, Donkers, and Bergveld, 2021).

$\bar{s}_p(t) = s_p(t, L - \delta_p)$, $\bar{c}_{e,0} = c_e(t, 0)/c_{e,\alpha}$, and $\bar{c}_{e,L} = c_e(t, L)/c_{e,\alpha}$, where $c_{e,\alpha}$ denotes the average electrolyte concentration. Furthermore, when establishing the surrogate model, we include not only the virtual outputs but also the voltage V_t, as illustrated in Figure 10.1. For a more comprehensive understanding of the rationale behind the selection of these specific DFN states of interest, we refer readers to Khalik, Bergveld, and Donkers, 2021.

10.1.1 Validation of the surrogate model

The surrogate model, originally presented by Khalik, Bergveld, and Donkers, 2021, incorporates $\mathbf{y}_k$ and $\mathbf{h}(s_k)$ as defined in (10.1). The parameterization of the ARX model is performed in MATLAB using the System Identification Toolbox. The selection of matrices $\mathbf{N}_A$ and $\mathbf{N}_B$ is a crucial step aimed at striking a suitable balance between model accuracy and complexity, and these matrices are provided by

$$\mathbf{N}_A = \begin{bmatrix} 0 & 1 & 1 & 1 & 1 & 1 \\ 0 & 1 & 1 & 1 & 0 & 1 \\ 0 & 1 & 1 & 0 & 1 & 0 \\ 0 & 1 & 0 & 2 & 1 & 0 \\ 0 & 1 & 1 & 0 & 1 & 1 \\ 0 & 1 & 0 & 1 & 1 & 1 \end{bmatrix}, \quad \mathbf{N}_B = \begin{bmatrix} 2 \\ 2 \\ 2 \\ 2 \\ 1 \\ 1 \end{bmatrix}. \tag{10.6}$$

To parameterize the ARX model (10.3), data for it is acquired through simulations of the DFN model using a predefined current profile, and this parameterization is achieved by applying the least-squares criterion (10.4). In this work TOOFAB described in Chapter 3.3.2 has been emplyed. The detailed procedure for parameterization involves two distinct phases, as outlined in Khalik, Bergveld, and Donkers, 2021. Figure 10.2 depicts the validation of the surrogate model, which was generated using a charging current profile spanning 100 minutes. The trajectories of the virtual outputs, voltage, and j_2 from the surrogate model (in blue) are compared with the corresponding trajectories from the DFN model (in red). It is evident that there exists a disparity between the DFN model and the surrogate model. Nevertheless,

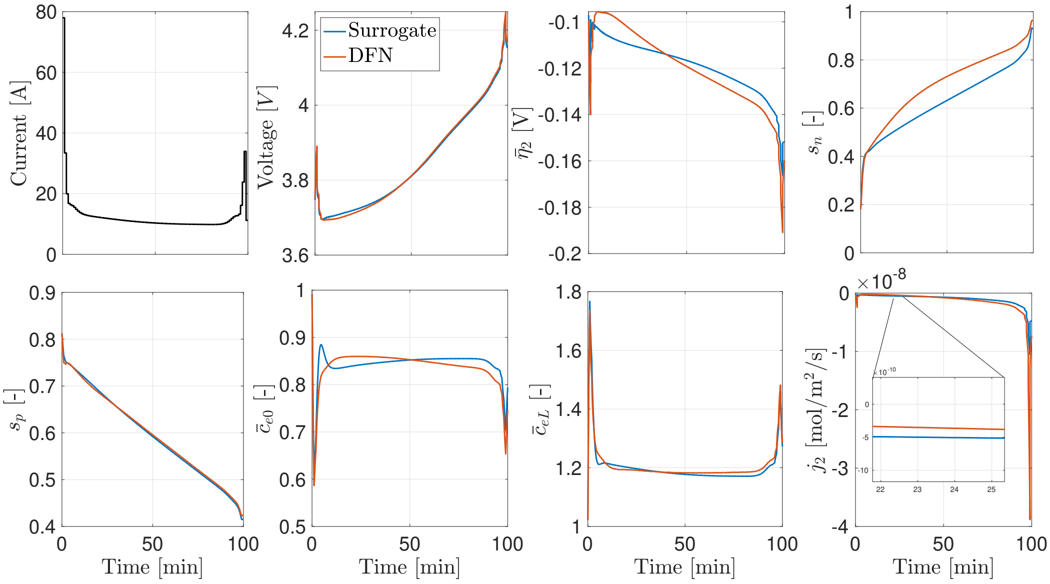

FIGURE 10.2: Validation of the surrogate model with the DFN model.

this difference is deemed acceptable, particularly when considering the computational advantages provided by the surrogate model.

10.2 Optimal ageing-aware strategy

In this section, we present our approach to ageing-aware charging that aims to balance the trade-off between battery ageing and charging time. To achieve this, we use a Shrinking-Horizon Model-Predictive Control (MPC) that solves an optimal control problem based on a surrogate model outlined in Section 10.1. The objective is to minimize Li-ion loss due to side reactions during charging, subject to input and output constraints, within a specified charging time. Fast charging and ageing reduction are typically competing objectives, and our approach aims to find a Pareto-optimal solution. In this scenario, the "shrinking" adaptation is required since the horizon available to take control actions shrinks as the battery charges. The control problem is formulated in this case so that ageing is minimized for a given charging time. We use a Sequential-Quadratic-Programming (SQP) approach to effectively address this optimal-control problem. Additionally, a state observer is required to close the loop, and we employ the Kalman Filter with a forgetting factor developed by Beelen, Bergveld, and Donkers, 2020 for this purpose.

The methodology is summarized in Figure 10.3. In the following, we first formulate the problem of optimal control for the ageing-aware charging method and then describe the resolution method and the state observer used.

10.2.1 Problem formulation

The aim is to minimize the Li-ion loss related to side reactions Q_l within a specified charging time t_f, where the integral $\int_0^{\delta_n} j_2 dx$ is simplified to $j_2(\delta_n, t)$ as described in

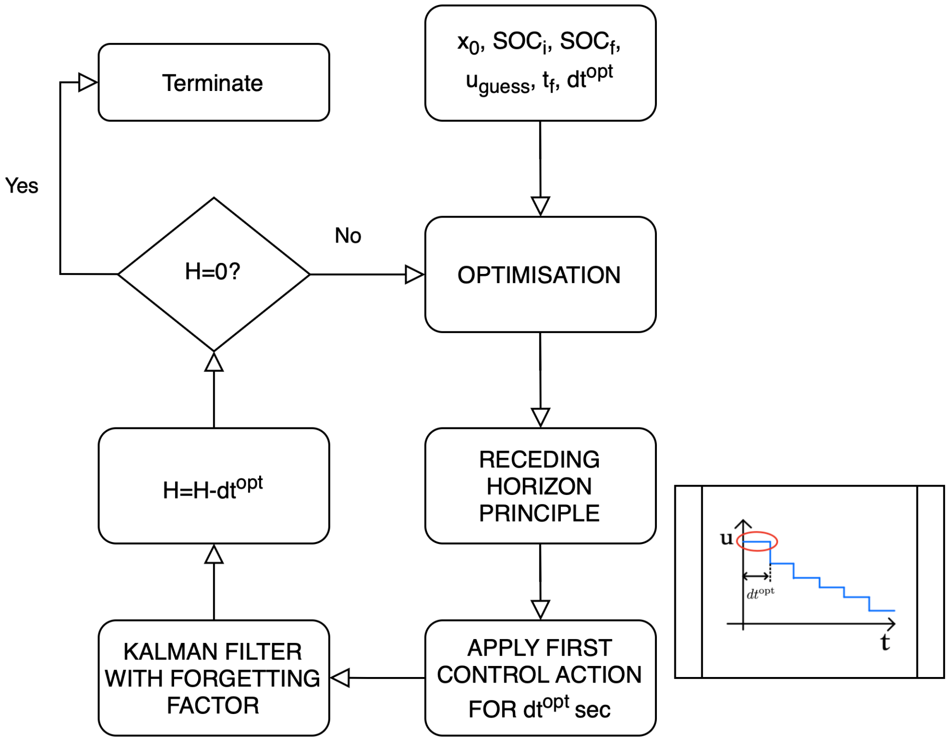

FIGURE 10.3: Closed-loop optimal ageing-aware control strategy.

the following:

$$\min_{x_k, I_k} \quad Q_l(x_k, I_k) = \sum \alpha_1 \exp(\alpha_2 \eta_{2,k}(x_k, I_k)) \tag{10.7}$$

$$\text{s.t.} \quad \text{state dynamics (10.5)} \quad \forall k \in \mathcal{K} = \{0, 1, \dots, K\}$$

$$I_{\min} \leq I_k \leq I_{\max} \tag{10.8}$$

$$y_{\min} \leq y_k \leq y_{\max} \tag{10.9}$$

$$s_K = s_0 + \frac{\delta_t}{C_b} \sum_{k \in \mathcal{K}} I_k \geq s_f. \tag{10.10}$$

The objective is to minimize the cost function given by (10.7) by finding the optimal values of x_k and I_k, subject to the state dynamics in (10.5), input constraints in (10.8), output constraints in (10.9), and minimum-stored-charge constraint described by (10.10) for a specified initial SOC s_0 and a desired final SOC s_f. The constants α_1, α_2, and $\eta_2(x_k, I_k)$ are defined in terms of $i_{0,2}$, α_s, A_{surf}, δ_t, δ_n, $\alpha_{c,2}$, F, R, T, C_2, D_2, and $h_2(s_k)$. Here, C_2, D_2, and $h_2(s_k)$ denote the second row of C, D, and h, respectively.

10.2.2 Extended Kalman filter with forgetting factor

This paper uses an Extended Kalman Filter (EKF) with cross-correlated noise and forgetting factor as a state observer. The forgetting factor is implemented in the estimation schemes to increase the relevance of new observations over previous ones. In particular, the new data is assumed to be exponentially more relevant than the old data, with a factor of γ.

Consider the linear time-varying system represented by the following equations:

$$\begin{cases} \mathbf{x}_{k+1} = \mathbf{A}\mathbf{x}_k + \mathbf{B}I_k + \tilde{\mathbf{w}}_k \\ \mathbf{y}_k = \mathbf{C}\mathbf{x}_k + \mathbf{D}I_k + \tilde{\mathbf{v}}_k, \end{cases} \tag{10.11}$$

where $\tilde{\mathbf{w}}_k = \mathbf{G}_k[\mathbf{w}_k^{\mathrm{T}}, \mathbf{v}_k^{\mathrm{T}}]^{\mathrm{T}}$ and $\tilde{\mathbf{v}}_k = \mathbf{M}_k[\mathbf{w}_k^{\mathrm{T}}, \mathbf{v}_k^{\mathrm{T}}]^{\mathrm{T}}$. We assume that $\mathbb{E}[\mathbf{w}_k\mathbf{w}_k^{\mathrm{T}}] = 1$, $\mathbb{E}[\mathbf{v}_k\mathbf{v}_k^{\mathrm{T}}] = 1$, and $\mathbb{E}[\mathbf{w}_k\mathbf{v}_k^{\mathrm{T}}] = 0$, such that

$$\mathbb{E}\left[\begin{bmatrix}\tilde{\mathbf{w}}_k \\ \tilde{\mathbf{v}}_k\end{bmatrix}\begin{bmatrix}\tilde{\mathbf{w}}_k \\ \tilde{\mathbf{v}}_k\end{bmatrix}^{\mathrm{T}}\right] = \begin{bmatrix}\mathbf{Q}_k & \mathbf{S}_k \\ \mathbf{S}_k & \mathbf{R}_k\end{bmatrix} = \begin{bmatrix}\mathbf{G}_k\mathbf{G}_k^{\mathrm{T}} & \mathbf{G}_k\mathbf{M}_k^{\mathrm{T}} \\ \mathbf{M}_k\mathbf{G}_k^{\mathrm{T}} & \mathbf{M}_k\mathbf{M}_k^{\mathrm{T}}\end{bmatrix}, \tag{10.12}$$

where $\mathbf{Q}_k$ and $\mathbf{R}_k$ are the (time-varying) process-noise covariance and measurement-noise covariance of the noises $\tilde{\mathbf{w}}_k$ and $\tilde{\mathbf{v}}_k$, respectively, and $\mathbf{S}_k$ denotes the cross-correlation between the noises $\tilde{\mathbf{w}}_k$ and $\tilde{\mathbf{v}}_k$. The present section provides an illustration of the essential information required for comprehending the implementation of Kalman Filtering for (10.11). The state equations are linearized for each time instant k to create an EKF implementation. For additional details, interested readers can refer to (Beelen, Bergveld, and Donkers, 2020). The state estimation approach consists of two stages. In the first stage, known as the measurement update, the following are returned:

$$\mathbf{L}_k = \tilde{\mathbf{P}}_k^+ + \mathbf{C}_k^{\mathrm{T}}(\mathbf{C}_k^{\mathrm{T}}\tilde{\mathbf{P}}_k^+ + \mathbf{C}_k + \gamma\mathbf{R}_k)^{-1}, \tag{10.13}$$

$$\hat{\mathbf{x}}_{k+1}^- = \hat{\mathbf{x}}_k^+ + \mathbf{L}_k(\mathbf{y}_k - \mathbf{C}_k\hat{\mathbf{x}}_k^+ - \mathbf{D}_k\, I_k), \tag{10.14}$$

$$\tilde{\mathbf{P}}_{k+1}^- = \frac{1}{\gamma}(\mathbf{I} - \mathbf{L}_k\mathbf{C}_k)\tilde{\mathbf{P}}_k^+, \tag{10.15}$$

whereas in the second stage, the time update computes the final estimate:

$$\begin{aligned}\hat{\mathbf{x}}_{k+1}^+ = {} & \mathbf{A}_k\hat{\mathbf{x}}_{k+1}^- + \mathbf{B}_k\, I_k \\ & + \mathbf{S}_k\mathbf{R}_k^{-1}(\mathbf{y}_k - \mathbf{C}_k\hat{\mathbf{x}}_{k+1}^+ - \mathbf{D}_kI_k),\end{aligned} \tag{10.16}$$

$$\begin{aligned}\tilde{\mathbf{P}}_{k+1}^+ = {} & (\mathbf{A}_k - \mathbf{S}_k\mathbf{R}^{-1}\mathbf{C}_k)\tilde{\mathbf{P}}_{k+1}^-(\mathbf{A}_k - \mathbf{S}_k\mathbf{R}^{-1}\mathbf{C}_k)^{\mathrm{T}} \\ & + \mathbf{Q}_k - \mathbf{S}_k\mathbf{R}^{-1}\mathbf{S}_k^{\mathrm{T}}\end{aligned} \tag{10.17}$$

where $\gamma \leq 1$ is the forgetting factor, which is typically chosen to be close to 1. Section 10.3 tests the proposed approach via simulation, utilizing the surrogate model for control and the more accurate DFN model as the “real" battery to create a realistic scenario.

10.3 Results

In this section, we describe an optimal aging-aware control strategy for battery charging. The strategy is tested in simulation in this section, using a surrogate model for control and a more accurate DFN model (describen in Chapter 3.3.2) as the "real" battery to achieve a realistic scenario. The method incorporates closed-loop optimal control and age-awareness to ensure safe and optimal battery operation during charging. Constraints are placed on the outputs, including the set of virtual outputs and the terminal voltage of the battery cell, to prevent unmodeled battery aging phenomena.

To implement the optimal-control problem in real-time, we have fixed the number of optimal variables to $n = 100$, resulting in an optimization step size of $\delta_t^{\mathrm{opt}} = t_f/n$.

The simulation sampling time is set to 1 second, and the SOC range during the simulation setup is from $s_0 = 0.2$ to $s_f = 0.9$.

To evaluate the performance of the charging method, we employ Pareto-front analysis, a multi-objective optimization technique. The objective of the analysis is to identify the optimal trade-off between two conflicting objectives: minimizing battery degradation and achieving a certain charging time. The Pareto-front represents the set of optimal solutions that provide the best possible trade-off between these two objectives. The ultimate goal is to minimize battery degradation while achieving a certain charging time, ensuring safe and optimal battery operation.

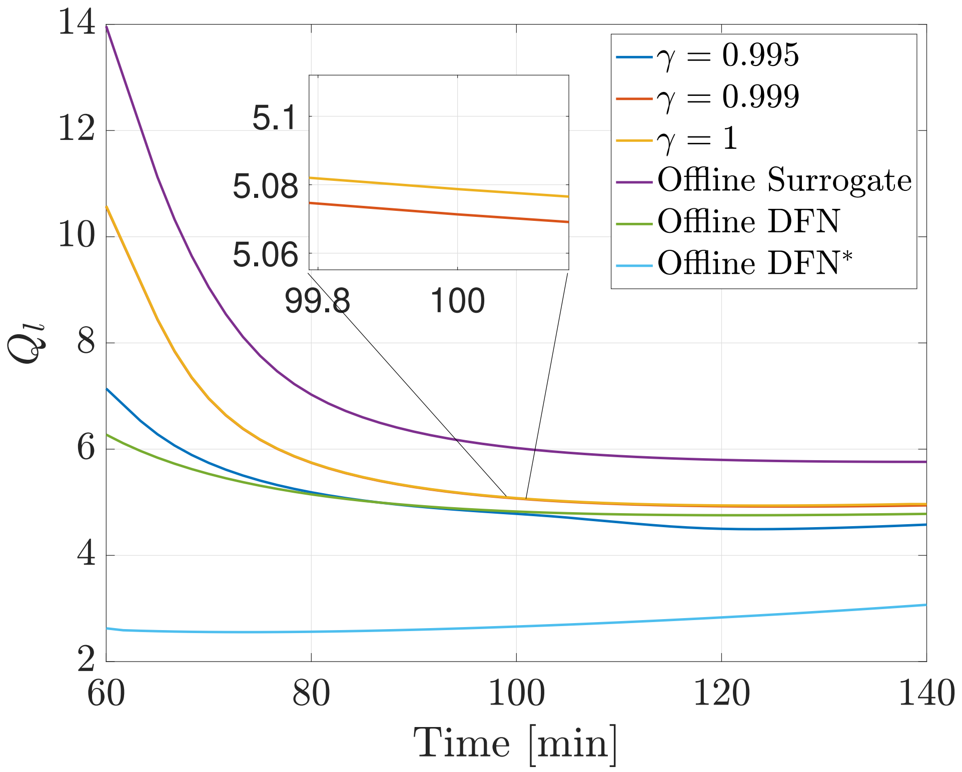

FIGURE 10.4: Trade-off between charging time and Li-ion loss (Q_l) for different ageing-aware charging techniques evaluated from 60 to 140 minutes.

Figure 10.4 presents the Pareto-fronts obtained with different optimal-control-based methods. We test the proposed closed-loop strategy with three values of the forgetting factor ($\gamma \in 0.995, 0.999, 1$), and compare the results with two open-loop optimal control strategies. The first one (offline surrogate) uses the same surrogate model as our proposed method, while the second one (offline DFN) employs the DFN model used for simulating the "real" battery as a benchmark since it uses the same model for optimization and the "real" battery.

Several observations can be made from this figure. First, the surrogate model is a simplification of the DFN model, and therefore the optimal control method based on this model is more effective when used in a closed-loop with an MPC strategy with a shrinking-horizon. The offline surrogate strategy is demonstrated to be better than the CC-CV and multistage protocols standards as analysed in Khalik, Bergveld, and Donkers, 2021.

By varying γ from 1 (pure Kalman Filter) towards lower values, the performances improve, meaning that for a given charging time, we have a lower degradation of the cell. For $\gamma = 0.995$, we notice an improvement concerning our optimality benchmark, which is solving the optimization problem with the true model. This is due to the fact that the problem is non-convex, and in the specific case of the open-loop case using the DFN model for optimization, a local solution is found. This is demonstrated by the fact that by varying the initial guess and setting them equal to the optimal solution found with $\gamma = 0.995$, we see a further improvement of the Pareto-front for the open-loop with the DFN model case (offline DFN*).

Although the open-loop DFN case yields the best achievable curve, it exhibits an increasing behavior over time. This is because, to make the method effectively implementable in real-time, we kept the number of optimization variables constant instead of the step size. This means that for longer charging times, the optimization step size is greater, and therefore the current profile has longer constant intervals.

10.3.1 Influence of the forgetting factor on the state observer

Figures 10.5 and 10.6 show the trends of the state of charge and the voltage across the cell, for a charging time $t_f = 67\text{min}$. It can be seen how as the γ value decreases, the SOC estimate worsens at the expense of better tracking of the voltage measurements. Although the surrogate model has been identified starting from the DFN model, with the open-loop optimization the final SOC is not achieved with precision. Furthermore, the estimate of the voltage made with the surrogate model in an open-loop differs more from the voltage of the "real plant".

10.3.2 Comparison of charging profiles

In this work we considered two cases: a first scenario where only a lower bound on the current has been considered ($I_{\text{min}} = 0$) and a second case in which also an upper bound is taken into account ($I_{\text{max}} = 1C$).

Figure 10.7 shows the optimal current profiles always obtained for $t_f = 67\text{min}$. The optimizations made with the surrogate model return different current profiles in open-loop and closed-loop. The main differences in those profiles are evident especially at both ends of the time interval. The offline surrogate strategy yields higher currents that result in a worse Pareto-front, i.e. worse performance in terms of ageing. Figure 10.8 exhibits the effect of the upper bound on the current. In this case, the current profiles are limited to the upper bound value at the start of charging. This inevitably limits the effect of lowering the degradation of the cell.

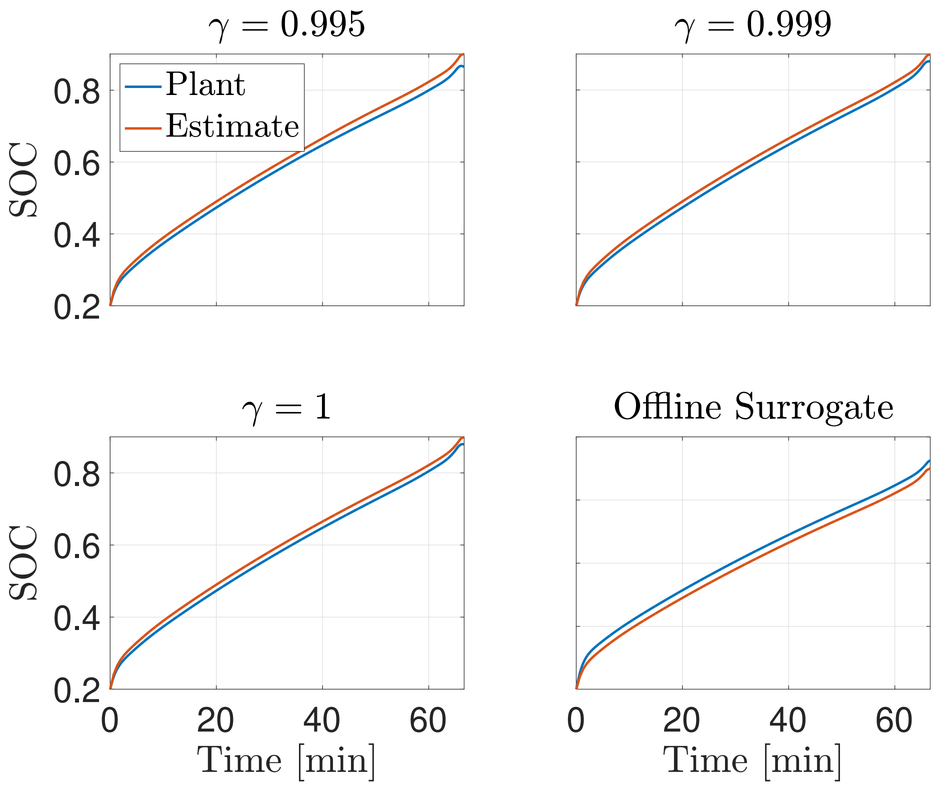

FIGURE 10.5: DFN state of charge (red) and estimated state of charge (blue) using the Kalman Filter with specified forgetting factors γ and simulating (10.11) for open-loop (bottom-right) during a 67-minute charging duration.

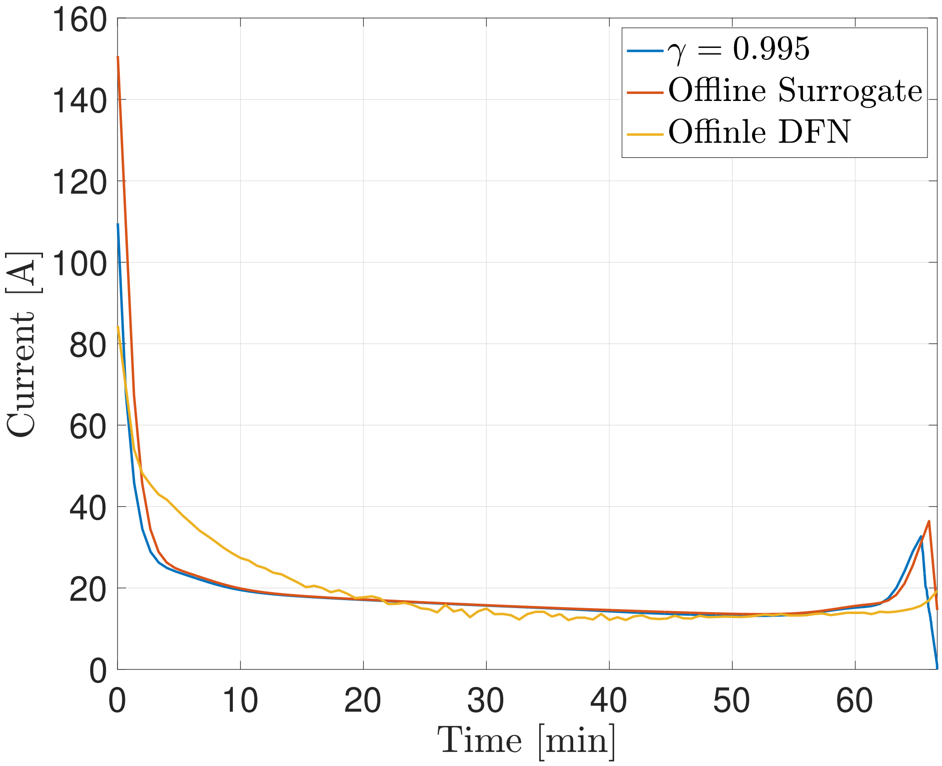

FIGURE 10.7: Current profiles for different ageing-aware charging methods obtained during a 67-minute charging time.

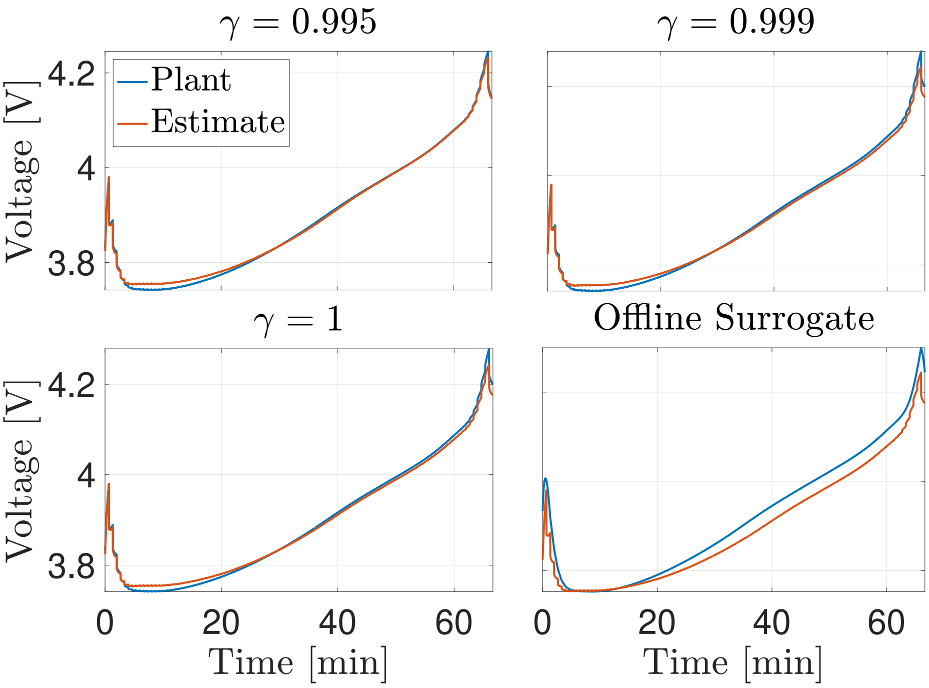

FIGURE 10.6: DFN voltage (red) and estimated voltage (blue) using the Kalman Filter with specified forgetting factors γ and simulating (10.11) for open-loop (bottom-right) during a 67-minute charging duration.

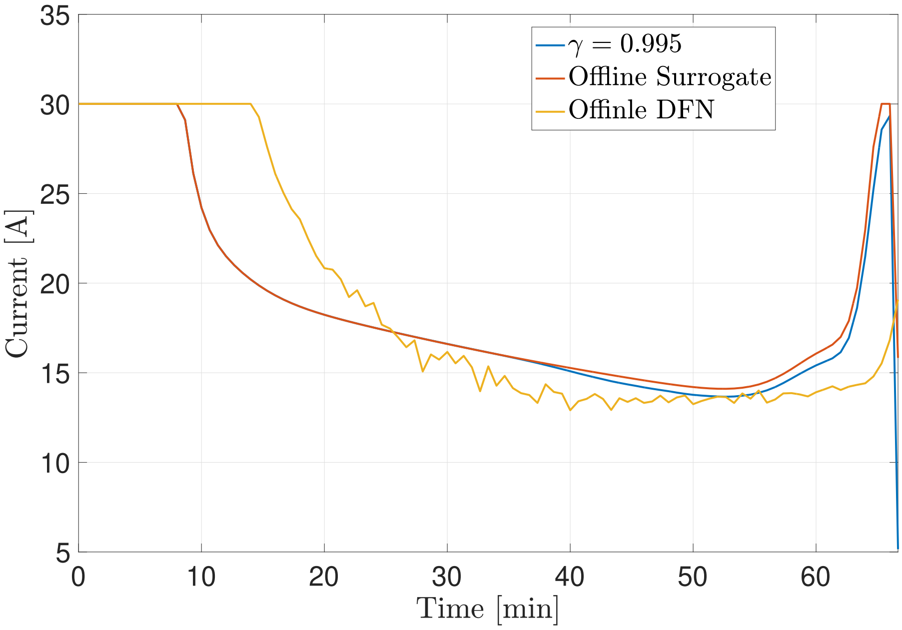

FIGURE 10.8: Current profiles for different ageing-aware charging methods obtained during a 67-minute charging time at $I_{\max} = 1C$.

10.4 Conclusions

In this chapter, we presented an optimal ageing-aware strategy for battery charging that seeks to balance the trade-off between battery ageing and charging time. The approach involves using a Shrinking-Horizon Model-Predictive Control to solve an optimal control problem based on a surrogate model, which minimizes Li-ion loss due to side reactions during charging, subject to input and output constraints, within a specified charging time. The control problem is formulated so that ageing is minimized for a given charging time, and a Sequential-Quadratic-Programming (SQP) approach is used to effectively address this optimal-control problem. Additionally, a state observer is required to close the loop, and we employ the Kalman Filter with a forgetting factor for this purpose.

The problem formulation involves finding the optimal current profile I_k, subject to state dynamics, input and output constraints, and minimum-stored-charge constraint for a specified initial SOC and a desired final SOC.

The approach presented in this chapter allows for a Pareto-optimal solution that balances fast charging and ageing reduction objectives. The chapter also describes the use of an Extended Kalman Filter with a forgetting factor as a state observer.

Overall, this optimal ageing-aware strategy provides a useful framework for balancing competing objectives during battery charging. The approach has significant potential to improve battery performance and increase the lifespan of Li-ion batteries, which are widely used in various applications, including electric vehicles and grid energy storage.

Chapter 11

Conclusions and future work

The rapid advancement of lithium-ion battery technology highlights the need for enhanced estimating and control methodologies for Battery Management Systems (BMS). This PhD thesis made major contributions to the area by tackling critical estimating and control issues. However, it is critical to contextualise the findings within the larger landscape of lithium-ion batteries and the rapidly expanding market.

Lithium-ion batteries are used in a variety of applications, including electric vehicles and portable electronic devices, and are becoming increasingly important in energy storage. Market trends show a growing demand for solutions that are efficient, safe, and long-lasting. In this context, research aiming at improving estimation and control strategies in BMS is critical for optimising battery performance and ensuring operational safety.

This thesis successfully addressed some of the sector's open difficulties, focusing on the development of enhanced estimate and control approaches. However, it is critical to recognise that the subject is constantly evolving, and some challenges remain open. For example, the complexities of ageing dynamics, temperature changes, and ion concentration distributions during fast charging require further investigation.

Among the sector's important outstanding concerns, the need to develop more accurate and computationally efficient models stands out, particularly when extending estimate methods to the closed-loop control phase. The link between the initial set-based estimation topics and subsequent control-related strategies represents a promising research area, emphasizing the necessity to build a deeper connection between the two.

Nevertheless, there exist some significant constraints to the study presented in this thesis and thing that can be further explained, that require attention in future investigations. This section will outline several suggestions for future study, derived on the discoveries made in this thesis.

11.0.1 Application and Computational Considerations

The selection of a battery model depends on the specific application requirements and computational constraints. For instance:

- In real-time control applications, where rapid decision-making and computational efficiency are crucial, simplified ECMs are generally used because they are computationally tractable.

- EMs offer useful insights for in-depth analysis and research-focused investigations that strive to comprehend intricate electrochemical interactions, despite their high processing requirements.

The research has utilised set-based strategies to analyse and manage Equivalent Circuit Models (ECMs) that are commonly used in control applications that need real-time implementation. These strategies provide flexibility by employing ways to reduce complexity, enabling the adjustment of processing time at the cost of a reduced accuracy.

Although this research primarily examined ECMs for their applicability in control-oriented applications, it is important to acknowledge the presence of different battery models in existing literature. These models can contain other variables, such as State of Health (SoH), various thermal dynamics, and ageing effects, to create a more thorough representation in Equivalent Circuit Models.

The approaches outlined in this thesis may be readily applied to diverse battery models, offering a strong foundation for tackling a range of difficulties in battery management. Further study might investigate the use of set-based methodologies on more intricate battery models, including supplementary variables and dynamics to improve the precision and dependability of battery management systems.

11.0.2 Integration of State Estimation Techniques in Battery Control

This thesis primarily focuses on the development and implementation of set-based approaches for robust state and parameter estimation in battery management systems. These strategies have shown promising outcomes in improving the accuracy and reliability of battery monitoring and control.

In Chapter 10, which focuses on battery control techniques, a Kalman filter was used for state estimation instead of the set-based approaches presented in the rest of the thesis. The reason for making this option was to take use of the well-established characteristics and computational effectiveness of the Kalman filter in control applications. While set-based techniques offer robustness and flexibility, the Kalman filter provides a more traditional and widely accepted approach in control theory.

Combining set-based approaches with optimal processes for control is a promising area for future study. The integration of set-based state estimation approaches with optimal control strategies has the potential to enhance the performance and efficiency of battery management systems. Further research might investigate the combined impact of these techniques in order to build battery control systems that are more advanced and adaptable.

This thesis primarily examined the use of set-based procedures for battery status and parameter estimation. However, in Chapter 10, a conscious decision was made to use a Kalman filter to investigate alternate ways in battery control. Combining various state estimation approaches with optimum control procedures has promising prospects for enhancing the battery management systems sector.

It would be advantageous to explore the integration of set-based methodologies with optimum control strategies to create comprehensive and adaptable solutions for battery monitoring and control. This integration has the potential to facilitate the creation of battery management systems that are more efficient, reliable, and flexible, and can satisfy the changing requirements in modern energy storage applications.

To conclude, future works will comprehend: (i) explore the application of set-based methods in the control phase, expanding the connection between estimation strategies and closed-loop control, (ii) conduct in-depth benchtop experiments to validate proposed methodologies under controlled conditions, assessing the robustness and effectiveness of developed models and algorithms, (iii) perform practical tests on real batteries, considering realistic scenarios and operational challenges, to evaluate the performance of proposed methodologies in real-world application contexts. Future research should also focus on the practical and industrial implications of the proposed methodologies, bridging the gap between academic research and the needs of the lithium-ion battery industry. In essence, the thesis lays the groundwork for further investigations aimed at optimizing the efficiency, safety, and lifespan of batteries in an ever-evolving context.

Chapter 12

List of publications

- (Locatelli et al., 2021) Locatelli, D., Rego, B. S., Raffo, G. V., Raimondo, D. M. (2021). Interval state estimation based on constraint propagation for a lithium-ion cell using an equivalent circuit model. IFAC-PapersOnLine, 54(3), 602-608.

- (Saccani et al., 2022) Saccani, G., Locatelli, D., Tottoli, A., Raimondo, D. M. (2022). Model-based thermal fault detection in Li-ion batteries using a set-based approach. IFAC-PapersOnLine, 55(6), 329-334.

- (Rego et al., 2022a) Rego, B. S., Locatelli, D., Raimondo, D. M., Raffo, G. V. (2022). Joint state and parameter estimation based on constrained zonotopes. Automatica, 142, 110425.

- (Locatelli et al., 2022a) Locatelli, D., Saccani, G., Rego, B. S., Raffo, G. V., Raimondo, D. M. (2022, November). Set-based joint state and parameter estimation of a Li-ion cell using constrained zonotopes. In 2022 IEEE Vehicle Power and Propulsion Conference (VPPC) (pp. 1-6). IEEE.

- (Locatelli et al., 2022b) Locatelli, D., Tottoli, A., Saccani, G., Raimondo, D. M. (2022, August). Thermal fault-detection in series connected Li-ion cells: a set-based approach using constrained zonotopes. In 2022 IEEE Conference on Control Technology and Applications (CCTA) (pp. 411-417). IEEE.

- (Locatelli et al., 2023) Locatelli, D., Raimondo, D. M., Khalik, Z., Bergveld, H. J., Donkers, M. T. (2023). Closed-loop Optimal Ageing-Aware Charging of Li-ion Batteries Using a Surrogate Model. In IFAC World Congres.

Bibliography

Abbas, Mazhar, Inho Cho, and Jonghoon Kim (2020). “Analysis of high-power charging limitations of a battery in a hybrid railway system”. In: *Electronics* 9.2, p. 212.

Abraham, DP et al. (2006). “Diagnostic examination of thermally abused high-power lithium-ion cells”. In: *Journal of power sources* 161.1, pp. 648–657.

Aiello, Orazio, Paolo S Crovetti, and Franco Fiori (2015). “Susceptibility to EMI of a Battery Management System IC for electric vehicles”. In: *2015 IEEE International Symposium on Electromagnetic Compatibility (EMC)*. IEEE, pp. 749–754.

Alamo, Teodoro, José Manuel Bravo, and Eduardo F Camacho (2005). “Guaranteed state estimation by zonotopes”. In: *Automatica* 41.6, pp. 1035–1043.

Alamo, Teodoro et al. (2008). “A set-membership state estimation algorithm based on DC programming”. In: *Automatica* 44.1, pp. 216–224.

Albertus, Paul and Johon Newman (2007). “Introduction to dualfoil 5.0”. In: *University of California Berkeley, Berkeley, CA, Tech. Rep.*

Althoff, M. and B. H. Krogh (2011). “Zonotope bundles for the efficient computation of reachable sets”. In: *Proc. of the 50th IEEE Conference on Decision and Control*, pp. 6814–6821.

Andersson, Joel A E et al. (2019). “CasADi – A software framework for nonlinear optimization and optimal control”. In: *Mathematical Programming Computation* 11.1, pp. 1–36.

Andrea, Davide (2010). *Battery management systems for large lithium-ion battery packs*. Artech house.

Balakrishnan, PG, R Ramesh, and T Prem Kumar (2006). “Safety mechanisms in lithium-ion batteries”. In: *Journal of power sources* 155.2, pp. 401–414.

Bandhauer, Todd M, Srinivas Garimella, and Thomas F Fuller (2011). “A critical review of thermal issues in lithium-ion batteries”. In: *Journal of the Electrochemical Society* 158.3.

Beelen, Henrik, Henk Jan Bergveld, and MCF Donkers (2020). “Joint estimation of battery parameters and state of charge using an extended Kalman filter: a single-parameter tuning approach”. In: *IEEE Transactions on Control Systems Technology* 29.3, pp. 1087–1101.

Bergveld, Henk Jan et al. (2002). *Battery management systems*. Springer.

Bhardwaj, Ramesh C, Taisup Hwang, and Richard M Mank (2014). *Modulated, temperature-based multi-CC-CV charging technique for Li-ion/Li-polymer batteries*. US Patent 8,816,648.

Bizeray, Adrien M et al. (2015). “Lithium-ion battery thermal-electrochemical model-based state estimation using orthogonal collocation and a modified extended Kalman filter”. In: *Journal of Power Sources* 296, pp. 400–412.

Bravo, José Manuel, Teodoro Alamo, and Eduardo F Camacho (2006). “Bounded error identification of systems with time-varying parameters”. In: *IEEE Transactions on Automatic Control* 51.7, pp. 1144–1150.

Campbell, Ian D et al. (2019). “Optimising lithium-ion cell design for plug-in hybrid and battery electric vehicles”. In: *Journal of Energy Storage* 22, pp. 228–238.

Chisci, Luigi, Andrea Garulli, and Giovanni Zappa (1996). “Recursive state bounding by parallelotopes”. In: *Automatica* 32.7, pp. 1049–1055.

Combastel, C. (2003). “A state bounding observer based on zonotopes”. In: *2003 European Control Conference (ECC)*, pp. 2589–2594. DOI: `10.23919/ECC.2003.7085991`.

Combastel, Christophe (2005). “A state bounding observer for uncertain non-linear continuous-time systems based on zonotopes”. In: *Proceedings of the 44th IEEE Conference on Decision and Control*. IEEE, pp. 7228–7234.

Daud, Muhamad Zalani, Azah Mohamed, and MA Hannan (2013). “An improved control method of battery energy storage system for hourly dispatch of photovoltaic power sources”. In: *Energy Conversion and Management* 73, pp. 256–270.

Dey, Satadru et al. (2015). “On-board thermal fault diagnosis of lithium-ion batteries for hybrid electric vehicle application”. In: *IFAC-PapersOnLine* 48.15, pp. 389–394.

Di Domenico, Domenico, Anna Stefanopoulou, and Giovanni Fiengo (2010). “Lithium-ion battery state of charge and critical surface charge estimation using an electrochemical model-based extended Kalman filter”. In: *Journal of Dynamic Systems, Measurement, and Control* 132.6.

Ding, Yuanli et al. (2019). “Automotive Li-ion batteries: current status and future perspectives”. In: *Electrochemical Energy Reviews* 2, pp. 1–28.

Doeff, MARCA M et al. (2000). “Transport properties of binary salt polymer electrolytes”. In: *Journal of Power Sources* 89.2, pp. 227–231.

Doyle, Marc, Thomas F Fuller, and John Newman (1993a). “Modeling of galvanostatic charge and discharge of the lithium/polymer/insertion cell”. In: *Journal of the Electrochemical society* 140.6, p. 1526.

Doyle, Marc, Thomas F. Fuller, and John Newman (1993b). “Modeling of Galvanostatic Charge and Discharge of the Lithium/Polymer/Insertion Cell”. In: *Journal of the Electrochemical Society* 140.6, pp. 1526–1533.

Ecker, Madeleine et al. (2015). “Parameterization of a physico-chemical model of a lithium-ion battery: II. Model validation”. In: *Journal of the Electrochemical Society* 162.9, A1849.

Eichi, Habiballah Rahimi and Mo-Yuen Chow (2012). “Modeling and analysis of battery hysteresis effects”. In: *2012 IEEE Energy Conversion Congress and Exposition (ECCE)*. IEEE, pp. 4479–4486.

Fleischer, Christian et al. (2016). “Development of software and strategies for Battery Management System testing on HIL simulator”. In: *2016 Eleventh International Conference on Ecological Vehicles and Renewable Energies (EVER)*. IEEE, pp. 1–12.

Gabbar, Hossam A, Ahmed M Othman, and Muhammad R Abdussami (2021). “Review of battery management systems (BMS) development and industrial standards”. In: *Technologies* 9.2, p. 28.

Gomadam, Parthasarathy M et al. (2002). “Mathematical modeling of lithium-ion and nickel battery systems”. In: *Journal of power sources* 110.2, pp. 267–284.

Gulbinska, M et al. (2011). “Comprehensive improvements in Li-ion batteries for demanding applications”. In: *Journal of Power Sources* 196.5, pp. 2899–2904.

Hagemann, Willem (2015). “Efficient geometric operations on convex polyhedra, with an application to reachability analysis of hybrid systems”. In: *Mathematics in Computer Science* 9.3, pp. 283–325.

Hannan, Mohammad A et al. (2017). “A review of lithium-ion battery state of charge estimation and management system in electric vehicle applications: Challenges and recommendations”. In: *Renewable and Sustainable Energy Reviews* 78, pp. 834–854.

Hansen, Eldon and G William Walster (2003). *Global optimization using interval analysis: revised and expanded.* CRC Press.

He, Hongwen, Rui Xiong, and Jinxin Fan (2011). "Evaluation of lithium-ion battery equivalent circuit models for state of charge estimation by an experimental approach". In: *energies* 4.4, pp. 582–598.

Hossein Nezhad Shirazi, Ali (2020). "Multi-Scale Modeling of Lithium ion Batteries: a thermal management approach and molecular dynamic studies". In.

Hu, X., D. Cao, and B. Egardt (2018). "Condition Monitoring in Advanced Battery Management Systems: Moving Horizon Estimation Using a Reduced Electrochemical Model". In: *IEEE/ASME Transactions on Mechatronics* 23.1, pp. 167–178.

Hu, Xiaosong et al. (2020). "Advanced fault diagnosis for lithium-ion battery systems: a review of fault mechanisms, fault features, and diagnosis procedures". In: *IEEE Industrial Electronics Magazine* 14.3, pp. 65–91.

Jackey, Robyn et al. (2013). "Battery model parameter estimation using a layered technique: an example using a lithium iron phosphate cell". In: *SAE Technical Paper* 2, pp. 1–14.

Jaulin, Luc et al. (2001). "Nonlinear state estimation using forward-backward propagation of intervals in an algorithm". In: *Scientific computing, validated numerics, interval methods.* Springer, pp. 191–201.

Jiang, Jiuchun et al. (2014). "Evaluation of acceptable charging current of power Li-ion batteries based on polarization characteristics". In: *IEEE Transactions on Industrial Electronics* 61.12, pp. 6844–6851.

Jiang, Li et al. (2020). "Optimization of multi-stage constant current charging pattern based on Taguchi method for Li-Ion battery". In: *Applied Energy* 259, p. 114148.

Kang, Taewoo et al. (2020). "Thermal analysis of a parallel-configured battery pack (1S18P) using 21700 cells for a battery-powered train". In: *Electronics* 9.3, p. 447.

Khalik, Zuan, Henk Jan Bergveld, and MCF Donkers (2020). "Ageing-aware charging of lithium-ion batteries using an electrochemistry-based model with capacity-loss side reactions". In: *2020 American Control Conference (ACC).* IEEE, pp. 2213–2218.

— (2021). "Ageing-Aware Charging of Lithium-ion Batteries Using a Surrogate Model". In: *2021 American Control Conference (ACC).* IEEE, pp. 4414–4420.

Khalik, Zuan, MCF Donkers, and Henk Jan Bergveld (2021). "Model simplifications and their impact on computational complexity for an electrochemistry-based battery modeling toolbox". In: *Journal of Power Sources* 488, p. 229427.

Khan, Abdul Basit and Woojin Choi (2018). "Optimal charge pattern for the high-performance multistage constant current charge method for the li-ion batteries". In: *IEEE transactions on energy conversion* 33.3, pp. 1132–1140.

Khan, Md Ashiqur Rahaman (2012). *Development of nanocomposites for energy storage devices.* The University of Texas at El Paso.

Kieffer, Michel, Luc Jaulin, and Eric Walter (1998). "Guaranteed recursive nonlinear state estimation using interval analysis". In: *Proceedings of the 37th IEEE Conference on Decision and Control (Cat. No. 98CH36171).* Vol. 4. IEEE, pp. 3966–3971.

Kiehne, Heinz Albert (2003). *Battery technology handbook.* Vol. 118. CRC Press.

Kim, IL-Song (2009). "A technique for estimating the state of health of lithium batteries through a dual-sliding-mode observer". In: *IEEE Transactions on Power Electronics* 25.4, pp. 1013–1022.

Koksbang, R et al. (1996). "Cathode materials for lithium rocking chair batteries". In: *Solid state ionics* 84.1-2, pp. 1–21.

Kühn, Wolfgang (1998). “Rigorously computed orbits of dynamical systems without the wrapping effect”. In: *Computing* 61, pp. 47–67.

Kvasnica, Michal et al. (2004). “Multi-parametric toolbox (MPT)”. In: *International Workshop on Hybrid Systems: Computation and Control*. Springer, pp. 448–462.

Lai, Qingzhi et al. (2021). “New data optimization framework for parameter estimation under uncertainties with application to lithium-ion battery”. In: *Applied Energy* 295, p. 117034. ISSN: 0306-2619.

Le, Vu Tuan Hieu et al. (2013). “Zonotopic guaranteed state estimation for uncertain systems”. In: *Automatica* 49.11, pp. 3418–3424.

Lee, Yuhyeon, Shrine Maria Nithya Jeghan, and Gibaek Lee (2021). “Boost charging lithium-ion battery using expanded graphite anode with enhanced performance”. In: *Materials Letters* 299, p. 130077.

Li, Jun et al. (2001). “The effects of pulse charging on cycling characteristics of commercial lithium-ion batteries”. In: *Journal of Power Sources* 102.1-2, pp. 302–309.

Li, Matthew et al. (2018). “30 years of lithium-ion batteries”. In: *Advanced Materials* 30.33, p. 1800561.

Li, Xiaoyu and Zhenpo Wang (2018). “A novel fault diagnosis method for lithium-Ion battery packs of electric vehicles”. In: *Measurement* 116, pp. 402–411.

Lin, Xinfan et al. (2014). “A lumped-parameter electro-thermal model for cylindrical batteries”. In: *Journal of Power Sources* 257, pp. 1–11. ISSN: 0378-7753.

Liu, Peng et al. (2018). “Entropy-based voltage fault diagnosis of battery systems for electric vehicles”. In: *Energies* 11.1, p. 136.

Liu, Zhentong et al. (2014). “Fault detection and isolation for lithium-ion battery system using structural analysis and sequential residual generation”. In: *Dynamic Systems and Control Conference*. Vol. 46193. American Society of Mechanical Engineers.

Locatelli, D et al. (2021). “Interval state estimation based on constraint propagation for a lithium-ion cell using an equivalent circuit model”. In: *IFAC-PapersOnLine* 54.3, pp. 602–608.

Locatelli, Diego et al. (2022a). “Set-based joint state and parameter estimation of a Li-ion cell using constrained zonotopes”. In: *2022 IEEE Vehicle Power and Propulsion Conference (VPPC)*. IEEE, pp. 1–6.

Locatelli, Diego et al. (2022b). “Thermal fault-detection in series connected Li-ion cells: a set-based approach using constrained zonotopes”. In: *2022 IEEE Conference on Control Technology and Applications (CCTA)*. IEEE, pp. 411–417.

Locatelli, Diego et al. (2023). “Closed-loop Optimal Ageing-Aware Charging of Li-ion Batteries Using a Surrogate Model”. In: *IFAC World Congres.*

Lu, Languang et al. (2013). “A review on the key issues for lithium-ion battery management in electric vehicles”. In: *Journal of Power Sources* 226, pp. 272–288.

Lucia, Sergio et al. (2017). “Towards adaptive health-aware charging of Li-ion batteries: A real-time predictive control approach using first-principles models”. In: *2017 American Control Conference (ACC)*. IEEE, pp. 4717–4722.

Manzetti, Sergio and Florin Mariasiu (2015). “Electric vehicle battery technologies: From present state to future systems”. In: *Renewable and Sustainable Energy Reviews* 51, pp. 1004–1012.

Meesala, Yedukondalu et al. (2017). “Recent advancements in Li-ion conductors for all-solid-state Li-ion batteries”. In: *ACS energy letters* 2.12, pp. 2734–2751.

Megahed, Sid and Bruno Scrosati (1994). “Lithium-ion rechargeable batteries”. In: *Journal of Power Sources* 51.1-2, pp. 79–104.

Mizushima, K et al. (1981). “Li x CO 2”. In: *Solid state ionics* 7, pp. 314–321.

Moore, Ramon E (1966). *Interval analysis*. Vol. 4. Prentice-Hall Englewood Cliffs.

Moore, Ramon E., R. Baker Kearfott, and Michael J. Cloud (2009). *Introduction to Interval Analysis*. Philadelphia, PA, USA: SIAM. ISBN: 0898716691, 9780898716696.

Moura, Scott J (2015). "Estimation and control of battery electrochemistry models: A tutorial". In: *2015 54th IEEE Conference on Decision and Control (CDC)*. IEEE, pp. 3906–3912.

Moura, Scott J et al. (2016). "Battery state estimation for a single particle model with electrolyte dynamics". In: *IEEE Transactions on Control Systems Technology* 25.2, pp. 453–468.

Nejad, Shahab, DT Gladwin, and DA Stone (2016). "A systematic review of lumped-parameter equivalent circuit models for real-time estimation of lithium-ion battery states". In: *Journal of Power Sources* 316, pp. 183–196.

Neumaier, Arnold (1990). *Interval methods for systems of equations*. 37. Cambridge university press.

Notten, Peter HL, JHG Op het Veld, and JRG Van Beek (2005). "Boostcharging Li-ion batteries: A challenging new charging concept". In: *Journal of Power Sources* 145.1, pp. 89–94.

Ocampo-Martinez, C et al. (2007). "Actuator fault-tolerance evaluation of linear constrained model predictive control using zonotope-based set computations". In: *Proceedings of the Institution of Mechanical Engineers, Part I: Journal of Systems and Control Engineering* 221.6, pp. 915–926.

Perez, Hector Eduardo, Xiaosong Hu, and Scott J Moura (2016). "Optimal charging of batteries via a single particle model with electrolyte and thermal dynamics". In: *2016 American Control Conference (ACC)*. IEEE, pp. 4000–4005.

Perez, Hector Eduardo and Scott J Moura (2015). "Sensitivity-based interval PDE observer for battery SOC estimation". In: *2015 American Control Conference (ACC)*. IEEE, pp. 323–328.

Perez, Hector Eduardo et al. (2017). "Optimal charging of Li-ion batteries with coupled electro-thermal-aging dynamics". In: *IEEE Transactions on Vehicular Technology* 66.9, pp. 7761–7770.

Piller, Sabine, Marion Perrin, and Andreas Jossen (2001). "Methods for state-of-charge determination and their applications". In: *Journal of Power Sources* 96.1, pp. 113–120.

Plett, Gregory L (2006). "Sigma-point Kalman filtering for battery management systems of LiPB-based HEV battery packs: Part 2: Simultaneous state and parameter estimation". In: *Journal of Power Sources* 161.2, pp. 1369–1384.

Poullikkas, Andreas (2015). "Sustainable options for electric vehicle technologies". In: *Renewable and Sustainable Energy Reviews* 41, pp. 1277–1287.

Pozzi, Andrea and Davide M Raimondo (2021). "Optimal Control and Reinforcement-Learning Strategies for Advanced Management of Lithium-Ion Battery Packs". In.

Pozzi, Andrea, Marcello Torchio, and Davide M Raimondo (2018). "Assessing the performance of model-based energy saving charging strategies in Li-ion cells". In: *2018 IEEE Conference on Control Technology and Applications (CCTA)*. IEEE, pp. 806–811.

Pozzi, Andrea et al. (2018). "Optimal design of experiments for a lithium-ion cell: parameters identification of an isothermal single particle model with electrolyte dynamics". In: *Industrial & Engineering Chemistry Research* 58.3, pp. 1286–1299.

Pozzi, Andrea et al. (2020). "Balancing-aware charging strategy for series-connected lithium-ion cells: A nonlinear model predictive control approach". In: *IEEE Transactions on Control Systems Technology* 28.5, pp. 1862–1877.

Rahimi-Eichi, Habiballah et al. (2013). “Battery management system: An overview of its application in the smart grid and electric vehicles”. In: *IEEE industrial electronics magazine* 7.2, pp. 4–16.

Raimondo, Davide M. et al. (2016). “Closed-loop input design for guaranteed fault diagnosis using set-valued observers”. In: *Automatica* 74, pp. 107–117.

Ramadass, P et al. (2004). “Development of first principles capacity fade model for Li-ion cells”. In: *Journal of the Electrochemical Society* 151.2, A196.

Ramadesigan, Venkatasailanathan et al. (2012). “Modeling and simulation of lithium-ion batteries from a systems engineering perspective”. In: *Journal of the electrochemical society* 159.3, R31.

Rauh, A and H Aschemann (2012). “Sensitivity-based state and parameter estimation for lithium-ion battery systems”. In: *Proc. of the IX International Conference SICPRO*, pp. 469–485.

Rausch, Matthias et al. (2014). “Set-based state of charge estimation for lithium-ion batteries”. In: *2014 American Control Conference*. IEEE, pp. 1566–1571.

Rego, Brenner S, Davide M Raimondo, and Guilherme V Raffo (2018). “Set-based state estimation of nonlinear systems using constrained zonotopes and interval arithmetic”. In: *2018 European Control Conference (ECC)*. IEEE, pp. 1584–1589.

Rego, Brenner S et al. (2020a). “Guaranteed methods based on constrained zonotopes for set-valued state estimation of nonlinear discrete-time systems”. In: *Automatica* 111, p. 108614.

Rego, Brenner S. et al. (2020b). “Guaranteed methods based on constrained zonotopes for set-valued state estimation of nonlinear discrete-time systems”. In: *Automatica* 111, p. 108614.

— (2020c). “Guaranteed methods based on constrained zonotopes for set-valued state estimation of nonlinear discrete-time systems”. In: *Automatica* 111, p. 108614. ISSN: 0005-1098.

Rego, Brenner S et al. (2021a). “Set-valued state estimation of nonlinear discrete-time systems with nonlinear invariants based on constrained zonotopes”. In: *Automatica* 129, p. 109638.

Rego, Brenner S. et al. (2021b). “Set-valued state estimation of nonlinear discrete-time systems with nonlinear invariants based on constrained zonotopes”. In: *Automatica* 129, p. 109628.

Rego, Brenner S. et al. (2022b). “Joint state and parameter estimation based on constrained zonotopes”. In: *Automatica*. Accepted. http://arxiv.org/abs/2204.09740.

Rego, Brenner S et al. (2022a). “Joint state and parameter estimation based on constrained zonotopes”. In: *Automatica* 142, p. 110425.

Rump, Siegfried M (1999). “INTLAB – INTerval LABoratory”. In: *Developments in reliable computing*. Springer, pp. 77–104.

Saccani, Giacomo, Gabriele Ciaramella, and Davide M Raimondo (2022). “A computationally efficient implementation of a battery pack electrochemical model using waveform relaxation”. In: *Journal of Energy Storage* 46, p. 103758.

Saccani, Giacomo et al. (2022). “Model-based thermal fault detection in Li-ion batteries using a set-based approach”. In: *IFAC-PapersOnLine* 55.6, pp. 329–334.

Saeedi, Sajad et al. (2016). “Multiple-robot simultaneous localization and mapping: A review”. In: *Journal of Field Robotics* 33.1, pp. 3–46.

Safari, M and C Delacourt (2010). “Mathematical modeling of lithium iron phosphate electrode: galvanostatic charge/discharge and path dependence”. In: *Journal of The Electrochemical Society* 158.2, A63.

Samadi, M.F., S.M.Mahdi Alavi, and M. Saif (2013). “Online state and parameter estimation of the Li-ion battery in a Bayesian framework”. In: *2013 American Control Conference*, pp. 4693–4698.

Santhanagopalan, Shriram et al. (2006). “Review of models for predicting the cycling performance of lithium ion batteries”. In: *Journal of power sources* 156.2, pp. 620–628.

Sarlioglu, Bulent et al. (2016). “Driving toward accessibility: a review of technological improvements for electric machines, power electronics, and batteries for electric and hybrid vehicles”. In: *IEEE Industry Applications Magazine* 23.1, pp. 14–25.

Saw, Lip Huat, Yonghuang Ye, and Andrew AO Tay (2016). “Integration issues of lithium-ion battery into electric vehicles battery pack”. In: *Journal of Cleaner Production* 113, pp. 1032–1045.

Schweppe, Fred (1968). “Recursive state estimation: Unknown but bounded errors and system inputs”. In: *IEEE Transactions on Automatic Control* 13.1, pp. 22–28.

Scott, Joseph K et al. (2016a). “Constrained zonotopes: A new tool for set-based estimation and fault detection”. In: *Automatica* 69, pp. 126–136.

Scott, Joseph K. et al. (2016b). “Constrained zonotopes: a new tool for set-based estimation and fault detection”. In: *Automatica* 69, pp. 126–136.

Scrosati, Bruno (2011). “History of lithium batteries”. In: *Journal of solid state electrochemistry* 15.7-8, pp. 1623–1630.

Shamma, Jeff S. and Kuang-Yang Tu (1997). “Approximate Set-Valued Observers for Nonlinear Systems”. In: *IEEE Transactions on Automatic Control* 42.5, pp. 648–658.

Shareef, Hussain, Md Mainul Islam, and Azah Mohamed (2016). “A review of the stage-of-the-art charging technologies, placement methodologies, and impacts of electric vehicles”. In: *Renewable and Sustainable Energy Reviews* 64, pp. 403–420.

Smith, Raymond B and Martin Z Bazant (2017). “Multiphase porous electrode theory”. In: *Journal of The Electrochemical Society* 164.11, E3291.

Subramanian, Venkat R, Vinten D Diwakar, and Deepak Tapriyal (2005). “Efficient macro-micro scale coupled modeling of batteries”. In: *Journal of the Electrochemical Society* 152.10, A2002.

Sulaiman, Nasrin et al. (2015). “A review on energy management system for fuel cell hybrid electric vehicle: Issues and challenges”. In: *Renewable and Sustainable Energy Reviews* 52, pp. 802–814.

Sulzer, Valentin et al. (2021). “Python battery mathematical modelling (PyBaMM)”. In: *Journal of Open Research Software* 9.1.

Tarascon, J-M and Michel Armand (2001). “Issues and challenges facing rechargeable lithium batteries”. In: *nature* 414.6861, pp. 359–367.

Tomaszewska, Anna et al. (2019). “Lithium-ion battery fast charging: A review”. In: *ETransportation* 1, p. 100011.

Torchio, Marcello et al. (2016). “Lionsimba: a matlab framework based on a finite volume model suitable for li-ion battery design, simulation, and control”. In: *Journal of The Electrochemical Society* 163.7, A1192.

Trasatti, Sergio (1999). “1799-1999: Alessandro Volta’s’ electric pile’-Two hundred years, but it doesn’t seem like it”. In: *Journal of electroanalytical chemistry* 460.1-2, pp. 1–4.

Tulsyan, Aditya et al. (2016). “State-of-charge estimation in lithium-ion batteries: A particle filter approach”. In: *Journal of Power Sources* 331, pp. 208–223.

Uno, Masatoshi, Teruhisa Ueno, and Koji Yoshino (2019). “Cell voltage equalizer using a selective voltage multiplier with a reduced selection switch count for series-connected energy storage cells”. In: *Electronics* 8.11, p. 1303.

Valøen, Lars Ole and Jan N Reimers (2005). “Transport properties of LiPF6-based Li-ion battery electrolytes”. In: *Journal of The Electrochemical Society* 152.5, A882.

Waag, Wladislaw, Christian Fleischer, and Dirk Uwe Sauer (2014). “Critical review of the methods for monitoring of lithium-ion batteries in electric and hybrid vehicles”. In: *Journal of Power Sources* 258, pp. 321–339.

Wang, Zhenpo et al. (2017). “Voltage fault diagnosis and prognosis of battery systems based on entropy and Z-score for electric vehicles”. In: *Applied energy* 196, pp. 289–302.

Weber, Ross M et al. (2019). “Process noise quantification in Kalman filters with application to electrochemical Lithium-ion battery state estimation”. In: *Proc. of 2019 IEEE International Symposium on Industrial Electronics*, pp. 1995–2000.

Whittingham, M Stanley (2004). “Lithium batteries and cathode materials”. In: *Chemical reviews* 104.10, pp. 4271–4302.

Xia, Bing et al. (2017a). “A correlation based fault detection method for short circuits in battery packs”. In: *Journal of power Sources* 337, pp. 1–10.

Xia, L et al. (2017b). “A computationally efficient implementation of a full and reduced-order electrochemistry-based model for Li-ion batteries”. In: *Applied Energy* 208, pp. 1285–1296.

Xiong, Jing et al. (2012). “Failure detection for over-discharged Li-ion batteries”. In: *2012 IEEE International Electric Vehicle Conference*. IEEE, pp. 1–5.

Xiong, Rui et al. (2017). “Critical review on the battery state of charge estimation methods for electric vehicles”. In: *Ieee Access* 6, pp. 1832–1843.

Xiong, Rui et al. (2019). “A sensor fault diagnosis method for a lithium-ion battery pack in electric vehicles”. In: *IEEE Transactions on Power Electronics* 34.10, pp. 9709–9718.

Zhang, Caiping et al. (2017). “Charging optimization in lithium-ion batteries based on temperature rise and charge time”. In: *Applied energy* 194, pp. 569–577.

Zhang, Dong et al. (2020). “Interval Observer for SOC Estimation in Parallel-Connected Lithium-ion Batteries”. In: *2020 American Control Conference*, pp. 1149–1154.

Zhang, Z, D Fouchard, and JR Rea (1998). “Differential scanning calorimetry material studies: implications for the safety of lithium-ion cells”. In: *Journal of power sources* 70.1, pp. 16–20.

Zhao, Yang et al. (2017). “Fault and defect diagnosis of battery for electric vehicles based on big data analysis methods”. In: *Applied Energy* 207, pp. 354–362.

Zhou, Wei et al. (2020). “A novel interval-based approach for quantifying practical parameter identifiability of a lithium-ion battery model”. In: *International Journal of Energy Research* 44.5, pp. 3558–3573.

Zubi, Ghassan et al. (2018). “The lithium-ion battery: State of the art and future perspectives”. In: *Renewable and Sustainable Energy Reviews* 89, pp. 292–308.